DEVELOPMENT AND VALIDATION OF AN ELECTRON MONTE CARLO MODEL FOR AN ELEKTA SYNERGY® LINEAR ACCELERATOR

by

Karl Nicholas Sachse

UNIVERSITY OF THE FREE STATE
UNIVERSITEIT VAN DIE VRYSTAAT
YUNIVESITHI YA FREISTATA

January 2019

Submitted in fulfilment of the requirements in respect of the MMedSc degree qualification in the department of Medical Physics in the Faculty of Health Sciences, at the University of the Free State, South Africa

Supervisor: Dr FCP du Plessis

I dedicate this dissertation to my Father and Mother, Sakkie and Madeléne,

whom without this would not have been possible.

Declaration

I, Karl Nicholas Sachse declare that the MMedSc (Medical Physics) research dissertation that I herewith submit at the University of the Free State, is my independent work and that I have not previously submitted it for qualification at another institution of higher education.

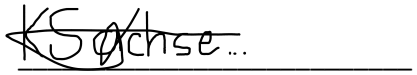

27/04/2019

Karl Nicholas Sachse **Date**

I, Karl Nicholas Sachse declare that I am aware that the copyright is vested in the University of the Free State.

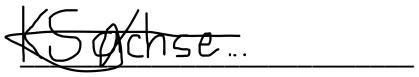

27/04/2019

Karl Nicholas Sachse **Date**

I, Karl Nicholas Sachse declare that all royalties as regards to intellectual property that was developed during the course of and/or in connection with the study at the University of the Free State, will accrue to the University.

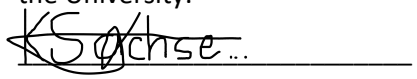

27/04/2019

Karl Nicholas Sachse **Date**

I, Karl Nicholas Sachse declare that I am aware that the research may only be published with the Dean's approval.

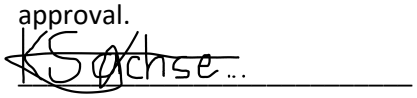

27/04/2019

Karl Nicholas Sachse **Date**

Table of Contents

Abbreviations

1-D	One Dimensional
2-D	Two Dimensional
3-D	Three Dimensional
AAPM	American Association of Physicists in Medicine
AC	Absorption Coefficient
AET	Absorption Equivalent Thickness
BCA	Boundary Crossing Algorithm
BD	Build-Down
BS	Bremsstrahlung Splitting
BSCE	Bremsstrahlung Cross Section Enhancement
BU	Build-Up
CAX	Central Axis
CET	Coefficient of Equivalent Thickness
CH	Condensed History
CM	Component Module
CPU	Central Processing Unit
CSV	Comma-separated Value
CT	Computed Tomography
DBS	Directional Bremsstrahlung Splitting
DTA	Distance to Agreement
EGS	Electron Gamma Shower
FWHM	Full Width at Half Maximum
GUI	Graphical User Interface
ICRU	International Commission on Radiation Units and Measurements
LCA	Lateral Correlation Algorithm
Linac	Linear Accelerator
MAC	Modified Absorption Coefficient
MC	Monte Carlo
MCS	Multiple Coulomb Scattering
MERT	Modulated Electron Radiotherapy
MLC	Multi-leaf Collimator
MP	Medical Physicist
MU	Monitor Units
NTCP	Normal Tissue Complication Probability
OAR	Off-Axis Ratio
ODI	Optical Distance Indicator
PB	Pencil Beam
PBS	Partial Beam Substitution

PDD	Percentage Depth Dose
PEGS	Pre-processor for EGS
PLC	Path-length Correction
PRESTA	Parameter Reduced Electron Step Algorithm
PRNG	Pseudo Random Number Generator
QA	Quality Assurance
RF	Radiofrequency
ROF	Relative Output Factor
SBS	Selective Bremsstrahlung Splitting
SSD	Source-to-surface Distance
TCP	Tumour Control Probability
UAH	Universitas Annex Hospital
UBS	Uniform Bremsstrahlung Splitting

List of Figures

List of Tables

Abstract

Background: The objective for this study was to develop a Monte Carlo (MC) EGSnrc based electron model for an Elekta Synergy® 160-leaf Agility™ linear accelerator (linac) and to validate it against measurements. The requirement was that the developed model should be able to reproduce central axis (CAX) percentage depth dose (PDD) curves, off-axis profiles (OAPs) and relative output factors (ROFs) within 2%/2mm of a subset of measured linac data.

Methods: EGSnrc/BEAMnrc component modules were used to model the linac according to vendor supplied specifications, where multi-leaf collimator and Jaw positions for each electron energy-applicator combination were obtained from log files. Since the initial electron beam properties (focal spot size and shape, energy spectrum) were unknown, the effects of these parameters on electron CAX PDDs and OAPs were investigated and by means of iterations the set of parameters producing the best match with measured water tank data were identified. Phase space files generated by these models were used as source input in EGSnrc/DOSXYZnrc where a unit-density water phantom was modelled, and dose distributions were calculated and extracted accordingly. Six electron nominal energies, 11 field sizes and two source-to-surface distances (SSDs) were evaluated. MATLAB® scripts were developed to process and analyze both simulated and measured data.

Results: BEAMnrc could successfully be used to model each component in the path of the initial electron beam. The electron focal spot shape was determined from measured inline and crossline profiles and was found to be circular since secondary scattering foil geometries exemplified radial symmetry. The full width at half maximum (FWHM) of the focal spot (assuming a Gaussian intensity distribution) was determined iteratively from simulations and a set value of 1.50 mm was chosen. A monoenergetic and two different poly-energetic energy spectrums (symmetrical Gaussian and asymmetrical experimental spectrum) were investigated for their effects on CAX PDDs and OAPs. The asymmetrical energy spectrum with a low-energy tail produced satisfactory results within component dimensional tolerances and solved the match in the build-up region for all electron energies. Simulated data complied to measured data with a 100 % pass rate using a 2%/2mm criterion.

Conclusions: The developed MC EGSnrc electron model was able to predict dose distributions within 2%/2mm of measured PDDs and OAPs, and ROFs within 3 %. The underlying success of the model is embedded in the experimental energy spectrum which provided a valuable free parameter which, by fine adjustment, improved the match in the build-up region of dose distributions. Furthermore, focal spot

parameters could be determined by means of simulations and thereby circumvented the difficulty associated with the measurement of the focal spot.

Keywords: Electron modelling, Monte Carlo, `EGSnrc`, `BEAMnrc`, `DOSXYZnrc`, Energy spectrum, Focal spot

Chapter 1: Introduction

1.1 A Positive View on a Negative Particle

It is in 1897 that English physicist and Nobel Laureate in Physics, *Joseph J. Thomson*, discovered and identified a new species of particle during experiments involving the well-known Crookes tube. Thomson named this elementary particle an *electron*, which originates from the Greek word "*elektor*" meaning "*beaming sun*", particularly referring to the, then unknown, cathode rays attracted to the anode of the Crookes tube. Thomson quantified the mass of the negatively charged electron to be approximately 1800 times less than that of a proton and also quantified the ratio of the electron's electric charge to its mass.[1,2] This extraordinary discovery not only had repercussions in the world of particle and quantum physics, but also opened the door to the clinical application of electrons in Radiotherapy for the treatment of superficial lesions.

Three decades following the discovery of the electron, high-energy electron beams were generated by a Van de Graaff generator for usage in Radiotherapy. However, these generators were replaced by the development of the betatron in 1940 by American physicist *Donald W. Kerst*; a cyclic electron accelerator able to produce higher clinical electron beams.[3,4] Though betatrons were able to produce electron beams with energies up to 50 MeV, these machines produced limited beam currents.[1,5] The betatron was superseded by the microtron in 1944 which was initially proposed by *Vladimir I. Veksler*, and was able to produce much higher beam currents. The microtron (racetrack and circular variants) was used in Radiotherapy since it was able to produce electrons with energies from 5-50 MeV, with the first prototype built in Canada in 1948.[2] However, over the past four decades cyclic linear accelerators (linacs) have undergone remarkable advancements up to the point where the generation of high energy megavoltage photon and electron beams is possible, with the option to modulate these beams for conformal dose delivery as well as on-board imaging devices for adaptive Radiotherapy.[2] Photon beams have always received more attention than electron beams, especially since Cobalt irradiators were widely available since the 1950s. Within the Radiotherapy community, the interest in electron beams started to develop when the MD Anderson Hospital and Tumor Institute started to illustrate the usefulness of megavoltage electron beams.[3]

1.2 Linear Accelerator

Modern linacs used in Radiotherapy produces megavoltage photon and electron radiation with different energies which can be shaped into almost any regular/irregular fields to optimize patient cancer treatments. Energetic radiation is produced by the acceleration of electrons with the use of microwaves, where these energetic electrons can then either be used for electron beam treatments or can be directed onto an X-ray target for photon production and associated treatments. Electrons gradually acquire energy while moving in a rectilinear motion throughout the waveguide[2] by interacting with a synchronized radiofrequency (RF) electromagnetic field.[1] This is made possible by 6 major components including the injection system, RF power generation system, accelerating waveguide, auxiliary system, beam transport system, beam collimation and beam monitoring system, as described in Podgorsak et al.[2]

Either diode or triode electron guns are used to inject electrons into the waveguide. Microwaves produced for electron acceleration in the waveguide in the energy range of 4-25 MeV are in the frequency range from 10^3 MHz (L band) to 10 MHz (X band). The waveguide is divided into cylindrical cavities using irises which controls the speed of propagation of the microwaves.[1,2] Accelerated electrons are focused by external magnets to stay close to the central axis (CAX) of the evacuated, water cooled waveguide as well as to ensure a small, sharply focused focal spot for the exit electrons. A bending magnet system[1,2] directs this beam into the treatment head, which is a 112.5° system for an Elekta Synergy® Agility™ (Elekta Oncology Systems, Crawley, UK) linac. This results in a sharply focused pencil beam with a narrow focal spot, typically Gaussian in profile.

For electron beams, the linac head contains scattering foils with an energy-dependent thickness and specific atomic number to favour electron scattering when using clinical electron beams. The change in the Gaussian-shaped intensity distribution of the electron beam due to scatter by a scattering foil is indicated in Figure 1-1. The intensity distribution of electrons emerging from the primary scattering foil has a Gaussian distribution, but this alone will not produce a flat beam at depth within a medium. This problem is either solved with the use of applicators to introduce a sufficient amount of scattering onto the edges of the beam (i.e., to improve flatness in the central region of the beam) in combination with optimal multi-leaf collimator (MLC) and diaphragm positions since these secondary collimation devices introduces scattered electrons into the field, or by introducing a secondary scattering foil (i.e., dual scatter foil systems). The secondary scattering foil contains several foils, each with varying thicknesses and radius as to gradually flatten out the beam. Figure 1-1 illustrates this effect. In the case of the Synergy® linac, a

low-energy and high-energy secondary scattering foil is used. Secondary collimation devices however still play a role in final beam formation.

Beam collimation is achieved with a primary collimator which projects a fixed cone angle and sets a limit on the maximum field size achievable at a given SSD.[1,2] Secondary collimation systems provide final beam collimation to the required field size for treatment and include, in modern linacs, a MLC and backup diaphragm(s)/Jaw(s). Electron beams furthermore require an externally attachable applicator/cone to provide additional shaping of electron beams. Electron applicators are an essential part of electron beam collimation even in dual-scatter foil linacs. Applicators not only delineate the field close to the patient surface, but also helps to "funnel" electrons toward the patient surface since electrons are scattered easily in air. This is achieved by introducing scattered electrons into the field to compensate for electrons scattered out of the beam and essentially aids in beam flatness. Modern day applicators are often more open and lighter and are made up of successive layers (or trimmers) that collimates any electron that scatters out of the field. The trimmer material is chosen as such to minimize bremsstrahlung production/contamination, and the field size collimated by the successive trimmer layers gradually decreases up to the required field size at the patient surface.

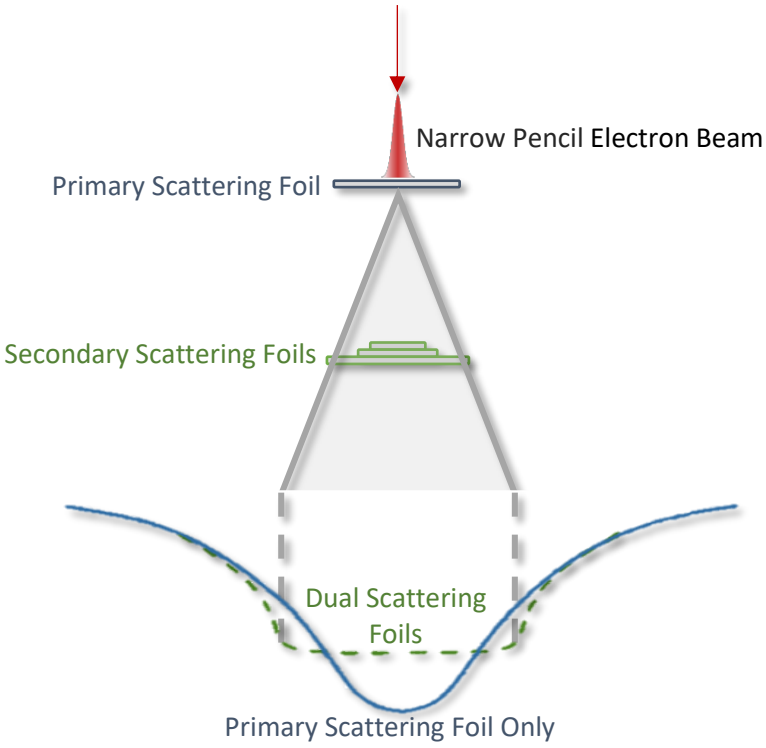

Figure 1-1: Electron pencil beam broadening with a dual scattering foil system. The broadening due to the primary scattering foil (blue) only results in a field which is Gaussian in intensity. This intensity is flattened out by the secondary scattering foils which gives a flat intensity beam throughout the central region of the field. The penumbra for the field produced by the dual scattering foil system is also decreased as compared with the field produced by the primary scattering foil only. Figure adapted from Karzmark.[6]

Figure 1-2 illustrates two different views of a linear accelerator and the definition of the major radiation axis used within Radiotherapy as well as within this project. The axis stretching from top to bottom is the Z-axis, which is also the CAX of the radiation beam, with the downwards position being the positive Z-direction. The X-axis stretches horizontally when looking at a view from the front of the accelerator, with the negative- and positive X-directions corresponding to left and right directions, respectively. Similarly, the linac is often described as having axis A-B, with direction A corresponding to the negative X-direction and direction B corresponding to the positive X-direction. Looking at a view from either side of the linac, the Y-axis is stretches horizontally, with the negative Y-axis towards to linac (corresponding to linac axis G – *Gun*) and the positive Y-axis away from the linac (corresponding to linac axis T – *Target*). In general, the X-axis is referred to as being in a crossline relative to the linac, whereas the Y- direction is referred to as being inline relative to the linac. For electron beams the nominal SSD is defined at the position of final

collimation which is at the position of the inferior part of the open field insert within the electron applicator, which corresponds to $SSD = 95$ cm.

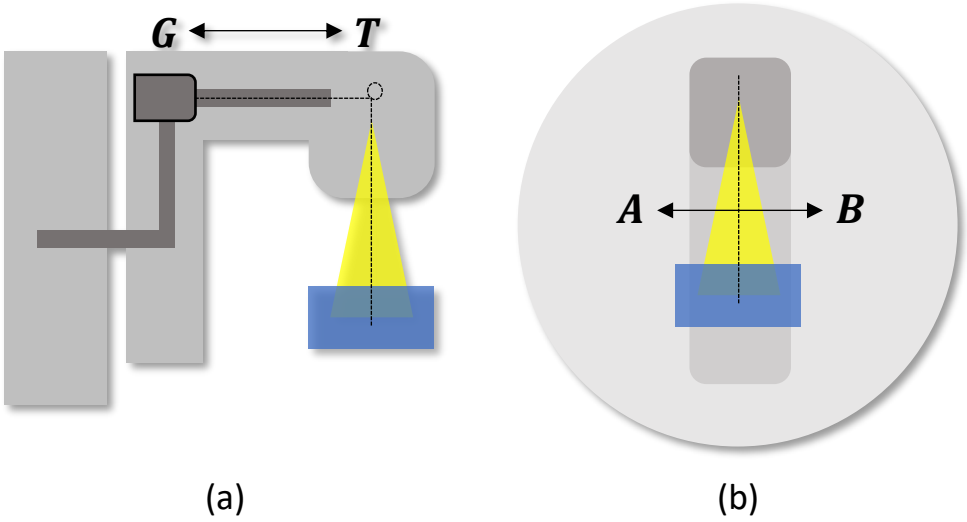

Figure 1-2: Schematic illustration of radiation axis used in radiotherapy as seen from a) a side view and b) a view from front of a linear accelerator.

1.3 Electrons in Radiotherapy

Clinical electron beams have been used to perform several cancer treatments, including the treatment of intact breast lesions, chest wall irradiation for breast cancer, skin cancers, total scalp treatments, cancer of the parotid, nose, eye/orbit and eyelid, retinoblastomas, craniospinal irradiation, boost treatments (breast, head-and-neck) and applications in Intraoperative Radiotherapy.[3,7] The major advantage of electrons is the sparing of healthy tissues distally to the target with a high degree of target dose conformity. At the Universitas Annex Hospital (UAH) Oncology Centre (Bloemfontein, South Africa), common electron treatment sites involve head-and-neck, boost treatments for breast cancer, vulva and total skin electron irradiation for Mycosis Fungoides. Total Skin Irradiation is performed by removing the electron applicator and collimating the electron beam to the maximum field size using only the backup jaws and the MLC, with zero gantry movement and a high dose rate delivery.[8] Electron arc therapy involves gantry movement with a stationary field and is most effective if the treated area has a constant radius of curvature. Intraoperative treatments usually involve custom linac designs to deliver small electron fields directly to the tumor bed following surgical resection with a short SSD.[7]

The interest in modulated electron radiotherapy (MERT) has grown lately, which aims to modulate electrons using the photon MLCs (or using an attachable electron MLC [eMLC]) without the use of any tertiary collimation devices such as electron applicators. Many studies have been performed where Monte Carlo (MC) based beam models have been developed using the `EGSnrc` code package. MERT treatments are performed at shorter SSDs (typically 60-70 cm) and field sizes can be both regular and irregular.[9–21]

1.4 Motivation for Study

Currently, electron treatment planning at the UAH Oncology is limited to older algorithms and does not include MC based methods with good machine commissioning. Manual hand calculations are performed by Medical Physicists to determine the Monitor Units (MUs) required to deliver the prescribed dose (this is of course dependent on the electron nominal energy, field size, cone and cutout factors and depth of dose prescription) to the patient. This is however insufficient for the purposes of MERT and therefore dose calculations must be replaced by a MC based algorithm (see section 2.2). The motivation for this particular study is to develop such a MC based model for the electron beam delivery system of one of the linacs at UAH Oncology, which can then be used in subsequent studies to develop MERT which will enable optimization of patient plans with decent MC treatment planning. Since MERT utilizes fields with any shape and size, the model must be extremely accurate and must also be benchmarked against measured data.

Though MC studies of linacs is a well covered topic, this particular study will also focus on the determination of unknown electron beam characteristics such as the electron focal spot and incident energy spectrum. These parameters are not vendor supplied and they are often very challenging to physically measure. In accordance to literature, both a monoenergetic and poly-energetic (Gaussian) energy spectrum will be investigated. However, an experimental poly-energetic energy spectrum will also be added in order to distinguish this study from other similarly published studies.

According to the American Association of Physicists in Medicine (AAPM) Task Group No. 65[22], an acceptable level of accuracy (or uncertainty) of the developed model is 2 %, therefore the model was assessed with a maximum Gamma criteria of 2%/2mm (see section 2.3). Electron beam setups evaluated included six clinical electron energies (4, 6, 8, 10, 12 and 15 MeV), 11 field sizes (2 x 2, 3 x 3, 6 x 6, 10 x 10, 14 x 14, 20 x 20, 6 x 10, 6 x 14, 8 x 16, 10 x 20 cm^2 and a 4 cm diameter circular field) and two SSDs (95 and 100 cm). CAX percentage depth dose (PDD) curves (see section 2.1.2), crossline and inline off-axis

profiles (see section 2.1.3) and relative output factors (see section 2.1.4) were used to compare the model with measurements.

1.5 Aim

The aim for this study was to develop an electron Monte Carlo model for an Elekta® Synergy 160-leaf Agility™ linear accelerator and to validate the model against measurements.

Chapter 2: Theory

2.1 Electrons

2.1.1 Electron Interactions

Electrons will interact with the atomic orbital electrons and atomic nuclei via Coulombic field interactions. These interactions are either collisional/radiative or elastic/inelastic events. Elastic scattering refers to the Coulomb interactions that are collisional and causes small angle deflections of the incident electrons, accompanied with small energy losses. Multiple of these elastic collisions occur within a medium and is the dominant interaction type of electrons within a medium.[1] Various *multiple scattering* theories have been developed to describe the elastic scattering nature of electrons (*Fermi-Eyges*[23], *Molière*[24,25], *Goudsmit-Saunderson*[26,27]).

Inelastic scattering events refer to the Coulomb interaction of incident electrons with atomic orbital electrons (Møller interactions) as well as those nuclear Coulomb interactions that are radiative of nature (bremsstrahlung interactions). Electrons lose energy continuously via inelastic collisions, which can lead to atomic excitation or even atomic ionization with the subsequent ejection of a knock-on electron, as is the case with Møller interactions. The knock-on electron can obtain up to half of the initial electron's kinetic energy since the two electrons are indistinguishable.[28] Now and then an electron-nucleus interaction is radiative, which means that the electron's path is significantly deflected by the Coulombic force exerted by the atomic nucleus when the electron is in close proximity to the nucleus. This causes a significant deceleration of the incident electron and the subsequent emission of a bremsstrahlung photon with an energy equal to the energy lost by the decelerated electron.[1–3]

If positrons are formed and subsequently interact with atomic orbital electrons, these inelastic interactions are described as Bhabha interactions. However, it is also possible for positrons to annihilate with atomic orbital electrons to produce characteristic photons in the process (which is in fact a radiative interaction which leads to the coupling of electron and photon fields). Inelastic scattering events can be regarded as discrete events since they cause large angle deflections and large energy losses.

2.1.2 Central Axis (CAX) Percentage Depth Dose (PDD) Curves

2.1.2.1 Overview

Electrons lose their energy continuously in water or tissue at a rate of approximately 2 $MeV \cdot cm^{-1}$. When entering a medium, electrons from a therapeutic electron beam are essentially incident parallel to one another (as well as to the CAX of the beam) and normal to the medium surface. However, the mean paths travelled by electrons quickly change with depth inside the medium due to elastic and inelastic events in agreement with the mean square scattering angle for the medium which will initially increase until the beam is fully dispersed. The rate of directional change of electrons depends on the energy of the electrons as well as the atomic number of the absorbing material. Higher energy electrons are harder to deflect and hence will experience a smaller degree of obliquity in pathlengths than that of lower energy electrons, whereas higher atomic number absorbers cause a greater amount of deflection per unit distance travelled.

The dose distribution along the CAX of the radiation beam is an essential component to describe the volume irradiated by a specific beam setup, and is therefore measured for each beam energy, field size and SSD combination used clinically. This gives a 1-dimensional (1 D) description of the dose distribution of the true beam with depth into the medium along the beam's CAX. Electron CAX PDD curves are characterized by a Build-Up (BU) region, a region of maximum dose, a Fall-Off/Build-Down (BD) region and a Tail/bremsstrahlung region. Energy and range parameters on these curves are good indicators of the appropriate beam energy to be used for treatment situations.

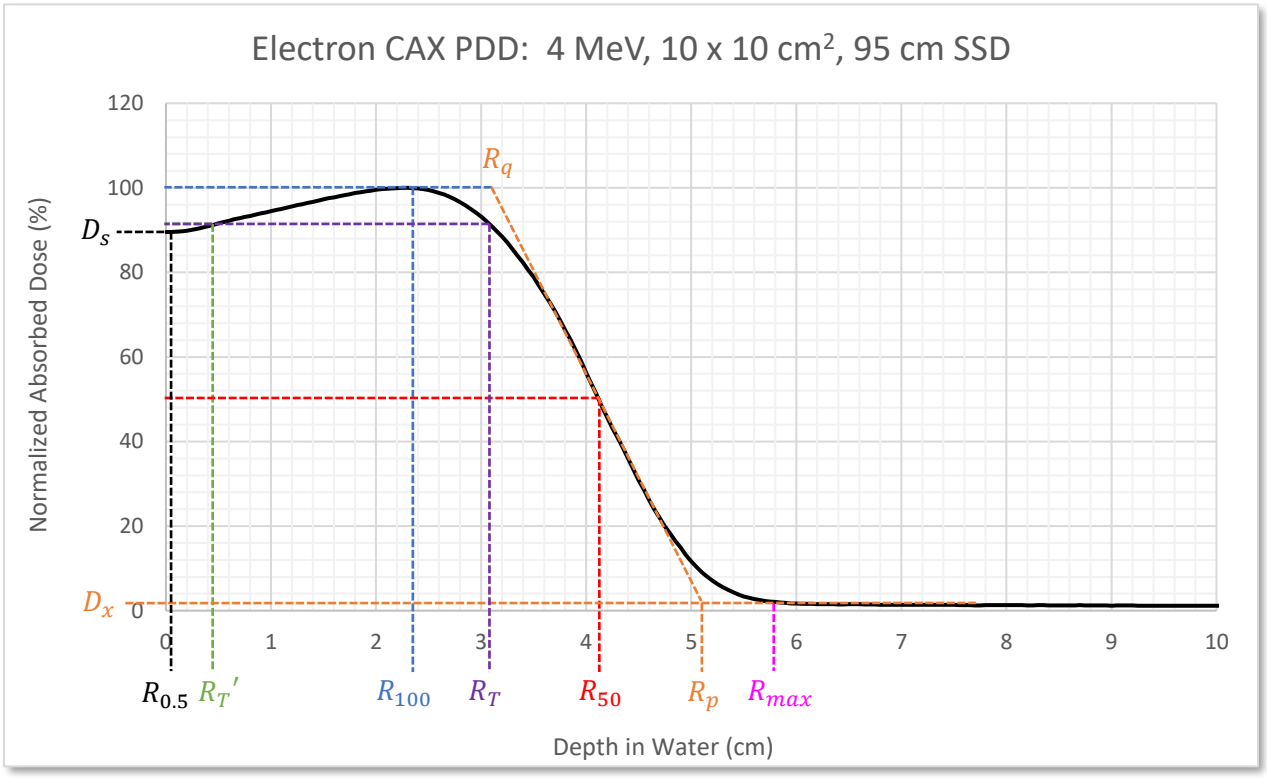

Figure 2-1: A CAX PDD for a 10 MeV, 10 x 10 cm² electron beam from an Elekta Synergy® 160-leaf Agility™ linear accelerator measured within water at an SSD of 95 cm with a Roos® Chamber. Dose and range parameters that characterize the PDD curve are indicated as per recommendation of the 32nd report of the International Commission on Radiation Units and Measurements, Radiation Dosimetry.[5,29] *The therapeutic range here represents 90 % dose level, however other dose values can be assigned to the therapeutic dose.*

2.1.2.2 Build-Up (BU) Region

The first region of the electron CAX PDD curve is the BU region. One of the most prominent and attractive characteristics for the therapeutic use of electrons includes the high surface dose exhibited, typically between 75 % - 100 % of the maximum dose depending on the electron beam parameters. This means that the BU region is much less pronounced and gives rise to the second attraction for the therapeutic use of electrons; a more uniform dose distribution from the surface to the distal 90 % (or 85 %) dose region (therapeutic range).[1]

The BU region seen in electron PDDs occurs due to the contribution of two phenomena which are described in detail in literature. [1,4] The first is a smaller contribution and is known as the knock-on electron BU, whereas the second and far more dominant contributor to the BU region is that of increasing oblique paths of the incident electrons. The knock-on electron BU occurs due to an initial increase of electron fluence (and hence a proportional increase in absorbed dose) with depth into the absorbing medium due

to secondary electron (δ-electron) formation in hard collisions. This effectively means that for a fixed depth segment, the fluence of electrons passing through the segment will increase with depth. However, the dose within a depth segment does not only depend on the fluence through the segment, but also depends on the path lengths of electrons traversing that segment.[1] With depth into the absorbing medium, the individual path lengths travelled by electrons will become more oblique as they are scattered by elastic and inelastic events. This effectively means that for a fixed depth segment traversed, electrons travelling with an oblique path will deposit more energy as electrons travelling with a straight path through that depth segment.

2.1.2.3 Depth of Maximum Dose

The depth of maximum dose is the depth within the medium at which an equilibrium exists between the build-up of electrons and the loss of electrons from the beam, which is also the point where the amount of dose deposited reaches its maximum value. At greater depths, more electrons travel at more oblique paths, however, more electrons are also lost from the beam since electrons are completely stopped within the medium. This region reflects the saturation of the mean square scattering angle which means that the beam is fully dispersed.

The difference in obliquity and the relation between the surface dose and the maximum dose for different energy electron beams is explained in detail in literature.[1,5] Lower energy electrons are easier to deflect than higher energy electrons, and assuming continuous energy loss, lower energy electrons will be less penetrative than higher energy electrons. Therefore, the depth of maximum dose shifts to higher depths for higher energy electrons, as indicated in Figure 2-2. However, since lower energy electrons are easier to deflect, the degree of obliquity at the depth of maximum dose is higher for lower energy electrons than for higher energy electrons. This effectively means that, since the pathlengths of electrons near the surface of the absorbing medium are essentially straight, the difference in obliquity on the surface and at the depth of maximum dose will be more pronounced for lower energy electron beams than for higher energy electron beams. Therefore, the surface dose increases (relative to the maximum dose) with an increase in electron energy, as shown in Figure 2-2. This feature does however depend on the design of the linac which is mentioned in section 2.1.2.8.

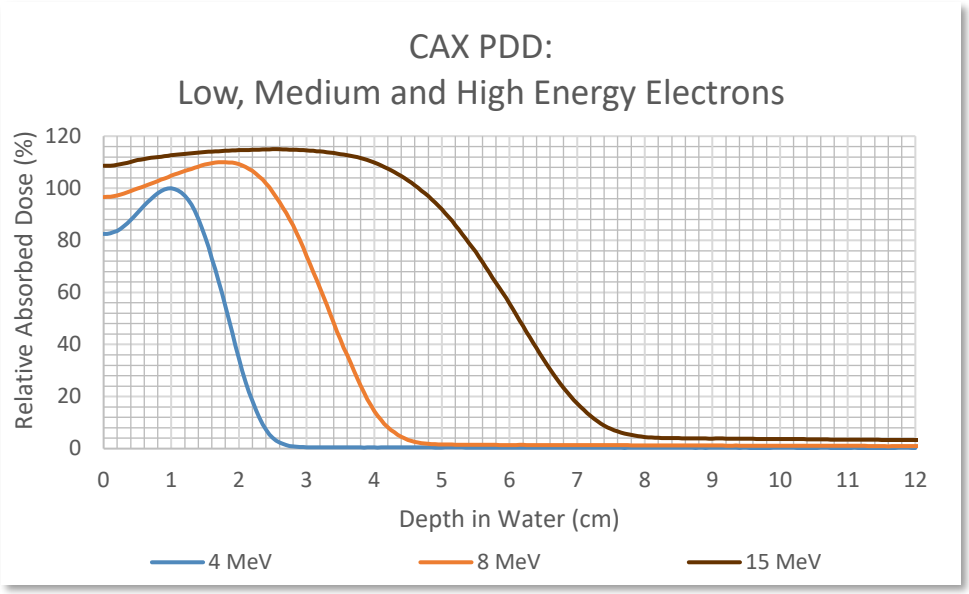

Figure 2-2: Graphical illustration of the differences in the BU region and the Maximum Dose region between a low energy (4 MeV), a medium energy (8 MeV) and a high energy (15MeV) electron beams from an Elekta Synergy® 160-leaf Agility™ linear accelerator measured within water with a Roos® Chamber, for a 10 x 10 cm^2 field size and SSD of 95 cm. Lower energy electrons are more prone to undergo multiple Coulomb scatter events and therefore there exists a higher difference in obliquity between the surface dose and the maximum dose, with a more pronounced BU region. This effect scales down with higher energy electron beams since those electrons are harder to deflect, in accordance with the inverse energy square dependence of the angular scattering power.

2.1.2.4 Build-Down (BD) Region

Beyond the depth of maximum dose, the BD region is reached where the dose starts to decrease rapidly with an almost constant rate. The BD, or dose fall-off region, occurs due to electrons being lost from the beam either due to the complete stopping of the electrons within the medium or due to the dispersing of electrons out from the beam (i.e., electrons are scattered out of the field).[4] Prior to the depth of maximum dose, very little electrons are lost from the beam since electrons are still energetic. However, beyond the depth of maximum dose the loss of electrons becomes the most prominent phenomenon. The rate at which these losses occur with depth depends mostly on the energy of the initial electron beam and is based on the phenomenon of energy-loss straggling, which is described in literature.[1]

Electron CAX PDD curves are typically characterized by, amongst other parameters, the dose gradient in the BD region. As defined by the International Commission on Radiation Units and Measurements (ICRU)[29], the dose gradient G_0 is given by the relation:

$$G_0 = \frac{R_p}{R_p - R_q} \qquad \text{Eq 2.1}$$

where R_p is the projected practical range of the electrons, and R_q is defined as in section 2.1.2.6.[29]

The electron CAX PDD curve can essentially be described as a balance between the increasing obliquity of the electron pathlengths and electrons being lost from the beam due to complete stopping within the medium. Within the BU region this balance is dominated by the increase in electron obliquity and fluence with depth, since very few electrons are lost from the beam. Beyond the depth of maximum dose the loss of electrons dominates the balance which results in a gradual dose decrease until all of the electrons are stopped within the medium.[1,4]

2.1.2.5 Tail Region

The final part of the electron CAX PDD curve is the tail region, also termed the bremsstrahlung tail since the dose within this part is entirely due to the contribution of bremsstrahlung photons. The total bremsstrahlung component consists of mainly bremsstrahlung photons produced within the linac head and those produced within the absorbing medium.[1,3–5] Bremsstrahlung generation occurs within the linac when electrons interact with beam broadening- and beam shaping devices, such as primary and secondary scattering foils, the MLC, the Jaw(s), applicator and open field insert. Some bremsstrahlung production also occurs within the air between the absorbing medium and the linac. It has been shown by Rustgi and Rogers[30] that the head-generated photons dominate the total photon dose component of an electron CAX PDD curve in water for electron beam energies of less than 18 MeV with a negligible contribution of phantom-generated photons. However, phantom-generated photons become significant once the beam energy and atomic number of the absorbing medium is increased, as illustrated in Eq 2.2.[31]

The rate of bremsstrahlung production, or the rate of energy loss, by electrons (or positrons) traversing a medium is governed by the mass radiative stopping power $\frac{S_{rad}}{\rho}$, which is given by:

$$\frac{S_{rad}}{\rho} = \sigma_0 \frac{N_A Z^2}{A} (E_k + m_e c^2)^2 \overline{B}_r \qquad \text{Eq 2.2}$$

where $\sigma = \alpha \left(\frac{e^2}{4\pi\varepsilon_0 m_e c^2}\right)^2$, with α the fine structure constant. $\bar{B}_r$ is a function of the absorbing medium atomic number Z and electron kinetic energy E_K.[1] From Eq 2.2 it is evident that bremsstrahlung production will increase if the factors Z and E_K increases (with an increase in Z and E_K the factor $\bar{B}_r$ also increases).

2.1.2.6 Range and Dose Parameters

Various electron range and dose parameters on the CAX PDD curve are identified by the ICRU as shown on the graph in Figure 2-1. These parameters are useful to characterize CAX PDD curves, but also act as indicators used in routine quality assurance (QA), beam energy specification as well as dose specification.[4] Dose and range parameters defined by the ICRU[29] are indicated in Table 2-1.

Table 2-1: Electron dose and range parameters typically used in the characterization of central-axis depth-dose curves as defined by the ICRU.[29]

Parameter	*Description*	*ICRU Report 35 Definition*
	DOSE PARAMETERS	
D_s	Relative Surface Dose	The entrance or surface absorbed dose expressed as a fraction of the maximum dose.
$D_T{}'$	Proximal Therapeutic Dose	The dose, usually 85% or 90 % of the maximum dose, between the surface and maximum dose.[a]
D_{max} *or* D_{100}	Maximum Dose	The point (or region) where the depth-dose curve reaches its maximum value.
D_T	Distal Therapeutic Dose	The dose, usually 85% or 90 % of the maximum dose, beyond the maximum dose.[a]
D_{50}	Distal 50 % dose	The point beyond the maximum dose where the depth-dose curve decreases to 50 % of its maximum value.
D_x	Exit/Bremsstrahlung Dose	The photon background absorbed dose.
	RANGE PARAMETERS	
$R_{0.5}$	Depth of Surface Dose	The depth of the surface/entrance dose, defined as a depth of 0.5 mm.
$R_T{}'$	Depth of Proximal Therapeutic Dose	The depth at which the extension of the therapeutic interval intersects the depth-dose curve at the dose level selected as the therapeutic dose value near the skin entrance.
R_{100} *or* z_{max}	Depth of maximum dose	The depth at which the depth-dose curve achieves a maximum value.
R_T	Depth of Distal Therapeutic Dose	The therapeutic range giving the depth interval that should coincide with the target volume.
R_{50}	Half-value depth	The depth at which the depth-dose curve has decreased to 50 % of its maximum value.
R_{max}	Maximum electron range	The depth at which extrapolation of the tail of the central-axis depth versus absorbed-dose curve meets the bremsstrahlung background. This is the largest penetration depth of electrons within the absorbing medium.
R_p	Practical range	The point where the tangent at the steepest point (the inflection point) on the almost straight descending portion

		of the depth versus absorbed dose curve meets the extrapolated bremsstrahlung background. The practical range parameter represents those electrons that have travelled with the straightest path through the absorbing medium.
R_q		The depth where the tangent through the dose inflection point intersects the maximum dose level.

a – the dose value assigned to the therapeutic dose depends on each individual practice.

As evident from the CAX PDD illustrated in Figure 2-1, electron beams offer the advantage of providing high, relatively uniform doses at a shallow depth with a rapid fall-off of in absorbed dose distal to the maximum dose. Dose and range parameters are strongly dependent on electron beam parameters such as beam energy, field size, SSD and angle of beam incidence, and it is a combination of these parameters that determine the appropriate beam for a given dose specification at depth within a treatment volume when dealing with 3D conventional electron beam treatments.[4]

2.1.2.7 Effects on PDD Curve due to a change in beam nominal energy

With an increase in the nominal energy of an electron beam, the following changes typically occurs on the CAX PDD curve as mentioned within the *Handbook of Radiotherapy Physics, Theory and Practice*[1], however it is also evident from measurements as indicated in section 4:

1. D_s increases due to the reduced difference in obliquity between $\mathrm{R}_{0.5}$ and R_{100}.
2. R_{100} increases since equilibrium is achieved at an increased depth. However, the real trend for the shift in the depth of maximum dose with energy depends strongly on the design of the linac.
3. The dose gradient G_0 becomes gentler, or less steep, since more electrons can penetrate the medium at depth.
4. Range parameters increase since the total beam penetration increases. This will reflect in range parameters, particularly R_{50} and R_p which is directly linked to the mean energy and most probable energy of the electron beam on the surface of the absorbing medium, respectively.[32] R_p and the dose at R_p will increase since more electrons would have travelled with straight paths through the medium.
5. The bremsstrahlung dose D_x increases.

2.1.2.8 Effects on PDD Curve due to a change in field size at nominal SSD

Field size effects on the CAX PDD of a given electron beam are generally small if conditions for lateral electronic equilibrium exists on the CAX. This condition will hold as long as the side of square field size is equal to or greater than the lateral range of the electrons for a fixed electron energy.

The condition for lateral electronic equilibrium also strongly depends on the energy of the beam for a fixed field size, since the practical range of electrons is directly linked to their kinetic energy. Refer to Figure 2-3. The CAX PDD is almost unaffected for a field size change above the limit for lateral electronic equilibrium (which in this case agrees to a field size of approximately 6 x 6 cm^2 for a 10 MeV electron beam). Once below this field size limit, the dose on the CAX changes significantly (the dose reduces at R_{100}) and this causes a shift of the higher dose region towards the surface of the absorbing medium. This results in an increase of D_s, R_{100} decreases, and the shoulder of the BD region occurs earlier. R_p remains unchanged, and for this reason G_0 becomes gentler since the BD commences at a shallower depth. However, above the threshold for lateral scatter equilibrium, the general trend is an increase in D_s with a decrease in field size.

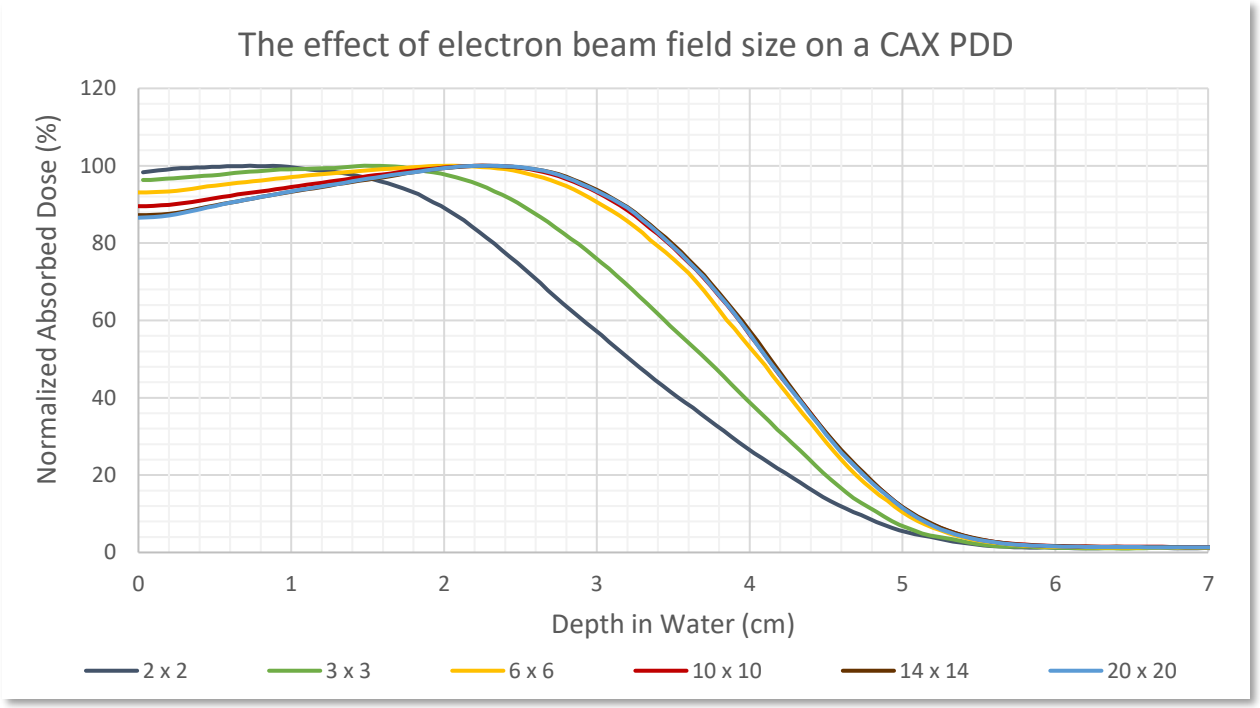

Figure 2-3: The effect of a change in electron beam field size on the CAX PDD curve. Curves were measured within a water tank for 10 MeV electron beams from an Elekta Synergy® 160-leaf Agility™ linear accelerator at 95 cm SSD. The loss of lateral electronic equilibrium is evident for field sizes smaller than 6 x 6 cm^2.

2.1.2.9 Effects on PDD Curve due to a change in nominal SSD (extended SSD)

In contrast with photon beams, the inverse square law cannot directly be applied to electrons without a modification. The modification involves the use of an effective SSD based on the distance from a virtual electron source rather than a true source. The need for the use of a virtual source comes from the fact that there are in effect many individual or multiple sources of scattered electrons.[3] The effective SSD is determined by measuring the ionization at various distances from the electron applicator, and with the use of ratios and a graphical plot the effective SSD can be determined experimentally for the electron beam.[4] Generally, the CAX PDD is affected slightly with a change in SSD as indicated in Figure 2-4. With an increase in SSD, say from the nominal SSD of 95 cm to 100 cm (5 cm stand-off), the changes on the CAX PDD curve include:

1. D_s decreases – when an absorbing medium is closer to electron applicator, it receives a concentrated dose of scattered and unscattered electrons. However, if the absorbing medium is further away from the electron applicator, as is the case with extended SSD scenarios, the scatter component of the beam spreads out. This means that less scattered electrons reach the absorbing medium and accordingly D_s decreases.[3,5]
2. The effective beam energy increases slightly – This occurs since the scatter component tends to shift towards the lower end of the energy spectrum, which means that the unscattered component of the beam contributes more to the dose than the scattered component. For this reason, the build-down of dose will be slower. R_T will increase; however, R_p remains unchanged.[1,5]

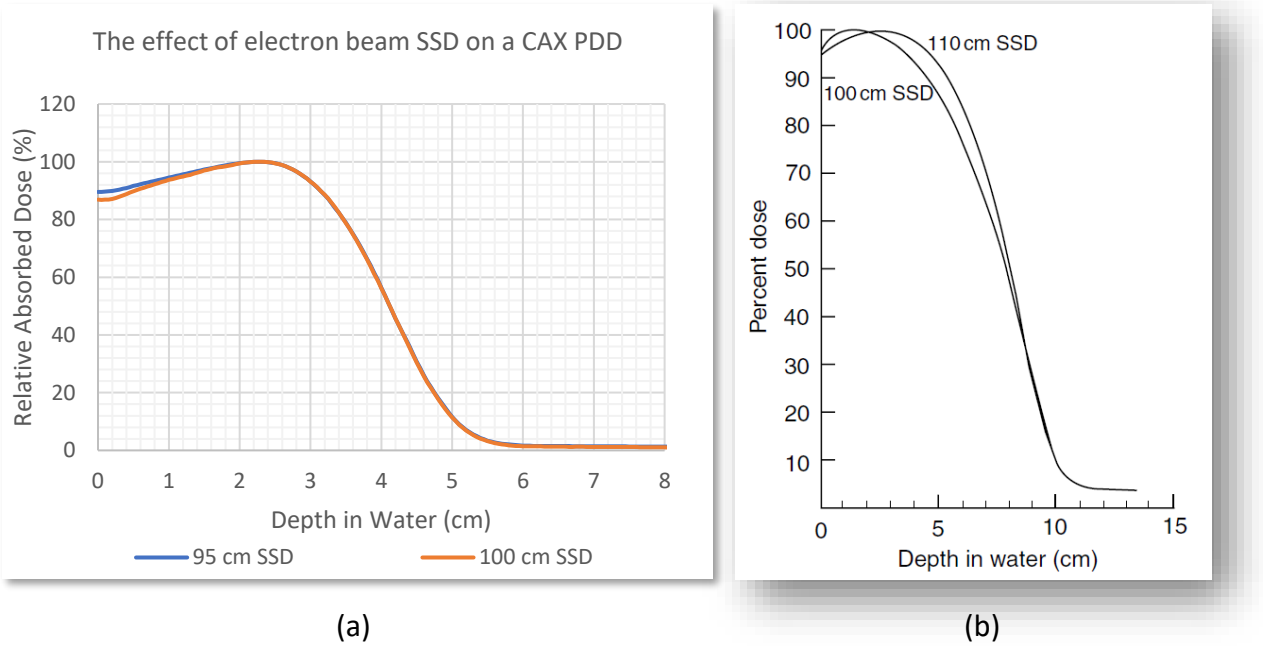

Figure 2-4: The effect of a change in electron beam Source-to-Surface Distance (SSD) on the CAX PDD curve. In a), 95 cm and 100 cm SSD Curves were measured within a water tank for 10 MeV electron beams with field size 10 x 10 cm^2 for beams from an Elekta Synergy® 160-leaf Agility™ linear accelerator. The curve illustrated in b) shows the effect of an SSD change for 100 cm and 110 cm SSD for 6 x 6 cm^2 20 MeV electron beams, and was obtained from the Handbook of Radiotherapy Physics, Theory and Practice.[1]

2.1.3 Off-Axis Dose Profiles

Off-axis dose profiles are obtained from cross-sections through an isodose distribution at any depth Z. Of major interest are profiles at fixed depths in the medium in both the inline- (Y) and crossline- (X) directions, as well as diagonal profiles. These profiles therefore represent the change in dose laterally to the CAX of the beam. Off-axis profiles together with output factors, isodose distributions and CAX PDD curves are essential beam characteristics to determine for commissioning of electron beams[33] and are used to benchmark dose calculation algorithms against measured data.[34]

2.1.4 Relative Output Factor (ROF)

Output factors depend on the applicator size, MLC setting, JAW setting and SSD.[1] Typically output factors are measured for all the applicators (sometimes referred to as cone factors) and open field inserts (referred to as cutout factors) and beam energy combinations.[5] This enables the conversion of linac MUs to absolute dose at depth within the medium, which is essential in order to know how much MUs to administer for a treatment. According to the 32th report of the AAPM which entails the report of the

Radiation Therapy Committee, Task Group No. 25, the output factor for a field size F at a particular SSD is defined as "the ratio of dose per monitor unit at d_{max} for a given field size F to that for the reference field size at its own d_{max}".[5] That is,

$$\mathrm{OF(F,E,SSD)} = \frac{\frac{\mathrm{D}}{\mathrm{MU}}(\mathrm{F,E,SSD,d_{max}})}{\frac{\mathrm{D}}{\mathrm{MU}}(\mathrm{F_0,E,SSD,d_{max,0}})} \qquad \text{Eq 2.3}$$

where E is the electron beam energy, SSD is the source-to-surface distance and $\frac{D}{MU}(F_0, E, SSD, d_{max,0})$ is the reference dose per monitor unit measured at the depth of maximum dose $d_{max,0}$ for the reference field size F_0 of 10 x 10 cm^2. $\frac{D}{MU}(F, E, SSD, d_{max})$ represents the dose per monitor unit for the field size F in question, measured at its own depth of maximum dose d_{max}. In case readings are not converted to dose, care should be taken with the calculation of output factors for small field sizes where conditions for scatter equilibrium are lost. When these conditions are kept, the depth of maximum dose generally does not drift too much with a change in field size and the output factors are essentially measured at the same depth. However, with small field sizes, the depth of maximum dose can significantly change and will typically shift toward the surface. This means that, if ionization readings are used to calculate output factors, the depth difference should be accounted for with the use of the appropriate stopping power ratios.[1] That is, when ionization readings are used:

$$\mathrm{OF(F,E,SSD)} = \frac{\frac{\mathrm{D}}{\mathrm{MU}}(\mathrm{F,E,SSD,d_{max}})}{\frac{\mathrm{D}}{\mathrm{MU}}(\mathrm{F_0,E,SSD,d_{max,0}})} \left[\frac{\mathrm{S(d_{max})}}{\mathrm{S(d_{max,0})}}\right] \qquad \text{Eq 2.4}$$

where $S(d_{max})$ is the stopping power for the medium and electron beam energy in question at the depth d_{max}. The reason why stopping power rations are not included in Eq 2.3 as it is in Eq 2.4 is simply because the use of dose readings to calculate an output factor implies that a stopping power has already been applied.

2.2 Electron Dose Calculation Algorithms

2.2.1 Overview

With the incorporation of Computed Tomography (CT) data in treatment planning systems, the need for algorithms to correctly account for the dose perturbations caused by the presence of heterogeneities, such as bone and air cavities[3,5,29], have become an absolute necessity. Empirical, semi-empirical and analytic approaches to electron beam dose calculation algorithms have been developed and used in treatment planning systems, however in modern treatment planning systems, MC based dose calculations

are preferred. Electron beam dose calculation algorithms are discussed in detail in literature, especially in articles by Andreo[35], Brahme[36], Huizenga[37], Sternick[38] and the ICRU[39].

2.2.2 Empirical Algorithms

Empirical algorithms tend to lack any sort of physical meaning, but usually have great accuracy compared with measurements.[35,38] Andreo[35] and the ICRU Report 42[39] highlighted several attempts[40–45] to derive 1-D empirical formulas to accurately describe the central axis (CAX) depth dose distribution for a given broad electron beam. With the inclusion of radial dose profiles, a two-dimensional (2-D) empirical representation of electron dose distributions could be obtained.

Empirical inhomogeneity correction methods such as the *Absorption Equivalent Thickness (AET)* accounts for the presence of inhomogeneities by considering the dose distribution along ray-lines ("rays") which originates from the same virtual source. Experimentally it has been shown that the AET is not constant for a given energy, but rather depends on the inhomogeneity's depth, extent and tissue characteristics. In an attempt to avoid the depth variation of the AET method, Holt et al.[46] developed a system that calculates an effective correction factor for an inhomogeneity.

Dahler et al.[47] introduced the *Absorption Coefficient (AC)* method which also attempts to overcome the depth variation of the AET method.[38] The AC method utilizes the 1-D CAX empirical formulation developed by Laughlin et al.[40] and modifies the equation with the introduction of experimental absorption coefficients for tissue, bone and lung.

The *Coefficient of Equivalent Thickness (CET)* method was developed by a group[48–50] at the M.D. Anderson Hospital. It is "the quotient of depths, where the percentage ionization in water and in the inhomogeneity were the same".

Three correction methods to correct the empirical 1-D electron dose distribution formulations for the presence of inhomogeneities have been outlined. All of them only considers an inhomogeneity along a ray-line and accordingly displaces an isodose. Andreo[35] states that these approaches were sufficient to handle to displacement of isodoses due to large inhomogeneities, but completely neglected to handle edge effects as well as small inhomogeneities. This is due to the dominance of electron scattering over absorption effects.

2.2.3 Semi-Empirical Algorithms

2.2.3.1 Overview

Semi-empirical algorithms are based on the solutions to statistical models for multiple scattering, with the incorporation of experimentally determined parameters to modify these models. Andreo[35] divides semi-empirical algorithms into two groups:

1. Models based on a semi-empirical modification of the Fermi-Eyges solution to the Boltzmann equation with additional modification – also known as models based on the *Fermi Age Diffusion Equation* (Group 1).
2. Models based on the original theory of equivalent approaches – also known as models based on the concept of *pencil beams* (Group 2).

2.2.3.2 Algorithms based on the concept of Pencil Beams

Andreo[35] includes another extensive list of authors that have made contribution towards this group, of which probably the best known model is that developed by Hogstrom[51–53]. Both Nahum[1] and Khan[3] gives a good description of the electron Pencil-Beam (PB) algorithm since it has repeated application in several treatment planning systems.

Hogstrom's Fermi-Eyges PB electron model is a well-known pure semi-empirical algorithm. Some fundamental physics are incorporated with the use of the Fermi-Eyges theory which models the off-axis dose as a result of multiple Coulomb scattering with a Gaussian distribution, but input data are also required. Input data includes measured CAX depth dose curves (for the calculation of $g(z)$), measured dose profiles (for the calculation of $W(x,y)$), the mean energy at the surface $\bar{E}_0$ (for the calculation of $\bar{E}_z$), the initial angular spread of the electrons (for the calculation of σ_{air}) as well as a final factor, termed the penumbra adjustment factor (FMCS), which adapts the value of σ_{med} as to improve the modeling of penumbras. FMCS factors usually are within the range of 1.0 to 1.4.[1]

From the results showed by Hogstrom et al.[51], it is evident that the PB model does not always portray a high level of accuracy when compared with measured data. This is due to the inherent assumptions made by the PB model, such as the Gaussian modeling of the scattering of beam at depth by the Fermi-Eyges theory, when in actual fact this is only true at large and shallow depths.[54,55]

In a study by Ade et al.[56], the dose perturbations caused by a Titanium hip prosthesis have been investigated using high energy electron beams. A novel pelvic nylon phantom was used which also

contains bone, and measurements was done using GAFCHROMIC EBT2® (Ashland Inc., Covington, Kentucky) film. The same geometry was also used in a CMS XiO treatment planning system in order to evaluate the ability of the PB algorithm to account for these inhomogeneities. From film measurements, the dose enhancements at the prosthesis entrance was found to be in the region of +20 %. However, the XiO treatment planning system was not able to reproduce these dose enhancements since large uncertainties in the region of 20-25 % was observed. The lack of accuracy of the PB algorithm to account for the dose perturbations caused by the presence of the hip prothesis was therefore outlined.

2.2.4 Analytical Algorithms

Analytical algorithms in radiotherapy use the fundamental physics principles/laws that govern radiation interactions to calculate dose distributions. Mathematical expressions based on these physics laws and principles are used to create models.[35,38] The main concern in using of analytical algorithms is the huge mathematical effort required to solve equations due to a large number of variables. This requires the use of powerful computers which, during the period of initial interest in electron dose calculation algorithms, were not invented yet.

The main interest in predicting dose distributions in a medium is to be able to predict how the radiation field would propagate. This propagation is based on the solution of the transport equation, which is characterized by the particle fluence rate at a determined position and time with a precisely known energy and direction.

2.2.5 Algorithms based on the Monte Carlo Method

2.2.5.1 Overview

Today, the use of MC based dose calculation algorithms is a practically feasible approach in Radiotherapy treatment planning since there has been a marked increase in computer power and availability thereof. The use of MC to predict dose distributions in media for photon- and electron beams, under almost all circumstances, is seen as the golden standard method, especially in the presence of inhomogeneities.[1,34,57–67] The basic principle of MC simulations is to reproduce radiation interactions (using physical laws of radiation scatter and absorption cross-sections) faithfully by simulating the transport of individual particles.[1]

2.2.5.2 History of EGSnrc

A complete discussion on the history of the EGS (***E**lectron-**G**amma-**S**hower*) range of codes up to EGS4 is given in an article by Bielajew et al,[68] and further developments from EGS4 to EGSnrc is discussed in the EGSnrc manual[69].

The first release of the EGS4 Code System in 1985 contained many corrections and extensions to the EGS3 Code System. One of the biggest improvements involved extending the lower-energy limits down to 1 and 10 keV for photons and electrons, respectively. Furthermore, Rogers made some very significant changes to ELECTR which gave the user control over what the maximum energy loss per electron step can be as well as what the maximum step size may be (these were labeled as parameters ESTEPE and SMAX, respectively). This improved the accuracy of lower energy electron transport. This new electron transport algorithm, called PRESTA (***P**arameter **R**educed **E**lectron **ST**ep **A**lgorithm*) included a path-length correction algorithm, lateral correlation algorithm and a boundary crossing algorithm. This allowed the accurate transport of electrons with the use of larger transport steps. In addition to many other corrections and improvements, the EGS4 Code System took into consideration the following physics processes:

- Production of bremsstrahlung.
- Positron annihilation in-flight and at rest.
- Molière multiple scattering for arbitrary randomly selected step sizes (provided they are not too large or small to violate the theory).
- Electron-electron (Møller) and electron-positron (Bhabha) scattering.
- Continuous energy loss is applied to charged particle tracks in between discrete interactions. The total stopping power included both soft radiative and collisional terms. Collisional loss is determined by the restricted Bethe-Bloch stopping power, with the treatment of the density effect (Sternheimer).
- Pair production, Compton scattering, Rayleigh scattering and the Photo-electric effect.

The current EGSnrc Code System is discussed in detail by Kawrakow et al. in the EGSnrc Code System user manual[69]. One of the most important developments by Kawrakow and Bielajew within EGSnrc was a new electron transport algorithm PRESTA-II which had improvements in the multiple scattering theory employed. In addition to the physics capabilities of the EGS4 Code System as discussed above, the following capabilities have been added to the EGSnrc Code System:

- Bremsstrahlung production can either be sampled from Bethe-Heitler or NIST cross sections. Angular sampling has been changed from a fixed angle approximation to sampling from an angular distribution.
- Positron annihilation quanta are followed to completion.
- The shortcomings of the Molière multiple scattering theory have been addressed which allows any step size, as well as seamless movement between a single scattering and multiple scattering mode. The transport in the vicinity of interfaces, or boundaries, is handled by a single scattering mode. Furthermore, either Rutherford scattering or scattering accounting for relativistic and spin effects can be chosen.
- An arbitrary density effect correction and data supplied to use the density effect recommended by the ICRU report 37.
- Klein-Nishina Compton and bound Compton scattering can be simulated.
- Photoelectric effect:
    - Fluorescent photons, Auger and Coster-Kronig electron produced by relaxation of excited atoms (K, L and M shells) can now be produced and tracked. The angular distribution of the photoelectron can be sampled.
    - Electron impact ionization can be modelled according to arbitrary theories. (Kawrakow, Casnati, Kolbenstvedt, Gryzinski, and Bote and Salvat)

In addition, many improvements have been made to the subroutine `HATCH` as well as to the user code. This is discussed in detail within the sixth printing of the `EGSnrc` Code System manual.

2.2.5.3 Accuracy and Histories

A simulation history is defined as the transport of an individual particle and of particles consequently set in motion. Since simulations are statistical events, the statistical uncertainty of a simulation depends on the number of histories simulated. This is governed by the *Central Limit Theorem* which in the case of Monte Carlo states that that the result of a simulation will approach the true result if the number of histories simulated is sufficiently large. This implies that the statistical uncertainty of a simulation result will approach zero if the number of histories approaches infinity. This of course is not clinically practical in any sense since accurate results need to be obtained as quickly as possible. Therefore the amount of histories simulated are usually chosen such that a statistical uncertainty of 1 % in results is attained, meaning that any result is either within a positive or negative 1 % interval of the true value.

In addition to the statistical uncertainty of the results obtained with a Monte Carlo based simulation, other sources of uncertainties also need to be taken into account before setting a limit on what is considered to be an acceptable uncertainty level. The discussions on this topic has been around the influence of the global uncertainty (added uncertainties between dose prescription and actual treatment delivery) on tumor control probability (TCP) and normal tissue complication probability (NTCP).[22] The global uncertainty is a result of various sources as described by the AAPM's TG-65 report, and it has been stated that for a 5 % change in dose, changes to TCP at a TCP level of 50 % can be anywhere within 10-20 %, and similarly 20-30 % changes in NTCP. This leads to the conclusion that an acceptable level of uncertainty for a dose calculation algorithm would be in the region of 2-3 %, which would lead to a total uncertainty of about 5 %.[22] Therefore, any Monte Carlo based model should be able to produce results within 2 % of measured data, taking into consideration the inherent 1 % statistical uncertainty of results. Any Monte Carlo based model would, in principle, never possess a statistical uncertainty of zero percent. This is explained by Reynaert et al.[70] who gave 4 reasons as to why not:

- There are always imperfections in the modeling of linear accelerators and the consequent benchmarking of the virtual beam with the true beam.
- The cross-section libraries used for radiation interaction sampling contains uncertainties of its own, although considered to be small enough to be negligible.
- The statistical uncertainty obtained when simulating a limited number of histories.
- Uncertainties in the conversion of CT data to material composition and density.

Application of Monte Carlo techniques for radiation transport has however shown its potential to comply with the stringent 2-3 % accuracy requirement as mentioned in section 2.2.5.1. It has also been mentioned that the more conventional electron dose calculation algorithms, such as the Fermi-Eyges PB algorithm (Hogstrom model) and earlier empirical formalisms may have had good accuracy within homogeneous media - but failed to predict dose distributions in the vicinity of inhomogeneities. This emphasizes once again the need for the use of an approach based on Monte Carlo.

The goal of a simulation is to obtain the trajectories of individual particles, since this can be used to unveil the pattern of energy deposition due to each trajectory. The individual particle trajectories will mirror the physical reality of particle interactions where energy is lost to the absorbing medium and subsequent particles are set in motion. The manner in which Monte Carlo based codes such as the `EGSnrc`-group of codes obtain these trajectories is to simulate both photon and electron transport which are based on the fundamental physical interaction processes and associative laws governing these processes. The

transport of particles is handled in a step-wise manner, where a set of decisions are made after each step which ultimately determines the fate of the incident particle and subsequent particles set in motion by the primary particle. Decisions include for instance the type of interaction and directional change (known as dynamic variables) and are usually sampled from probability distributions. Sampling from these probability distributions must be random and in effect each history created remains random (more on this in section 2.2.5.4). Of course, these probability distributions depend highly on the energy of the particle as well as the medium traversed. Usually the transport of a particle is performed until its energy is totally expended (or up until a certain cut-of value) or until a particle leaves a geometry of interest (if it had sufficient energy to traverse the geometry). With the transport of each new particle, the primary particle and all the secondary particles formed have their transport parameters stored within a stack of variables. Only one particle is transported at a time and after each transport step, the particle's transport parameters are updated within the data stack and the transport of the most recent particle commences. On this manner the primary particle as well as all the subsequent secondary particles formed are transported in a step-wise manner until an energy cut-off is reached or until the particle transported leaves the geometry of interest. The transport of the primary particle and all the particles set in motion by the primary particle is referred to as a *particle history*.

In many Monte Carlo based codes, such as the `EGSnrc`-codes, simulations are split up into batches (usually 10 batches per simulation). Each batch contains an amount of histories equal to $\frac{\text{Total amount of histories}}{\text{Number of batches}}$, with each batch having different initial random number seeds. The reason for this is that quantities of interest, such as absorbed dose, are obtained from the average values of batches. The standard error in the mean, σ is also calculated from the average values of the batches. This gives an indication of the statistical uncertainty of the results. The standard deviation of results can be minimized by simulating a large amount of histories. However, from 2002, a history-by-history method of estimating uncertainties was employed by `BEAMnrc`, which involves grouping scored quantities (fluence, energy deposited, etc.) according to primary-history during a run and then determining the root mean square standard deviation on the mean of the groupings.[69]

2.2.5.4 Random Numbers

The sampling of electron transport parameters is done with the use of random numbers. Random numbers are generated by some algorithm which means that these numbers are in actual fact pseudo-random. Two pseudo random number generators (PRNGs) are well known for their use in the `EGS`-range

of codes. The *RANMAR* PRNG was used in the EGS4 generation codes while the *RANLUX* PRNG is more so used within the EGSnrc generation of codes. Since MC simulations requires reliable quantitative results, using a PRNG with a good quality is a very important requirement.[71] However, the quality of PRNGs that existed in the period when the use of Monte Carlo in Medical Physics became popular was not high enough. These PRNGs gave incorrect results in some simulations[72] and frequently acted as a source of systematic error.[71,72] The partial reason for this is due to the inherent difficulty to assess PRNGs on the bases of their quality.[72] With the introduction of new stringent statistical tests for randomness, most of the PRNGs initially thought to have good statistical properties failed these new tests very quickly.[73] This inspired Swiss inventor Martin Lüscher to develop a new PRNG algorithm with the primary intent to pass all of the new statistical tests for randomness.[72] Lüscher went on to do this in 1994 and developed the RANLUX PRNG, which was the algorithm considered to be the first of its sort to be of utmost high statistical quality.[71]

With regards to initial seeds the EGSnrc range of codes requires two initial seeds, $IXXIN$ and $JXXIN$, for either RANMAR or RANLUX. The meaning and values allowed for both seeds depend on the type of PRNG used. For the RANMAR algorithm, both $IXXIN$ and $JXXIN$ are random number seeds and the allowed values include $0 < IXXIN \leq 31328$ and $0 < JXXIN \leq 30081$. Default values can be selected by choosing $IXXIN = JXXIN = 0$, which will default $IXXIN$ to a value of 1802 and $JXXIN$ to a value of 9373. With the RANLUX PRNG however, $IXXIN$ represents the luxury level and $JXXIN$ represents an initial random number seed. This means that the allowed value for $IXXIN$ is 0, 1, 2, 3, 4 which reflects the different luxury levels incorporated into the RANLUX PRNG, or $0 < IXXIN \leq 4$. Any value other than this will reset $IXXIN$ back to its default value of 1 (hence a luxury level of 1). With RANLUX, higher values are allowed for the random number seed $JXXIN$, with $0 < JXXIN \leq 1073741824$ with the same default value as with the RANMAR PRNG.[74,75]

2.2.5.5 PEGS4

PEGS4 (***Pre-processor for EGS***) is a stand-alone data pre-processor code.[75,76] PEGS4 generates quantities such as material-dependent cross section data, mean free paths and electron stopping powers which is required by the EGSnrc MC shower code in order to faithfully simulate coupled radiation transport. PEGS4 has several operational functions, including:

- Construction of piecewise-linear fits over a large number of energy intervals of the cross section and branching ratio data.

- Generation of printed plots of selected functions.
- Evaluation of different functions at selected points or comparison with sampled spectra.

The `$MAIN` subroutine in the `EGSnrc` User Code is responsible for calling the `$HATCH` subroutine before calling the `$SSHOWER` subroutine. `$HATCH` reads material data into the user code from `PEGS4` that have been previously created before initialization of the `$SSHOWER` subroutine. `PEGS4` cross section data is created for both photon and electron interaction processes, including photoelectric absorption, coherent (Rayleigh) and incoherent (Compton) scatter, pair and triplet production, bremsstrahlung X-ray production, Molière multiple elastic (Coulomb) scattering, Møller (electron-electron) and Bhabha (positron-electron) scattering and positron annihilation (in-flight and at rest).[69]

Cross section data can be generated by the user over a large range of energies between cut-off energies for any material, provided that the material's atomic composition and physical density is supplied. `PEGS4` can generate data for liquids, solids and gasses, and produce these data in discrete energy intervals over the energy range required for the simulation. Interpolation is performed between energy intervals.[76]

2.2.5.6 Electron Transport

2.2.5.6.1 Introduction

Energetic electrons immediately start to interact with a medium upon entry, as electron interactions are much more dense than those of photons. Berger and Wang[28] has estimated that in the slowing down of electrons from 500 to 250 keV in aluminum, these electrons undergo about 4000 elastic scatterings; this number increasing to 7000 if the material is gold. All these interactions generally cause small angle deflections and leads to small energy losses. The transport of electrons in MC simulations involves explicit simulation of discrete events (such as bremsstrahlung production and Møller interactions, given that these events generate radiation quanta above an energy threshold) in a similar manner than with photon transport. However, elastic events (and sub-threshold bremsstrahlung and Møller events) are handled with a condensed history (CH) technique, since it would computationally be very intensive to do this in an explicit manner. Like photons, each electron interaction type has a probability or cross section, where the total electron cross section σ_{T} is equal to:

$$\sigma_T = \sigma_{brem} + \sigma_{inel} + \sigma_{el}\delta(0) \qquad \text{Eq 2.5}$$

where σ_{brem} is the bremsstrahlung cross section, σ_{inel} is the inelastic cross section and σ_{el} is the elastic cross section. Dirac's function $\delta(0)$ is included to express the fact that elastic events are essentially zero

energy loss events. Should positrons be transported, an additional cross-section is added to Eq 2.5, σ_{annih} which is the cross section for positron annihilation.[69]

The bremsstrahlung cross section is either modelled according to the NIST bremsstrahlung cross section data base, or according to a new set of tabulations prepared at the NRC. The NRC tabulation uses the NIST cross-sections but replaces the electron-electron part of the interaction with exact calculations in the first-Born approximation. Furthermore, exact formulae for the Møller scattering cross section are used rather than asymptotic formulae.

2.2.5.6.2 Condensed History Schemes

As mentioned, MC techniques involves handling the multiple scattering of electrons in a condensed history manner, which means that every elastic scattering event is not simulated explicitly but will rather be subject to grouping, where the cumulative effect of the multiple events are applied to a single "condensed" transport step. This technique was introduced by Martin Berger in 1963 and improves the overall efficiency of simulations.[77] The motive for this technique lies in the fact that since many of the individual elastic scattering events cause small angle deflections and small-energy losses, they can be grouped together while other discrete interactions are still handled in an explicit manner.

`EGSnrc` makes use of a Class II Condensed History (CH) technique.[69] This means that inelastic collisions which set in motion atomic electrons with kinetic energies above the threshold T_c (or AE, as used in `EGSnrc`), as well as bremsstrahlung processes that result in the creation of photons above an energy threshold k_c (or AP, as used in `EGSnrc`), are simulated explicitly and the secondaries created are transported. These types of interactions are then referred to as "catastrophic" events. Any sub-threshold inelastic and radiative events, as well as elastic collisions in general will be subject to grouping/condensing. Generally, two groupings are distinguished. The one grouping will account for elastic scattering events causing a large number of small angular deflections. The second grouping uses an continuous energy-loss model to account for the large number of small energy losses.[28] Other MC based codes, such as ETRAN, uses a Class I CH technique, which groups energy losses and angular defections associated with all individual events together, and the energy and direction of the primary electron are not affected by the creation of secondary particles.

The CSDA model treats energy loss as a continuous process, meaning that a transported electron will lose the same amount of energy per unit path travelled during a transport step and will slow down accordingly. Secondly, no secondary particles are created during the slowing down and the energy loss after each step

is accounted for with the use of the unrestricted total stopping power.[28] All angular deflections are treated using a multiple scattering theory such as the Molière multiple scattering theory (as incorporated in some Class II CH schemes such as the EGS4) or the multiple scattering theory of Goudsmit and Saunderson (as implemented in Class I CH schemes such as ETRAN MC based codes).

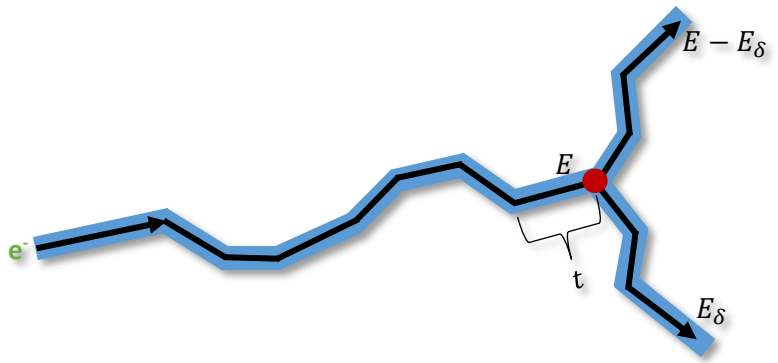

Figure 2-5: Class II Condensed History Technique. The blue regions around each step is the region into which energy deposition occur, but for simplicity energy deposition is assumed to occur along each path length. Figure adapted from Rogers et al.[28]

Figure 2-5 illustrates how an electron is handled by a Class II CH scheme. Multiple elastic scattering events, as well as inelastic events producing knock-on electrons and photons below energy thresholds (AE and AP) are grouped together. The electron steps are short and straight as determined by the multiple scattering theory (the maximum and minimum step lengths being dependent on the electron's energy), where the energy lost in this step is determined by the restricted total stopping power. After each step a new direction is sampled from the multiple scattering theory angular distribution, after which the electron travels a new path. If a discrete ("catastrophic") interaction occurs (the red dot in Figure 2-5), a secondary particle is created with an energy above the energy threshold (AE or AP), and both the primary and secondary particle will be transported as discussed above. Of course, the primary particle will have an energy loss during the discrete interaction equal to the secondary's particle kinetic energy. The energy thresholds AE and AP hence are production thresholds. In the EGSnrc Code System, global cut-off energy parameters exist, ECUT and PCUT, which determines down to what total electron and photon energy a history will be followed before its transport is terminated.

Refer to Figure 2-5. Before the discrete interaction at the red dot where a knock-on electron with kinetic energy $E_\delta >$ AE is created, the primary electron with initial energy E_0 traveled along a straight path with step length t. Along the path t, energy is lost continuously to multiple elastic scattering as well as to sub-threshold inelastic and radiative collisions. Since the Class II CH technique treats the energy lost as being

at a continuous rate, the restricted stopping power $L_{\text{tot}}^{\text{AE,AP}}$ is used. Therefore, the primary electron's energy after the discrete interaction is $E = E_0 - tL_{\text{tot}}^{\text{AE,AP}} - E_\delta$. This effectively means that the energy deposited during the step t is equal to $tL_{\text{tot}}^{\text{AE,AP}}$.

2.2.5.6.3 Electron Transport Algorithm

The fundamental electron step algorithm employed in the EGS Code System is PRESTA which was developed by Bielajew and Rogers[78], and handles the fundamental electron transport during a condensed history step. The PRESTA algorithm has three components, namely a path-length correction (PLC) algorithm, a lateral correlation algorithm (LCA) and a boundary crossing algorithm (BCA). The PRESTA algorithm was originally implemented in the EGS4 Code System and has been updated to PRESTA-II in the EGSnrc Code System. In general, the PRESTA algorithm allows accurate transport of electrons when larger steps are taken which in effect causes simulation time to decrease. The PRESTA algorithm is based on Molière's multiple scattering theory (although the newer PRESTA-II algorithm uses a different multiple scattering theory)[69] which condenses multiple electron steps into a single step, where the electron suffered a net angle of deflection and energy loss after the condensed step. This must be done since it would be computationally too intensive at the present stage to simulate electron multiple scattering in an analogue manner.

The multiple scattering angle θ is sampled from the Molière multiple scattering angle distribution after each condensed step, which is in the form

$$f(\theta)\theta\, d\theta = f_r(\phi)\phi\, d\phi \qquad \text{Eq 2.6}$$

where θ is the scattering angle, ϕ is a "reduced" angle and $f_r(\phi)$ can be explained in terms of a power series. The PLC algorithm takes into consideration that an electron's path within a medium is curved due to its elastic scattering from the medium's atomic nuclei and atomic electrons. The PLC algorithm is based upon the Molière scattering theory, and is defined as

$$PLC = \frac{t}{s} - 1 \qquad \text{Eq 2.7}$$

where s is the straight electron path and t is the curved electron path, as indicated in the Figure 2-6. The curved electron path t is calculated depending on whether it is greater or less than the minimum step size for which the Molière multiple scattering theory holds, t_{min}. Included in this calculation is a correction factor as derived by Bethe[78] to correct for large angle scatter.

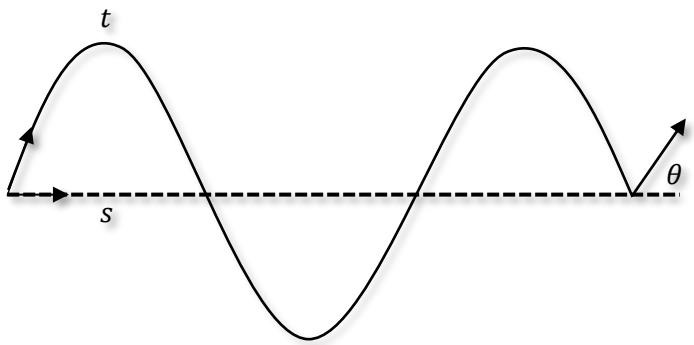

Figure 2-6: An illustration of a straight path traveled by an electron, s and a curved path t taken by an electron as a result of atomic nuclei and atomic electron scatter. This is the basis of the PLC algorithm.

The LCA takes into consideration the lateral transport of electrons. This is required since the PLC algorithm allows larger steps at which lateral displacement becomes significant. Therefore, during an electron transport step, the LCA performs a translation which is perpendicular to the direction of motion as indicated in the Figure 2-7.

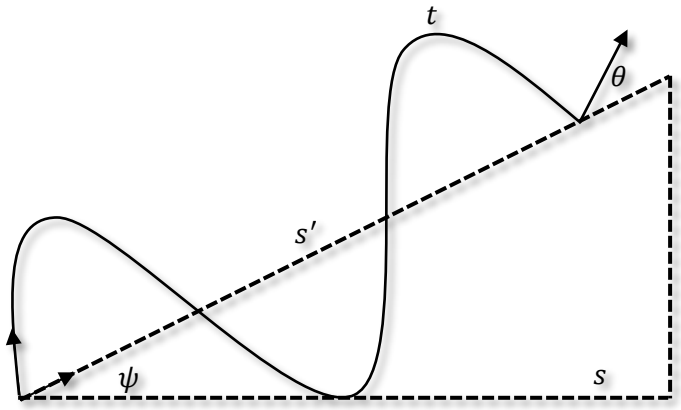

Figure 2-7: The LCA performs a lateral translation of s into s′, where s′ has an angle ψ relative to s in a plane perpendicular to the direction of motion.

From the figure above, it is evident that initially an electron travelled along the curved path t, after which its direction changed by the angle θ. A lateral translation perpendicular to the direction of motion is applied, which deflects the path s by an angle ψ. Now the electron travels along the curved path t which is defined on s', with x and y cooridnates:

$$\mathrm{x} = \frac{1}{2}\mathrm{t}\, sin\,\theta\, cos\,\alpha$$

$$\mathrm{y} = \frac{1}{2}\mathrm{t}\, sin\,\theta\, sin\,\alpha \qquad \text{Eq 2.8}$$

where α is an azimuthal angle selected randomly over the range $0 \leq \alpha < 2\pi$.The LCA algorithm also makes use of the BCA algorithm to ensure that a lateral deflection does not deflect the electron out of its current geometry region. Should steps be very close to a boundary, the LCA is turned off.

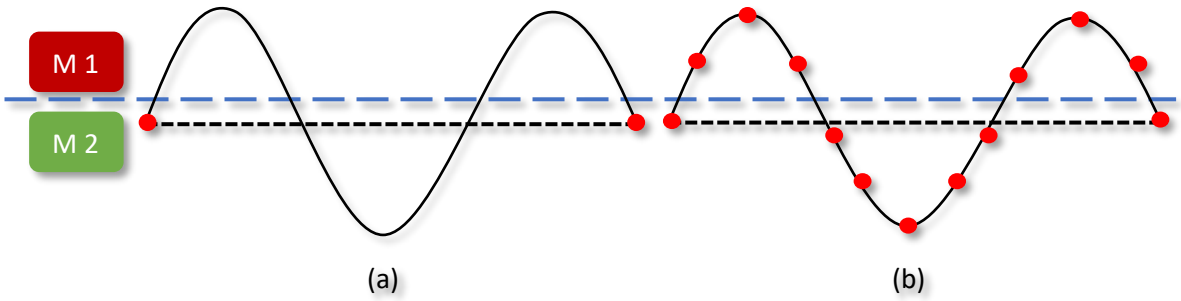

Figure 2-8: The curved path length of an electron in the vicinity of an interface between 2 mediums. In a) a large step length is taken (the step length is the figure is the distance between two red points), which seems as if the electron was only in medium 2, when in actual fact it was in medium 1 as well. This problem is solved in b) where the step size is reduced, which means that the electron is now accurately transported in both mediums.

An essential component to the PRESTA algorithm is the BCA which handles the transport of electrons in the vicinity of geometrical boundaries since the Molière theory is only valid in infinite and semi-infinite media.[1] The necessity for this is illustrated in Figure 2-8. Suppose a large step length is taken (which is made possible by the PLC algorithm) near the interface between two boundaries. Even though the electron's curved path crosses the boundary, the start- and end-point of the large step indicates that it has in fact not crossed the boundary. This means that the electron would not be accurately transported. This problem is solved by reducing the step size such that the total curved path is divided into smaller segments, which means that the electron will be transported in both mediums, as it should be. This is incorporated into the PRESTA algorithm by switching from the multiple scattering mode to a single scattering mode which will decrease the step lengths as to correct for inaccurate transport near boundaries.

The PLC, LCA and BCA algorithm are all directly linked to the underlying Molière multiple scattering theory which sets a limit on the maximum and minimum step sizes, t_{max} and t_{min}, respectively, depending on the electron energy (beyond these limits the Molière theory would be invalid). The upper limit on step-size is due to the fact that angular deflections are small (since the Molière theory is based on a small angle approximation), and the lower limit on step-size is due to the fact that multiple atomic collisions is condensed into a single "collision" or step.[1] In the lower-limit, t_{max} and t_{min} converges to a single value,

which means that for low-energy transport small step sizes are used. Furthermore, at the vicinity of boundaries, step sizes are limited to $t \leq t_{perp}$, where t_{perp} is the distance to the nearest boundary. However, another condition must be satisfied, which entails that no transport of an electron step may occur across a boundary. Therefore, when near a boundary the PLC algorithm, LCA algorithm and multiple scattering are turned off and the step sizes are shortened down to a minimum value depending on the energy cut-off parameter. Since Molière's theory does not model energy loss, the CSDA must be used to account for the energy loss during each condensed step.

Due to the shortcoming of the Molière multiple scattering theory, `EGSnrc` adopted a new multiple scattering theory which is valid for steps of any sizes and moves seamlessly from a single scattering mode to an accurate multiple scattering mode. The `EGSnrc` code system employed a multiple scattering theory based on the screened Rutherford theory, with spin effects that can be added should the user choose to do so.[69] Including spin effects has been shown to produce much more accurate results as illustrated in a report by Lockwood et al.[79] For the electron transport in an infinite, homogeneous medium for a path-length s, which corresponds to an energy loss $E_0 - E$, the multiple elastic scattering distribution can be obtained by:[69]

$$\frac{\partial \Phi_0(\vec{x},\vec{\Omega},s)}{\partial s} + \vec{\Omega}\vec{\nabla}\Phi_0(\vec{x},\vec{\Omega},s) = \int_{4\pi} d\vec{\Omega}\left[\Phi_0(\vec{x},\vec{\Omega},s)\Sigma'_{el}(\vec{x},s,\vec{\Omega}\cdot\vec{\Omega}') - \Phi_0(\vec{x},\vec{\Omega},s)\Sigma'_{el}(\vec{x},\vec{\Omega},s)\right] \qquad \text{Eq 2.9}$$

Integrating Eq 2.9 over the position, expanding Φ_0 and the cross sections in Legendre polynomials P_l, the following is obtained:

$$\Phi_0(\mu,\phi,E) = \frac{1}{2\pi}\sum_{t=0}^{\infty}\left(l+\frac{1}{2}\right)e^{-G_l P_l(\mu)} \qquad \text{Eq 2.10}$$

where μ is the cosine of the polar angle θ and the process is considered in a frame where the electron is initially moving along the Z −axis. This expression was first obtained by Goudsmit and Saunderson.

In contrast with Class I CH techniques that uses pre-computed multiple distributions, the path-lengths in Class II schemes are stochastic which means that pre-computation is not an option. This favoured the small-angle Molière theory as used in `EGS4`.

The major difference between the `PRESTA-I` and `PRESTA-II` algorithm as outlined in the `BEAMnrc` manual[74], is mainly that `PRESTA-I`:

- Underestimates lateral deflections

- Underestimates longitudinal straggling
- Produces a singularity in the distribution describing the lateral spread of electrons in a single condensed history.

It is worthy to note that a MC based code such as ETRAN uses the multiple scattering theory of Goudsmit and Saunderson[27]. The multiple scattering theory of Goudsmit and Saunderson avoids the small angle approximation which is in contrast with the Molière theory which was constructed as a small angle theory. Though different, both theories have been proven to give similar angular distributions[77,80].

2.2.5.7 Phase Space Files

In BEAMnrc[74] at least one scoring plane must be defined to capture particles in a digital phase space file. This is done by specifying the component module level after which the scoring plane(s) should be. In this study a single scoring plane is defined after the last component module in both models. A phase space file can be thought of as a digital representation of a radiation beam which is "frozen" the moment it passes through the scoring plane. Information such as the particle's position, direction, energy, history and weight are recorded for each particle captured. Phase space files are binary files depending on which type of system they were written.

2.2.5.8 Variance Reduction Techniques

2.2.5.8.1 Introduction

The efficiency ϵ of a MC simulation depends on two factors, namely the variance σ^2 (square of the statistical uncertainty) of a simulation as well as the associated simulation time T:

$$\epsilon = \frac{1}{\sigma^2 T}, \qquad \text{with } \sigma^2 \propto \frac{1}{N} \text{ and } T \propto N \qquad \text{Eq 2.11}$$

where N is the number of histories simulated.[81] A high MC efficiency is always sought which agrees with a low variance and simulation time. However, the variance or statistical uncertainty for a simulation is linearly dependent on the amount of histories simulated, which means that simulating more histories will lead to a reduction in the variance.[82] The only method to improve the efficiency for a particular MC simulation is to decrease the simulation time by effectively employing variance reduction techniques (which decreases σ^2 for a given T).

In the EGSnrc Code System about 6 variance reduction techniques can be implemented should the user choose to. This include geometry interrogation, range rejection, Russian Roulette, bremsstrahlung splitting (BS), photon forcing and bremsstrahlung cross section enhancement. The re-use of phase space

files is also considered to be an efficiency improving tool. The focus for variance reduction techniques will only be the ones suitable for electron transport.

2.2.5.8.2 Geometry Interrogation

Geometry Interrogation is a variance reduction technique performed automatically which stores the current closest distance to a boundary in the variable DNEAR. In this manner, the subroutine $HOWFAR is only called if DNEAR reaches a certain minimum.

2.2.5.8.3 Range Rejection

Before each electron transport step the range of the electron with energy E is determined. This allows the EGSnrc Code System to check the distance to the nearest boundary DNEAR at the beginning of each step and to terminate the current particle's history should E_RANGE be shorter than this distance.[69]

In EGSnrc the range rejection variance reduction technique is implemented on a region-by-region basis, which means that the user can choose in which regions to apply range rejection.[69,74] Range Rejection saves a large amount of simulation time especially since the range and distance to the nearest boundary is calculated for other purposes, which means that it is a very fast check.[75] This is especially applied in large regions where it is less likely for electrons to escape the boundaries, for example within linac head simulations.

2.2.5.8.4 Russian Roulette

Russian Roulette is typically used in combination with bremsstrahlung splitting. Russian Roulette is played on particles or photons and determines whether a particle is allowed to be transported further or is terminated.[69,74]

Charged particle Russian Roulette is also available to use should the interest not be in charged particle dose deposition. This would be required since the large number of charged particles formed by split photons would require a large excess of simulation time. If the interest is therefore in photons only, Russian Roulette can be played on all charged particles formed by split photons which will significantly reduce CPU time while still preserving variance reduction advantages.

2.2.5.8.5 Bremsstrahlung Splitting

Bremsstrahlung splitting (BS) is a variance reduction technique that increases the amount of bremsstrahlung photons at an interaction site. This is of more concern in photon beam simulations.

2.2.5.8.6 Photon Forcing

This variance reduction technique allows the user to specify components in which photons will be forced to interact and is also more applicable to photon beams.

2.2.5.8.7 Bremsstrahlung Cross Section Enhancement

Bremsstrahlung cross section enhancement (BCSE) is a variance reduction technique typically used in photon beam simulations.

2.2.5.8.8 Using Precomputed Results

Though not a variance reduction technique per se, it acts as a direct technique to decrease simulation time by simply reusing phase space files.[28,61] Within this study, the modelling of the linac is split into two models; an upper patient-independent (invariant) model and a lower patient-dependent (variant) model. The invariant part represents the electron beam up to just before the secondary collimators (MLCs, JAW, Applicator) and therefore the phase space file generated here only depends on the initial beam properties such as the focal spot and energy spectrum and not on any field size collimation. This means that this invariant phase space file can be reused within subsequent simulations in the variant model where the beam will be collimated to the required field size. This effectively saves simulation time through the invariant model.

2.2.5.9 EGSnrc Based Codes

2.2.5.9.1 BEAMnrc

`BEAMnrc` is a MC based simulation package which is designed specifically to model radiotherapy sources such as medical linacs and was developed as part of the OMEGA project to develop a full 3-D electron beam treatment planning system in order to calculate doses to patients.[74] `BEAMnrc` comes with a graphical user interface (GUI) which replaces the need for user-written subroutines (`HOWFAR` and `AUSGAB`). The user must first specify an accelerator by selecting various component module (CM) geometries from a supplied list. These CMs must be chosen in the same order as the order of components

to be modelled. The next step is to specify each CM in terms of its structural variables and regional simulation parameters. The geometry specification or modelling is done with the help of detailed technical information about the linac such as schematics, drawings or physical measurements. BEAMnrc also allows the implementation of variance reduction techniques as mentioned in section 2.2.5.8. Global simulation parameters also have to be specified, as well as a PEGS4 data file containing the relevant cross section data. Various source options are also supplied from which the user can choose the most applicable source option. In addition, scoring planes must be defined which defines the phase space level, as mentioned in section 2.2.5.7. This phase space file can either be used for subsequent BEAMnrc simulations as source input or can be used for phantom dose calculations in DOSXYZnrc.

2.2.5.9.2 DOSXYZnrc

DOSXYZnrc is based directly on the DOSXYZ code which was developed for the EGS4 code system and is an EGSnrc-based MC simulation code for calculating dose distributions in a rectilinear voxel phantom.[75,83] The Cartesian geometry used in DOSXYZnrc can represent a full 3-D voxel phantom. Phantoms can either be created manually by specifying individual or groups of voxels in the X, Y and Z direction where each voxel can have a different material and density, or phantoms can be created from CT datasets using the utility code ctcreate which converts a CT dataset of Hounsfield numbers into a usable form for DOSXYZnrc. Incorporation of SSD is done by specifying the coordinates of the isocentre and constructing the phantom accordingly. Source specification includes the use of different types of sources, including phase space files and beams characterized by Beam Characterization Models. Simulation parameters such as global energy cut-off parameters must be specified, and features such as a restart facility is also available for use. DOSXYZnrc can be run on parallel computing platforms, where statistics are calculated on a history-by-history basis.

2.2.5.9.3 DOSRZnrc, FLURZnrc, SPRRZnrc, CAVRZnrc, CAVSPHnrc and EDKnrc

The NRC has developed and distributed a whole series of codes for the use with the EGS4 MC simulation system over the years which have been widely used with results prepared to experiments in many cases. These codes have been altered to use the EGSncrMP system. More specific, codes that have been developed for cylindrical RZ and spherical geometries include DOSRZnrc, FLURZnrc, SPRRZnrc, CAVRZnrc, CAVSPHnrc and EDKnrc.[84]

DOSRZnrc is used to simulate the passage of an electron or photon beam in a finite, right cylindrical geometry. The energy which is deposited within these regions is scored and analyzed statistically. Pulse

height distributions in an arbitrary volume made up of several regions can also be scored. The DOSRZnrc code is the "work-horse" dose scoring code as developed by the NRC.

FLURZnrc can be used to calculate the fluence of different particles in a RZ geometry. The fluence is calculated in each region in the differential in energy by dividing the total path length in a given energy bin with the volume of the region, since this has been shown to be equivalent to the fluence averaged over a volume. Outputs from FLURZnrc include fluence as a function of position, spectra in each region as well as spectra of primaries vs secondaries of any types.

The SPRRZnrc code is used in RZ geometries to calculate Spencer-Attix restricted collision stopping-power ratios. Although it uses a different calculation technique to calculate these values (an "on-the-fly" technique is used), these calculations have been shown to have good agreement with calculations from other codes.

CAVRZnrc is used when cavity ionization chambers are of interest and can be used to calculate various factors of interest such as A_{scat} and A_{wall}. The results of CAVRZnrc calculations have been shown to have good agreement with standard theory.

CAVSPHnrc is very similar to CAVRZnrc in that it calculates various factors of interest for cavity ionization chambers such as K_{att}, K_{scat} and K_{wall} and the dose to the cavity region per unit incident fluence. CAVSPHnrc is however different than CAVRZnrc in that its calculations are for spherical geometry.

EDKnrc is used for spherical geometries to calculate energy deposition kernels (EDKs) for photons or electrons, albeit mono- or polyenergetic, forced to interact at the centre. This code therefore outputs EDKs and dose distributions within the phantom or dose to defined regions as the cavity of a spherical ionization chamber.

2.2.5.10 Other Monte Carlo Based Codes

2.2.5.10.1.1 Introduction

Even though this study is performed using the EGSnrc Code System, many other MC based codes have been developed which is a result of decades of research and developments. The majority of these codes are freely distributed online, where latest versions can be obtained and used within the bounds of the license agreements.[1] The EGSnrc code system has perhaps been the most used MC package in medical physics especially for research purposes.[34] Even though all MC based codes take into consideration the

underlying physics involved, they are all inherently different to one another and therefore produce different results, which is important to consider if something like charged particle transport is of importance. Fortunately intensive benchmarking tests have been carried out by numerous authors to evaluate these codes against something like the EGS code system.[34]

2.2.5.10.1.2 PENELOPE

The PENELOPE code package is a sophisticated electron transport package which is typically used as a research code.[1] PENELOPE includes a detailed treatment of cross sections for low-energy transport as well as a flexible geometry package which allows the simulation of accelerator beams.[85] A mixed simulation algorithm is used to transport particles, where interactions that invoke changes in the kinetic energy or the direction of flight above certain thresholds are simulated explicitly. The rest of the interactions are condensed into a single transport step, very similar to a Class II CH technique.[86]

2.2.5.10.1.3 GEANT4

The GEANT4 code is a many-particle general purpose code developed specifically for particle physics applications.[1,85] It can simulate a wide selection of particles (e.g. neutrons, protons, pions) and physics processes over a wide energy range.[86] GEANT4 forms the basis of the GATE simulation toolkit for nuclear medicine applications in PET and SPECT. Although the system is very powerful, it is quite slower than the EGSnrc system and demonstrates some problems with electron transport.[85] Typically the models used in GEANT4 contains parameters tuned for electron scattering, where the tuning is performed by the developers and not by the user.[86]

2.2.5.10.1.4 PEREGRINE

PEREGRINE is a MC based code developed specifically for Radiotherapy planning purposes to improve the efficiency of dose calculations.[1,87] It is basically an EGS4 CH implementation and utilizes the random hinge approach for electron transport mechanics, with several variance reduction techniques being used such as reusing source particles, bremsstrahlung splitting, Russian Roulette, range rejection and photon forcing. PEREGRINE can run simulations in parallel which also reduces the total computation time. [34,85] PEREGRINE furthermore constructs a model by using a full MC simulation of a linac head in the BEAM code.

2.2.5.10.1.5 MCNP

The MCNP code system was originally intended for extensive use as a neutron-photon code in nuclear reactor calculations. The code has a very powerful geometry package and the electron transport physics of the ETRAN code system, which is based on a Class I CH technique. MCNP runs considerably slower than the EGSnrc system since geometries are interpreted rather than compiled. This makes the code very flexible.[1,34,85] A MCNP based code, RT_MCNP, has been used in Radiotherapy planning for research purposes from radiosurgery to Intensity Modulated Radiotherapy (IMRT) planning using a micro-MLC. Another code, ITS, has about the same efficiency than the MCNP code system when used in very simple geometries.[34] ORANGE is another MCNP based dose engine which has been used in Radiotherapy treatment planning.[1]

2.2.5.10.1.6 Dose Planning Method (DPM)

DPM is a research code which was developed specifically for fast Radiotherapy treatment planning purposes and to perform electron beam dose calculations in a voxelated geometry. Its electron transport scheme involves the use of large CH steps when crossing medium boundaries, which means that particles do not stop when crossing these boundaries. It uses the Kawrakow-Bielajew multiple scattering formalism and the random hinge approach for transport mechanics.[1,34]

2.2.5.10.1.7 MCDOSE & MCSIM

MCDOSE and MCSIM are based on the EGS4/BEAM code system and have been developed specifically for fast treatment planning, therefore optimization includes electron-track repeating which is used in combination with the variance reduction techniques already available in the EGSnrc system. It comprises of a user-friendly, measurement-based clinical beam commissioning system.[1] MCDOSE has been shown to give very similar results than EGS4.[34]

2.2.5.10.1.8 Macro Monte Carlo (MMC)

The MMC code is a semi-numerical hybrid electron transport beam for fast electron beam Radiotherapy treatment planning. MMC uses pre-calculated data from EGSnrc simulations of electron transport through small spheres of varying sizes and materials and follows a random walk through the CT phantom based on these pre-calculated values. MMC may use some pre-calculated accelerator-specific information, but fluence intensities from various sub-sources are fitted to the user's measured data.[1,34]

2.2.5.10.1.9 Voxel Monte Carlo (VMC) and XVMC

The VMC algorithm was developed in 1996 by Kawrakow et al. who applied some approximations and simplifications to the electron transport algorithm.[88] Initially, VMC was only applicable to electron beams and involved approximations such as a simplified treatment of the multiple scattering theory as compared to EGS4 and produced good results very fast.[34,88] In 1997 PENELOPE's random hinge approach was incorporated into VMC, and by the year 2000 all approximations were removed.[34] The code was extended to photon transport which lead to the development of XVMC in 1998 by Fippel.[89] In 1999 a series of variance reduction techniques were incorporated into XVMC which lead to a factor 5-9 increase in calculation speed. VMC and XVMC have been redeveloped in C++ along with improvements in the modelling of physical processes and variance reduction techniques, which is known as the VMC++ code as developed by Kawrakow. The VMC++ code produces the fastest electron/photon transport compared with other MC based codes. This is due to its history repetition technique, known as "Simultaneous Transport Of Electron Particle Steps" (STOPS). This works on the basis of calculating one electron history in water and repeating the history at various positions on the patient or phantom surface, correcting the history for the presence of heterogeneities. The VMC++ algorithm also takes larger steps than the EGS4 system, which increases calculation efficiency.[1,34,88] The XVMC algorithm is incorporated into different planning systems such as *Monaco* (CMS), *PrecisePlan* (Elekta), and *iPlan* (BrainLab).

2.2.5.10.1.10 Monte Carlo Vista (MCV)

The MCV code was developed for clinical IMRT purposes as well as for research applications. Photon-electron MC dose algorithms are interfaced to the Pinnacle commercial planning system and calculations are done in parallel. Linac simulations are based on the BEAM code, which divides the linac up into its patient-independent and patient-dependent components. Both patient and phantom calculations are performed by DOSXYZnrc, VMC++ or MCVRTP (a C++ MC code developed by Philips which uses many EGS4 algorithms). MCV also makes use of variance reduction techniques which are inherent to the sub-codes used, such as EGS4.[87] Another code, Particle DMLC is a further development of the EGS/BEAM-based MCV system which involves fast particle transport through a dynamic MLC geometry and is designed specifically for IMRT purposes.[1]

2.2.5.10.1.11 GATE, FLUKA, IDEAL-DOSE

The GATE (***G**eant4 **A**pplication for **T**omographic **E**mission*) code is based on the general purpose GEANT4 toolkit for applications in external beam nuclear medicine, Radiotherapy, brachytherapy, intraoperative Radiotherapy, hadron therapy and *in vivo* dose monitoring. FLUKA (***FLU**ktuierende **KA**skade*) is a general-purpose code for particle interaction and transport for radiation protection studies at high energy accelerators. The IDEAL-DOSE code is used for microdosimetry.[90]

2.2.5.11 Multiple Source Models

Multiple source models are usually constructed to replace phase space files for the calculation of dose distributions in a phantom or patient, since they generally produce reasonably accurate results much faster than full MC simulations. A multiple-source model is a beam model based on the fact that particles from the same components of a linac have very similar characteristics in terms of their energies and incident directions, and that particles from different components have different energy angular and spatial distributions.[57,60,91] Many published studies have used multiple source models to predict dose distributions.[57,60,65,66,91–93]

A multiple-source model is constructed from a phase space file produced in a full MC simulation. The requirement is set that each linac component within the full MC simulation be given a LATCH bit. The multiple-source model is based on the principle that particles from different components of an accelerator can be treated as if they were from different sub-sources, where each sub-source would represent a critical component within the treatment head. Each sub-source has its own energy spectrum and planar fluence derived from the phase space file.

With the EGSnrc code system comes a utility program called BEAMDP which can be used for constructing multiple source models. BEAMDP then produces an output which can be used within DOSXYZnrc to simulate dose distributions within rectilinear voxels.

Various types of source models can be modeled depending on the component modeled within the linac. In general, each component within the linac can be represented by a 2-D source within a $X-Y$ plane perpendicular to the central Z-axis, with the same $X-Y$ dimensions as the component. The Z-position of each plane is taken as the midpoint of the thickness of the component. A variety of sub-sources therefore exist including ring, cone and point sources, as well as applicator-, collimator-, rectangular- and circular-plane sources.

In a study by Jabbari et al.[57] a multiple source model was constructed for a NEPTUNE 10PC medical linac using the BEAMDP code. Central axis percentage depth dose curves and d_{max} off-axis profiles were measured and simulated (for both the phase space and multiple source models) for three electron energies (6, 8 and 10 MeV) and for three field sizes (3 x 3 cm^2, 10 x 10 cm^2 and 25 x 25 cm^2) in water. Both the phase space and multiple-source models agreed within 1.3 % to measured data. The multiple source model simulation time was a factor of 10 less than for the phase space file with significant reduction in storage space.

In another study by Ali et al.[66] a two-point source model was constructed for an Elekta Precise linac, one representing an electron source and another representing head generated bremsstrahlung photons, where the relative intensity of each was determined from measured data depth dose data in water. The EGSnrc/DOSXYZnrc code was utilized to construct the two-point model and to perform dose calculations. Central axis depth dose curves and d_{max} off-axis profiles were used to compare measured and simulated data for six electron energies (4, 6, 8, 10, 12 and 15 MeV), four field sizes (6 x 6 cm^2, 10 x 10 cm^2, 14 x 14 cm^2 and 20 x 20 cm^2) and three SSD's (95, 100 and 110 cm). Dose distributions were also obtained for a paranasal sinus treatment case using a Rando phantom. In most cases the agreement of measured and simulated data was within the 2 %/2 mm criterion, however discrepancies within the first 6 mm of the water phantom was observed.

2.2.5.12 Limitations of Monte Carlo Simulations

Generally, when using MC based codes some limitations are involved. With regards to the EGSnrc code system, this limitation usually involves long calculation times to obtain a certain statistical uncertainty and storage space issues. Phase space files generated can be very large (can be tens of gigabytes per phase space file), and often this can lead to storage space problems if many phase space files are produced. The long calculation time is associated with the inherent transport algorithm used. The EGSnrc Code System generally suffers from long calculation times especially when compared to other MC based codes.

With the implementation of variance reduction techniques, both the simulation time and space of phase space files can be decreased. Furthermore, modern day computers are capable of performing much more calculations per unit time than, say, a decade ago. The availability of computer clusters has also increased which is perfect for running simulations in parallel or to perform multiple simulations at once using hundreds (if not thousands) of processors with an enormous amount of storage space. The use of

something like multiple source models also decreases simulation time and storage space, of course with a possible sacrifice in accuracy.

2.2.5.13 Role of Monte Carlo Simulations in this Study

Since it has been shown repeatedly that MC is the most accurate formulism to calculate dose distributions within homo- and heterogeneous media, MC as employed in the `EGSnrc` code system was selected to model and generate benchmark data for the Elekta Synergy® 160-leaf Agility™ linac. `BEAMnrc` (section 2.2.5.9.1) offers many geometry packages which can effectively be used to model the different components in the linac, and `DOSXYZnrc` (section 2.2.5.9.2) can accurately handle dose calculations within any geometry in a Cartesian coordinate system. Since a lot of research is performed with the `EGSnrc` code system, the model can also be available for future use and datasets produced can be stored.

One of the major issues as recognized by the AAPM[87] is the discrepancies in the build-up region of simulated electron CAX PDD curves when compared to measured data. Various possible causes for this phenomenon have been ruled out. Therefore, Monte Carlo simulations in this study will also be used to possibly solve this should it be a problem.

2.3 Gamma Dose Distribution Evaluation Tool

In Radiotherapy it is common that two sets of dose distributions be compared with one another, albeit two sets of measured dose data or a single set of measured and computed dose data. It is a requirement that the method of comparison must not only be quantitative but must also be efficient and accurate.[94] The γ (Gamma) dose distribution evaluation tool is a method used by many authors in order to compare dose distributions (hence, to perform a Gamma analysis), and also is commonly used in routine QA processes clinically.

The γ distribution tool is used as a point-by-point search. For each evaluated point, the distance to each reference point is computed. Each value calculated, labelled $\Gamma(\vec{r}_e, \vec{r}_r)$, is a generalized Euclidian distance in the renormalized dose and distance space. From the Γ distribution, the minimum value is selected and represents the γ value for that evaluated point. The process is then repeated for the remainder of the evaluated points. This produces a γ distribution which accurately and effectively quantifies the magnitude of success or failure of a dose distribution. $\Gamma(\vec{r}_e, \vec{r}_r)$ is calculated as follows:

$$\Gamma(\vec{r}_e, \vec{r}_r) = \sqrt{\frac{|\vec{r}_e - \vec{r}_r|^2}{\Delta d^2} + \frac{[D_e(\vec{r}_e) - D_r(\vec{r}_r)]^2}{\Delta D^2}}$$ Eq 2.12

The first and second terms within the square root represents the generalized distance and the generalized dose, respectively. $\vec{r}_e$ and $\vec{r}_r$ represents the vector positions of the evaluated and reference points. $D_e(\vec{r}_e)$ and $D_r(\vec{r}_r)$ are the evaluated and reference doses at the evaluated and reference vector positions, respectively, and Δd and ΔD are the *DTA* and *dose difference* criteria, respectively.

A set of $\Gamma(\vec{r}_e, \vec{r}_r)$ values are therefore computed for each evaluated point, with each set containing the same amount of values than the amount of reference points, and with the number of sets being the same than the number of evaluated points. From each set, γ is computed as follows:

$$\gamma(\vec{r}_r) = min\{\Gamma(\vec{r}_e, \vec{r}_r)\} \forall \{\vec{r}_e\}$$ Eq 2.13

Eq 2.13 simply states that the minimum value is extracted from each Γ set, and accordingly a γ distribution is produced with the same amount of points than the evaluated set of points.

Chapter 3: Materials and Methods

3.1 Monte Carlo Simulations

3.1.1 BEAMnrc

As discussed in the theory section 2.2.5.9.1, BEAMnrc is an EGSnrc based code which allows the modelling of medical linear accelerators. During the BEAMnrc modelling process, the user first has to "specify" an accelerator after which modelling can commence. Once modeling is completed, the accelerator must be built and compiled before the start of a simulation.

Also mentioned in section 2.2.5.9.1 is BEAMnrc's list of CMs that are offered to the user from which the most appropriate CMs can be chosen to model the linac. Even though each CM has a specific name, they have a wide variety of application, which means that each CM may be used to model something completely different. The list of CMs available in BEAMnrc include: SLABS, CONS3R, CONESTAK, FLATFILT, CHAMBER, JAWS, DYNJAWS, APPLICAT, CIRCAPP, PYRAMIDS, BLOCK, MLC, MLCQ, VARMLC, MLCE, DYNVMLC, MESH, MIRROR, XTUBE, SIDETUBE, ARCCHM, SYNCJAWS, SYNCVMLC and SYNCMLCE. CMs work on the basis that each component within the linac is assumed to take up a horizontal slab portion. CMs are re-usable and each CM is independent on one another. Gaps between CMs are filled with air.

For this study the components within the Elekta Synergy® 160-leaf Agility™ are to be modelled, which in electron mode includes: Electron Exit Window, Primary Scattering Foil, Primary Collimator, Secondary Scattering Foils, Dual Ionization Chamber, Light-field Mirror, Multi-leaf Collimator, Backup Jaw/Diaphragm, Screen, Electron Applicator and Applicator Open Field Insert. For the purposes of re-using phase space files, two modes were created, namely a patient-independent (invariant) and a patient-dependent (variant) model. Table 3-1 illustrates which CMs were chosen to model which components. Appendix 1 and Appendix 2 gives an example of the invariant and variant BEAMnrc input files.

The actual modeling of each component involves geometry specification for each CM. Each CM has a set of geometry parameters which define the various regions that exist within the CM. The user has the task to correlate these parameters with specifications given on schematics/drawings as supplied by the

vendor, as well as with physical measurement (for example, measuring the trimmers/scrapers of the electron applicator with a measuring tape). Permission was given by Elekta to the Medical Physics Department of the University of the Free State for the use of proprietary radiation machine information only for research purposes (Appendix 7). Due to this proprietary agreement, exact details of components could not be divulged.

Table 3-1: `BEAMnrc` component modules chosen to model the components in the Elekta Synergy® Agility™ linac.

LINAC COMPONENT	*`BEAMnrc` COMPONENT MODULE*
PATIENT-INDEPENDENT MODEL	
Electron Exit Window	CONSETAK
Primary Scattering Foil	CONESTAK
Primary Collimator	CONESTAK
Secondary Scattering Foil	FLATFILT
Dual Ionization Transmission Chamber	CHAMBER
Light-field Mirror	MIRROR
PATIENT-DEPENDENT MODEL	
Air Gap	SLABS
Multi-leaf Collimator	MLCQ
Backup Jaw/Diaphragm	MLCQ
Screen	CONESTAK
Electron Applicator	APPLICAT
Applicator Open Field Insert	PYRAMIDS

3.1.1.1 Patient-independent/Invariant/Upper Model

3.1.1.1.1 Electron Exit Window

The electron exit window was modelled using the CM CONESTAK.[74] CONESTAK allows the user to model stacks (or layers) of coaxial truncated cones and has a cylindrical outer wall. The medium of the region inside and outside the cone, as well of the outer wall, may differ. The geometry of the exit window is a copper block which contains a central cylindrical hole with a thin metal foil. The region above the metal foil contains a vacuum (part of the waveguide-bending magnet system) and the region below contains air (part of the linac head). The electron exit window model parameters for the CM CONESTAK are indicated in Table 3-2.

Table 3-2: CM CONESTAK model parameters for the electron exit window component. Note that the materials specified are air and two different metals. Each material is represented by the cross-sectional data as given by ICRU37 with a lower electron energy of 0.7 MeV.

	Outer Radial Boundary (cm)		*2*
	Distance of front of material in CM to reference plane (cm)		0
	Number of conical layers		3
	LAYER DIMENSIONS (cm)		
LAYER 1	Thickness		0.85
	Front radius		0.5
	Back radius		0.5
LAYER 2	Thickness		0.0125
	Front radius		0.6
	Back radius		0.6
LAYER 3	Thickness		0.1375
	Front radius		0.6
	Back radius		0.6
	LAYER PROPERTIES		
LAYER 1		Inside Cone	Outside Cone
	ECUTIN (MeV)	0.7	0.7
	PCUTIN (MeV)	0.01	0.01
	Dose Zone	0	0
	LATCH bit	23	2
	Material	AIR700ICRU	METAL 1
LAYER 2		Inside Cone	Outside Cone
	ECUTIN (MeV)	0.7	0.7
	PCUTIN (MeV)	0.01	0.01
	Dose Zone	0	0
	LATCH bit	1	2
	Material	METAL 2	METAL 1
LAYER 3		Inside Cone	Outside Cone
	ECUTIN (MeV)	0.7	0.7
	PCUTIN (MeV)	0.01	0.01
	Dose Zone	0	0
	LATCH bit	23	2
	Material	AIR700ICRU	METAL 1
	Outer Wall		Yes
	Inner radius of outer wall (cm)		1.9
	ECUTIN (MeV)		0.7
	PCUTIN (MeV)		0.01
	Dose zone		0
	LATCH bit		2
	Material		METAL 1

3.1.1.1.2 Primary Scattering Foil

The primary scattering foil is a single metal foil with a thickness depending on the electron nominal energy. Each foil (one for each electron energy) is contained in a stainless-steel fan-like carousel, which rotates with the selection of a different electron nominal energy as to introduce to appropriate foil into the path of the narrow pencil-like beam. The primary scattering foil was modelled using the CM CONESTAK.[74] The primary scattering foil model parameters for the CM CONESTAK are indicated in Table 3-3.

Table 3-3: CM CONESTAK model parameters for the primary scattering foil component. The materials specified are air and two different metals. Each material is represented by the cross-sectional data as given by ICRU37 with a lower electron energy of 0.7 MeV. The tolerances on scattering foil thicknesses are also indicated.

	Outer Radial Boundary (cm)		*2*
	Distance of front of material in CM to reference plane (cm)		1.2
	Number of conical layers		1
	LAYER DIMENSIONS (cm)		
LAYER 1	Thickness		x
	Front radius		0.5
	Back radius		0.5
	LAYER PROPERTIES		
		Inside Cone	Outside Cone
LAYER 1	ECUTIN (MeV)	0.7	0.7
	PCUTIN (MeV)	0.01	0.01
	Dose Zone	0	0
	LATCH bit	4	3
	Material	METAL 3	METAL 4
	Outer Wall		Yes
	Inner radius of outer wall (cm)		1.9
	ECUTIN (MeV)		0.7
	PCUTIN (MeV)		0.01
	Dose zone		0
	LATCH bit		3
	Material		METAL 4

Foil Thickness Variation x

Electron Nominal Energy (MeV)	Thickness (mm)
4	0.0345 ± 0.0015
6	0.069 ± 0.003
8	0.1035 ± 0.0045
10	0.069 ± 0.003
12	0.1038 ± 0.006
15	0.1935 ± 0.0085

3.1.1.1.3 Primary Collimator

The primary collimator is a solid-alloy block composed of tungsten, nickel and iron. It is conical in shape and projects a fixed angle of 27°48', or 27.8°. The collimator has cylindrical symmetry. The primary collimator was modelled using the CM CONESTAK.[74] The primary collimator model parameters for the CM CONESTAK are indicated in Table 3-4.

Table 3-4: CM CONESTAK model parameters for the primary collimator component. Materials specified include air and a metal. Each material is represented by the cross-sectional data as given by ICRU37 with a lower electron energy of 0.7 MeV. Note that no outer wall was required to model the primary collimator.

	Outer Radial Boundary (cm)		*7*
	Distance of front of material in CM to reference plane (cm)		1.5
	Number of conical layers		1
	LAYER DIMENSIONS (cm)		
LAYER 1	Thickness		10.1
	Front radius		0.3712
	Back radius		2.8707
	LAYER PROPERTIES		
		Inside Cone	Outside Cone
LAYER 1	ECUTIN (MeV)	0.7	0.7
	PCUTIN (MeV)	0.01	0.01
	Dose Zone	0	0
	LATCH bit	23	5
	Material	AIR700ICRU	METAL 5
	Outer Wall		No

3.1.1.1.4 Secondary Scattering Foils

The secondary scattering foils was modelled using the CM FLATFILT.[74] Though designed to model flattening filters present in photon beams, FLATFILT allows simple layer-by-layer definition of conical structures with a front and back radius. The secondary scattering foil consists of a holder with certain thickness and contains a certain number of metal foils; each foil with its own radius and thickness. The foils are held together by a central metal rivet. Two types of scattering foils are used in the Synergy linac, a low- and high-energy secondary scattering foil. The low-energy scattering foil is used for nominal electron energies of 4, 6 and 8 MeV, whereas the high energy scattering foil is used for nominal electron energies of 10, 12 and 15 MeV. The bottom view of the high-energy scattering foil is indicated in Figure 3-1 as well as the top views of both the low- and high-energy secondary scattering foils. The high- and

low energy secondary scattering foil model parameters for the CM FLATFILT are indicated in Table 3-5 and Table 3-6, respectively.

Figure 3-1: On the left side a bottom view of the high-energy scattering foil is given. Both the images on the right side represent a top view of the scattering foils, illustrating the difference in the number and radii of foils used within each scattering foil holder. The top right image is the low-energy scattering foil and the bottom right image is the high-energy secondary scattering foil.

Table 3-5: CM FLATFILT model parameters for the high-energy secondary scattering foil component. Materials specified are air and a metal. Each material is represented by the cross-sectional data as given by ICRU37 with a lower electron energy of 0.7 MeV.

Outer Radial Boundary (cm)		*4*
Distance of front of material in CM to reference plane (cm)		13.7
Number of layers		6
LAYER DEFINITIONS (cm)		
LAYER 1	Thickness	2.1048
	Number of cones	1
LAYER 2	Thickness	0.001
	Number of cones	2
LAYER 3	Thickness	0.055
	Number of cones	2
LAYER 4	Thickness	0.04
	Number of cones	2
LAYER 5	Thickness	0.0075
	Number of cones	1

LAYER 6			Thickness	0.001
			Number of cones	2

LAYER-CONE PROPERTIES

LAYER 1		Cone 1	Outer Region
	ECUTIN (MeV)	0.7	0.7
	PCUTIN (MeV)	0.01	0.01
	Dose Zone	0	0
	LATCH bit	23	1
	Material	AIR700ICRU	METAL 6
	Top Radius (cm)	3.7	4
	Bottom Radius (cm)	3.7	4

LAYER 2		Cone 1	Cone 2	Outer Region
	ECUTIN (MeV)	0.7	0.7	0.7
	PCUTIN (MeV)	0.01	0.01	0.01
	Dose Zone	0	0	0
	LATCH bit	1	23	1
	Material	METAL 6	AIR700ICRU	METAL 6
	Top Radius (cm)	0.05	3.7	4
	Bottom Radius (cm)	0.05	3.7	4

LAYER 3		Cone 1	Cone 2	Outer Region
	ECUTIN (MeV)	0.7	0.7	0.7
	PCUTIN (MeV)	0.01	0.01	0.01
	Dose Zone	0	0	0
	LATCH bit	1	23	1
	Material	METAL 6	AIR700ICRU	METAL 6
	Top Radius (cm)	1.25	3.7	4
	Bottom Radius (cm)	1.25	3.7	4

LAYER 4		Cone 1	Cone 2	Outer Region
	ECUTIN (MeV)	0.7	0.7	0.7
	PCUTIN (MeV)	0.01	0.01	0.01
	Dose Zone	0	0	0
	LATCH bit	1	23	1
	Material	METAL 6	AIR700ICRU	METAL 6
	Top Radius (cm)	2.25	3.7	4
	Bottom Radius (cm)	2.25	3.7	4

LAYER 5		Cone 1	Outer Region
	ECUTIN (MeV)	0.7	0.7
	PCUTIN (MeV)	0.01	0.01
	Dose Zone	0	0
	LATCH bit	1	23
	Material	METAL 6	METAL 6
	Top Radius (cm)	3.7	4
	Bottom Radius (cm)	3.7	4

LAYER 6		Cone 1	Cone 2	Outer Region
	ECUTIN (MeV)	0.7	0.7	0.7
	PCUTIN (MeV)	0.01	0.01	0.01
	Dose Zone	0	0	0
	LATCH bit	1	23	4

	Material	METAL 6	AIR700ICRU	METAL 6
	Top Radius (cm)	0.05	3.7	4
	Bottom Radius (cm)	0.05	3.7	4

Table 3-6: CM FLATFILT model parameters for the low-energy secondary scattering foil component. Materials specified are air and a metal. Each material is represented by the cross-sectional data as given by ICRU37 with a lower electron energy of 0.7 MeV.

	Outer Radial Boundary (cm)			*4*
	Distance of front of material in CM to reference plane (cm)			13.7
	Number of layers			7
	LAYER DEFINITIONS (cm)			
LAYER 1	Thickness			2.0775
	Number of cones			1
LAYER 2	Thickness			0.001
	Number of cones			2
LAYER 3	Thickness			0.005
	Number of cones			2
LAYER 4	Thickness			0.03
	Number of cones			2
LAYER 5	Thickness			0.03
	Number of cones			2
LAYER 6	Thickness			0.0075
	Number of cones			1
LAYER 7	Thickness			0.001
	Number of cones			2
	LAYER-CONE PROPERTIES			
LAYER 1		Cone 1		Outer Region
	ECUTIN (MeV)	0.7		0.7
	PCUTIN (MeV)	0.01		0.01
	Dose Zone	0		0
	LATCH bit	23		1
	Material	AIR700ICRU		METAL 6
	Top Radius (cm)	3.7		4
	Bottom Radius (cm)	3.7		4
LAYER 2		Cone 1	Cone 2	Outer Region
	ECUTIN (MeV)	0.7	0.7	0.7
	PCUTIN (MeV)	0.01	0.01	0.01
	Dose Zone	0	0	0
	LATCH bit	1	23	1
	Material	METAL 6	AIR700ICRU	METAL 6
	Top Radius (cm)	0.03	3.7	4
	Bottom Radius (cm)	0.03	3.7	4
LAYER 3		Cone 1	Cone 2	Outer Region
	ECUTIN (MeV)	0.7	0.7	0.7
	PCUTIN (MeV)	0.01	0.01	0.01

	Dose Zone	0	0	0
	LATCH bit	1	23	1
	Material	METAL 6	AIR700ICRU	METAL 6
	Top Radius (cm)	0.25	3.7	4
	Bottom Radius (cm)	0.25	3.7	4
		Cone 1	Cone 2	Outer Region
	ECUTIN (MeV)	0.7	0.7	0.7
	PCUTIN (MeV)	0.01	0.01	0.01
	Dose Zone	0	0	0
LAYER 4	LATCH bit	1	23	1
	Material	METAL 6	AIR700ICRU	METAL 6
	Top Radius (cm)	2	3.7	4
	Bottom Radius (cm)	2	3.7	4
		Cone 1	Cone 2	Outer Region
	ECUTIN (MeV)	0.7	0.7	0.7
	PCUTIN (MeV)	0.01	0.01	0.01
	Dose Zone	0	0	0
LAYER 5	LATCH bit	1	23	1
	Material	METAL 6	AIR700ICRU	METAL 6
	Top Radius (cm)	2.5	3.7	4
	Bottom Radius (cm)	2.5	3.7	4
			Cone 1	Outer Region
	ECUTIN (MeV)		0.7	0.7
	PCUTIN (MeV)		0.01	0.01
	Dose Zone		0	0
LAYER 6	LATCH bit		1	23
	Material		METAL 6	AIR700ICRU
	Top Radius (cm)		3.7	4
	Bottom Radius (cm)		3.7	4
		Cone 1	Cone 2	Outer Region
	ECUTIN (MeV)	0.7	0.7	0.7
	PCUTIN (MeV)	0.01	0.01	0.01
	Dose Zone	0	0	0
LAYER 7	LATCH bit	1	23	23
	Material	METAL 6	AIR700ICRU	AIR700ICRU
	Top Radius (cm)	0.03	3.7	4
	Bottom Radius (cm)	0.03	3.7	4

3.1.1.1.5 Dual Ionization Chamber

The dual ionization chamber was modelled using the CM CHAMBER.[74] The dual ionization chamber is cylindrical in geometry and contains several central layers consisting of mylar and a solid alumina chamber wall. The dual ionization chamber model parameters for the CM CHAMBER are indicated in Table 3-7.

Table 3-7: CM CHAMBER model parameters for the dual ionization chamber. Note that the materials specified are air, alumina and mylar which are represented by AIR700ICRU, ALUMINA700ICRU and MYLAR700ICRU, respectively, which represents the cross-sectional data as given by ICRU37 with a lower electron energy of 0.7 MeV.

Outer Radial Boundary (cm)	*10*
Distance of front of material in CM to reference plane (cm)	16.4
Top Part	No
Number of Layers in Central region	14
Bottom Part	No

LAYER DEFINITIONS (cm)

Layer	Thickness (cm)	ECUTIN (MeV)	PCUTIN (MeV)	Dose Zone	LATCH bit	Material
1	0.16	0.7	0.01	0	23	AIR700ICRU
2	0.0012	0.7	0.01	0	8	MYLAR700ICRU
3	0.1	0.7	0.01	0	23	AIR700ICRU
4	0.0012	0.7	0.01	0	8	MYLAR700ICRU
5	0.16	0.7	0.01	0	23	AIR700ICRU
6	0.0012	0.7	0.01	0	8	MYLAR700ICRU
7	0.1	0.7	0.01	0	23	AIR700ICRU
8	0.0012	0.7	0.01	0	8	MYLAR700ICRU
9	0.16	0.7	0.01	0	23	AIR700ICRU
10	0.0012	0.7	0.01	0	8	MYLAR700ICRU
11	0.22	0.7	0.01	0	23	AIR700ICRU
12	0.0012	0.7	0.01	0	8	MYLAR700ICRU
13	0.16	0.7	0.01	0	23	AIR700ICRU
14	0.16	0.7	0.01	0	23	AIR700ICRU

3.1.1.1.6 Mirror

The light-field mirror of the linac was modelled using the CM MIRROR.[74] The CM MIRROR can have an arbitrary angle of less than 85° with respect to the central axis and can also have multiple layers with different thicknesses and media. The Synergy's mirror has an angle of 37.55° relative to the central-axis. The mirror model parameters for the CM MIRROR are indicated in Table 3-8.

Table 3-8: CM MIRROR model parameters for the light-field mirror. Materials specified are air, mylar and aluminum which are represented by AIR700ICRU, MYLAR700ICRU and AL700ICRU, respectively, which represents the cross-sectional data as given by ICRU37 with a lower electron energy of 0.7 MeV.

Half-width of outer square boundary (cm)	*6*
Distance of front of material in CM to reference plane (cm)	18.15
Z-direction span	8.7
X-coordinate of mirror at top, from Z-axis to first layer (cm)	3.2744
X-coordinate of mirror at bottom, from Z-axis to first layer (cm)	-3.4146
Number of layers	2

LAYER DEFINITIONS

LAYER 1	ECUTIN (MeV)	0.7
	PCUTIN (MeV)	0.01
	Dose Zone	0
	LATCH bit	9
	Material	MYLAR700ICRU
LAYER 2	ECUTIN (MeV)	0.7
	PCUTIN (MeV)	0.01
	Dose Zone	0
	LATCH bit	9
	Material	AL700ICRU

Region Behind and In Front of Mirror

	Region behind Mirror	Region in front of Mirror
ECUTIN (MeV)	0.7	0.7
PCUTIN (MeV)	0.01	0.01
Dose Zone	0	0
LATCH bit	23	23
Material	AIR700ICRU	AIR700ICRU

3.1.1.2 Patient-dependent/Variant/Lower Model

3.1.1.2.1 Air Gap

Prior to the MLCs an air gap exists between the scoring plane for the patient-independent model (which is after the CM MIRROR) and the front of the first CM in the patient-dependent model (CM MLCQ). The air gap was modelled with the CM SLABS.[74] SLABS can be used to model a stack of semi-infinite planes, each with different thickness and material, with square symmetry about the central axis. The scoring plane in the patient-independent model was defined at $Z = 26.85$ cm, and the distance to the front of

the MLC is equal to $Z = 31.18$ cm. Therefore, the air gap must be equal to 4.329 cm (with the inclusion of a minimum gap of 0.01 cm). The mirror model parameters for the CM SLABS are indicated in Table 3-9.

Table 3-9: CM SLABS model parameters for the modeling of an air gap. Air is modelled using AIR700ICRU, the cross-sectional data as given by ICRU37 with a lower electron energy of 0.7 MeV.

	Half-width of outer square boundary (cm)	*30*
	Distance of front of material in CM to reference plane (cm)	26.85
	Number of slabs	1
	LAYER DEFINITIONS	
LAYER 1	Slab thickness (cm)	4.329
	ECUTIN (MeV)	0.7
	PCUTIN (MeV)	0.01
	Dose Zone	0
	LATCH bit	23
	ESAVE	0
	Material	AIR700ICRU

3.1.1.2.2 Multi-Leaf Collimator

The Agility™ has two leaf banks, each with 80 leaves which move parallel to the X-direction. The leaves have rounded leaf tips with a radius of 17 cm, and the leaf width at isocenter is 0.5 cm. The leaves consist of an alloy of different metals. The CM MLCQ was chosen to model rounded leaf ends.[74] With the CM MLCQ, the Z-position of the origin of the radius of the leaves are specified, and leaf positions (positive and negative) along the X-axis are defined on this Z-level. The modelling parameters for the CM MLCQ are indicated in Table 3-10.

Table 3-10: CM MLCQ model parameters for the MLC. Materials specified include air and a metal alloy. Each material is represented by the cross-sectional data as given by ICRU37 with a lower electron energy of 0.7 MeV.

	Half-width of outer square boundary (cm)	*21.5*
	Distance of front of material in CM to reference plane (cm)	31.18
	Leaves parallel to	X
	Thickness of leaves (cm)	9
	Number of leaves	80
	Total width of leaves (cm)	15.28
	Focal point on Z-axis of leaf sides	0
	Radius of circle defining leaf ends (cm)	17
	Z of origin of circle defining leaf ends	34.93
COLLIMATOR PROPERTIES		
Inside Collimator	ECUTIN (MeV)	0.7
	PCUTIN (MeV)	0.01
	Dose Zone	0
	LATCH bit	23
	Material	AIR700ICRU
Collimator leaves	ECUTIN (MeV)	0.7
	PCUTIN (MeV)	0.01
	Dose Zone	0
	LATCH bit	23
	Material	METAL 5

When dealing with photon beams, it is quite easy to calculate what the positions of individual leaves should be on their respective Z-positions for a given field size and SSD with the use of a similar triangle calculation. The number of open and closed leaves can then also be calculated by making use of the leaf width at isocenter with the inclusion of guard leaves. However, with electron beams it is not that straightforward. For each electron applicator-energy combination, predefined MLC and JAW positions are determined by the vendor. The electron applicator, as well as the MLCs and JAW are responsible to ensure that the appropriate amount of beam flatness is reached at depth in water. The applicator mostly takes care of this, but also plays an important role in the final beam shaping to the required field size. This means that the MLCs and JAW are located at positions that are relatively out of the field.

The challenge is to obtain the precise positions of the MLC, as well as the JAW, for each electron applicator-energy combination. The first approach is to measure the light field produced by a specific applicator-energy combination, and to use a similar triangle calculation to obtain the positions of the JAW

and MLCs. However, this approach would require the user to override the linac to keep its configurations once detaching the applicator, but this method can also be inconsistent and inaccurate. The more accurate and efficient method chosen was to extract the relevant information from the linac using Elekta's iCom Customer Acceptance Test (CAT) program. With the attachment and selection of each electron applicator-energy combination, the MLCs and JAW will move to their respective positions, which can be read from iCom CAT. The positional values obtained from iCom CAT represent the positions in units of cm given at isocentre. The steps followed are shown in Figure 3-2.

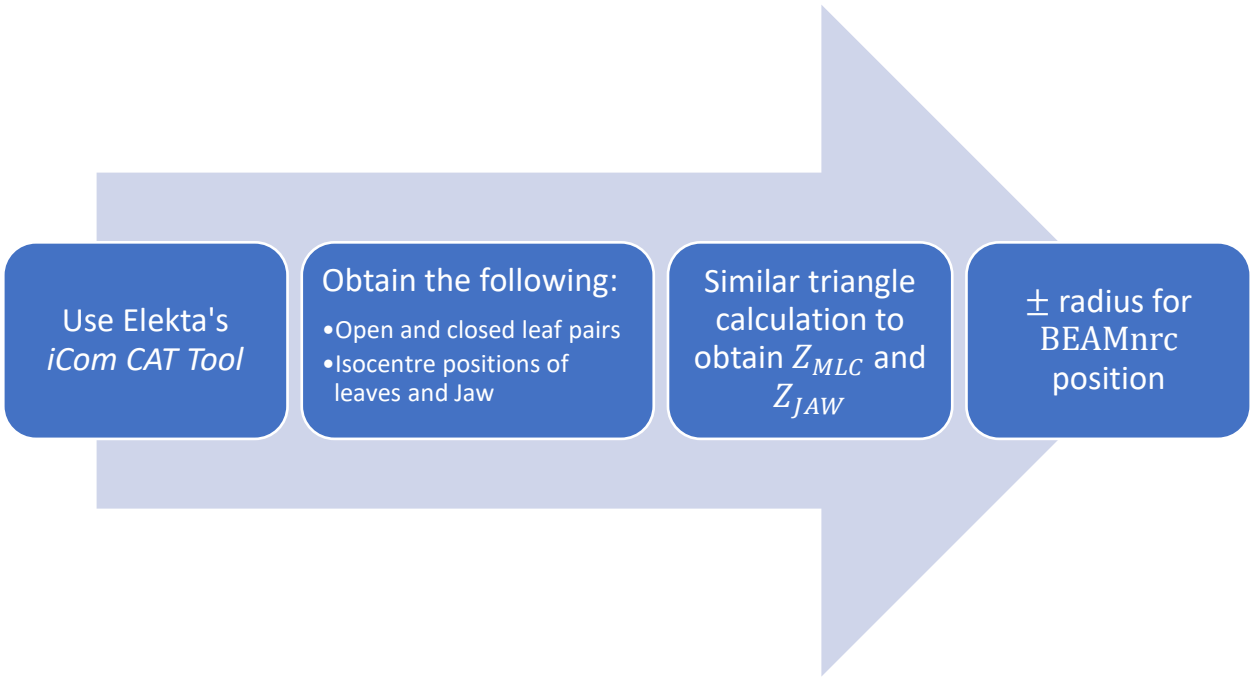

Figure 3-2: A flow diagram to illustrate the steps followed to obtain the `BEAMnrc` *positions for both the MLCs and Jaw, as well as the number of open and closed leaves, for each electron applicator-energy combination.*

With regards to the similar triangle calculation, consider the illustration in Figure 3-3 which indicates a YZ/XZ-view of the MLCs/Jaw. The goal is to obtain the `BEAMnrc` positions XON/YON and XOP/YOP, which is the negative and positive circle origin positions for the MLCs and Jaw, respectively. These origins are located at the level of the MLC and Jaw, ZO_{MLC} and ZO_{JAW}, respectively. In order to calculate this, the similar triangle calculation will involve the positions at isocentre ($Z_{MLC_{\text{iso}}}$ or $Z_{JAW_{\text{iso}}}$) and the positions at the level of the MLC and Jaw (Z_{MLC} or Z_{JAW}). Therefore:

$$\frac{Z_{MLC}}{ZO_{MLC}} = \frac{Z_{MLC_{iso}}}{100}$$

$$\therefore Z_{MLC} = \left(\frac{Z_{MLC_{iso}}}{100}\right) ZO_{MLC} \quad \text{Eq 3.1}$$

$$\therefore XON = Z_{MLC} - RO_{MLC} = \left(\frac{Z_{MLC_{iso}}}{100}\right) ZO_{MLC} - RO_{MLC} \quad \text{Eq 3.2}$$

$$\therefore XOP = Z_{MLC} + RO_{MLC} = \left(\frac{Z_{MLC_{iso}}}{100}\right) ZO_{MLC} + RO_{MLC} \quad \text{Eq 3.3}$$

$$\therefore YON = Z_{JAW} - RO_{JAW} = \left(\frac{Z_{JAW_{iso}}}{100}\right) ZO_{JAW} - RO_{JAW} \quad \text{Eq 3.4}$$

$$\therefore YOP = Z_{JAW} + RO_{JAW} = \left(\frac{Z_{JAW_{iso}}}{100}\right) ZO_{JAW} + RO_{JAW} \quad \text{Eq 3.5}$$

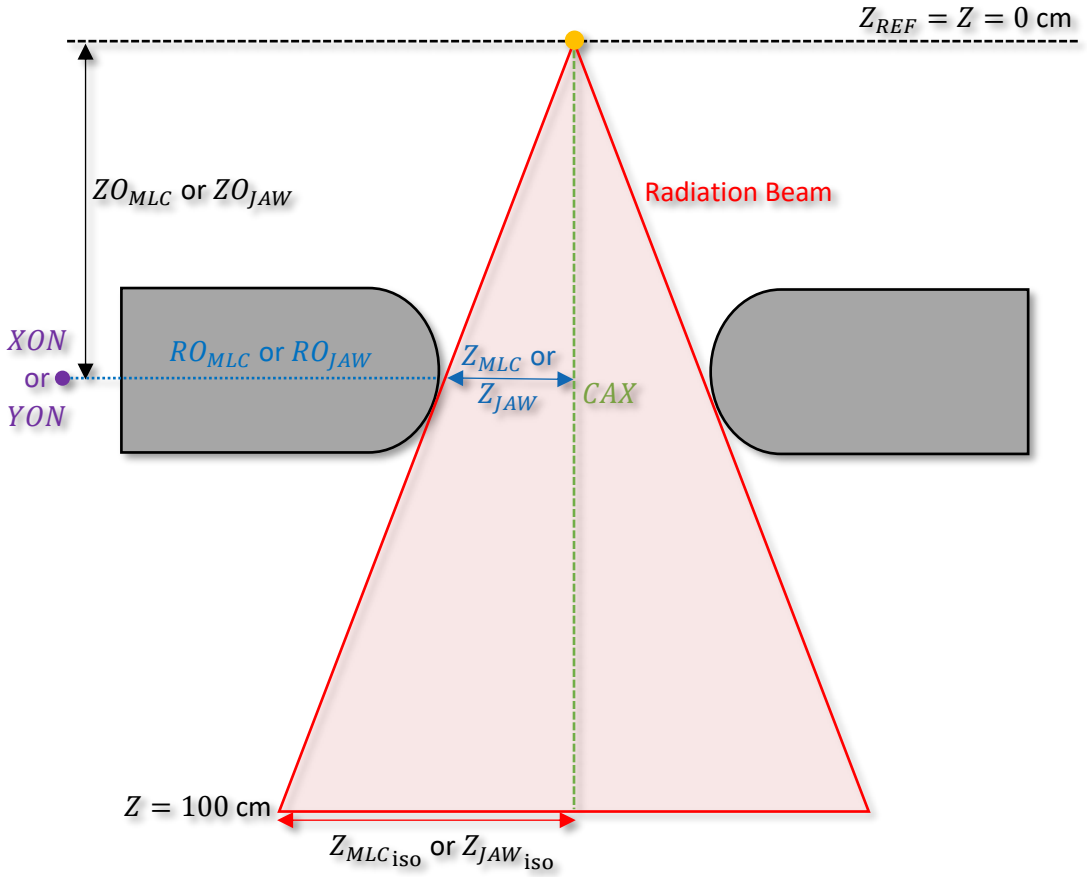

Figure 3-3: Schematic illustration of the determination of the `BEAMnrc` parameters XON/YON (and XOP/YOP, although not shown) for the MLCs and JAW, respectively for MLC and JAW positions $Z_{MLC_{iso}}$ or $Z_{JAW_{iso}}$ at the isocentre, as obtained from iCom CAT. The `BEAMnrc` reference plane Z_{REF} is located at $Z = 0$ cm. An YZ-view will be for the MLCs and a XZ-view will be for the JAW. Note that the positive X- or Y-direction is to the right, and vice versa.

The BEAMnrc MLC and JAW positions are calculated using Eq 3.2, Eq 3.3, Eq 3.4 and Eq 3.5. The MLC and JAW positions, as well as the number of open and closed leaves for each field size-electron energy combination are given in Table 3-11 to Table 3-14. With the CM MLCQ, definition of open and closed leaves with their respective positive and negative positions are done by specifying leaf-pair groups that are at the same positions. For instance, leaf pair 1-20 (all closed), leaf pair 21-60 (open) and leaf pair 61-80 (all closed). 'Closed' leaves means leaves separated with a leaf gap of 1 mm.

Table 3-11: JAW and MLC positions, as well as the number of closed and open MLCs, for each electron energy and a 10 x 10 cm^2 electron applicator. Note than in this case, X1 and X2 refer to the Jaw, and Y1 and Y2 refer to the two opposite leaf banks (each bank has 80 leaves). Note that the closed MLCs have a minimum leaf gap of 1 mm at isocentre.

	10 x 10 cm^2					
	4 MeV	**6 MeV**	**8 MeV**	**10 MeV**	**12 MeV**	**15 MeV**
	JAW POSITIONS (cm)					
X1 Diaphragm	18.7351	18.2634	18.4502	18.1700	17.6563	17.4695
X2 Diaphragm	-18.7351	-18.2634	-18.4502	-18.1700	-17.6563	-17.4695
	NUMBER OF OPEN AND CLOSED LEAVES					
# Y1 Closed	1 to 16 65 to 80	1 to 18 63 to 80	1 to 17 64 to 80	1 to 18 63 to 80	1 to 20 61 to 80	1 to 21 60 to 80
# Y1 Open	17 to 64	19 to 62	18 to 63	19 to 62	21 to 60	22 to 59
# Y2 Closed	1 to 16 65 to 80	1 to 18 63 to 80	1 to 17 64 to 80	1 to 18 63 to 80	1 to 20 61 to 80	1 to 21 60 to 80
# Y2 Open	17 to 64	19 to 62	18 to 63	19 to 62	21 to 60	22 to 59
	LEAF POSITIONS (cm)					
Y1 Closed	17.1223	17.1223	17.1223	17.1223	17.1223	17.1223
Y140	21.1916	20.80737	20.94709	20.8423	20.35328	20.31835
Y2 Closed	-17.1223	-17.1223	-17.1223	-17.1223	-17.1223	-17.1223
Y240	-21.1916	-20.80737	-20.94709	-20.8423	-20.35328	-20.31835

Table 3-12: Open MLC positions at isocentre for each electron energy and electron applicator combination. The 2 x 2 cm^2 and 3 x 3 cm^2 fields use the same settings as the 6 x 6 cm^2 applicator. Closed leaves have positions at isocenter of 0.35 cm.

MLC positions (cm) at SSD = 100 cm

	Field Size at 95 cm SSD (cm^2)							
	6 x 6	*6 x 10*	*6 x 14*	*8 x 16*	*10 x 20*	*14 x 14*	*20 x 20*	*4 cm Circ*
4 MeV	8.20	12.00	14.80	15.20	16.10	14.80	16.10	5.00
6 MeV	8.10	10.90	12.90	12.50	15.10	12.90	15.10	5.00
8 MeV	8.10	11.30	12.60	11.99	15.20	12.59	15.20	5.00
10 MeV	7.70	11.00	11.30	11.00	13.40	11.30	13.40	5.00
12 MeV	7.70	9.60	10.60	10.50	13.30	10.60	13.30	5.00
15 MeV	7.70	9.50	9.80	10.50	12.80	9.80	12.80	5.00

Table 3-13: Number of open leaf pairs for each electron energy and electron applicator combination. The 2 x 2 cm^2 and 3 x 3 cm^2 fields use the same settings as the 6 x 6 cm^2 applicator. The values in brackets indicate the number of open leaves. All other leaf pairs are closed to the minimum leaf gap.

Number of Open Leaves

	Field Size at 95 cm SSD (cm^2)							
	6 x 6	*6 x 10*	*6 x 14*	*8 x 16*	*10 x 20*	*14 x 14*	*20 x 20*	*4 cm Circ*
4 MeV	24 to 57 (34)	24 to 57 (34)	24 to 57 (34)	20 to 61 (42)	17 to 64 (48)	11 to 70 (60)	8 to 73 (66)	29 to 52 (24)
6 MeV	24 to 57 (34)	24 to 57 (34)	24 to 57 (34)	21 to 60 (40)	19 to 62 (44)	14 to 67 (54)	10 to 71 (62)	29 to 52 (24)
8 MeV	24 to 57 (34)	24 to 57 (34)	24 to 57 (34)	20 to 61 (42)	18 to 63 (46)	15 to 66 (52)	10 to 71 (62)	29 to 52 (24)
10 MeV	25 to 56 (32)	25 to 56 (32)	25 to 56 (32)	21 to 60 (40)	19 to 62 (44)	18 to 63 (46)	13 to 68 (56)	29 to 52 (24)
12 MeV	25 to 56 (32)	25 to 56 (32)	25 to 56 (32)	21 to 60 (40)	21 to 60 (40)	19 to 62 (44)	14 to 67 (54)	29 to 52 (24)
15 MeV	25 to 56 (32)	25 to 56 (32)	25 to 56 (32)	21 to 60 (40)	22 to 59 (38)	21 to 60 (40)	15 to 66 (52)	29 to 52 (24)

Table 3-14: JAW positions at isocentre for each electron energy and electron applicator combination. The 2 x 2 cm² and 3 x 3 cm² fields use the same settings as the 6 x 6 cm² applicator.

JAW positions (cm) at SSD = 100 cm

	Field Size at 95 cm SSD (cm²)							
	6 x 6	*6 x 10*	*6 x 14*	*8 x 16*	*10 x 20*	*14 x 14*	*20 x 20*	*4 cm Circ*
4 MeV	7.39	7.40	7.41	9.30	11.21	14.22	15.31	5.00
6 MeV	7.39	7.40	7.41	9.00	10.20	12.29	14.30	5.00
8 MeV	7.31	7.30	7.31	9.50	10.60	11.90	14.40	5.00
10 MeV	7.01	7.00	7.00	9.00	10.00	10.50	12.80	5.00
12 MeV	7.01	7.00	7.00	9.00	8.89	9.90	12.70	5.00
15 MeV	7.01	7.00	7.00	9.00	8.50	9.20	12.20	5.00

3.1.1.2.3 Backup Diaphragm/JAW

The Synergy® Agility™ has one pair of JAWS parallel to the Y-axis with dimensions very similar to that of the MLCs as described in section 3.1.1.2.2. Each JAW has a curved tip with a radius equal to 13.5 cm. Since it is very similar to the MLCs, the CM MLCQ was used to model the JAW.[74] Each JAW can be thought of as being a single MLC leaf with an increased width. The CM MLCQ does however not allow a single leaf pair to be modelled; therefore 2 leaf pairs were modelled, each with half the width of the JAW. The modelling parameters for the CM MLCQ are indicated in Table 3-15. The JAW positions for each electron applicator-energy combination are indicated in Table 3-11 to Table 3-14.

Table 3-15: CM MLCQ model parameters for the Jaws. Materials specified include air and a metal alloy. Each material is represented by the cross-sectional data as given by ICRU37 with a lower electron energy of 0.7 MeV.

	Half-width of outer square boundary (cm)	*20*
	Distance of front of material in CM to reference plane (cm)	43.2
	Leaves parallel to	Y
	Thickness of leaves (cm)	7.7
	Number of leaves	2
	Total width of leaves (cm)	15.28
	Focal point on Z-axis of leaf sides	0
	Radius of circle defining leaf ends (cm)	13.5
	Z of origin of circle defining leaf ends	46.7
	COLLIMATOR PROPERTIES	
Inside Collimator	ECUTIN (MeV)	0.7
	PCUTIN (MeV)	0.01

	Dose Zone	0
	LATCH bit	23
	Material	AIR700ICRU
	ECUTIN (MeV)	0.7
	PCUTIN (MeV)	0.01
Collimator leaves	Dose Zone	0
	LATCH bit	23
	Material	METAL 6

3.1.1.2.4 Screen

The screen component is a thin circular mylar sheet which shields the linac head components from external sources of contamination like dust particles. The screen was modelled using the CM CONESTAK.[74] The modelling parameters for the CM CONESTAK are indicated in Table 3-16.

Table 3-16: CM CONESTAK model parameters for the screen. Air and mylar are represented by AIR700ICRU and MYLAR700ICRU, respectively, which is the cross-sectional data as given by ICRU37 with a lower electron energy of 0.7 MeV.

	Outer Radial Boundary (cm)		*14*
	Distance of front of material in CM to reference plane (cm)		52.91
	Number of conical layers		1
	LAYER DIMENSIONS (cm)		
LAYER 1	Thickness		0.0175
	Front radius		14
	Back radius		14
	LAYER PROPERTIES		
		Inside Cone	Outside Cone
LAYER 1	ECUTIN (MeV)	0.7	0.7
	PCUTIN (MeV)	0.01	0.01
	Dose Zone	0	0
	LATCH bit	12	23
	Material	MYLAR700ICRU	AIR700ICRU
	Outer Wall		No

3.1.1.2.5 Applicators

Each electron applicator consists of a base plate, a series of trimmer levels and an open field insert slot which allows the insertion of different lead shaped inserts. The trimmer levels have open dimensions such that the field size gradually decreases down to the final field size as defined by the open field insert. The CM APPLICAT is specifically designed to allow the modelling of layers of scrapers (or trimmers), where each trimmer level can have a different size as is the case with an electron applicator.[74] 9 different electron applicators had to be modelled including square applicators (6 x 6, 10 x 10, 14 x 14 and 20 x 20 applicator), rectangular applicators (6 x 10, 6 x 14, 8 x 16 and 10 x 20) and one circular applicator (4 cm diameter) which was not modeled with the APPLICAT CM since it does not allow circular geometries. Note that the field inserts were modelled separately and was therefore not included in this CM. Since there are 4 square- and 4 rectangular applicators to be modeled, the complete list of modelling parameters for the 6 x 6 cm^2 applicator is indicated in Table 3-17, whereas only the dimensional parameters for the rest of the applicators are given in Table 3-18 and Table 3-19.

Table 3-17: CM APPLICAT model parameters for the 6 x 6 cm^2 applicator. Materials specified are air, aluminum and lead which is represented by AIR700ICRU, AL700ICRU and PB700ICRU, respectively, which are the cross-sectional data as given by ICRU37 with a lower electron energy of 0.7 MeV.

Half-width of outer square boundary (cm)	*18.25*
Z of back of CM (cm)	94
Number of scrapers	6
Shape of Applicator	Square

SURROUNDING AIR PROPERTIES

ECUTIN (MeV)	0.7
PCUTIN (MeV)	0.01
Dose Zone	0
LATCH bit	23

SCRAPER DEFINITION

SCRAPER	1	2	3	4	5	6
Z of front face of scraper (cm)	54.86	76.02	76.63	84.93	85.54	93.34
Thickness of scraper (cm)	0.6	0.6	0.6	0.6	0.6	0.6
Half-width of inner opening in X and Y (cm)	5	4.7	4.7	3.6	3.6	3
Width of scraper bar in X and Y (cm)	13.25	5.7	5.7	3.65	3.65	2.45
Dose scoring zone	0	0	0	0	0	0
LATCH bit	14	14	15	15	14	14

Material	AL700IC RU	AL700IC RU	PB700IC RU	PB700IC RU	AL700IC RU	AL700IC RU

Table 3-18: Square applicator dimensional parameters as modelled with the CM APPLICAT. The rest of the modelling parameters are exactly the same as given in Table 3-17.

SQUARE APPLICATORS						
SCRAPER	1	2	3	4	5	6
10 x 10 cm²						
Half-width of outer square boundary (cm)	18.25					
Z of front face of scraper (cm)	54.22	72.02	72.63	84.93	85.54	93.34
Half-width of inner opening in X and Y (cm)	7.1	6.5	6.5	5.55	5.55	5.05
Width of scraper bar in X and Y (cm)	11.15	5.4	5.4	4.7	4.7	2.25
14 x 14 cm²						
Half-width of outer square boundary (cm)	18.4					
Z of front face of scraper (cm)	54.07	71.87	72.48	84.88	85.49	93.29
Half-width of inner opening in X and Y (cm)	8	8	8	7	7	7
Width of scraper bar in X and Y (cm)	10.4	5.35	5.35	5.3	5.3	2.05
20 x 20 cm²						
Half-width of outer square boundary (cm)	18.35					
Z of front face of scraper (cm)	54.22	71.92	72.53	84.93	85.54	93.34
Half-width of inner opening in X and Y (cm)	9	10	10	10	10	10
Width of scraper bar in X and Y (cm)	9.35	5.4	5.4	4.3	4.3	2.1

Table 3-19: Rectangular applicator dimensional parameters as modelled with the CM APPLICAT. The rest of the modelling parameters are exactly the same as given in Table 3-17.

RECTANGULAR APPLICATORS						
SCRAPER	1	2	3	4	5	6
6 x 10 cm²						
Half-width of outer square boundary (cm)	18.35					
Z of front face of scraper (cm)	54.32	75.93	76.53	84.93	85.54	93.34
Half-width of inner opening in X (cm)	7.2	6.5	6.5	5.5	5.5	5
Half-width of inner opening in Y (cm)	5	4.75	4.75	3.55	3.55	3
Width of scraper bar in X (cm)	11.3	6.45	6.45	4.75	4.75	2.1
Width of scraper bar in Y (cm)	4.1	5.7	5.7	3.5	3.5	2.4
6 x 14 cm²						
Half-width of outer square boundary (cm)	18.35					
Z of front face of scraper (cm)	54.02	75.72	76.33	84.83	85.44	93.34
Half-width of inner opening in X (cm)	8	8	8	7	7	7

Half-width of inner opening in Y (cm)	5	4.7	4.7	3.55	3.55	3
Width of scraper bar in X (cm)	10.4	6.4	4.5	3.95	2	2
Width of scraper bar in Y (cm)	4.15	5.7	4.5	3.8	3.6	2.4
8 x 16 cm²						
Half-width of outer square boundary (cm)	18.35					
Z of front face of scraper (cm)	56.02	73.12	73.73	84.93	85.54	93.34
Half-width of inner opening in X (cm)	8.4	8.7	8.7	8.05	8.05	8
Half-width of inner opening in Y (cm)	6	5.55	5.55	4.5	4.5	4
Width of scraper bar in X (cm)	9.95	5.9	4.55	5.25	4.9	2
Width of scraper bar in Y (cm)	3.1	6.45	4.55	3.75	7	2.15
10 x 20 cm²						
Half-width of outer square boundary (cm)	18.35					
Z of front face of scraper (cm)	54.32	72.02	72.63	84.83	85.44	93.34
Half-width of inner opening in X (cm)	9	10	10	10	10	10
Half-width of inner opening in Y (cm)	7.1	6.5	6.5	5.4	5.4	5
Width of scraper bar in X (cm)	9.4	5.35	4.5	4.3	3.5	2
Width of scraper bar in Y (cm)	4.9	5.35	4.5	6.5	6.3	2.5

The circular electron applicator used was fitted with a circular field insert with a field diameter of 4 cm, which using Day's rule[4] is equivalent to a square field size with side length of 3.55 cm. Since the geometry of the circular applicator differ significantly from the square and rectangular applicators, the CM APPLICAT could not be used to model the circular applicator. Furthermore, the CM CIRCAPP provides insufficient geometry to accurately model this specific applicator. The solution was to use 5 CONESTAK CMs to model the applicator layer by layer, including the circular field insert. The modelling parameters for the first CM are indicated in Table 3-20 whereas the dimensional parameters for the second-to-fifth CMs are indicated in Table 3-21.

Table 3-20: First CM CONESTAK model parameters for the circular applicator and 4 cm diameter field insert. Air and aluminum are represented by AIR700ICRU and AL700ICRU, respectively, the cross-sectional data as given by ICRU37 with a lower electron energy of 0.7 MeV.

Outer Radial Boundary (cm)		*4*
Distance of front of material in CM to reference plane (cm)		53.1
Number of conical layers		1
LAYER DIMENSIONS (cm)		
LAYER 1	Thickness	1
	Front radius	2.4

		Back radius	2.4
	LAYER PROPERTIES		
		Inside Cone	Outside Cone
LAYER 1	ECUTIN (MeV)	0.7	0.7
	PCUTIN (MeV)	0.01	0.01
	Dose Zone	0	0
	LATCH bit	23	2
	Material	AIR700ICRU	AL700ICRU
		Outer Wall	Yes
		Inner radius of outer wall (cm)	18.4
		ECUTIN (MeV)	0.7
		PCUTIN (MeV)	0.01
		Dose zone	0
		LATCH bit	23
		Material	AIR700ICRU

Table 3-21: Second to fifth CM CONESTAK dimensional parameters for the circular applicator and 4 cm diameter field insert. The other modelling parameters are exactly the same as indicated in Table 3-20.

CM number #	*2*	*3*	*4*	*5*
Outer Radial Boundary (cm)	18.4	3.2	3.15	2.85
Distance of front of material in CM to reference plane (cm)	54.1	54.7	85	88
Thickness	0.6	30.3	3.0	7.0
Front radius	2.4	2.4	2.35	2.0
Back radius	2.4	2.4	2.35	2.0
Inner radius of outer wall (cm)	2.4	3.2	3.15	2.8

3.1.1.2.6 Open Field Inserts

The open field inserts are made of lead and performs the final electron beam field definition. Each insert is about 1 cm thick and is beveled in such a way that the top opening is smaller than the bottom opening. In this study each insert was attached to their respective applicator, meaning the 6 x 6 cm^2 field insert was attached to the 6 x 6 cm^2 applicator, etc., except for the 2 x 2 cm^2 and 3 x 3 cm^2 inserts which was attached to the 6 x 6 cm^2 applicator. Since beveled, the CM PYRAMIDS was chosen to model each insert.[74] Since 10 open field inserts had to be modelled, the modelling parameters for the 10 x 10 cm^2 open field insert is shown in Table 3-22, whereas only the modelling dimensions for the rest of the inserts are given in Table 3-23.

Table 3-22: CM PYRAMIDS model parameters for the 10 x 10 cm^2 open field insert. Air and lead are represented by AIR700ICRU and PB700ICRU, respectively, which are the cross-sectional data as given by ICRU37 with a lower electron energy of 0.7 MeV.

Half-width of outer square boundary (cm)	*7.5*
Central & outer regions contain	AIR
Number of layers	1
AIR REGIONS	
ECUTIN (MeV)	0.7
PCUTIN (MeV)	0.01
Dose Zone	0
LATCH bit	23
LAYER DEFINITION	
LAYER	1
Distance from front to reference plane (cm)	94.01
Distance from back to reference plane (cm)	95
Positive X dimension of opening at front (cm)	4.85
Positive X dimension of opening at back (cm)	5
Negative X dimension of opening at front (cm)	-4.85
Negative X dimension of opening at back (cm)	-5
Positive Y dimension of opening at front (cm)	4.85
Positive Y dimension of opening at back (cm)	5
Negative Y dimension of opening at front (cm)	-4.85
Negative Y dimension of opening at back (cm)	5
Outer X edge (cm)	6.5
Outer Y edge (cm)	6.5
ECUTIN (MeV)	0.7
PCUTIN (MeV)	0.01
Dose zone	0
LATCH bit	15
Material	PB700ICRU

Table 3-23: The modelling dimensions for the rest of the square and rectangular open field inserts modelled with the PYRAMIDS CM. Note that for all of the inserts the other modelling parameters are exactly the same as for the 10 x 10 cm^2 insert as shown in Table 3-22Table 3-22. All the inserts are beveled, except the 2 x 2 cm^2 and 3 x 3 cm^2 inserts.

SQUARE OPEN FIELD INSERTS

FIELD INSERT SIZE (cm^2)	**2 x 2**	**3 x 3**	**6 x 6**	**14 x 14**	**20 x 20**
Half-width of outer square boundary (cm)	4.5	4.5	4.5	8.5	11.5
Distance from front to reference plane (cm)	94.01	94.105	94.01	94.01	94.01

Distance from back to reference plane (cm)	95	95	95	95	95
Positive X dimension of opening at front (cm)	1	1.5	2.85	6.85	9.85
Positive X dimension of opening at back (cm)	1	1.5	3	7	10
Negative X dimension of opening at front (cm)	-1	-1.5	-2.85	-6.85	-9.85
Negative X dimension of opening at back (cm)	-1	-1.5	-3	-7	-10
Positive Y dimension of opening at front (cm)	1	1.5	2.85	6.85	9.85
Positive Y dimension of opening at back (cm)	1	1.5	3	7	10
Negative Y dimension of opening at front (cm)	-1	-1.5	-2.85	-6.85	-9.85
Negative Y dimension of opening at back (cm)	-1	-1.5	-3	-7	-10
Outer X edge (cm)	4.5	4.5	4.5	8.5	11.5
Outer Y edge (cm)	4.5	4.5	4.5	8.5	11.5

RECTANGULAR OPEN FIELD INSERTS

FIELD INSERT SIZE (cm^2)	**6 x 10**	**6 x 14**	**8 x 16**	**10 x 20**
Half-width of outer square boundary (cm)	12	12	12	12
Distance from front to reference plane (cm)	94.01	94.01	94.01	94.01
Distance from back to reference plane (cm)	95	95	95	95
Positive X dimension of opening at front (cm)	4.85	6.85	7.85	9.85
Positive X dimension of opening at back (cm)	5	7	8	10
Negative X dimension of opening at front (cm)	-4.85	-6.85	-7.85	-9.85
Negative X dimension of opening at back (cm)	-5	-7	-8	-10
Positive Y dimension of opening at front (cm)	2.85	2.85	3.85	4.85
Positive Y dimension of opening at back (cm)	3	3	4	5
Negative Y dimension of opening at front (cm)	-2.85	-2.85	-3.85	-4.85
Negative Y dimension of opening at back (cm)	-3	-3	-4	-5
Outer X edge (cm)	7.1	9	9.5	11.5
Outer Y edge (cm)	5.4	5.4	5.5	6.5

3.1.1.3 EGSnrc Rendered Model

A XZ-view of the upper-head and lower-head models as rendered by the `BEAMnrc` accelerator preview is given in Figure 3-4 for a 4 MeV electron beam with a field size of 10 x 10 cm^2. Although displayed on the same image, the two models are completely separate and therefore two phase space planes are defined. The second phase space file is defined at the nominal electron SSD of 95 cm.

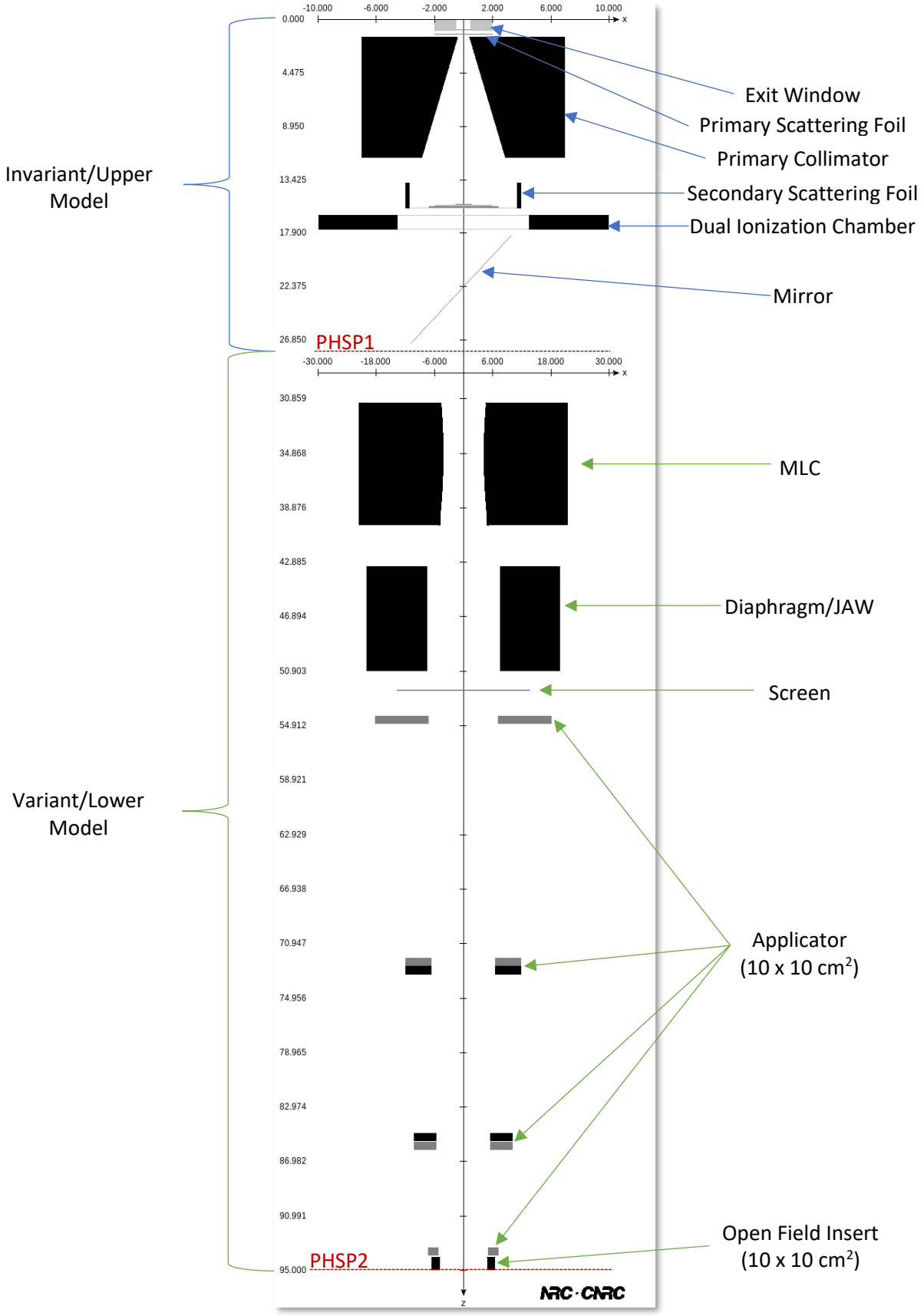

Figure 3-4: The variant (4 MeV) and invariant (10 x 10 cm^2) electron model developed for the Elekta Synergy® Agility™ linac as rendered by the `BEAMnrc` accelerator preview. The Z- levels of the two phase space (PHSP) files are indicated with dashed red lines.

3.1.1.4 EGSnrc Parameters

The medium within the linac head was set to air, which is represented by the ICRU 37 cross-sectional data with an electron cut-off energy of 0.7 MeV, AIR700ICRU.

The IWATCH parameter, which governs the output to the screen of to the EGS log file during beam execution, was set to the default (IWATCH = 0) which means that on completion of each batch, IWATCH outputs information regarding the batch such as elapsed time, $\frac{\text{elapsed time}}{\text{CPU time}}$, initial random number seeds as well as total number of random seeds used in batch, total number of histories run up to and including the batch, and the total number of particles scored in the phase space file.

The RNG Seed Options is controlled by the ISTORE parameter which decides how BEAMnrc reads and writes the state of the RNG used in simulations. ISTORE was set to the default (ISTORE = 0), which means that BEAMnrc stores the state of the RNG for the first history in each batch.

The Run option IRESTART was set to the default value (IRESTART = 0), ensuring that with the execution of the simulation a new run is initiated by BEAMnrc and all the output files from previous runs (with the same name) will be deleted, if present.

Output options IO_OPT controls the phase space output. IO_OPT was set to the default (IO_OPT = 0), which outputs a phase space file at each scoring plane defined.

IDAT, the Store Data Arrays parameter, controls the output to the data file .egsdat which contains data from a previous run should it be required for a restart run. IDAT was set to the default value of 0, which will output data such as the energy deposited and fluence, number of histories completed, elapsed time and the current RNG state to the .egsdat file.

The LATCH option was set to the default (LATCH_OPTION = 2, comprehensive LATCH setting, inherited latch – set by passage), which means that LATCH values from primaries are passed onto the subsequent secondaries formed. LATCH bits 1-23 for the secondaries will represent all the regions where the secondaries have been as well as where its ancestors have been up to the point of secondary formation.

IZLAST was set to the default value of 0 which means that ZLAST will not be scored in phase space files. ZLAST represents the Z-position of last interaction for photons, as well as the Z-position of where an electron or its ancestors was set in motion by a photon.

The number of histories NCASE for the patient-independent and patient-dependent model are given in Appendix 3. Since the default number of batches in EGSnrc are set to 10, the number of histories per batch is simply $\frac{\text{NCASE}}{10}$. Prior to EGSnrc batch running was required for statistics, however in EGSnrc statistics are calculated on a history-by-history basis. The motivation to still use batches in EGSnrc is only for the sake of saving intermediate data and diagnostics.

The values for the initial RNG seed 1 and 2, or IXXIN and JXXIN, are dependent on which RNG is used. EGSnrc offers the use of both RANMAR and RANLUX, as discussed in section 2.2.5.4. The RANLUX RNG was used which means that IXXIN represents the luxury value and only a single RNG seed (JXXIN) is used. The default EGSnrc value for IXXIN is 1 which, despite being the statistical-purity equivalent of RANMAR, has not been documented to give incorrect Monte Carlo results. The value for JXXIN was selected based on a set of random numbers constructed in Microsoft Excel.

The maximum CPU hours allowed for a simulation, TIMMAX, was set to an arbitrary large number as to allow simulations with a big amount of histories to be executed and finished without interruption as this is the function of TIMMAX. TIMMAX was set to be equal to 500 hours (which gives a simulation almost 21 days to be completed, which is a complete overkill).

BS was implemented with a splitting number of 200. No BCSE was selected nor electron/photon splitting. Electron range rejection and photon forcing was turned off. The global electron and photon energy cut-off parameters, ECUT and PCUT was set to 0.7 MeV and 0.01 MeV, respectively. This was also the values chosen for the regional ECUTIN and PCUTIN parameters. Of course, the production energy threshold parameters for electrons and photons (as required by the Class II CH scheme), AE and AP is equal to ECUT and PCUT, respectively.

For both the invariant and variant models a single scoring plane was defined after the last CM present within the model; that is, CM MIRROR in the invariant model and CM PYRAMIDS in the variant model (except for the circular applicator which ends with the CM CONESTAK). The scoring plane was modelled to have annular zones which is the BEAMnrc default. BEAMnrc calculates the maximum number of zones available with equal zone areas and in this manner determines the number of scoring zones automatically.

The dose calculation option was set to *total dose* (BEAMnrc default) and therefore only the total dose is calculated. The distance of the front of the first CM to the reference plane, was set equal to 0 cm and 26.85 cm for the invariant and variant models, respectively, as determined from schematics.

- Maximum electron step length (SMAXIR):
    - Since the EXACT boundary crossing algorithm and PRESTA-II electron step algorithm is used, no restriction on the maximum step length is required. For this reason, SMAXIR automatically defaults to a value of 1×10^{10} cm.
- Maximum fractional energy loss per electron step (ESTEPE):
    - The default value of 0.25 is chosen since this is required for accurate electron transport when using the PRESTA-II electron transport algorithm.
- Maximum first multiple elastic scattering moment per electron step (XImax):
    - This should be equal to, approximately, half the average multiple scattering angle squared. The default value is used which is 0.5.
- Boundary Crossing Algorithm (bca_algorithm):
    - The user has a selection of two possible boundary crossing algorithms. The first is the EXACT algorithm which was developed to eliminate a fluence singularity when forcing a multiple scattering event at a boundary. The EXACT algorithm is dependent on the Skin_depth_for_BCA parameter (to be discussed), which governs at which distance from a boundary the EXACT algorithm should transport electrons in a single scattering mode.
    - The other BCA is the PRESTA-I algorithm which was used with EGS4/PRESTA in which the LCA is switched off if the perpendicular distance from the electron to the boundary is less than Skin_depth_for_BCA, after which a multiple scattering event is forced at the boundary.
    - The EXACT algorithm was selected.
- Skin Depth for BCA (skindepth_for_BCA):
    - If the chosen BCA is the EXACT algorithm, the Skin_Depth_for_BCA parameter determines at which perpendicular distance from the electron to the boundary, in elastic mean free paths, electron transport should switch over to a single scattering mode. The default value of 3 elastic mean free paths was chosen. The entire simulation can be performed in single scattering mode if Skin_Depth_for_BCA is set to a very large value.
    - If the PRESTA-I BCA is chosen, Skin_Depth_for_BCA represents the perpendicular distance from the electron to a boundary at which lateral pathlength corrections are turned off, which in effect means that the electron will be transported in a straight line until it reaches the boundary.

- Electron-Step Algorithm (transport_algorithm):
    - This option determines which algorithm to use to perform lateral and longitudinal corrections in order to account for elastic scattering events in a condensed history electrons step. PRESTA-II and PRESTA-I can be chosen. For reasons as discussed in section 2.2.5.6.3, the PRESTA-II algorithm was the chosen electron-step algorithm.
- Spin Effects (spin_effects):
    - If spin effects are turned on, the elastic scattering cross-sections that consider relativistic spin effects are used in the transport of electrons. If spin effects are turned off, the screened Rutherford cross-sections are used for elastic scattering. Spin effects were turned on for each simulation.
- Electron Impact Ionization (eii_flag):
    - Different theories can be selected such as those by Casnati, Kolbenstvedt, Gryzinski and Kawrakow in order to simulate electron impact ionization. Electron impact ionization was turned on with the use of Kawrakow's theory.
- Bremsstrahlung angular sampling (IBRDST):
    - IBRDST determines the type of angular sampling that must be done when a bremsstrahlung photon is created during an inelastic collision event. Two options are available. If IBRDST = Simple, bremsstrahlung angles are sampled using the leading term of the modified equations of Koch and Motz. If IBRDST = KM, the entire modified equation of Koch and Motz is used for the sampling of bremsstrahlung angles. This option was chosen for simulations.
- Bremsstrahlung cross sections (IBR_NIST):
    - This option determines what differential cross-sectional data should be used for bremsstrahlung interactions. Three options are available including the Bethe-Heitler cross-sections that are Coulomb corrected above 50 MeV (IBR_NIST = BH), the differential cross-sections from the NIST bremsstrahlung cross-section data (IBR_NIST = NIST) and the NRC differential cross-sections which basically corrects the NIST cross-sectional data for electron-electron bremsstrahlung (IBR_NIST = NRC). The chosen option was IBR_NIST = BH.
- Bound Compton Scattering (IBCMP):
    - Bound Compton scattering can be turned on for an entire simulation or can be applied in selected regions. If IBCMP = on, the original Klein-Nishina formula for Compton

scattering is augmented with an impulse approximation in order to simulate binding effects and Doppler broadening. If IBCMP = off, only the Klein-Nishina formula is used to determine the differential cross-sections for Compton scattering. IBCMP = Norej uses the total bound Compton cross sections without any impulse corrections and does not reject any Compton interactions. IBCMP = on was chosen.

- Pair angular sampling (IPRDST):
    - IPRDST determines the method of sampling of emission angles of the electron and positron emitted following a pair production event. Three settings are possible. If IPRDST = off, the positron and electron created by the pair production event have fixed polar angles given by the ratio of the electron mass to the energy of the original photon. If IPRDST = KM, then an equation developed by Motz et al. is used to determine emission angles. If IPRDST = Simple, the default, then only the first term in the equation by Motz et al. is used. This was the chosen option.
- Pair cross sections (pair_nrc):
    - This option determines which cross-sections are used for pair production events. Two options are available. If pair_nrc = BH, the Bethe-Heitler cross-sections are used, and if pair_nrc = NRC, cross-sections developed at the NRC that include asymmetry in the positron-electron energy distribution are used. pair_nrc = BH was selected.
- Photoelectron angular sampling (IPHTER):
    - This option determines which sampling method to use for the angle of emission of photoelectrons. If IPHTER = off, which is the default option, photoelectrons inherit the direction of the incident photon. If IPHTER = On, Sauter's formula is used to determine the emission angle of the photoelectron. IPHTER was turned off.
- Rayleigh scattering (IRAYLR):
    - With this option it can be selected whether Rayleigh scattering should be simulated or not. If IRAYLR = on, then Rayleigh events are simulated with the use of the total coherent cross-sections from Storm and Israel and the atomic form factors form Hubbel and Øverbø. Rayleigh scattering can also be turned on and off in selective regions. If IRAYLR = off then Rayleigh events will not be simulated. This was the selected option.
- Atomic Relaxations (IEDGFL):
    - If IEDGFL = on, then atomic relaxation after a Compton and/or photoelectric event is simulated via the emission of any combination of K-, L-, M- and N-shell fluorescent

photons, Auger electrons and Coster-Kronig electrons. Atomic relaxation can also be turned on and off in selective regions. If IEDGFL = off, atomic relaxations are not simulated, which means that if there is a photoelectric event, all the photon's energy is transported to the photoelectron. IEDGFL = on was chosen.

- Photon cross-sections (photon_xsections):
    - This determines what photon cross-sectional data must be used for the simulation. Included cross-sections are the Storm-Israel, EPDl and xcom cross-sections. The Storm-Israel are the standard PEGS4 cross-sections, epdl selects the cross-sections from the evaluated photon data library (EPDL) from Lawrence Livermore, and xcom uses the XCOM photon cross-sections from Burger and Hubbell. The user can also select the option PEGS, where customized photon cross-sectional data will be used. This was chosen, since data from the ICRU was used (700icrucaw).
- Photon cross-sections output (xsec_out):
    - This setting can be turned on if the user wants to output a file containing the photon cross sectional data used during the simulation. This was turned off.

3.1.1.5 Focal Spot Modelling

BEAMnrc offers the user a range of source options which can be used to model the radiation source incident onto the modelled geometry. For the invariant model source number 19 (ISOURCE = 19) was chosen in BEAMnrc as shown in Figure 3-5, which entails an elliptical parallel beam from the front with a Gaussian distribution in the crossline (X) and inline (Y) directions. ISOURCE = 19 not only allows the modelling of the intensity distribution of the source focal spot, but also the specification of the source beam energy (section 3.1.1.6).

Since the focal spot of the beam at Z = 0 cm is chosen to be Gaussian in intensity, the size of the focal spot was defined in terms of the full width at half maximum (FWHM) of the Gaussian distribution. The FWHM was chosen to be 1.5 mm in both the X and Y directions (hence a circular focal spot was modelled). An elliptical beam (different FWHM for the X and Y directions) was not required since measured inline and crossline profiles agreed within 1 mm/1 %; this number improving (decreasing) with an increase in electron nominal energy (section 4.1.1).

An electron beam incident parallel to the Z-axis was modelled with directional cosines UINC = 0, VINC =0, and WINC = 1, with no angular spread present in the beam. It must be noted that there is a difference

between the intrinsic and initial electron beam. The intrinsic electron beam refers to the beam leaving the accelerator structure (waveguide) and entering the beam handling system (quadrupoles and bending magnet). The initial electron beam means the electron beam that has passed through the beam transport system of the accelerator and impinges on its exit vacuum window. The initial beam is modelled and not the intrinsic beam.[95]

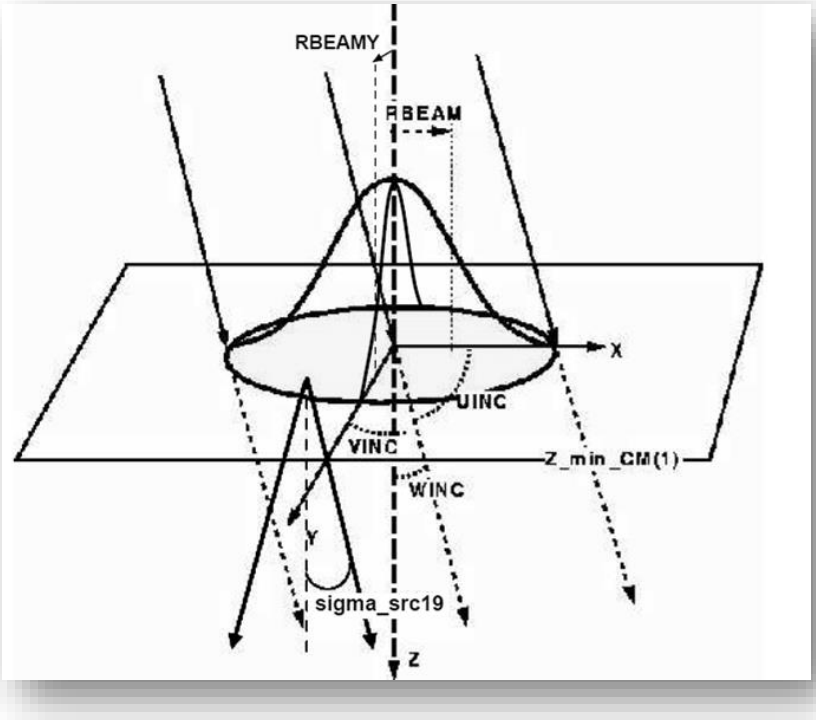

Figure 3-5: `BEAMnrc` source number 19, an elliptical beam with Gaussian intensity distributions in both the X and Y directions. The width of the beam is defined in terms of the distribution's sigma or FWHM value. A mean angular spread with respect to the central axis can be incorporated, or parallel beam with incident direction cosines UINC, VINC and WINC can be specified.

The choice of focal spot size and shape (circular or elliptical) depends highly on the linac itself and can play an important role in improving the match between simulated and measured data. Since electron beam properties of the initial electron beam such as focal spot size and shape, as well as energy spectral information are usually not specified by the linac manufacturer, the user is left with the task to find some means to identify these properties. With regards to the electron focal spot, performing physical measurements is one method to estimate the focal spot size and shape. In a study by Huang et al.[96] the focal spot size and shape for a CL21EX linac for electron energies of 6, 9, 12 and 16 MeV was estimated from measurements with a slit camera composed of alternating lead and paper sheets. The study found

that the focal spot was elliptical and Gaussian in intensity with a FWHM ranging from 1.69 mm to 2.24 mm. Another method of estimating the focal spot size and shape is to investigate the changes in profile penumbra with a change in focal spot size. This can be done with the aid of simulations, which was the approach followed by Wang and Leszczynski[97] who found the focal spot of a Siemens Primus linac to be between 3-4 mm. A study by Rodrigues et al.[98] investigated, amongst other things, the focal spot size and its influence on depth-dose and off-axis profiles were investigated with EGSnrc-based simulations. They concluded the study with a focal spot FWHM of 1.6 mm and with the observation that dose distributions were not sensitive to the focal spot size. Another study by Schreiber et al.[99] investigated flatness, symmetry and penumbral changes due to electron focal spot size variations using the EGS4 code system. It was found in this study that changes from a 2 mm to a 4 mm diameter brought about a maximum change of 0.2 % to profile flatness and a maximum change of 1.1 % to the penumbral width. These changes also did not follow a specific trend with increasing electron energy. The conclusion was also made that electron focal spot diameter had very little effect on the dose distributions for any electron energy. In a study by Björk et al.[95] the focal spot FWHM was reported to be between 1 mm and 2 mm for Elekta linacs. Various studies on the effect of the focal spot size on photon dose distributions have been done and published.[34,100–102]

Due to the difficulty associated with the measurement of the focal spot, the focal spot shape (circular or elliptical) was deduced from the shape of inline and crossline 10 x 10 cm^2, 95 cm SSD profiles for all electron energies, meaning, if there were no discrepancy between inline and crossline profiles, the focal spot could be assumed to be circular (i.e., the FWHM in the X-direction and Y-direction is the same) taking into consideration the radial symmetry of the scattering foils. The FWHM (focal spot size) was deduced from a set of simulations, each with different FWHM, in order to find the FWHM that gave the best match with measured data. This is illustrated in section 4.1.1.

With regards to the variant model, the phase space file produced in the invariant model is used as source input in BEAMnrc. This is ISOURCE = 21 which allows a full phase space file to be used as source of radiation. In this case the incident particle option is set to *all* which simply means that every type of particle in the phase space file (electrons, photons and positrons) will be used. CM number 1 is chosen as the CM at which particles must start. NRCYCL, the number of times each incident particle must be recycled before moving on to the next particle in the phase space file, is set to 0, which means that each particle will be used one time. When choosing NRCYCL = 0, BEAMnrc automatically calculates a value for NRCYCL based on the amount of histories required in the simulation. Should the amount of histories

be less than the number of particles in the phase space file, no recycling is required. Should the amount of histories be greater than the number of particles in the phase space file, recycling must take place.

3.1.1.6 Energy Modelling

The energy specification of the initial electron beam (energy of the electron beam at Z = 0 cm) is probably one of the most important electron beam properties that can be altered to improve the match with measured data. Generally, the energy of the initial electron beam only influences the dose on the CAX of the beam and has little to no effect on off-axis profiles. In `BEAMnrc` either a monoenergetic beam can be chosen or an energy spread can be incorporated if a polyenergetic electron beam is modelled. The disadvantage of using a monoenergetic beam is the difficulty to match simulated data with measurements. In some monoenergetic beam studies[67,101,103–105] good agreement with measured data was obtained using a monoenergetic beam by adjusting the energy of the beam to match PDD range parameters (such as R_{50}) in combination with adjustments to the thickness of scattering foils to alter dose gradients and BU regions. However, components such as scattering foils have dimensional tolerances which sets a limit on the degree of freedom to which these parameters can be changed. This highlights the advantage of using a polyenergetic energy spectrum, which is the ability to fine tune the spectrum's energy-specific parameters to achieve better agreement with measured data without the need to adjust CM parameters beyond their dimensional tolerances.

The most commonly used energy spectrum for the initial beam specification is an energy spectrum $f_G(E;\overline{E_0},\sigma)$ with a Gaussian spread about a most probable energy value $\overline{E_0}$, with a FWHM (related to the standard deviation σ) defined in terms of the spread relative to the most probable energy, and lower- and upper energy cut-off values. This is,

$$f_G(E;\overline{E_0},\sigma)=\frac{1}{\sigma\sqrt{2\pi}}e^{-\frac{1}{2}\left(\frac{E-\overline{E_0}}{\sigma}\right)^2};\ \text{with}\ FWHM=2\sigma\sqrt{2\ln 2}\,,\ f_G\in[-a\sigma;+b\sigma] \qquad \text{Eq 3.6}$$

This gives the user four parameters ($\overline{E_0}$, $FWHM$, lower- and higher energy cut-offs $-a\sigma$ and $+b\sigma$) to adjust as to improve different regions of CAX PDD curves, and supplies a method by which the fine tuning (section 3.2) process can be performed with the minimum amount of iterations as possible. Both a monoenergetic and a poly-energetic (Gaussian) spectrum was tested within this study.

In an extensive study by Björk et al.[95] a monoenergetic, Gaussian and wedge-shaped energy spectrum was investigated for a Philips/Elekta SL25 linac for a 12 MeV electron beam. The Gaussian and wedge-shaped distributions were also investigated in terms of their effects when altering the most probable energy and

the width of the energy spectrum. It was found that, firstly, the lateral dose profiles are unaffected by the energy spectrum of the initial electron beam. Furthermore, the effects of the energy spectrum on the CAX depth-dose curve is negligible should the initial energy spectrum be symmetric (for instance, a Gaussian energy spectrum with the same lower- and upper limits) and if its FWHM is less than approximately 10 % of the most probable energy. They have further found that increasing this FWHM above 10 % will decrease the normalized dose gradient in the CAX PDD curve without any effects on the build-up region. Another finding included that, with the use of an asymmetric energy spectrum with a low-energy extension (wedge-shaped energy spectrum), the dose gradient in the CAX PDD curve will decrease while also increasing the dose in the build-up region. Also pointed out in this study is the limitations of the use of a monoenergetic beam. The spectra at the phantom surface are only moderately influenced by the scattering foil design since the scattering foil thickness cannot account for spectral width or shape. Since with a monoenergetic beam there are no other energy parameters to change (such as spectral width and shape), it may be impossible to achieve the correct spectral shape and width at the phantom surface. For this reason, the energy spectrum at the surface is highly dependent on the details of the accelerator tube tuning characteristics. In addition the dose in the build-up region as well as the dose gradient of the CAX PDD curve are very sensitive to the entire shape of the energy distribution. Various other studies have all used a Gaussian energy spectrum for the initial electron beam with FWHM generally smaller than 20 % and has acquired a match with measured data with a gamma criterion of 2 %/2 mm.[87,95,98,99,106–110]

A monoenergetic and Gaussian energy spectrum underestimated the dose in the BU region on the CAX (see section 4.2.2) by more than 2%/2mm, while also not providing adjustable parameters to fix this issue. In addition to this, the energy dispersion occurring in the bending magnets is better characterized as a straggling effect, and therefore an 'experimental' asymmetric negative skew energy spectrum was constructed and investigated. This experimental spectrum involves the modelling of a Landau distribution[111] according to a special case $f_L(E;\mu,c)$ in Paul Lévy's family of alpha-stable distributions[112], adapting it to the case of an energy spectrum. This is,

$$f_L(E;\mu,c) = A\frac{e^{-\frac{c}{2(E-\mu)}}}{(E-\mu)^{\frac{3}{2}}}\text{; with } f_L \in [\mu,\infty] \qquad \text{Eq 3.7}$$

where μ and c are location and scaling parameters, respectively, E is the electron energy and A is a normalization constant. Choosing the location parameter $\mu = 0$, the spectrum is valid for any positive energy and both the mode and median of the distribution is defined mathematically. The spectrum is first

constructed using energy values as input which produces a positive skew distribution. The positive skew Lévy distribution is then reflected about the Y-axis to produce a negative skew distribution and shifted towards to relevant most probable energy (mode), producing a distribution as shown in Figure 3-6. Though it is possible to quantify the Lévy energy spectrum with parameters such as the median and mode, quantifying the energy spectra produced at $Z = 26.85$ cm and $Z = 95$ cm (where phase space files are produced) is extremely difficult due to their complexity and is beyond the scope of this study.

The major factor that governs the width of the Lévy distribution is the scaling parameter c, where an increase in the scaling parameter gives rise to broader distribution where the broadening occurs towards lower energy side, increases the lower-energy part of the spectrum as well as decreases the most probable energy $\overline{E_0}$ with a small amount. This is indicated in Figure 3-6 which shows the spectrum for various values of c. The effect of the most probable energy and scaling parameter on CAX PDDs and off-axis profiles were investigated and are discussed in section 4.2.1.

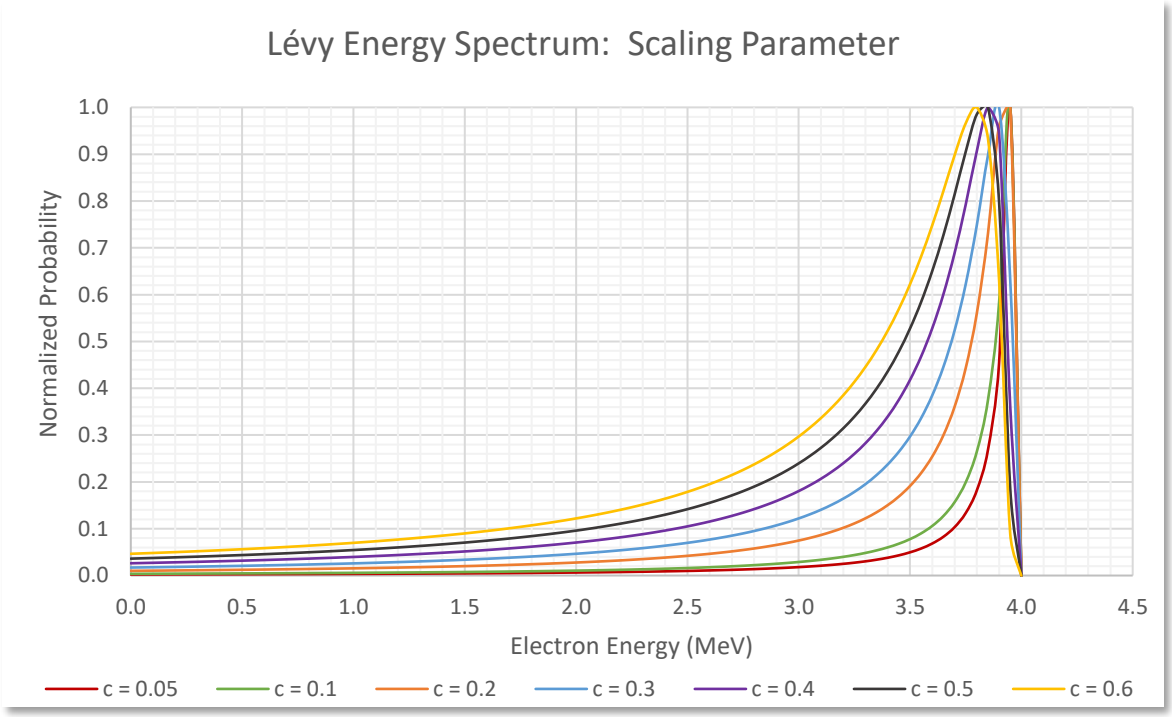

Figure 3-6: The energy spectrum in Eq 3.7 for a 4 MeV electron beam and the influence on the spectrum due to various values for the scaling parameter, c. Not that the spectrum is normalized to 1 with the use of the normalization constant, A.

If the user chooses to use an energy spectrum as input in `BEAMnrc` (as opposed to specifying a single monoenergetic energy value), a .spectrum file has to be created manually. This is done in a simple text

(.txt) file by renaming the .txt extension to .spectrum (Appendix 4). The spectrum file has a specific format as described in the BEAMnrc manual[74], which is as follows:

SPEC_TITLE
NENSRC, ENMIN, IMODE
ENSRCD(I), SRCPDF(I)

where SPEC_TITLE is an 80-character spectrum title, NENSRC is the number of energy bins in the spectrum histogram, ENMIN is the lower energy (MeV) of the first bin, IMODE defines to histogram units to either counts/bin (IMODE=0) or counts/MeV (IMODE=0), ENSRCD(I) is the upper energy (MeV) of bin I, and SRCPDF(I) is the normalized probability of finding a particle in bin I. The maximum number of bins has a default value of 200, but the user can change this value in the relevant user.mortran file.

3.1.1.7 BEAMnrc Outputs

One the CM modelling is done, and all the Monte Carlo parameters are set, the accelerator can be built and compiled. Building an accelerator involves the concatenation of all the relevant source code for the CMS and editing it to avoid duplicate variable names. This means that the accelerator should be re-built each time after modifications are made to the CMs. In addition, building an accelerator creates the necessary *makefiles* for accelerator compilation. Once built, the accelerator must be compiled which is done with the use of a MORTRAN compiler followed by a FORTRAN compiler. Different compilation options are available, with the default being a compilation of the accelerator executable with default optimization turned on.

Once the accelerator is specified, built and compiled, the simulation can be executed. This can either be done from the GUI or can be done directly from a terminal (terminal execution requires input file and pegs file specification). Phase space files produced can be analysed using `BEAMDP`[113], a utility program designed as part of the OMEGA project with the specific intent to analyse phase-space parameters.

3.1.2 DOSXYZnrc

3.1.2.1 Inputs

`DOSXYZnrc` can either be used to construct a phantom manually or to transform a CT dataset into a useable form, in which dose calculations can be performed due to radiation interactions from a defined source. In this study a simple water phantom was constructed for each field size and beam energy

combination. This was to ensure that profiles can be extracted exactly at or very close to the depth of maximum dose, as well as to minimize the number of voxels used for a particular field size.

When constructing a phantom manually in DOSXYZnrc, voxels in the X-, Y- and Z- direction must be specified which can be done either individually or as groups, where each defined group has a certain width. When specifying voxels as groups, a minimum boundary (negative value) is selected after which each group must be defined in terms of the number of voxels in the group, as well as what the width of the voxels would be in the group. This is ideal if voxel sizes are not constant throughout a plane, which may be the case if voxels are constructed with a low resolution in low dose gradient sections and a high resolution in high dose gradients. It must be noted that DOSXYZnrc scores the dose at the centre of each voxel, therefore care must be taken when defining voxels to ensure that dose values are extracted at the correct depths or off-axis positions. For instance, if the dose on the central axis of the beam is required, and a 2 mm spatial resolution is used, both the X- and Y- directions should have a voxel from -0.1 to +0.1, which means the dose in those voxels will be scored exactly at $X = Y = 0$ cm. The voxel definitions for different field sizes and beam energies, as well as the number of histories required for a maximum of 1 % statistical uncertainty in dose calculations are indicated in Table 3-24 -Table 3-26. Note that Table 3-25 illustrate the Z-voxel dimensions for phantoms positioned at 95 cm SSD, which is the nominal SSD of electron beams. This means that the applicator is positioned on top of the phantom with a zero-air gap. Due to the coordinate system of DOSXYZnrc, for 95 cm SSD setups, the Z-position of the phantom starts at $Z = -5$ cm. For 100 cm SSD setups the phantom will start at $Z = 0$ cm with a 5 cm air gap between the applicator and the phantom surface. The medium chosen for each voxel is water, H20ICRU700, which is the cross-section data as given by the ICRU37 with a lower electron energy of 0.7 MeV. The IPHANT parameter was set to 1 which outputs a phantom data to a *.egsphant* file in addition to a *.3ddose* file which is produced by a simulation. Appendix 5 gives an example of a DOSXYZnrc input file.

Table 3-24: The X- and Y- voxel ranges for all field sizes as defined at 95 cm and 100 cm SSD. The voxel width is 2 mm in both the X- and Y-direction, and voxels are constructed such that the central voxels stretches from -0.1 cm to +0.1 cm to allow dose scoring at exactly 0 cm. Voxel dimensions remain the same for each electron energy.

Field Size (cm^2)	***X*** *range (cm)*	***Y*** *range (cm)*
2 x 2	-4.1 to 4.1	-4.1 to 4.1
3 x 3	-4.1 to 4.1	-4.1 to 4.1
6 x 6	-5.1 to 5.1	-5.1 to 5.1
6 x 10	-7.1 to 7.1	-5.1 to 5.1
6 x 14	-9.1 to 9.1	-5.1 to 5.1
8 x 16	-10.1 to 10.1	-6.1 to 6.1
10 x 10	-8.1 to 8.1	-8.1 to 8.1
10 x 20	-12.1 to 12.1	-7.1 to 7.1
14 x 14	-9.1 to 9.1	-9.1 to 9.1
20 x 20	-14.1 to 14.1	-14.1 to 14.1
4 cm Ø	-6.1 to 6.1	-6.1 to 6.1

Table 3-25: The Z-voxel ranges for different electron nominal energies. The depth of the water phantom is constructed to include at least 2 cm of the Bremsstrahlung tail. Furthermore, voxels are constructed to allow profile extraction at exactly the depth of maximum dose, keeping in mind the dose scoring of DOSXYZnrc. Voxel widths are 2 mm, while the inclusion of one 1 mm voxel in the 6 MeV and 10 MeV water tank is required to offset voxels to ensure correct depth of profile extraction.

Electron Nominal Energy (MeV)	***Z*** *range (cm)*	*Voxel Width (cm)*
4	-5 to 0	0.2
6	-5 to -3.8	0.2
	-3.8 to -3.7	0.1
	-3.7 to 0.1	0.2
8	-5 to 1	0.2
10	-5 to -3	0.2
	-3 to -2.9	0.1
	-2.9 to 3.1	0.2
12	-5 to 3	0.2
15	-5 to 5	0.2

Table 3-26: The minimum number of histories required in DOSXYZnrc for each field-energy combination to ensure a maximum of 1% statistical uncertainty of calculated doses, based on the number of voxels as defined in Table 3-24 and Table 3-25.

	# Histories x 10^6					
Field Size (cm^2)	**4 MeV**	**6 MeV**	**8 MeV**	**10 MeV**	**12 MeV**	**15 MeV**
2 x 2	336.20	437.06	504.30	689.21	672.40	840.50
3 x 3	353.01	453.87	521.11	706.02	689.21	857.31
6 x 6	572.22	728.28	832.32	1118.43	1092.42	1352.52
6 x 10	832.83	1050.09	1194.93	1593.24	1557.03	1919.13
6 x 14	1113.84	1392.30	1577.94	2088.45	2042.04	2506.14
8 x 16	1540.25	1909.91	2156.35	2834.06	2772.45	3388.55
10 x 10	1705.86	2099.52	2361.96	3083.67	3018.06	3674.16
10 x 20	2319.57	2835.03	3178.67	4123.68	4037.77	4896.87
14 x 14	2318.68	2815.54	3146.78	4057.69	3974.88	4802.98
20 x 20	5765.49	6958.35	7753.59	9940.50	9741.69	11729.79
4 cm Ø	1116.30	1339.56	1488.40	1897.71	1860.50	2232.60

3.1.2.2 Source Modelling

This section involves modelling of the source of radiation used for dose calculations inside the phantom. Various source options (ISOURCE) are supplied in `DOSXYZnrc` where ISOURCE = 2 was chosen to select a phase-space source incident from any direction. This is indicated in Figure 3-7.

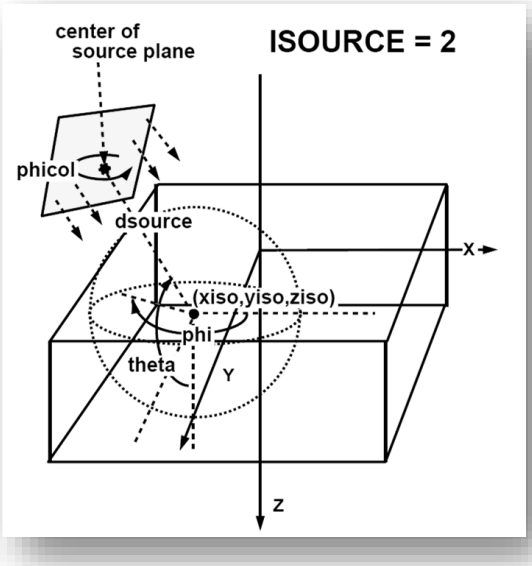

Figure 3-7: ISOURCE = 2 as given in the `DOSXYZnrc` manual.[83] The radiation isocentre is defined with the coordinates $(0,0,0)$ and the centre of the plane containing the phase space file is defined at a distance $dsource$ from the isocentre. Furthermore, the orientation of the plane containing the phase space file can be altered in terms of its angle relative to the Z-axis $(theta)$ and X-axis (phi), as well as in terms of its rotation about the plane's central axis, $phicol$.

As mentioned in the description of Figure 3-7, the coordinates of the isocentre (xiso, yiso, ziso) was set to (0,0,0). The distance of the plane containing the phase space file was set at dsource = 5 cm since the isocentre is at $Z = 100$ cm in BEAMnrc's coordinate system ($Z = 0$ cm in DOSXYZnrc's coordinate system). Both theta and phi were set equal to 180°. To maintain the same coordinate system between BEAMnrc and DOSXYZnrc phicol must also be set to 180°. This is due to a general coordinate transformation performed when moving from BEAMnrc to DOSXYZnrc. The phase space file format was set to "no ZLAST" and phase space data redistribution was enabled should the particle's in the phase space file be re-used (redistribution in this case refers to the redistribution of phase space-particles for a subsequent use once all particles have been used one time).

3.1.2.3 EGSnrc Parameters

The number of histories, NCASE, was set equal to a minimum of the values indicated in Table 3-24 - Table 3-26 which varies with field size and beam energy. The number of histories is approximated according to Eq 2.11 to obtain at least 1 % statistical accuracy.

The IWATCH parameter was set to zero, the default, which means that on completion of each batch information about the batch will be stored.

The maximum CPU hours allowed for a simulation, TIMMAX, was set to 500 hours.

The values for the initial RNG seed 1 and 2 were set to IXXIN = 1 and the value for JXXIN was selected based on a set of random numbers constructed in Microsoft Excel.

BEAM_SIZE is a parameter in DOSXYZnrc which will discard particles with coordinates that fall outside BEAM_SIZE, and is defined as the side of a square field in units of cm. Therefore BEAM_SIZE differs for different field sizes and when rectangular field sizes are used, the longest side length is used for BEAM_SIZE. BEAM_SIZE was selected to be 10 cm larger for each field size as to not exclude particles outside the actual field size.

HOWFARLESS was turned off. The HOWFARLESS algorithm significantly increases the efficiency of dose calculations in a homogeneous phantom by changing the boundaries considered by the HOWFAR and HOWNEAR subroutines. Only the outer most boundaries are considered which eliminates the need to stop at voxel boundaries.

Since for 100 cm SSD setups there is a 5 cm air gap between the applicator and the phantom surface, this was incorporated into the simulation with the use of the "Thickness of region outside phantom option". This thickness was chosen to be uniform air (AIR700ICRU) and was set to 0 cm and 5 cm thickness for 95 cm SSD and 100 cm SSD setups, respectively.

The Run option IRESTART was set to the default value (IRESTART = 0), ensuring that with the execution of the simulation a new run is initiated by `BEAMnrc` and all the output files from previous runs (with the same name) will be deleted, if present.

Range rejection was turned off, as well as electron and photon splitting. The number of times to recycle particles was calculated automatically by `DOSXYZnrc`. Additional `EGSnrc` parameters chosen for simulations in `DOSXYZnrc` are indicated in Table 3-27.

Table 3-27: The `EGSnrc` parameters as selected for each `DOSXYZnrc` simulation. Each parameter is the same as those explained in the `BEAMnrc` section ***Error! Reference source not found.****.*

Maximum Electron Step Length SMAXIR	$1\ x\ 10^{10}$ *cm*	*Bound Compton Scattering* ***IBCMP***	*On*
Maximum Fractional Energy Loss Per Electron Step ESTEPE	0.25	*Pair Angular Sampling* ***IPRDST***	Simple
Maximum First Multiple Elastic Scattering Moment Per Electron Step XImax	0.5	*Pair Cross-Sections* ***pair_nrc***	Bethe-Heitler
Boundary Crossing Algorithm bca_algorithm	EXACT	*Photoelectron Angular Sampling* ***IPHTER***	Off
Skin Depth for BCA skindepth_for_BCA	3 elastic mean free paths	*Rayleigh Scattering* ***IRAYLR***	Off
Electron-Step Algorithm transport_algorithm	PRESTA-II	*Atomic Relaxations* ***IEDGFL***	On
Spin Effects spin_effects	ON	*Photon Cross-Sections* ***photon_xsection****s*	PEGS4
Electron Impact Ionization eii_flag	On	*Photon Cross-Sections Output* ***xsec_out***	Off
Bremsstrahlung angular sampling IBRDST	Koch-Motz		
Bremsstrahlung cross sections IBR_NIST	Bethe-Heitler		

3.1.2.4 DOSXYZnrc Outputs

Files obtained from a DOSXYZnrc simulation include an EGS list file (.egslst), a 3-D dose file (.3ddose) and a EGS phantom file .egsphant (if requested). A .egsphant file contains the boundaries, densities and media for each voxel. The .3ddose file contains voxel by voxel doses as calculated during the transport process as well as the error values associated with the dose in each voxel. Since MATLAB® scripts were written to extract relevant dose values, the format of a .3ddose file had to be clear. In summary, the format of a .3ddose file is as follows:

Row 1: number of voxels in the X, Y, Z directions (e.g., n_X, n_Y, n_Z)
Row 2: voxel boundaries (cm) in X direction (n_X +1 values)
Row 3: voxel boundaries (cm) in Y direction (n_Y +1 values)
Row 4: voxel boundaries (cm) in Z direction (n_Z +1 values)
Row 5: dose values array ($[n_X \text{ x } n_Y \text{ x } n_Z]$ values)
Row 6: error values array ($[n_X \text{ x } n_Y \text{ x } n_Z]$ values)

Dose values are scored as the dose (Gy) per incident particle. As already discussed, the relative error values are calculated on a history-by-history basis rather than based on average values of batches.

3.2 Fine Tuning

The tuning procedure involved in beam modelling is an iterative process which involves adjustments to several electron beam parameters such as the electron focal spot size, initial electron energy spectrum parameters, angular divergence, scattering foil and ionization chamber window thicknesses. The goal of the tuning procedure is to achieve an acceptable degree of comparison with measured data with the adjustment of a minimal set of parameters. The amount of iterations typically depends on user experience. It is also important to keep in mind what the manufacturer's tolerances are on these parameters since this sets a lower and upper limit on the range in which allowable adjustments can be made.

For electron beams, the primary goal is to match CAX PDD curves and off-axis profiles. As discussed in section 3.1.1.5 and section 3.1.1.6, electron CAX PDD curves are mostly sensitive to the energy spectrum of the initial electron beam and mostly insensitive to the focal spot size and shape. However, the CAX PDD is mostly unaffected by changes in the scattering foils within manufacturer tolerances (see section 4.3). Off-axis profiles does however exhibit some sensitivity to the focal spot size and shape as well as to

the design of the secondary scattering foil but is mainly unaffected by the energy distribution of the initial electron beam. Keeping this in mind, some sort of a protocol can be designed to firstly match the CAX PDD curve by adjusting the energy spectrum of the initial electron beam, and secondly to match off-axis profiles (if required) by adjusting the focal spot size and shape as well as secondary scattering foil design (thickness of foils and radii of foils, remaining within manufacturer tolerances).

CAX PDD matching usually starts off with the matching of R_{50} which is directly linked to the most probable energy of the electron energy spectrum incident on the phantom surface by

$$\overline{E_0} = CR_{50} \qquad \text{Eq 3.7}$$

where C is in units of MeV·cm^{-1}.

Secondly the dose gradient must be matched which is largely dependent on the width of the energy spectrum used. The dose in the bremsstrahlung tail is in turn dependent on the maximum energy present in the spectrum. The issue however, as mentioned in section 2.2.5.13, is the matching of the build-up region and this requires some iterative adjustment to the energy spectrum to decrease the discrepancy versus measured data. The advantage of the Lévy energy spectrum is that a small adjustment in the scaling parameter produces little to no effect beyond the depth of maximum dose of the CAX PDD but does however alter (increase or decrease) the dose in the BU region. The monoenergetic or Gaussian spectra did not provide such a parameter.

3.3 Measurements

3.3.1 Water Tank Measurements

The 6 x 6 cm^2, 6 x 10 cm^2, 6 x 14 cm^2, 8 x 16 cm^2, 10 x 10 cm^2, 10 x 20 cm^2, 14 x 14 cm^2 and 20 x 20 cm^2 data used within this study were collected during the commissioning of the Agility™ head for the Elekta Synergy® in 2015 at UAH Oncotherapy. Clinical Medical Physicists (MPs) at UAH Oncotherapy commissioned the accelerator using data collecting techniques according to the recommendations of the AAPM Task Group no. 106.[114]

Electron beam dosimetry measurements were performed in a three-dimensional dosimetry scanning system (Blue Phantom, IBA dosimetry, Bartlett, TN), which includes a CU500E electrometer. For electron CAX PDDs, a plane parallel chamber (Roos® Chamber Type 34001, PTW, Freiburg, Germany) with a nominal sensitive volume of 0.35 cm^3 (7.8 mm radius and 2 mm depth), a water equivalent thickness of 1.3 mm and a guard ring width of 4 mm, was used as the field detector. OAPs were measured using a

compact volume ionization chamber (CC13, IBA Dosimetry, Bartlett, TN) with a volume of 0.13 cm^3, an air cavity diameter of 6.0 mm and an air cavity length of 5.8 mm. A CC13 chamber was also used as the reference detector. A continuous scanning method was used for both profiles and PDDs with 0.05 cm resolution. ROFs were measured at the depth of maximum dose for each respective energy-field-SSD combination, administering 100 MUs per setup.

Profiles and PDDs for the 2 x 2 cm^2, 3 x 3 cm^2 and 4 cm Circular fields were measured in the same 3-D dosimetry scanning system as mentioned above, using a pinpoint ionization chamber (CC01, IBA Dosimetry, Bartlett, TN) with a volume of 0.01 cm^3, an air cavity diameter of 2.0 mm and an air cavity length of 3.6 mm. The chamber was positioned parallel with the beam for both profiles and PDDs. A CC13 chamber was used as a reference detector. A step-by-step method was used to collect profile and PDD data, with a 0.05 cm step size and 5 samples per point being collected. ROFs were measured at the depth of maximum dose administering 100 MUs per field. Daisy chaining was used to relate the output of the CC01 chamber with the output of a Farmer® Chamber (Type 34001, PTW, Freiburg, Germany) in Perspex for a 5 x 5 cm^2 field size. An important consideration in small field dosimetry is volume averaging effects that occur typically when the sensitive volume of a chamber is large in comparison with the width of the measured field. This may result in a reduced CAX dose value, which means that penumbrae of profiles will be overestimated causing an overall wider field than the true radiation field measured. If a small chamber is not used, volume effects must be corrected for. However, since the CC01 chamber was used for small field dosimetry, volume effects were minimized and therefore no corrections were applied.

The uncertainty in water tank measurements was assumed to be 1 %, given careful setup protocols of chambers within the water tank. In the light of the 1 % statistical uncertainty of simulations, a 2%/2mm criterion is justifiable should modelling be extremely accurate. All measured data were collected using OmniPro™ Accept (version 6.5A, IBA Dosimetry GmbH, Schwarzenbruck, Germany). OmniPro was used to control the scanning dosimetry system, to convert ionization measurements to relative dose values using the TRS398 protocol and to smooth data. For CAX PDD curves, 8 mm least squares smoothing with a spline width of 0.2 was performed and for off-axis profiles 5 mm median smoothing with a spline width of 0.2 was used. Each measured data set were exported to comma-separated files (.csv or CSV) for processing in MATLAB® R2017a (Math Works, Natick, MA). This means that for each electron energy, field size, SSD and profile type (off-axis profile or CAX PDD) combination, a CSV file was exported. A summary of written MATLAB® scripts are given in Appendix 6.

3.3.2 Gafchromic® Film Measurement

The small fields in this study were initially measured with Gafchromic® XR-RV3 film[115] placed within an in-house developed Perspex phantom for CAX PDD measurements, and using water-equivalent slabs (PTW, RW3 slab phantoms) to measure off-axis profiles. Though film has proven its worth for quality control purposes[116] and can be very useful for measuring small fields, the curves extracted from the exposed XR-RV3 film (post 24 hours) contained an excess of noise which made them unusable for benchmarking purposes.

3.4 Processing and Analysis

All measured (water tank and film) and simulated data were processed using MATLAB®. Scripts were written to perform specific tasks on data, such as normalization (CAX PDDs and Profiles), symmetrizing and centralizing (Profiles) and smoothing. All measured data were stored in CSV format. Processed data were also saved in CSV format for ease of import into Microsoft Excel for plotting.

Water tank data were measured with a spatial resolution of 0.5 mm, so for the sake of gamma analysis no resampling was performed. Off-axis profiles were normalized to the CAX, symmetrized as well as centralized to the CAX. No smoothing was required since this was already done in OmniPro Accept.

Scripts were also written to extract the relevant axial dose information from the .3ddose files produced by `DOSXYZnrc`. This includes CAX PDDs and off-axis profiles at the depth of maximum dose. 3D average filtering was performed prior to extraction of dose data. CAX PDDs were normalized to the maximum dose and off-axis profiles were normalized to the CAX. Off-axis profiles were also symmetrized and centralized.

A simple 1-D Gamma analysis script was written based on the theory section 2.3. For each evaluated point, a point-by-point search is made in the reference data set to find the closest point to the evaluated point. Since the reference set has a finite resolution, the points before and after this closest point are then used as boundaries (a lower and upper boundary). Linear interpolation is then used to divide this section between the lower and upper boundary into very small segments. Now another search is made to find the “new” closest point.

Chapter 4: Results and Discussion

4.1 Focal Spot

4.1.1 Shape

The choice between an elliptical or circular focal spot shape depends on the design of the secondary scattering foils, as well as on the difference between measured inline and crossline off-axis profiles (as discussed in section 3.1.1.5). Both the low- and high-energy secondary scattering foil of the Synergy linac have circular geometries. Refer to Figure 4-1, which represent 10 x 10 cm^2 crossline and inline off-axis profiles measured at 95 cm SSD and at the depth of maximum dose. The left side of the graph represent crossline and inline profiles for a 4 MeV electron beam (measured at a depth of $d_{\max} = 0.9$ cm) whereas the right side of the graph represent crossline and inline profiles for a 15 MeV electron beam (measured at a depth of $d_{\max} = 2.9$ cm). A Gamma analysis was performed on both the 4 MeV and 15 MeV curves with a dose/DTA criterion of 2%/2mm to quantify the difference.

The difference between the crossline and inline profile of the 4 MeV electron beam was, except for the shoulder of the profile, less than 1%/1mm. A Gamma value of 0.795, which corresponds to 1.59%/1.59mm, was noted for the difference in the shoulder of the profiles. The difference in the shoulders generally decreased to a Gamma value of 0.3 (0.6%/0.6mm) with an increase in electron energy, as evident in the 15 MeV beam. The 15 MeV electron beam showed a maximum Gamma value of 0.287 (0.574%/0.574mm) in the central and penumbral regions, and a maximum Gamma value of 0.54 (1.08%/1.05mm) in the umbra. The penumbra width for the 4 MeV crossline and inline profiles in Figure 4-1 is 8.63 mm and 8.50 mm, respectively, which corresponds to a 1.51 % difference, whereas for the 15 MeV beam the respective penumbras are 11.59 mm and 11.51 mm, corresponding to a 0.74 % difference. There is no trend for this difference with electron nominal energy.

Since the difference between measured crossline and inline profiles is generally less than 1% with penumbral differences less than 0.4 mm and taking into consideration the circular geometry of the secondary scattering foils, the focal spot shape was chosen as circular; that is, $FWHM_X = FWHM_Y$.

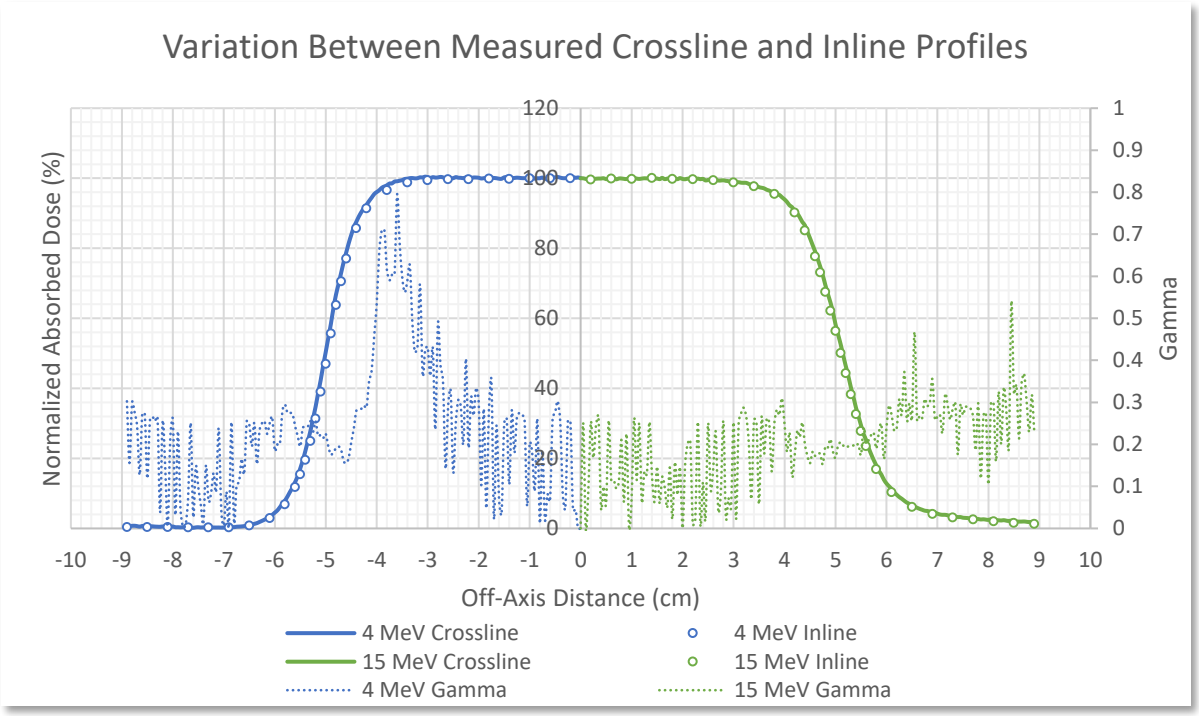

Figure 4-1: The variation between crossline and inline off-axis profiles for a 10 x 10 cm² field measured at an SSD of 95 cm. The left side of the graph (blue line, orange dots and grey dashed line) represents a 4 MeV electron beam whereas the right side of the graph (green line, yellow dots and grey dashed line) represents a 15 MeV electron beam. The dashed curves represent a Gamma analysis between the crossline and inline profiles using a 2%/2mm criterion.

4.1.2 Size

12 Different focal spots sizes ranging from 0.5 mm to 10 mm FWHM was simulated for a 4 MeV, 10 x 10 cm² electron beam using a Lévy energy spectrum with a most probable energy of $\overline{E_0} = 5.685$ MeV and a scaling parameter of $c = 0.05$ at $Z = 0$ cm. The resulting PDDs and off-axis profiles (at $d_{\max} = 0.9$ cm) were extracted as well as the energy spectrums at an SSD of 95 cm SSD. Below a FWHM of 0.5 mm the intensity distribution of the beam converges to that of a uniform intensity distribution, therefore this value was selected as a minimum.

The influence of the focal spot FWHM size on the CAX PDD is mainly evident in the BU region, with little to no effect beyond the depth of maximum dose, as shown in Figure 4-2. There is however no specific trend between the focal spot size and the variations observed in the BU. With a change in the FWHM from 0.5 mm to 10 mm, the % change in the dose at 1 mm depth in water varied by 6.979 %, ranging from 76.791 % to 83.77 % relative to the maximum dose. Focal spot sizes of 0.5 mm, 1.5 mm, 3 mm, 4 mm, 5 mm and 10 mm underestimated the BU region and produced a % dose at 1 mm depth within 2 % relative to each other (ranging from 78.349 % to 80.683 %), with very little variations beyond the depth of

maximum dose. In contrast, focal spot sizes of 1 mm, 2 mm, 6 mm and 7 mm overestimated the BU region and produced a % dose at 1 mm depth within 2 % relative to each other (ranging from 81.622 % to 83.765 %), along with an observable underestimation of the dose in the shoulder of the BD region. Focal spot sizes of 8 mm and 9 mm largely underestimated the BU region and produced the lowest % dose values at a depth of 1 mm of 76.791 % and 77.110 %, respectively, with no effect on the dose beyond the maximum dose.

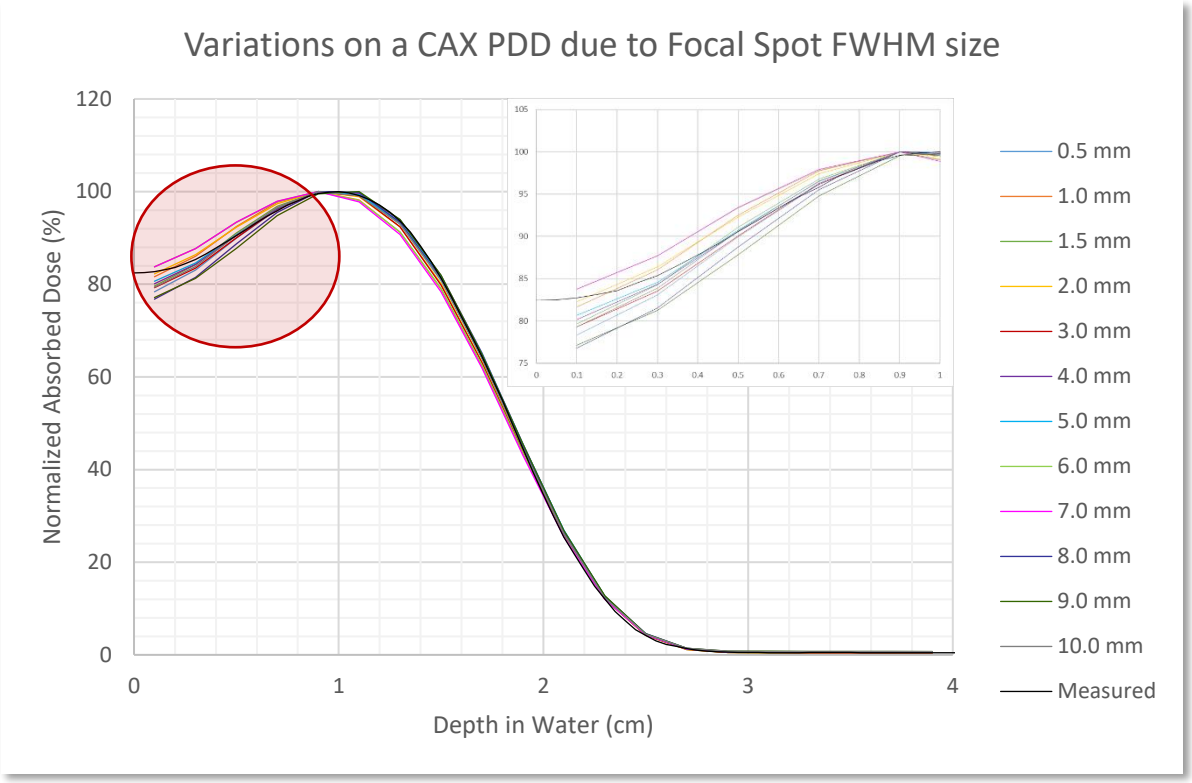

Figure 4-2: The effect of different focal spot sizes on a CAX PDD for a 4 MeV, 10 x 10 cm^2 electron beam in water with an SSD of 95 cm SSD. An inlay magnifies the BU region to better illustrate the dose discrepancies in the BU region.

Since the shape of the CAX PDD depends on the energy spectrum present at the surface, the effect of different focal spot FWHM sizes on the energy spectrum was also investigated. In Figure 4-3 (a), the energy spectrum at $Z = 0$ cm and at $Z = 26.85$ cm (for a 0.15 mm FWHM) is given, as well as the energy spectra at $Z = 95$ cm for FWHM from 0.5 mm to 10 mm. Figure 4-3 (b) is a plot of the difference between the different spectra at $Z = 95$ cm, with the 1.5 mm FWHM spectrum being the reference spectrum. These differences are in units of planar fluence per electron energy per incident particle as obtained by BEAMDP. Energy and angular spectra were extracted in BEAMDP using 200 bins (the default value), where

the respective bin width (albeit energy or angular bins) depends on the lower- and higher bin values. Firstly, the largest differences occurred at the area of the most probable energy where large gradients exist. The differences are generally negligible for a FWHM up to 3.00 mm. However, with an increase in FWHM beyond 3.00 mm the lower energy tail of the spectrum increases (hence a large difference), with noticeable changes around the most probable energy area as well (an increase in the magnitude of the alternating positive and negative differences). This definitive change in the energy spectrum due to a change in the focal spot FWHM correlates with the dose discrepancies observed in the CAX PDD in Figure 4-2.

As mentioned in section 3.1.1.5, the focal spot FWHM mostly affects off-axis profiles. Figure 4-4 illustrates crossline (solid lines) and inline (dashed lines) curves for a 4 MeV electron beam with different focal spot FWHM. By visually inspecting the different profiles it is clear that there are a couple of profiles that are over- and under-flat, meaning the dose in the shoulder regions are higher and lower, respectively, than the dose on the central axis. The flatness of the profiles was calculated according to the maximum and minimum doses in the central 80 % of the geometrical field edge (defined at the 50 % dose level). Focal spot FWHM sizes of 0.5 mm, 1.5 mm, 2 mm, 4 mm, 6 mm and 10 mm all produced profiles with a flatness of less than the acceptable 3 %, while the rest exceeded this limit. The 0.5 mm, 3.0 mm and 7.0 mm FWHM underestimated the dose in both the shoulders and the central region, whereas the 9.0 mm FWHM overestimated the dose in both these regions. While the 8.0 mm FWHM underestimated the dose in the shoulders, the 5.0 mm FWHM overestimated the dose in the shoulders. It is clear that there is no overall trend for over- or underestimation of the dose in the shoulders and central regions of profiles with the focal spot FWHM.

However, visual inspection of the comparison of simulated profiles with an acceptable flatness to measured profiles was still required to identify regions of dose over- and underestimation. The 2 mm and 6 mm focal spot FWHM underestimates the dose in the central region, whereas the 4 mm and 10 mm focal spot FWHM overestimates the dose on the shoulders of the profiles. Both the 0.5 mm and the 1.5 mm focal spot FWHM agreed well with the measured profiles, however the best fit was achieved by the 1.5 mm FWHM with a flatness of 2.66 % and 2.51 % for the crossline and inline curves, respectively.

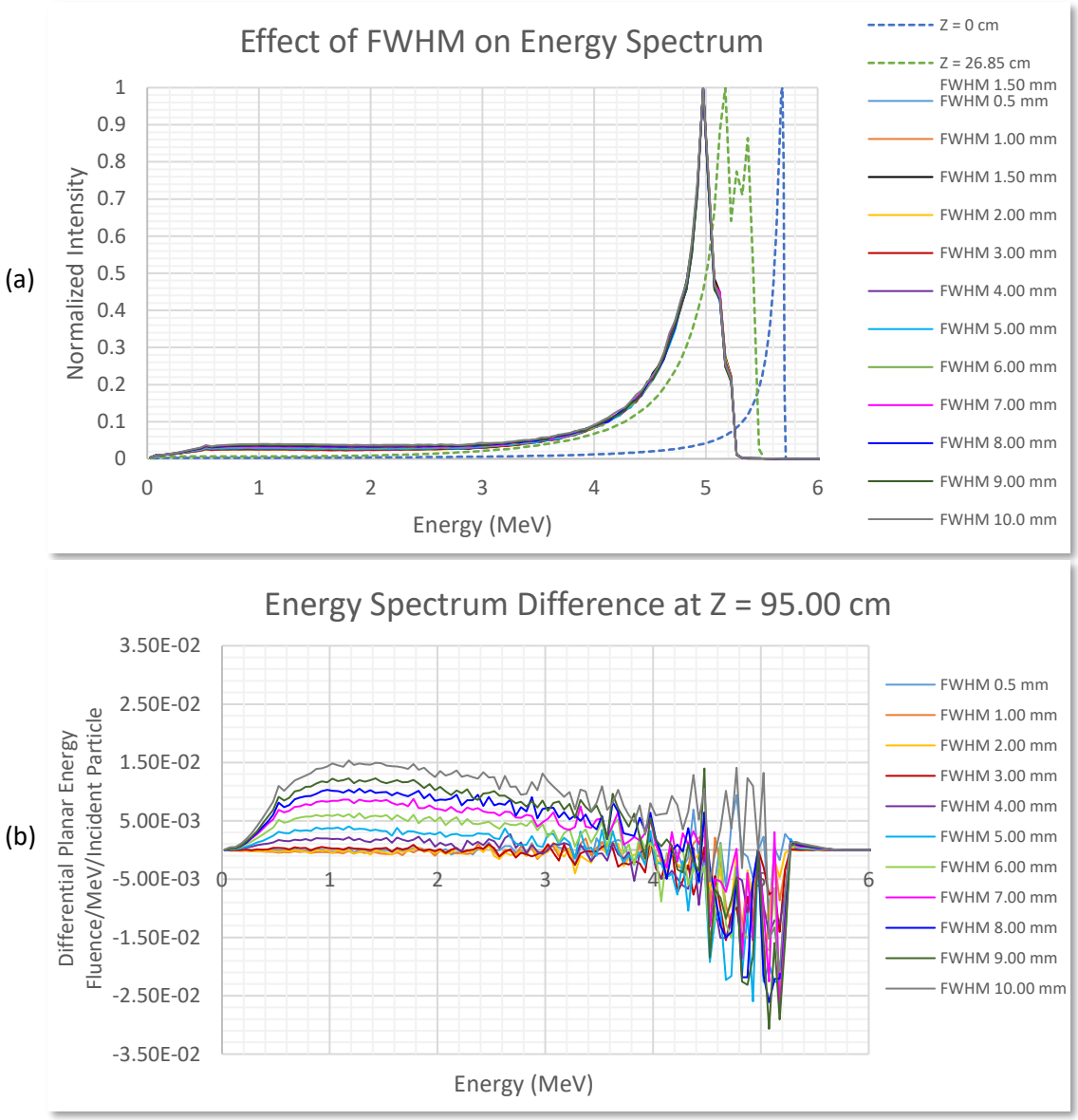

Figure 4-3: The effect of different focal spot FWHM on the energy spectrum at an SSD of 95 cm SSD for a 4 MeV electron beam, characterized by a Lévy energy spectrum at Z = 0 cm with a most probable energy of 5.685 MeV and a scaling parameter of 0.05. The spectrum at Z = 0 cm (dashed blue line), Z = 26.85 cm (green dashed line) and at 95 cm SSD (FWHM 0.5 mm to 10 mm) is shown in a). The difference in the energy spectrum at 95 cm SSD brought about by different focal spot FWHM using the 1.5 mm FWHM as reference is indicated in b). Spectra in both a) and b) were obtained using BEAMDP.

The crossline penumbras varied by 1 mm between the range of FWHM, whereas for the inline penumbras this value dropped to 0.71 mm. No clear trend (linear fits produced regression constants of 0.2632 and 0.5526 for crossline and inline penumbras, respectively) between the variation in penumbra size for both crossline and inline profiles were observed with a change in the focal spot FWHM. It should be noted that

2 mm voxels were used in dose calculations, and therefore it would be difficult to identify a trend that exist with a penumbra variation of 1 mm.

The dose discrepancies observed on the CAX PDD caused by the focal spot FWHM size, as shown in Figure 4-2, as well as the dose discrepancies in the central and shoulder regions of profiles in Figure 4-4 contradicts the findings by Rodrigues et al.[98] and Schreiber et al.[99]. The % change in the dose at 1 mm depth in water on the CAX PDD curve in Figure 4-2 varied by 6.979 % with some discrepancies in the start of the BD region. Furthermore, the flatness of simulated profiles varied from a minimum of 1.60 % to 4.78 %, which indicates the sensitivity of the central region to a FWHM change. In agreement to the findings by Schreiber et al.[99], the changes brought about by different FWHM did not follow a specific trend with different FWHM as well as with an increasing electron energy.

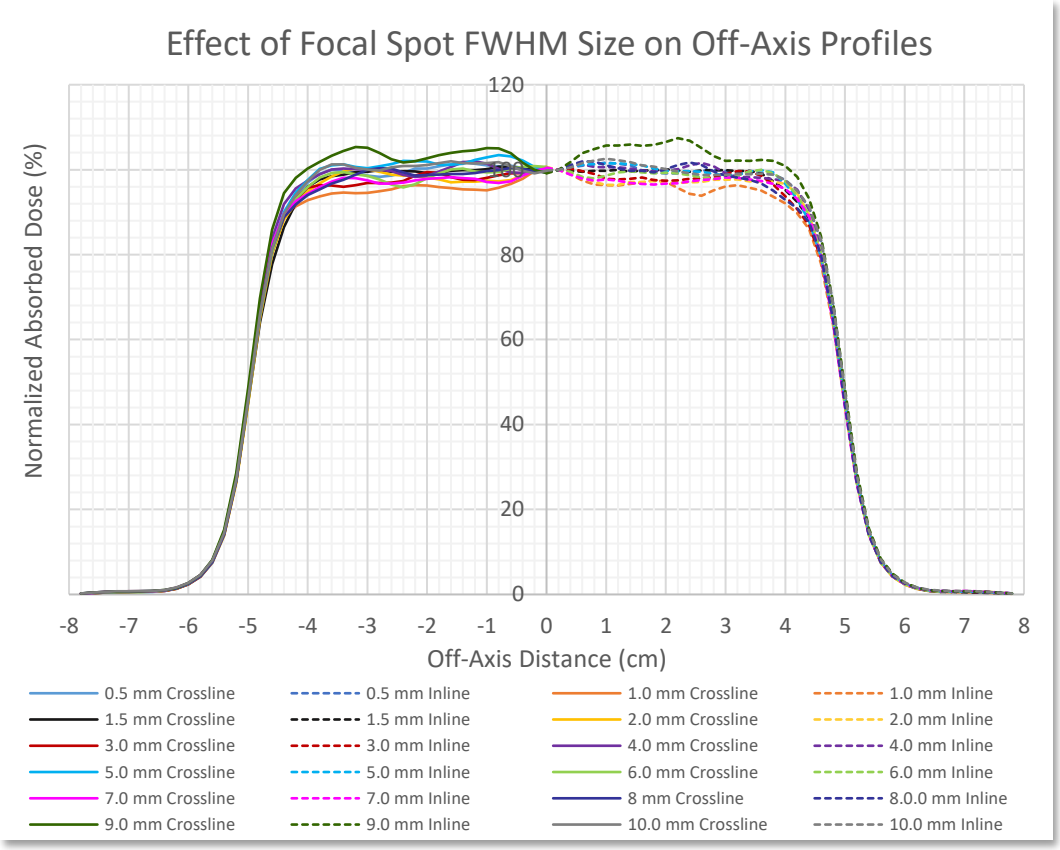

Figure 4-4: Crossline (left side of graph, solid lines) and Inline (right side of graph, dashed lines) off-axis profiles for different focal spot FWHM. Profiles were extracted at the depth of maximum dose (0.9 cm) of a 4 MeV, 10 x 10 cm^2 electron beam with an SSD of 95 cm.

4.2 Energy Spectrum

4.2.1 Lévy

4.2.1.1 Scaling Parameter

Six 6 MeV initial Lévy energy spectra with a most probable electron energy of 7.605 MeV was constructed with different scaling parameters of $c_1 = 0.05, c_2 = 0.07, c_3 = 0.1, c_4 = 0.2, c_5 = 0.3$ and $c_6 = 0.4$ as indicated in Figure 4-5. The change in the energy and angular spectra at $Z = 26.85$ cm and $Z = 95$ cm was investigated as well as the change in CAX PDDs and off-axis profiles at the depth of maximum dose ($d_{\max} = 1.4$ cm). All modelling and simulation parameters were kept constant for the six scenarios, and simulation statistics was below 1%. As evident from Figure 4-5, the width of energy spectra increases with an increase in scaling parameter, whereas an increase in the lower energy tail is also observed with an increase in scaling parameter.

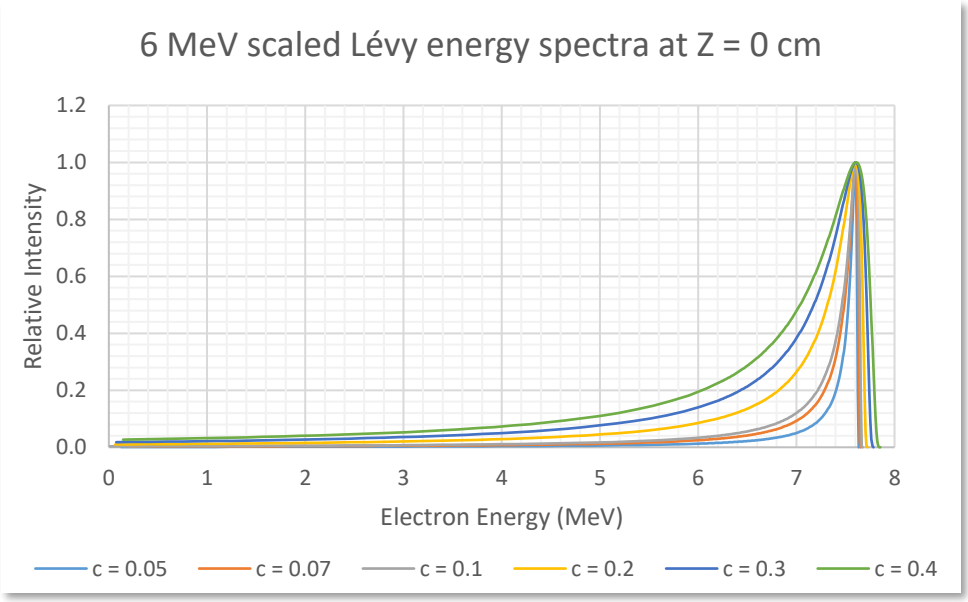

Figure 4-5: 6 MeV Lévy energy spectra as defined at Z = 0 cm with different scaling parameters ranging from 0.05 to 0.4. All spectra have the same most probable electron energy of 7.605 MeV.

The energy spectra obtained at $Z = 26.85$ cm and the associated differences of spectra with scaling parameters of c_2 - c_6 to the spectrum with scaling parameter c_1 are illustrated in Figure 4-6 (a-b). The first observation from these spectra is the obvious trend of an increase in the width and lower energy tail with an increase in scaling parameter. The most probable energy was 6.975 MeV for scaling parameters of c_1 - c_4, and increased by 0.05 MeV for scaling parameters of c_5 - c_6. The second observation is the gradual disappearance of secondary peaks with an increase in scaling parameter, where the secondary

peaks are unobservable beyond a scaling of 0.1. This is evident in Figure 4-6 (b) where the difference in the secondary peak area is the highest for scaling parameters beyond 0.1. At $Z = 95$ cm, a secondary peak is not evident in any of the scaling parameter energy spectra and overall the spectra were shifted to lower most probable energies as indicated in Figure 4-6 (c-d). The most probable energies for scaling parameters c_1, c_2, c_4 and c_5 are 6.775 MeV (a 10.91 % decrease in the initial most probable energy), whereas for c_4 and c_6 the most probable energies are 6.825 MeV (10.26 % decrease) and 6.725 MeV (11.57 % decrease), respectively. The same trend as at $Z = 26.85$ cm was observed; that is, with an increase in scaling parameter an increase in spectra width was observed. Similarly, the lower energy tails increased with an increase in the scaling parameter, and overall increased from those observed at $Z = 26.85$ cm. However, spectra width decreased overall compared to those at $Z = 26.85$ cm, where the decrease observed in spectra widths at $Z = 95$ cm compared to those at $Z = 26.85$ cm decreased with an increase in scaling parameter. The difference curve in Figure 4-6 (d) shows the largest difference in the region distal to the most probable energy, where an extremely sharp fall-off in probability with an increase in electron energy produced these large differences.

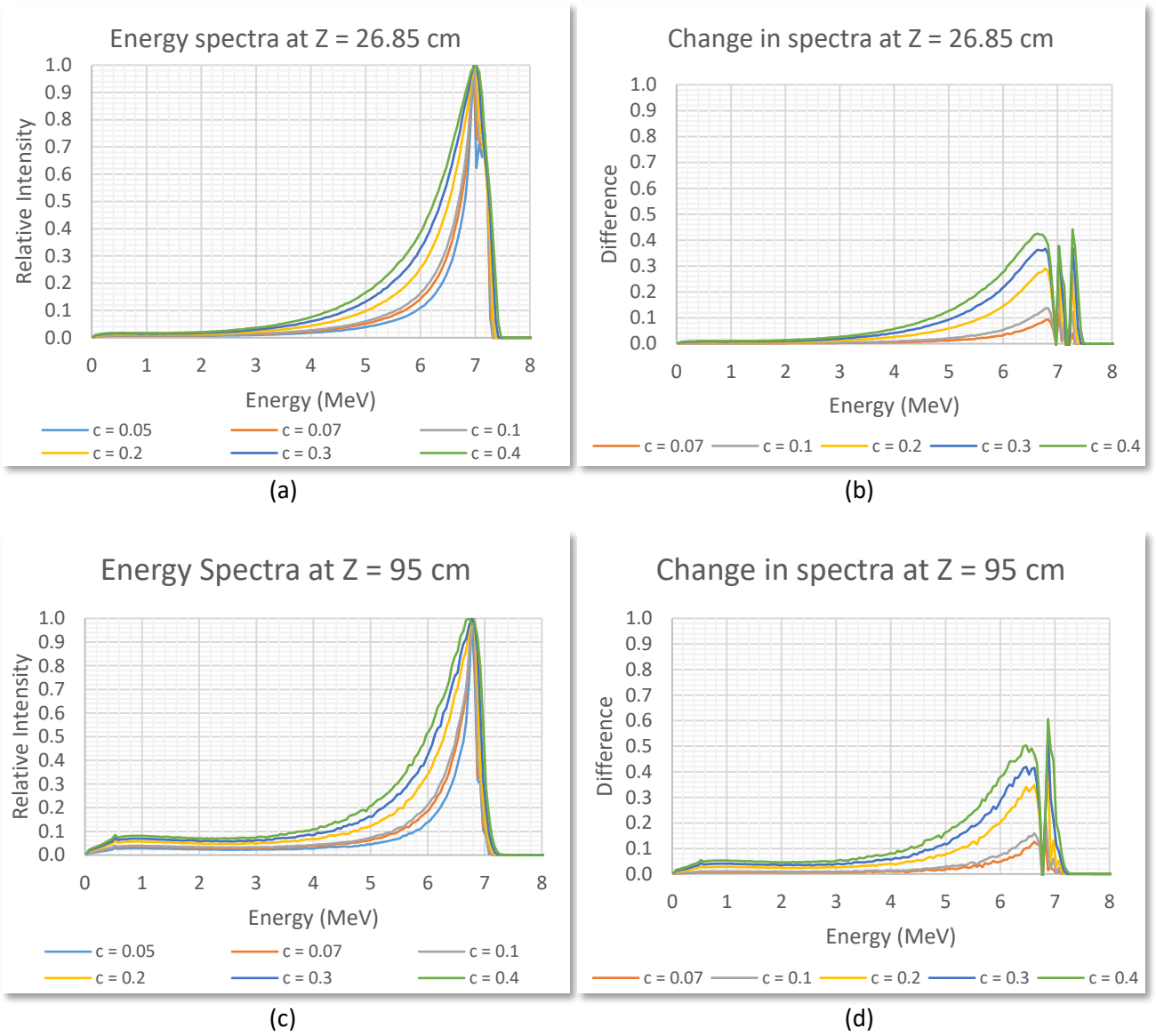

Figure 4-6: a) The energy spectra at Z = 26.85 cm for scaling parameters from 0.05 to 0.4 and b) the difference of spectra relative to the spectrum of c = 0.05. Likewise, in c) the energy spectra at Z = 95 cm are shown and the difference of spectra relative to the spectrum of c = 0.05 are shown in d).

Figure 4-7 (a-b) shows the angular spectra for the 6 MeV Lévy energy spectra at $Z = 26.85$ cm and at $Z = 95$ cm for scaling parameters $c_1 = 0.05$ and $c_6 = 0.4$. Both the angular spectra in (a) have a maximum peak at 11.925 degrees and a relative probability of 0.025 at 0.225 degrees (lowest energy bine). Overall the difference between the two spectra are less than 1 %, except for the region between 14.3 degrees and 27.1 degrees where the difference increases to a maximum of 3 %, with the 0.4 scaling parameter having the higher probability at these angles. It can be deduced that with an increase in the scaling

parameter, the difference in the mid angular range will increase while the difference in the low- and high-angular range will remain within 1.00 %. At $Z = 95$ cm the angular spectra narrowed and the maximum peak shifted to a lower angle of 2.925 degrees for both the 0.05 and 0.4 scaling parameter, whereas the relative probability at 0.225 degrees increased to 0.10. The difference between the two spectra in (b) is less than 1.30 %.

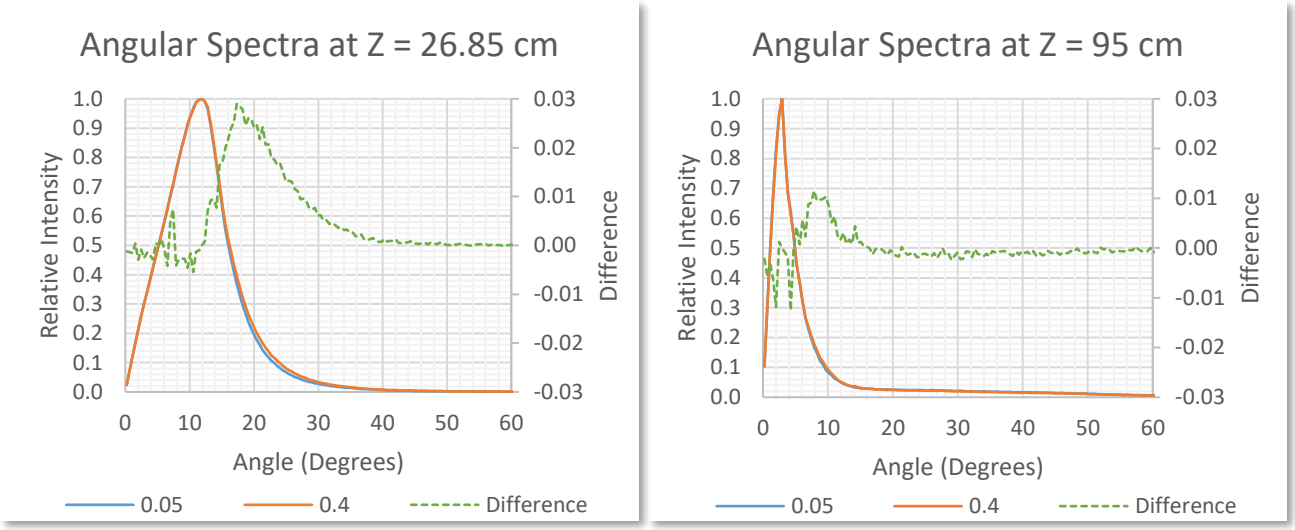

Figure 4-7: Angular spectra for a scaling parameter of 0.05 (solid blue line) and 0.4 (solid orange line) as well as the difference between spectra at a) Z = 26.85 cm and b) Z = 95 cm.

Figure 4-8 illustrates the effect of different scaling parameters (c_1 - c_6) on a CAX PDD and on crossline and inline off-axis profiles simulated in water. The overall effect on the CAX PDD curve is best described with the investigation of dose and range parameters such as the dose at a depth of 1 mm $D_{1\text{mm}}$, R_{100}, R_{80}, R_{50} and D_g, the dose gradient between the 80 % and 20 % dose level. By visual inspection it is evident that there are noticeable changes on the CAX PDD curve with an increase in scaling parameter. Discrepancies in the BU region are observed along with differences in range parameters. However, the practical range and Bremsstrahlung tail seems unchanged which was expected since the maximum peak and maximum energies in the energy spectra at $Z = 95$ cm (Figure 4-6c) are nearly the same. The effect of the scaling parameter on $D_{1\text{mm}}$, R_{100}, R_{80}, R_{50} and D_g are plotted in separate graphs in Figure 4-9 (a-d).

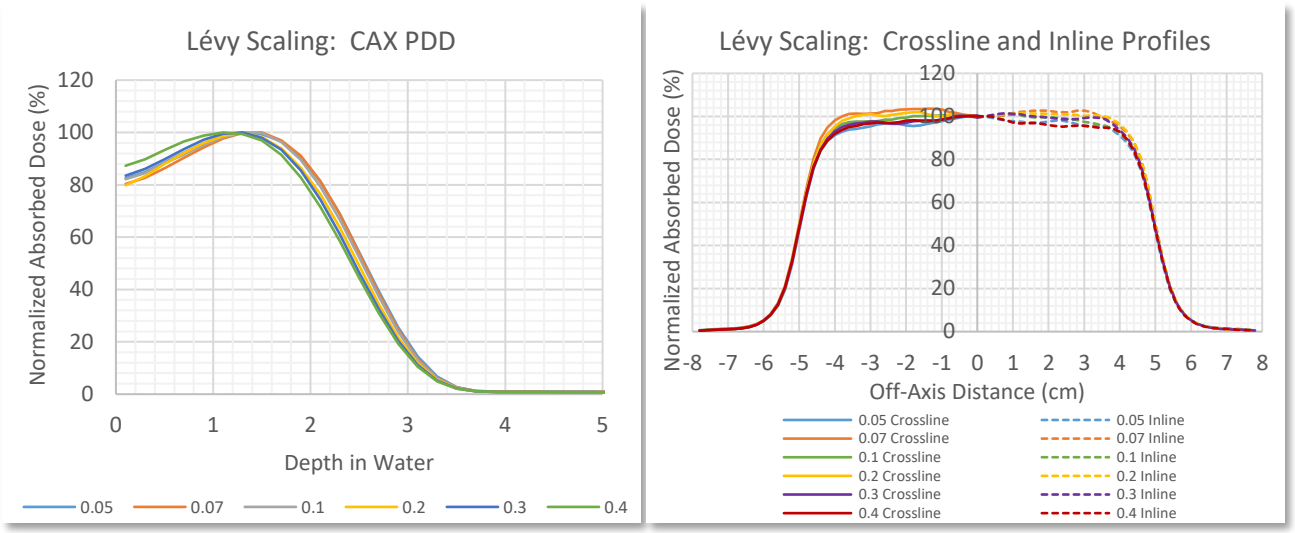

Figure 4-8: The effect of different scaling parameters ($c_1 - c_6$) on the a) CAX PDD and on b) crossline (solid lines) and inline (dashed lines) off-axis profiles at the depth of maximum dose (1.4 cm) as simulated in water.

The variation in $D_{1\text{mm}}$ for the range of scaling parameters tested was a maximum of 7.428 %. A quadratic fit with a regression constant of 0.8793 was made to the data points (Figure 4-9a). However, the variation in $D_{1\text{mm}}$ for different scaling parameters between a scaling parameter of 0.05 and 0.1 does not yield a specific trend. In a preliminary investigation into the Lévy energy spectrum, scaling parameters of 0.06, 0.07, 0.08 and 0.09 for a most probable energy of 7.59 MeV at $Z = 0$ cm yielded $D_{1\text{mm}}$ values of 92.03 %, 82.81 %, 84.87 % and 81.12 %, respectively. The argument can therefore be made that it may not be possible to fit a trendline to the variation in $D_{1\text{mm}}$ for different scaling parameters, especially not for scaling parameters less than 0.1.

The variation in R_{100} was small with scaling parameters of 0.05, 0.1, 0.2 and 0.3 producing values of 1.3 cm, whereas scaling parameters of 0.07 and 0.4 produced values of 1.5 cm and 1.1 cm, respectively. Given the 2 mm voxel resolution used in dose calculation as well as the minor difference in angular spectra and maximum peak energy of the energy spectra at $Z = 95$ cm, the deviation in R_{100} is insignificant.

Both R_{80} and R_{50} showed a linear decrease with an increase in scaling parameter as depicted in Figure 4-9b and Figure 4-9c, respectively. Linear fits were made to data points, producing a gradient of -0.4952 cm·c^{-1} with a regression constant of 0.9791 for the R_{80} plot, whereas for the R_{50} plot the gradient was -0.3966 cm·c^{-1} with a regression constant of 0.9913. This indicates a more rapid change in R_{80} with an increase in scaling parameter than R_{50}. Measured R_{80} and R_{50} parameters were 2.12 cm and 2.56 cm, respectively. Using these measured parameters as input into the trendline equations obtained for the

R_{80} and R_{50} plots, scaling parameter values of 0.045 and 0.039 were obtained. This suggests that using a scaling parameter within these bounds would produce R_{80} and R_{50} to within 0.03 mm.

The dose gradient D_g became gentler (counter intuitively this means an increase in the negative gradient) with an increase in the scaling parameter. Similar to the case of $D_{1\text{mm}}$, the variation in D_g is unclear for scaling parameters less than 0.1. However, a linear fit was made to points which yielded a gradient of 13.779 % dose·cm^{-1}·c^{-1} and a regression constant of 0.8843. The decrease in R_{80} with an increase in scaling parameter is more than the decrease in R_{20} (see Figure 4-8a) which describes the trend in D_g as observed.

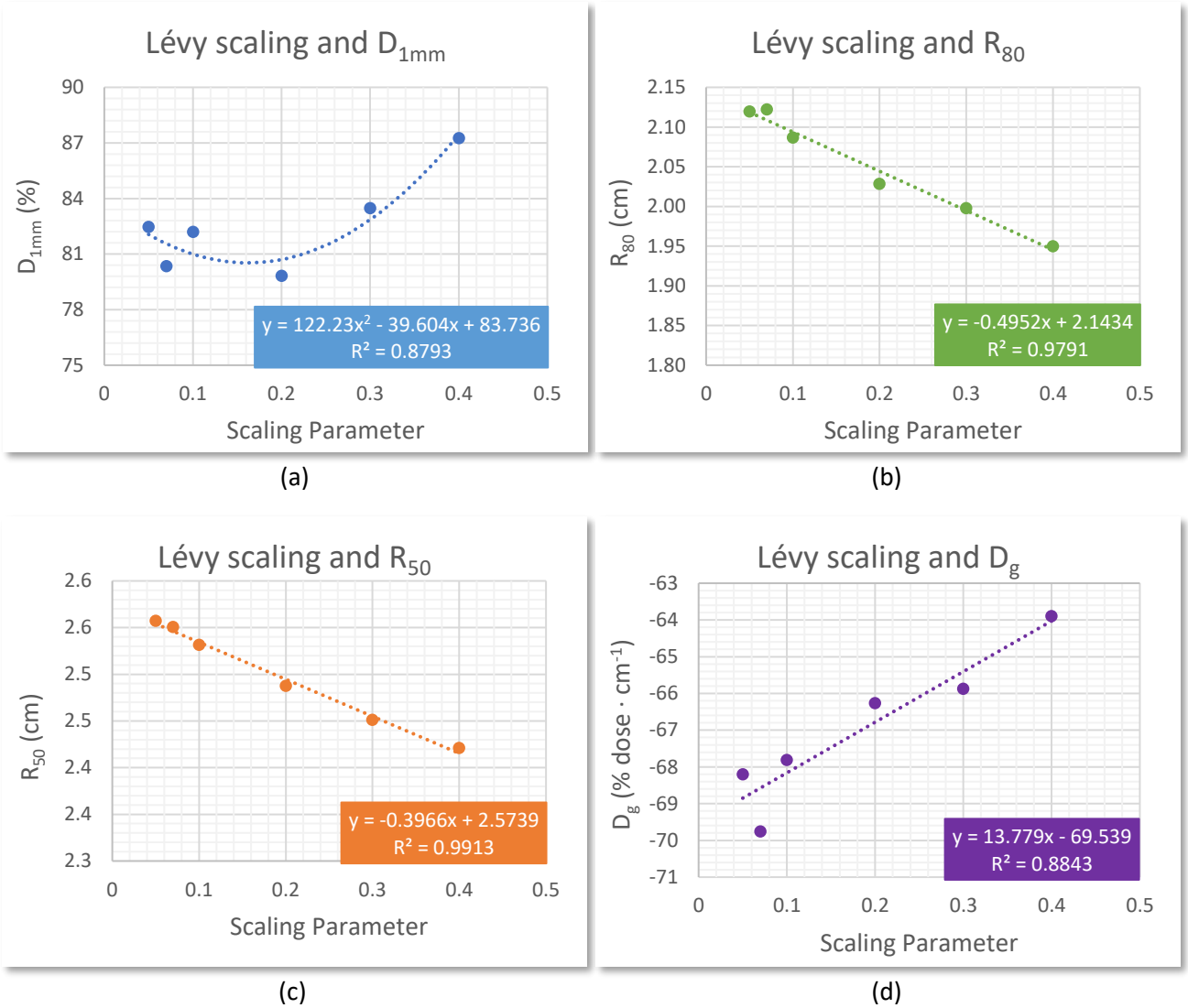

Figure 4-9: Plots of the observed PDD parameters a) D_{1mm}, b) R_{80}, c) R_{50} and d) D_g versus different scaling parameters. Trendlines have been fitted to data with trendline equations and regression constants indicated on each graph.

The effect of the scaling parameter on crossline and inline of-axis profiles are indicated in Figure 4-8b. Crossline profile flatness was 4.67 %, 2.85 %, 3.38 %, 3.41 %, 4.15 % and 4.37 % for scaling parameters of c_1 - c_6, respectively. Inline profile flatness was 4.79 %, 3.73 %, 4.39 %, 2.84 %, 4.40 % and 4.16 % for scaling parameters of c_1 - c_6, respectively. The maximum change in flatness for crossline and inline profiles with an increase in scaling parameter was 1.82 % and 1.96 %, respectively. The trend for the change in crossline and inline flatness with an increase in scaling parameter was unclear. Crossline profile penumbras varied by a maximum of 0.72 mm, with scaling parameters c_1 - c_6 producing penumbras of 8.92 mm, 8.29 mm, 8.60 mm, 8.66 mm, 9.01 mm and 8.91 mm, respectively. Inline profiles penumbras were 9.27 mm, 8.45 mm, 9.11 mm, 8.33 mm, 9.10 mm and 9.20 mm for scaling parameters of c_1 - c_6, respectively. A maximum variation of 0.94 mm was observed in inline penumbras. As with profile flatness, no trend for a change in crossline or inline penumbras was observed with a change in scaling parameter.

4.2.1.2 Most probable Energy

The previous section dealt with the influence of the Lévy scaling parameter on energy- and angular spectra as well as on the CAX PDD and off-axis profiles. The influence of changing the most probable electron energy of the initial energy spectrum (at $Z = 0$ cm) while keeping the scaling parameter constant was also investigated. Two 6 MeV spectra were constructed: spectrum 1 with a scaling of 0.05 and a most probable energy of 7.605 MeV and spectrum 2 with a scaling of 0.05 and a most probable energy of 7.785 MeV. Spectrum 1 and 2 therefore had almost identical widths relative to the most probable energy and the difference between lower energy tails were insignificant.

At $Z = 26.85$ cm the most probable energies of spectrum 1 and 2 decreased to 6.975 MeV (8.28 % decrease relative to the most probable energy at $Z = 0$ cm) and 7.225 MeV (7.19 % decrease), respectively. The width and lower energy tail of spectrum 1 was slightly higher than for spectrum 2. At $Z = 95$ cm the energy spectra narrowed compared to the spectra at $Z = 26.85$ cm, however the difference in width between spectrum 1 and 2 increased, where the width of spectrum 1 was the largest. The most probable energies decreased further to 6.775 MeV (10.91 % decrease relative to the most probable energy at $Z = 0$ cm) and 7.075 MeV (9.12 % decrease) for spectrum 1 and 2, respectively. The lower energy tail of both spectra at $Z = 95$ cm increased from $Z = 26.85$ cm. Since both spectra had almost identical widths and lower energy tails at $Z = 0$ cm, spectrum 1 widened more than spectrum 2 at $Z = 95$ cm, and the lower energy tail proved to be higher for spectrum 1 than for spectrum. In addition, the decrease in the most probable energy relative to the most probable energy of the initial spectra was 1.79 % more for spectrum 1 than for spectrum 2. To put this into perspective, consider the following: for

the same scaling parameter, increasing the most probable energy of the Lévy energy spectrum produces a narrower spectrum at $Z = 95$ cm with a lower decrease in the most probable energy, while the energy tail decreases as observed by the half-energy probability.

The angular spectra of spectrum 1 and 2 differed by less than 1 % at both $Z = 26.85$ cm and $Z = 95$ cm. At $Z = 26.85$ cm the maximum probability for both spectra occurred at 11.925 degrees and a relative probability of 0.025 was observed at 0.225 degrees for both spectra. The maximum probability decreased to 2.925 degrees at $Z = 95$ cm whereas the relative probability at 0.225 degrees increased to 0.10 for both spectra.

$D_{1\text{mm}}$, R_{100}, R_{80}, R_{50} and D_g for the two spectra was 82.477 % and 82.785 %, 1.3 cm and 1.5 cm, 2.12 cm and 2.19 cm, 2.56 cm and 2.66 cm, -68.20 % dose·MeV^{-1} and -65.12 % dose·MeV^{-1}, respectively. It comes as no surprise that with an increase in energy from spectrum 1 to spectrum 2, an increase in all the parameters was observed. This relates to the discussion about CAX PDD curves in section 2.1.2. Crossline and inline profile (at the depth of maximum dose, $d_{\max} = 1.4$ cm) flatness was 4.67 % and 4.79 % for spectrum 1, respectively and 4.09 % and 3.23 % for spectrum 2. Penumbras also decreased from spectrum 1 to spectrum 2, where spectrum 1 produced crossline and inline penumbras of 8.92 mm and 9.27 mm, and spectrum 2 produced penumbras of 8.52 mm and 8.62 mm, respectively.

4.2.1.3 Chosen Parameters

The choice of the most probable electron energy and scaling parameter of the initial energy spectrum is somewhat of a trial-and-error situation. To develop a precise quantified method was beyond the scope of this study. However, from sections 4.2.1.1 and 4.2.1.2 the effect of the scaling parameter and most probable electron energy of the initial energy spectrum on CAX PDD and off-axis profile parameters have been discussed. The results obtained in those sections served as a guideline to approximate the chosen parameters for each electron nominal energy.

A good start is to match R_{50} which is linked to the most probable energy $\overline{E_0}$ of the energy spectrum at $Z = 95$ cm by a factor of between 2.55 MeV·cm^{-1} and 2.70 MeV·cm^{-1} depending on the electron nominal energy (typically the factor decreases for an increase in electron nominal energy). Using this as a starting point, the most probable energies for each electron nominal energy at $Z = 95$ cm can be estimated. To relate this energy to the most probable energy at $Z = 0$ cm, the % decrease in $\overline{E_0}$ as discussed in section 4.2.1.2 can be used, taking note that the % decrease in the most probable energy decreases with an increase in energy. Choosing an arbitrary scaling parameter of 0.05 has shown to be a good estimate of

the initial energy spectra width, however this value can be altered to match R_{80} and D_g as discussed in section 4.2.1.1.

For nominal energies of 4 MeV, 6 MeV, 8 MeV, 10 MeV, 12 MeV and 15 MeV, the above-mentioned factor linking $\overline{E_0}$ to R_{50} was found to be 2.70 MeV·cm^{-1}, 2.64 MeV·cm^{-1}, 2.61 MeV·cm^{-1}, 2.54 MeV·cm^{-1}, 2.51 MeV·cm^{-1} and 2.55 MeV·cm^{-1}, respectively. This corresponded to most probable energies at $Z = 95$ cm of 4.975 MeV, 6.775 MeV, 8.625 MeV, 10.470 MeV, 11.935 MeV and 15.257 MeV, respectively, as shown in Table 4-1. The % decrease in the most probable energy of energy spectra from $Z = 0$ cm to $Z = 95$ cm was found to be 13.25 %, 10.91 %, 9.35 %, 8.20 %, 8.09 % and 5.21 % for electron nominal energies of 4-15 MeV, respectively, as indicated in Table 4-1. A scaling parameter of 0.05 was found to be suitable for all nominal energies, except for 6 MeV where a scaling of 0.07 was required.

The same trends regarding the most probable energy, spectra width and half-energy probabilities are observed as in sections 4.2.1.1 and 4.2.1.2. At $Z = 95$ cm each nominal energy spectrum had lower energy tails of similar magnitude, whereas spectra width was the highest for lower nominal energies. Using the most probable energies and scaling parameters at $Z = 0$ cm for each nominal energy, $D_{1\mathrm{mm}}$ was calculated with a difference of less than 1.46 %. Similarly, R_{100} was calculated within 1.5 mm, R_{80} was calculated within 0.3 mm, R_{50} was calculated within 0.1 mm and D_g was calculated with a difference of less than 2.56 %·cm^{-1}.

Once the CAX PDD is matched after the adjustment of initial energy spectrum parameters such as the most probable electron energy and scaling, off-axis profile parameters such as flatness and penumbra width can be improved should it be required by adjustment of the primary scattering foil thickness and the focal spot FWHM. The effects of both these parameters on off-axis profiles have been discussed in sections 4.1 and 4.3.

Table 4-1: Most probable energies and decrease in said energies of energy spectra at Z = 0 cm, Z = 26.85 cm and Z = 95 cm for electron nominal energies of 4-15 MeV.

Electron Nominal Energy (MeV)	*c*	$Z = 0$ *cm*	$Z = 26.85$ *cm*		$Z = 95$ *cm*	
		$\overline{E_0}$ (MeV)	$\overline{E_0}$ (MeV)	% Decrease	$\overline{E_0}$ (MeV)	% Decrease
4	0.05	5.735	5.175	9.765	4.975	13.252
6	0.07	7.605	6.975	8.284	6.775	10.914
8	0.05	9.515	8.79	7.620	8.625	9.3537
10	0.05	11.405	10.83	5.042	10.47	8.1982
12	0.05	12.985	12.355	4.852	11.935	8.0863
15	0.05	16.095	15.427	4.150	15.257	5.2066

The angular spectra of electron nominal energies of 4-15 MeV are shown in Figure 4-10. At $Z = 26.85$ cm, spectra exhibited maxima at 12.375 degrees, 11.925 degrees, 11.475 degrees, 11.025 degrees, 10.575 degrees and 10.575 degrees, respectively. As evident in Figure 4-10a, the width of the angular spectrum decreases with an increase in electron nominal energy, which goes along with an increase in the maximum peak with an increase in electron nominal energy. Figure 4-10b shows the angular spectra at $Z = 95$ cm, where an overall narrowing of the spectra was observed with a shift of the maximum peak to lower angles. More so, the maximum peak of each nominal energy was 2.925 degrees, where the width of the angular spectra decreased with an increase in electron nominal energy, similar to the case at $Z = 26.85$ cm. Also noticeable from Figure 4-10b is that the higher angle tail is decreasing with a decrease in electron nominal energy.

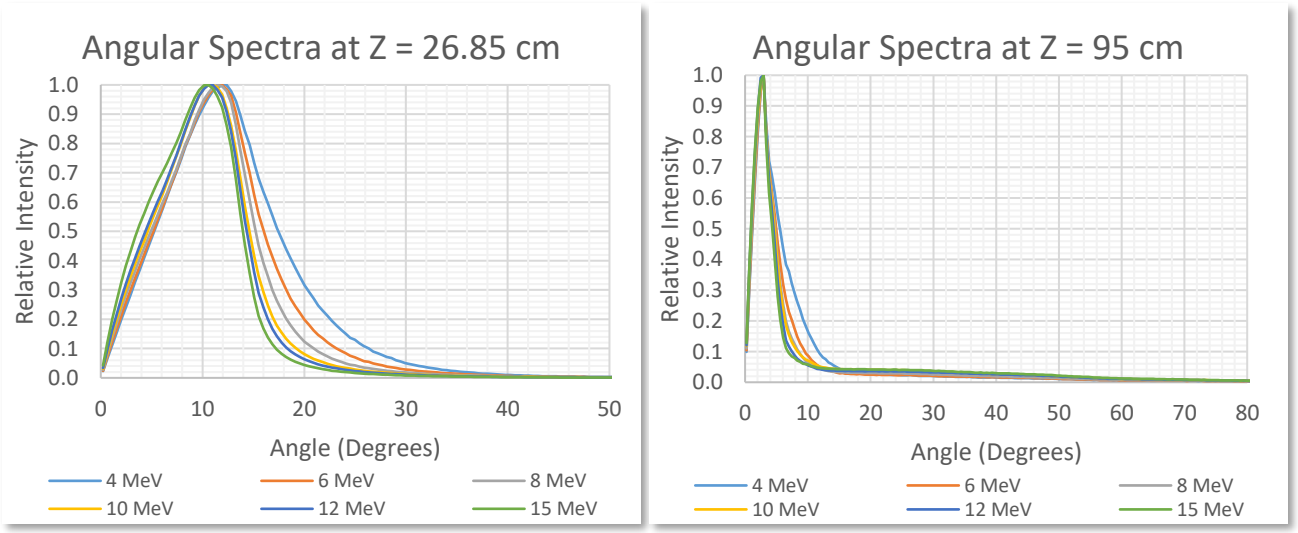

(a) (b)

Figure 4-10: Angular spectra at a) Z = 26.85 cm and at b) Z = 95 cm for electron nominal energies of 4-15 MeV.

4.2.2 Gaussian and Monoenergetic

A monoenergetic spectrum was used in the initial stages of this study, after which a polyenergetic Gaussian spectrum was investigated. The motive for the use of the experimental Lévy energy spectrum was discussed in sections 4.2.1, however to put the spectrum into perspective it needs to be compared with a Gaussian and monoenergetic energy spectrum, since these are the usual approaches followed by most authors (see section 3.1.1.6). It is however difficult to compare different initial spectra which are each characterized by different parameters. The monoenergetic spectrum is only characterized by a single parameter, whereas the Gaussian spectrum is characterized by 4 parameters (most probable energy $\overline{E_0}$, $FWHM$ as a % of $\overline{E_0}$, lower- and upper cut-offs $-a\sigma$ and $+b\sigma$) and the Lévy spectrum is characterized by 2 parameters (most probable energy $\overline{E_0}$, scaling parameter c).

Three monoenergetic spectra and three Gaussian spectra were constructed and compared with a 6 MeV Lévy energy spectrum with $\overline{E_0} = 7.605$ MeV and $c = 0.07$. Monoenergetic spectra 1-3 had energies of 7.4 MeV, 7.5 MeV and 7.6 MeV, respectively. Gaussian spectra 1-3 each had a set of parameters ($\overline{E_0}$, $FWHM$, $-a\sigma$, $+b\sigma$) equal to $(7.17\ \text{MeV}, 15\ \%, -3\sigma, +3\sigma)_1$, $(7.17\ \text{MeV}, 18\ \%, -3\sigma, +3\sigma)_2$ and $(7.17\ \text{MeV}, 25\ \%, -3\sigma, +3\sigma)_3$ respectively. The respective energy spectra at $Z = 0$ cm is shown in Figure 4-11a. The change of each energy spectrum at $Z = 26.85$ cm and $Z = 95$ cm (see Figure 4-11b) was investigated in terms of the most probable energy, the width of the spectrum and the lower energy tail. The change in the most probable energy for all spectra at $Z = 26.85$ cm and $Z = 95$ cm is summarized in Table 4-2.

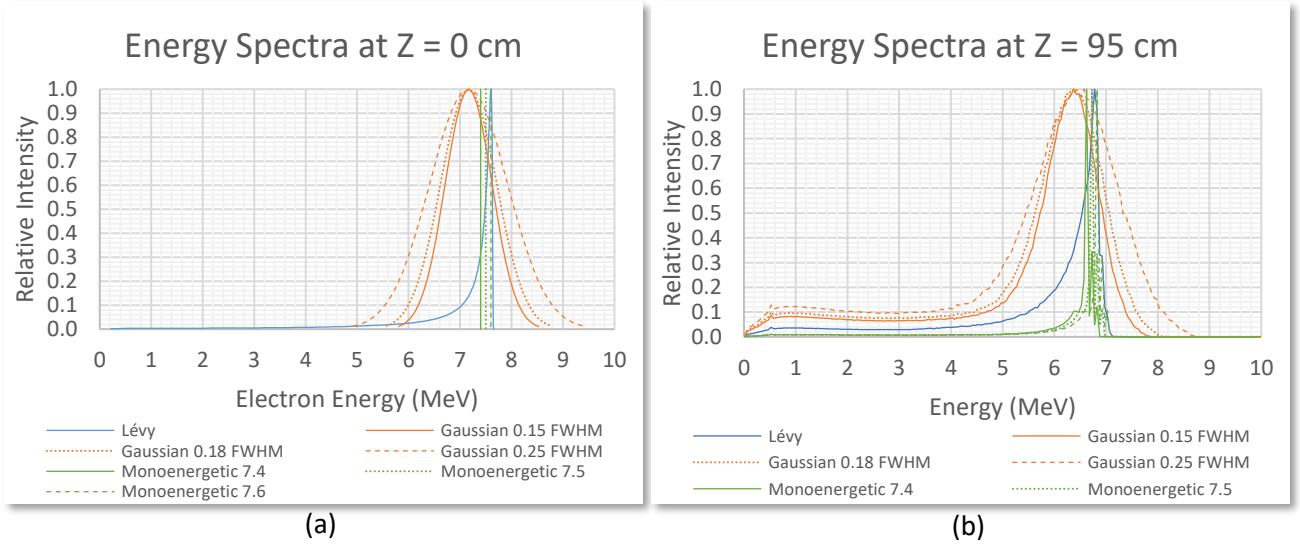

(a) (b)

Figure 4-11: Lévy (solid blue line), Gaussian (orange solid, dotted and dashed lines) and monoenergetic (green solid, dotted and dashed lines) spectra at a) Z = 0 cm and at c) Z = 95 cm.

An overall decrease in the most probable energies at $Z = 95$ cm was observed in comparison with the most probable energies at $Z = 0$ cm. The highest decrease occurred for the Lévy energy spectrum (11.9 %), whereas the minimum decrease was observed to be 8.914 % for the third Gaussian energy spectrum. For Gaussian spectra, this decrease in the most probable energy was less for larger FWHM values. For monoenergetic spectra, the decrease in the most probable energy increased with a decrease in the energy at $Z = 0$ cm. Furthermore, an overall widening of spectra at $Z = 95$ cm occurred along with an increase in the magnitude of the lower energy tail. For Gaussian spectra, the width at $Z = 95$ cm was dependent on the original width (FWHM) at $Z = 0$ cm, whereas the lower energy tail increased for higher FWHM values. Monoenergetic spectra showed almost no difference in terms of width and the magnitude of the lower energy tail. From Figure 4-11b it can be seen that the Lévy energy spectrum is situated between Gaussian and monoenergetic spectra in terms of the spectra width and magnitude of the lower energy tail.

Angular spectra for the different initial spectra showed an overall difference of less than 1.63 %. At $Z = 26.85$ cm, all angular spectra were peaked at 11.9 degrees, this value decreasing to 2.93 at at $Z = 95$ cm. The angular spectra at $Z = 95$ cm produced by the Gaussian energy spectra differed less than 1 % from the angular spectrum produced by the Lévy energy spectrum, whereas the angular spectra produced at $Z = 95$ cm by the monoenergetic spectrum differed by less than 1.63 % from the Lévy angular spectrum.

Table 4-2: The most probable energy and associated decrease for the Lévy, Gaussian and monoenergetic spectra at Z = 0 cm, Z = 26.85 cm and Z = 95 cm.

Spectrum	$Z = 0$ *cm*	$Z = 26.85$ *cm*		$Z = 95$ *cm*	
	$\overline{E_0}$ (MeV)	$\overline{E_0}$ (MeV)	% Decrease	$\overline{E_0}$ (MeV)	% Decrease
Lévy	7.605	6.975	8.284	6.775	11.900
Gaussian 1	7.170	6.625	7.601	6.375	12.000
Gaussian 2	7.170	6.625	7.601	6.425	11.245
Gaussian 3	7.170	6.675	6.904	6.575	8.914
Monoenergetic 1	7.400	7.025	5.068	6.625	11.032
Monoenergetic 2	7.500	7.125	5.000	6.725	10.877
Monoenergetic 2	7.600	7.225	4.934	6.825	10.727

CAX PDD parameters including $D_{1\mathrm{mm}}$, R_{80}, R_{50} and D_g were assessed with a change in Gaussian FWHM width and a change in the energy of the Monoenergetic spectrum. The assessment of these parameters with changes in the Lévy energy spectrum parameters have been discussed in section 4.2.1.

$D_{1\mathrm{mm}}$ was 79.592 %, 83.055 % and 80.355 % for Gaussian FWHMs of 15 %, 18 % and 25 % relative to the most probable electron energy, respectively. No trend was observed in $D_{1\mathrm{mm}}$ with a change in the FWHM. R_{80} was 2.06 cm, 2.04 cm and 2.12 cm for FWHMs of 15 %, 18 % and 25 %, respectively. A linear trendline was fitted to data and produced a regression constant of 0.7871, with a gradient of 0.7366 cm·FHWM^{-1} and a Y-intercept of 1.93 cm. Using the most probable energy of the Gaussian spectra (7.17 MeV) as input in the equation obtained from the linear trendline fitted to the R_{80} variation for monoenergetic spectra (assuming now the FWHM is decreased to zero, collapsing the Gaussian spectrum to a monoenergetic spectrum), a value of 2.06 cm was obtained, which differed with 0.13 cm (6.31 %) from the predicted R_{80} value of 1.93 cm. R_{50} was 2.59 cm, 2.64 cm and 2.69 cm for FWHMs of 15 %, 18 % and 25 %, respectively. This produced a linear trendline with a much better regression of 0.9853 with a gradient of 0.5497 cm·FHWM^{-1} and a Y-intercept of 2.41 cm. Again, using a 7.17 MeV (with a FWHM of zero) value as input to the linear equation fitted to the Monoenergetic data, an R_{50} value of 2.48 cm, which differed by 0.07 cm (2.84 %) from the predicted value of 2.41 cm. The trend in D_g was however unclear, where for FWHMs of 15 %, 18 % and 25 % produced dose gradients of -66.99 %·cm^{-1}·FHWM^{-1}, -62.06 %·cm^{-1}·FHWM^{-1} and -69.76 %·cm^{-1}·FHWM^{-1}, respectively.

Monoenergetic spectra with energies of 7.4 MeV, 7.5 MeV and 7.6 MeV produced $D_{1\mathrm{mm}}$ values of 82.61 %, 81.31 % and 81.142 %, respectively. Though these doses decrease with an increase in energy, fitting a linear trendline would seem rather unrealistic since it would not describe the actual trend of $D_{1\mathrm{mm}}$ with an increase in electron energy. R_{80} was 2.06 cm, 2.04 cm and 2.12 cm for energies of 7.4 MeV, 7.5 MeV and 7.6 MeV, respectively. A linear trendline with a regression of 0.9989 was fitted to data, which produced a gradient of 0.4246 cm·MeV^{-1} and a Y-intercept of -0.9836 cm. This predicts the rather obvious trend that R_{80} increases with an increase in electron energy. R_{50} values for monoenergetic spectra were 2.50 cm, 2.51 cm and 2.55 cm, respectively, and as expected an increase in R_{50} is observed with an increase in electron energy. A linear trendline yielded a regression of 0.9993 with a gradient of 0.4833 cm·MeV^{-1} and a Y-intercept of -0.9828 cm. The trend in D_g was an increase with an increase in electron energy, where values of -70.47 %·cm^{-1}·MeV^{-1}, -70.35 %·cm^{-1}·MeV^{-1} and -69.96 %·cm^{-1}·MeV^{-1} was observed. This means that with an increase in monoenergetic energy, the dose gradient becomes gentler with a slower fall-off in dose with depth beyond the depth of maximum dose.

It should be mentioned that the observed trends and associated fitted trendlines will only be true over a narrow range of electron energies, since the thickness of the primary scattering foil differs for each electron nominal energy. Therefore, the equations serve as a means to finely adjust the energy (and/or

width of the initial spectrum) to improve the match with measured data. However, in the case of the Gaussian and monoenergetic spectra, adjusting parameters changes $D_{1\mathrm{mm}}$, R_{80}, R_{50} and D_g significantly. This complicates the fine-tuning process, since it is often required to only change some of the mentioned parameters without altering the other parameters. In most cases, all parameters on the CAX PDD will be matched with measured data, but the surface dose will typically be underestimated by more than 2 % and therefore requires adjustment to the incident energy spectra. The advantage of the Lévy energy spectrum is that it offers a scaling parameter which, if finely adjusted, varies the dose in the BU region without significantly adjusting the rest of the CAX PDD. This therefore offers a method (although not precisely quantified) which by trial-and-error can produce a sufficient amount of dose in the BU region. This was the main motivation for using the Lévy energy spectrum.

The flatness of crossline and inline off-axis profiles was more sensitive to FWHM changes in Gaussian energy spectra, producing crossline values of 3.56 %, 3.76 % and 4.41 % and inline values of 3.16 %, 5.15 % and 5.19 % for FWHMs of 15 %, 15 % and 25 %, respectively. Monoenergetic spectra with energies of 7.4 MeV, 7.5 MeV and 7.6 MeV produced crossline flatness values of 3.74 %, 4.77 % and 2.67 % and inline flatness values of 3.77 %, 3.89 % and 2.70 %, respectively. Both crossline and inline penumbras varied by less than 0.4 mm for Gaussian spectra, whereas this variation increased to 0.58 mm for monoenergetic spectra. As with the Lévy energy spectrum, the change in profile flatness and penumbra width with a change in Gaussian and monoenergetic spectrum parameters is significant and therefore it is important to consider these changes when adapting the energy spectrum to improve the match with measured data.

4.3 Primary Scattering Foil

The primary scattering foil thickness for each nominal electron energy is supplied by the vendor along with tolerance values. These tolerances give the allowable thickness range for each primary scattering foil, as discussed in section 3.1.1.1.2. The variation in primary scattering foil thickness within the tolerance range and the changes brought about in the CAX PDD, crossline and inline profiles, energy spectra and angular spectra were investigated for a 4 MeV electron beam using a Lévy energy spectrum with a most probable energy of 5.685 MeV and a scaling parameter of 0.05. The primary scattering foil thickness range for the 4 MeV electron beam is 0.0033 cm – 0.0036 cm, hence thicknesses in 0.0001 cm increments were used.

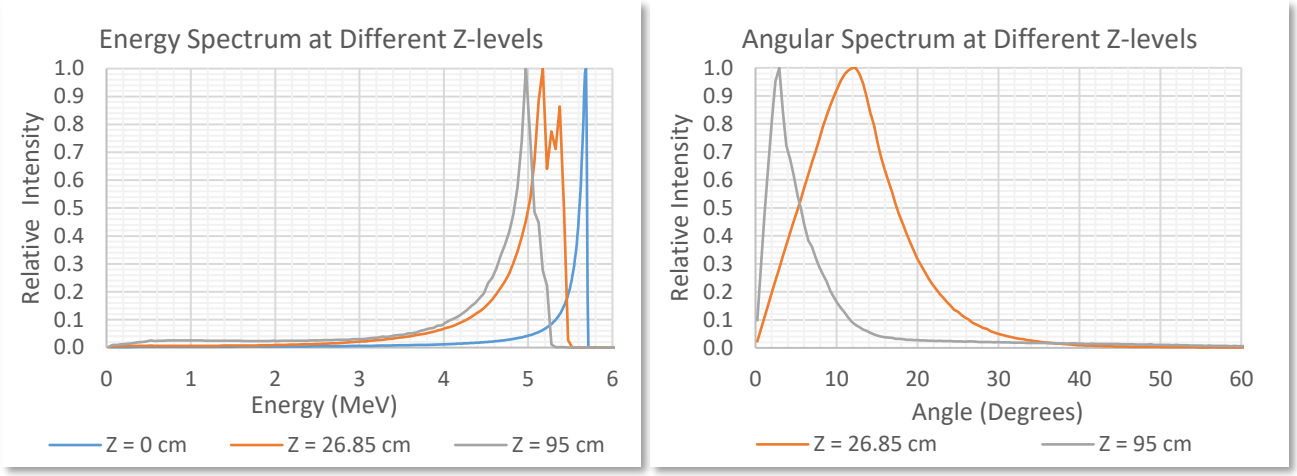

(a) (b)

Figure 4-12: The change in the a) initial 4 MeV Lévy energy spectrum (Z = 0 cm, solid blue line) at Z = 26.85 cm (solid orange line) and Z = 95 cm SSD (solid grey line) for a primary scattering foil thickness of 0.0036 cm, along with the change in the b) angular distribution at Z = 26.85 cm (solid orange line) and at Z = 95 cm (solid grey line). Both the energy and angular spectra include electrons, photons and positrons.

The energy spectra in Figure 4-12 (a) illustrates the energy broadening and extension to lower electron energies that occurs during the transport of electrons, photons and positrons through the linac head. The initial energy spectrum ($Z = 0$ cm) had a most probable energy of 5.685 MeV. This lowered to 5.18 MeV (8.88 % decrease relative to the most probable energy at $Z = 0$ cm) at $Z = 26.85$ cm and 4.98 MeV (13.61 % decrease) at $Z = 95$ cm. It is evident that for a fixed primary scattering foil thickness, the most probable energy of the energy spectrum decreases with an increase in SSD, whereas the lower energy tail increases with an SSD increase. The width of the energy spectrum initially broadens out at $Z = 26.85$ cm and narrows as it approaches $Z = 95$ cm, where the width at $Z = 95$ cm is still higher than at $Z = 0$ cm. The angular spectrum in Figure 4-12 (b) shows a much broader spectrum at an SSD of 26.85 cm with a peak at 12.4 degrees, which narrows and shifts to lower angles at an SSD of 95 cm with a peak at 2.93 degrees. The angular broadening of the total beam at $Z = 26.85$ cm is due to the contribution of the scattering effects of the primary scattering foil and the secondary scattering foils. However, the electron applicator filters the higher end of the angular spectrum and shifts the spectrum towards lower angles, effectively giving rise to a total beam with a smaller angular component.

The next step is to investigate the change in the spectra due to a change in primary scattering foil thickness. This is indicated in Figure 4-13 (a-d), which gives the change in the energy spectra at SSDs of $Z = 26.85$ cm and $Z = 95$ cm for primary scattering foils of 0.0033 cm – 0.0036 cm. The most probable

energies of were the same for all spectra at the respective Z-level. The difference between the 0.0033 cm – 0.0035 cm foils and the 0.0036 cm foil. At $Z = 26.85$ cm, the biggest differences occur in the peaks, where the trend is noted that secondary peak intensities decrease with a decrease in primary scattering foil thickness. A maximum change of 5.40 % in the secondary peak was observed for the 0.0033 cm foil, this value decreasing to 2.67 % and 1.39 % for the 0.0034 cm and 0.0035 cm foil, respectively. At $Z = 95$ cm the biggest differences were also observed in the peaks, where the general trend is for secondary peaks to increase with a decrease in primary scattering foil thickness, opposite to the trend at $Z = 26.85$ cm. In fact, the secondary peaks tend to disappear with an increase in primary scattering foil. The biggest difference observed was 10.86 % for the 0.0033 cm primary scattering foil, this value decreasing to 5.32 % and 4.12 % for the 0.0034 cm and 0.0035 cm foils, respectively. At $Z = 26.85$ cm the width of the energy spectrum as well as the magnitude of the lower energy tail increases slightly with an increase in primary scattering foil thickness. Excluding the 0.0033 cm results, at $Z = 95$ cm the same trend as observed at $Z = 26.85$ cm exists.

Changes to the angular spectra due to a primary scattering foil change were less than 1 % in all cases, where the differences at both $Z = 26.85$ cm and $Z = 95$ cm SSD occurred mainly in the peak areas (refer to Figure 4-12 b for identification of peak areas) of the angular spectra.

The final step is to investigate the changes in the CAX PDD and profiles brought about by a change in the primary scattering foil thickness. The changes in $D_{1\mathrm{mm}}$, R_{100}, R_{80}, R_{20} and the dose gradient D_G for the range of primary scattering foil thicknesses investigated are indicated in Table 4-3. It is evident that the changes brought about on the CAX PDD are extremely small. For both R_{80} and R_{50} all thicknesses produced values within 0.1 mm of each other, whereas no change was observed for R_{100} (taking into consideration a 2 mm voxel resolution). $D_{1\mathrm{mm}}$ varied by a maximum of 1.097 % with no trend between the observed change and the change in primary scattering foil thickness. The maximum observed change in D_G was 0.3 MeV·cm^{-1}.

Table 4-3: The change in CAX PDD parameters including D_{1mm}, R_{100}, R_{80}, R_{50} and D_G due to a change in the primary scattering foil thickness.

	D_{1mm} (%)	R_{100} (cm)	R_{80} (cm)	R_{50} (cm)	D_G (MeV·cm^{-1})
0.0033 cm	80.453	0.900	1.522	1.854	39.415
0.0034 cm	79.766	0.900	1.511	1.849	39.715
0.0035 cm	80.738	0.900	1.520	1.853	39.468
0.0036 cm	79.641	0.900	1.515	1.848	39.601

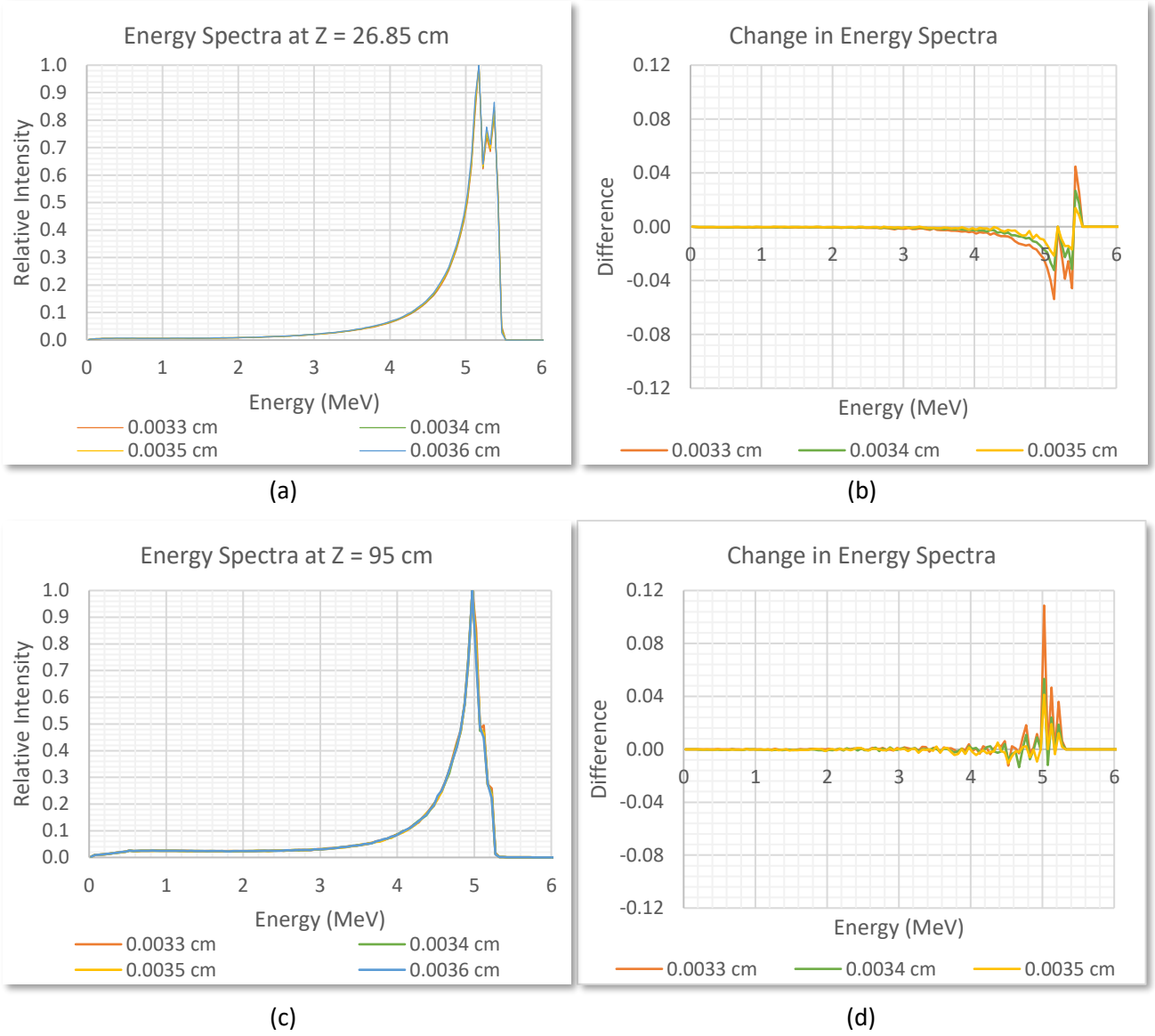

Figure 4-13: The change in the energy spectra (along with inlays of the high-change regions) for different primary scattering foil thicknesses are indicated at a) Z = 26.85 cm and at c) Z = 95 cm. The corresponding differences between the 0.0033 cm – 0.0035 cm foils and the 0.0036 cm foil are indicated at b) Z = 26.85 cm and c) Z = 95 cm.

A flatness of 2.38 % and 2.90 % was observed for crossline and inline profiles, respectively, for the 0.0033 cm primary scattering foil. These values decreased to 2.05 % and 2.46 % for the 0.034 cm primary scattering foil, where the 0.0035 cm primary scattering foil yielded a flatness of 2.24 % and 2.84 %, respectively. The flatness of crossline profiles varied with a maximum of 0.41 %, whereas this value increased for inline profiles to 0.66 %. Crossline penumbras decreased from 7.08 mm to 6.75 mm between

the 0.0033 cm and 0.0035 cm primary scattering foils, where the inline penumbras decreased from 6.98 mm to 6.56 mm, respectively. Crossline penumbras varied by a maximum of 0.33 mm, whereas the observed maximum change in the inline penumbras were 0.42 mm.

4.4 MLC and JAW positions

As mentioned in section 3.1.1.2.2, for each electron applicator-energy combination, the MLCs and JAW move to preset positions as determined by the vendor. These positions are wider relative to the field size at 95 cm SSD, and with an increase in electron energy both the MLCs and JAW move inwards. Since relatively out of the field, the influence of these components on profiles are kept at a minimum. For sake of interest, offsets in MLC and JAW positions for a fixed electron applicator and energy (10 x 10 cm^2 applicator and 4 MeV) were introduced as to investigate what the influence would be on the CAX PDD and off-axis profiles. Offsets of -2.0 cm, -1.5 cm, -1.0 cm and -0.5 cm were introduced separately in both the MLC and JAW positions, where the negative sign indicates a narrower field. The MLC and JAW offsets introduced are indicated in Table 4-4.

Table 4-4: MLC (red) and JAW (green) offsets introduced for the 10 x 10 cm^2 electron applicator and 4 MeV electron beam. The first entry (blue) represents the zero offset (control) setting.

MLC Offset @ 100 cm SSD (cm)	*JAW Offset @ 100 cm SSD (cm)*	*MLC Positions @ 100 cm SSD (cm)*	*JAW Positions @ 100 cm SSD (cm)*
0	0	± 12.0	± 11.21
0	-2.0	± 12.0	± 9.21
0	-1.5	± 12.0	± 9.71
0	-1.0	± 12.0	± 10.21
0	-0.5	± 12.0	± 10.71
-2.0	0	± 10.0	± 11.21
-1.5	0	± 10.5	± 11.21
-1.0	0	± 11.0	± 11.21
-0.5	0	± 11.5	± 11.21

The influence of each MLC/JAW combination in Table 4-4 on the CAX PDDs was investigated for differences in the absorbed dose at a depth of 1 mm, R_{80} and R_{50}. Overall the PDD and the energy spectrum was insensitive to the changes in MLC and JAW positions. The maximum deviation in the dose at 1 mm depth was brought about by the -2.0 cm MLC offset with a 2.06 % (-1.68 %) difference relative to the control (80.99 %). The maximum deviation in R_{80} was also brought about by the -2.0 cm MLC offset with a 1.19 % (-0.022 cm) difference relative to the control (1.84 cm). The -1.5 cm JAW offset brought

about the maximum deviation in R_{50} with a 1.02 % (-0.015 cm) difference relative to the control (1.51 cm). However, there is no specific trend for these differences with the introduced offset. The change in the energy spectrum at 95 cm SSD was negligible for the lower energy tail of the spectrum. The higher energy part of the spectrum at 95 cm SSD showed differences that correlated with the size of the offset introduced. The higher the introduced offset, the larger the differences observed in the spectrum. In addition, the MLC introduced offset yielded negative differences whereas the JAW offsets yielded positive differences. Compared to the differences in the spectrum as observed for the focal spot FWHM in Figure 4-3 (b), the differences brought about by both the MLC and JAW offsets are smaller by a magnitude of 10^4.

Off-axis profiles at the depth of maximum dose (0.9 cm for the 4 MeV electron beam) were more sensitive to the introduced MLC and JAW offsets. The MLC offsets affected the flatness of crossline profiles and JAW offsets affected the flatness of inline profiles, which agrees with the plane in which the MLC and JAW collimates the electron beam. The dose in the crossline profile shoulder and central region decreased as the introduced MLC offset increased. For MLC offsets of -0.5 cm, -1.0 cm, -1.5 cm and -2.0 cm the corresponding profile flatness was 2.94 %, 3.12 %, 3.92 % and 4.87 % respectively. Over the range of MLC offsets investigated, a quadratic fit with a regression of 0.9954 estimates a 3.02 % flatness at a zero MLC offset, which is 0.36 % higher than the observed crossline profile flatness. The dose in the inline profile shoulder and central region also decreased as the introduced JAW offset increased, however the trend was not as clear as with the MLC offsets. For JAW offsets of -0.5 cm, -1.0 cm, -1.5 cm and -2.0 cm the corresponding profile flatness was 3.16 %, 4.66 %, 3.22 % and 3.94 % respectively. No realistic fit could be performed without excluding the result of the -1.0 cm offset. In this case, a linear fit with a rather poor regression of 0.6424 estimates a 2.84 % flatness at a zero JAW offset, which is 0.33 % higher than the observed inline profile flatness.

It is evident that for a fixed electron applicator-energy combination, MLC and JAW positions have a direct influence on the flatness of profiles, where the CAX PDD is almost entirely insensitive to these positions which is reflected in the minor (for all purposes, negligible) differences observed in the energy spectrum.

4.5 PDDs

Simulated PDD curves complied with measured PDD curves with a 100 % pass rate using a 2%/2mm criterion for all energies, fields and SSDs. Generally, the PDDs simulated at 100 cm SSD complied better with measurements than those simulated at 95 cm SSD, especially in the BU region. The energy spectrum

for each electron energy was fine tuned to improve the match with measured data. This includes firstly matching the depth of maximum dose and the dose gradient which are dependent on the peak energy of the spectrum. Once this is done, a spatial misalignment in the dose fall-off region may be solved by adjusting the primary scattering foil thickness, which will consequently also influence the dose in the BU region. This BU dose change can then be altered by adjusting the scaling parameter of the energy spectrum which will not affect the dose beyond the maximum dose, as discussed in section 4.2.1.1. For a fixed field size, and especially for a fixed small field size, the variation in the BU and BD dose becomes more significant with an increase in electron energy. Therefore, it is often easier to fine tune the model for lower electron energies than for higher electron energies. The reference field size of 10 x 10 cm^2 was used as the initial field for fine tuning, since for all electron energies scatter equilibrium will be present on the CAX of the beam. Since this model involves a full simulation through the treatment head, the upper model's phase space file was re-used as source input for the rest of the fields in the lower model, which was able to predict both larger and smaller fields within the tolerance criteria. CAX PDDs at an SSD of 95 cm SSD are shown in Figure 4-14 - Figure 4-24, whereas CAX PDDs at an SSD of 100 cm are shown in Figure 4-25 - Figure 4-35.

The number of histories chosen in `DOSXYZnrc` simulations reflected a maximum statistical uncertainty of 1%, as mentioned in section 3.1.2.3. All simulations were run on 2 Intel® Xeon® E5620 processors (2.4 GHz clock speed), 16 GB DDR3 computer operating on an openSUSE 12.2 (x86_64) platform.

4.5.1 95 cm SSD

4.5.1.1 2 x 2 cm²

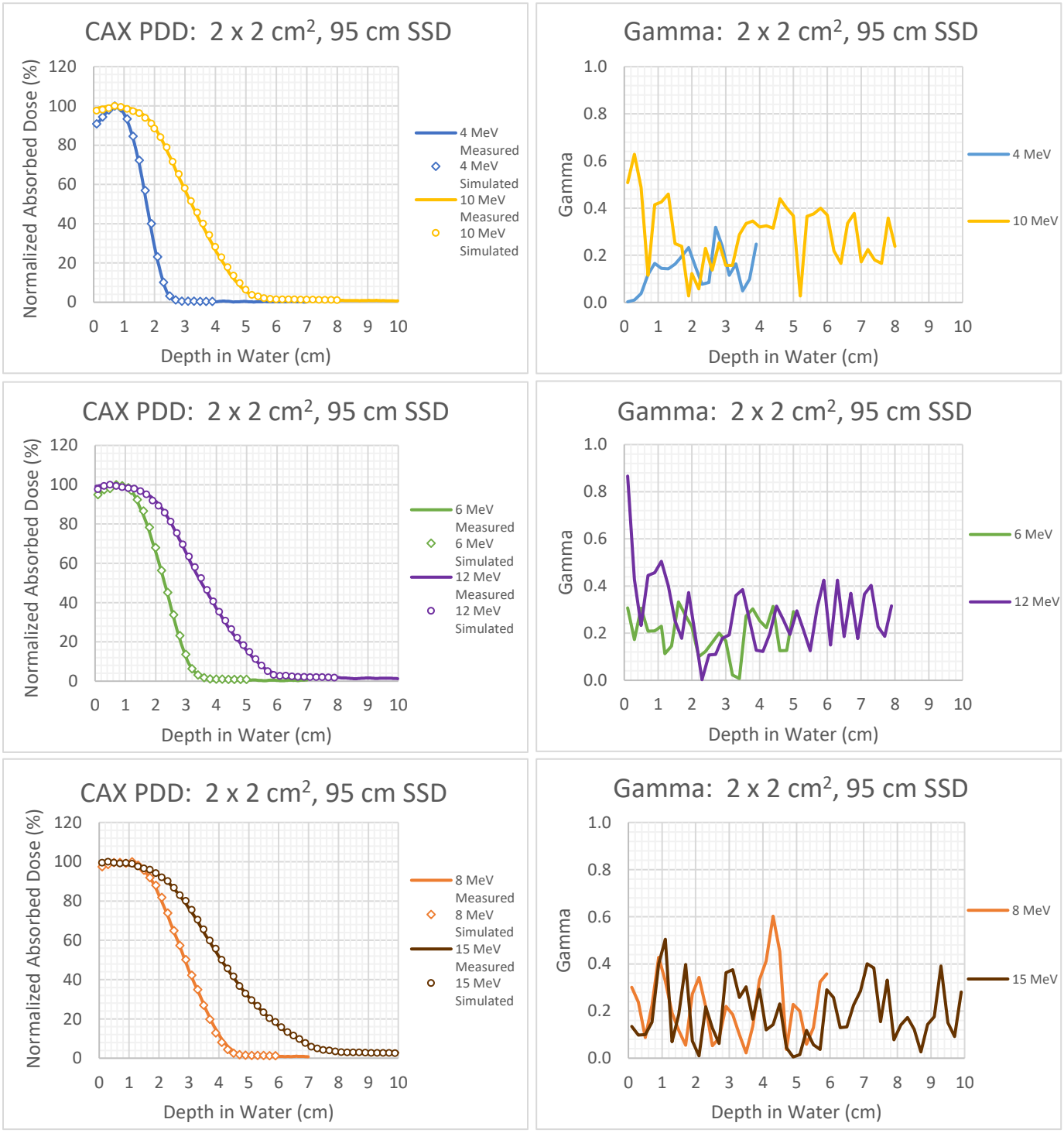

Figure 4-14: CAX PDDs (left sides) at 95 cm SSD for a 2 x 2 cm² field size and for electron nominal energies of 4-15 MeV. The associated Gamma analysis for each measured-simulated curve is indicated on the right side with a criterion of 2%/2mm.

4.5.1.2 3 x 3 cm²

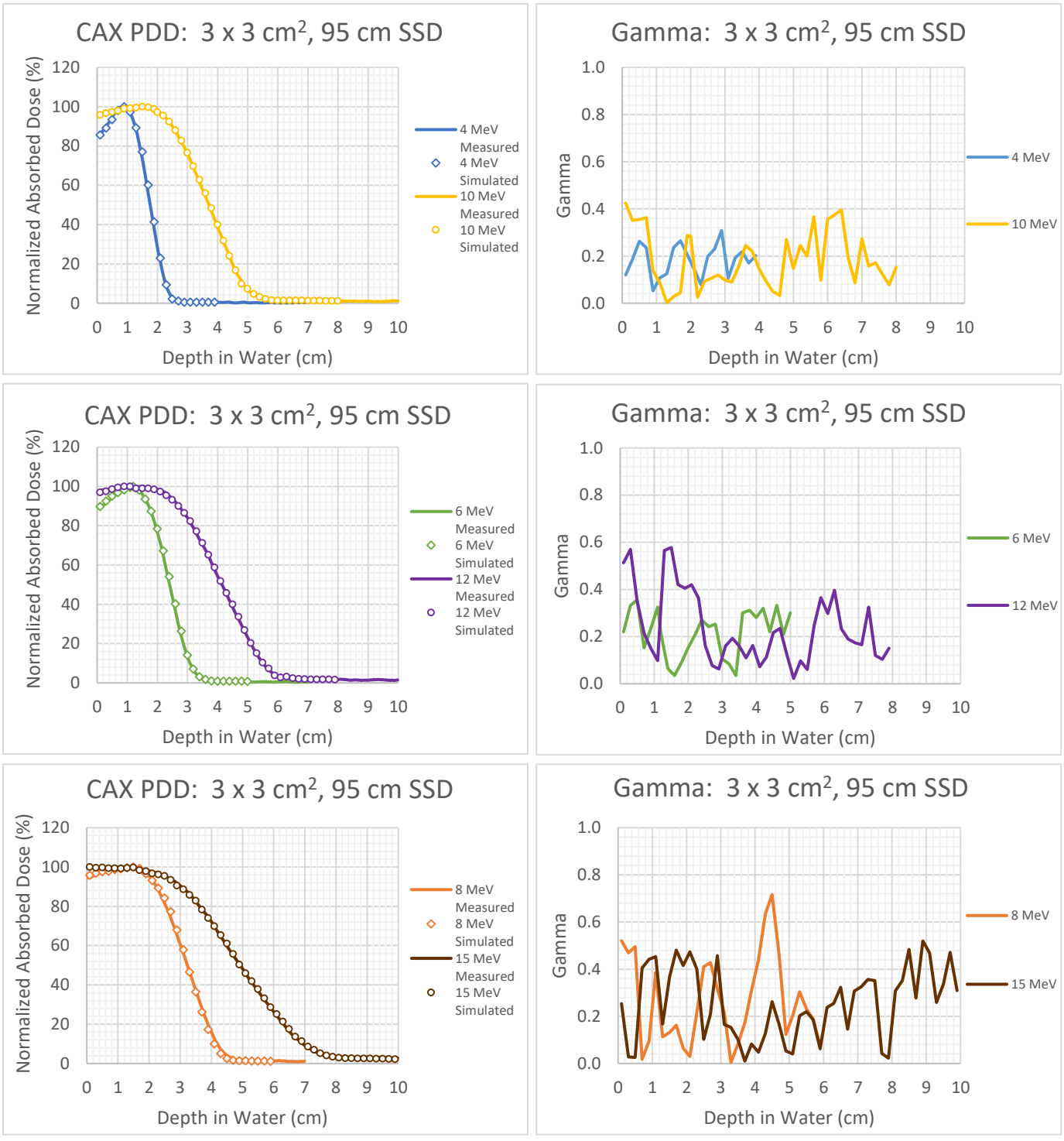

Figure 4-15: CAX PDDs (left sides) at 95 cm SSD for a 3 x 3 cm² field size and for electron nominal energies of 4-15 MeV. The associated Gamma analysis for each measured-simulated curve is indicated on the right side with a criterion of 2%/2mm.

4.5.1.3 6 x 6 cm^2

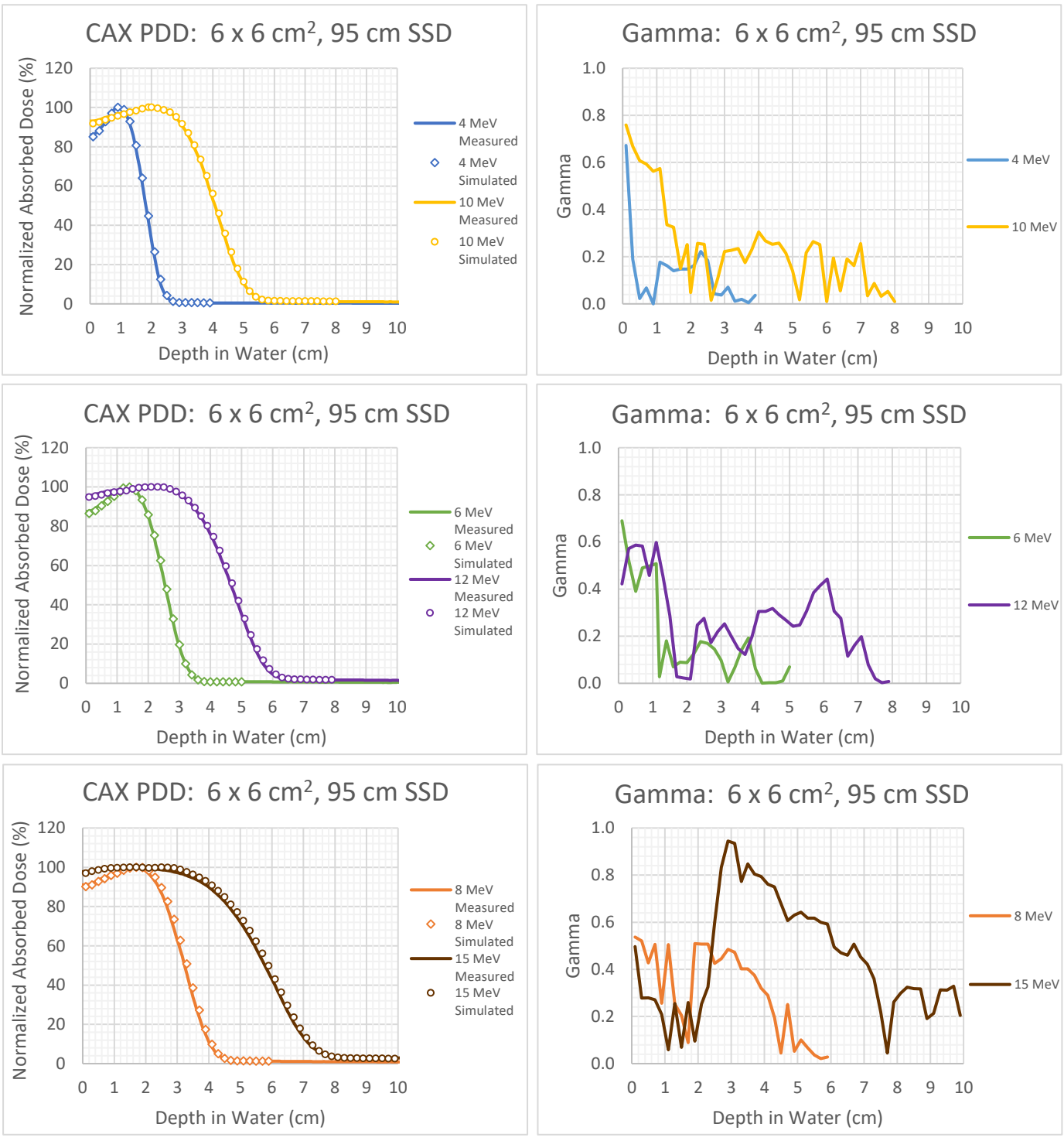

Figure 4-16: CAX PDDs (left sides) at 95 cm SSD for a 6 x 6 cm^2 field size and for electron nominal energies of 4-15 MeV. The associated Gamma analysis for each measured-simulated curve is indicated on the right side with a criterion of 2%/2mm.

4.5.1.4 6 x 10 cm²

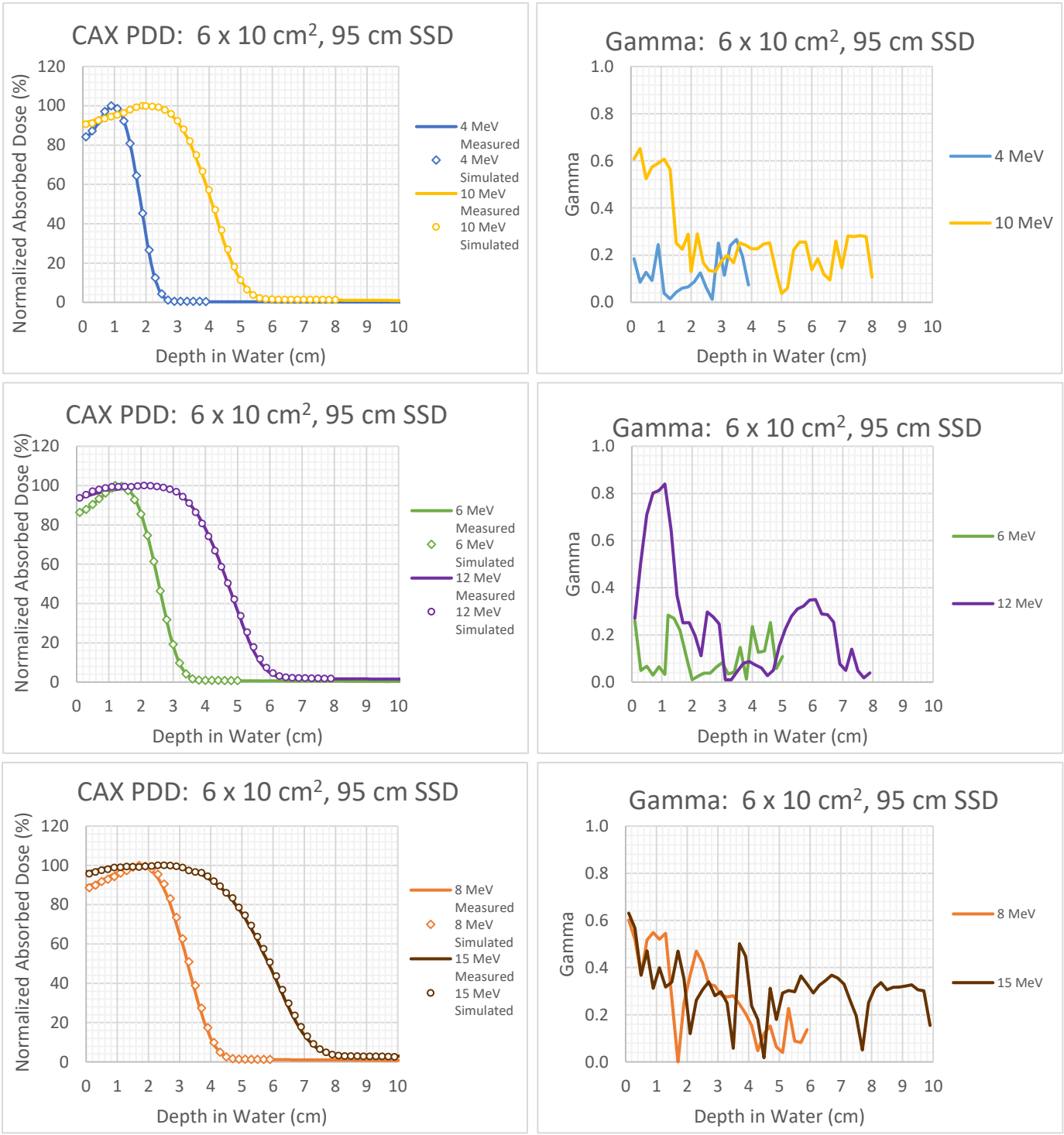

Figure 4-17: CAX PDDs (left sides) at 95 cm SSD for a 6 x 10 cm² field size and for electron nominal energies of 4-15 MeV. The associated Gamma analysis for each measured-simulated curve is indicated on the right side with a criterion of 2%/2mm.

4.5.1.5 6 x 14 cm²

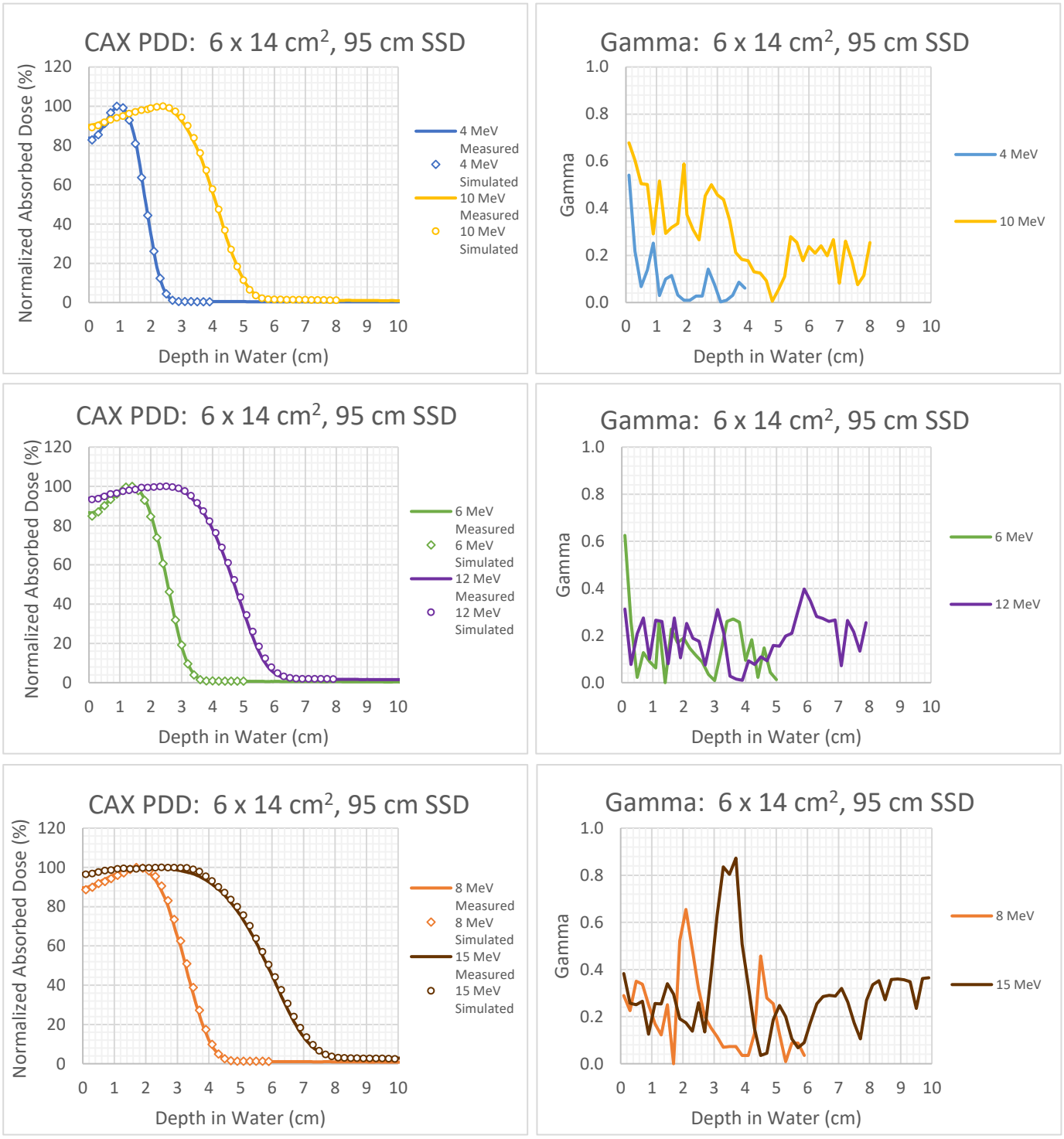

Figure 4-18: CAX PDDs (left sides) at 95 cm SSD for a 6 x 14 cm² field size and for electron nominal energies of 4-15 MeV. The associated Gamma analysis for each measured-simulated curve is indicated on the right side with a criterion of 2%/2mm.

4.5.1.6 8 x 16 cm²

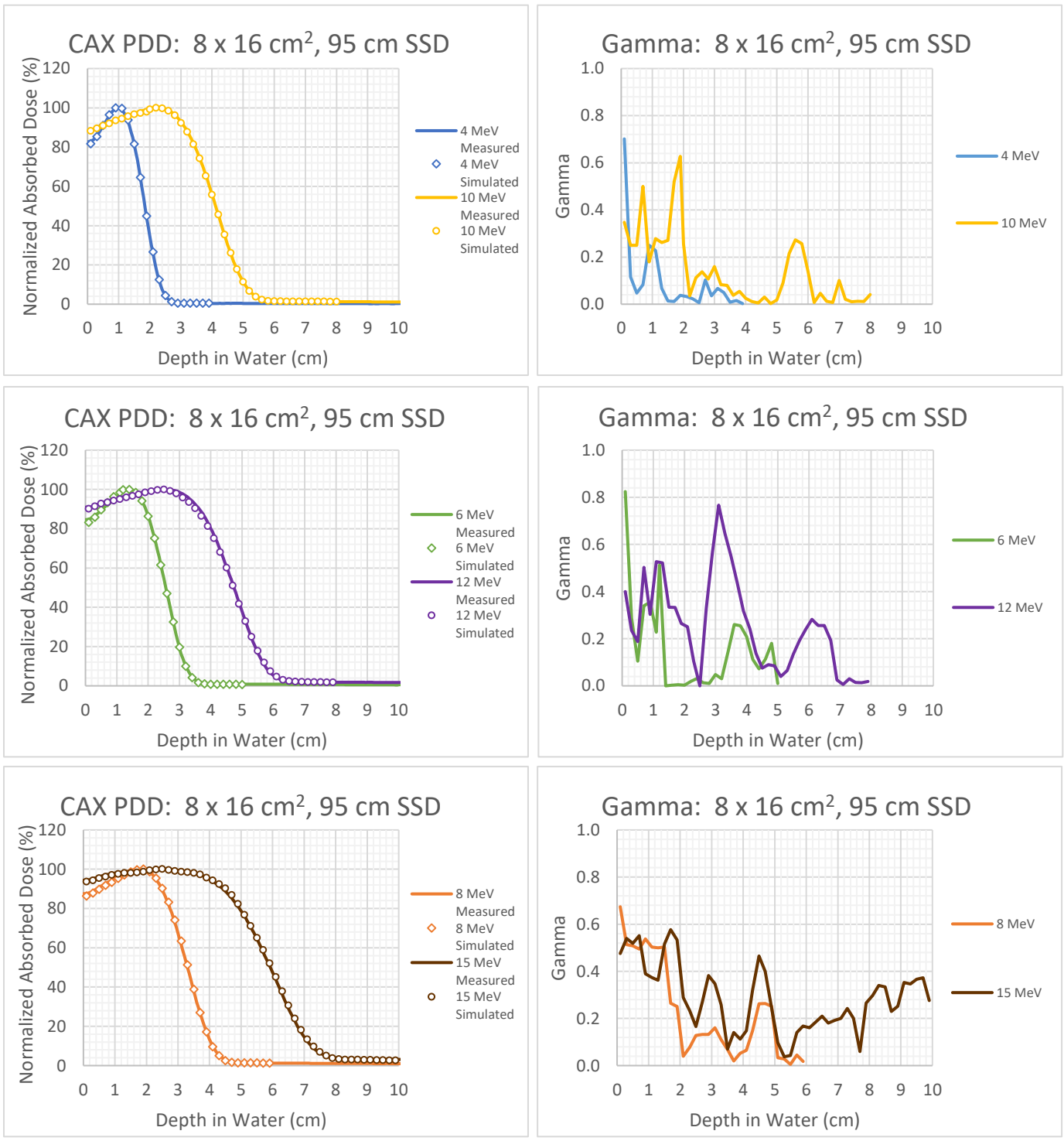

Figure 4-19: CAX PDDs (left sides) at 95 cm SSD for a 8 x 16 cm² field size and for electron nominal energies of 4-15 MeV. The associated Gamma analysis for each measured-simulated curve is indicated on the right side with a criterion of 2%/2mm.

4.5.1.7 10 x 10 cm²

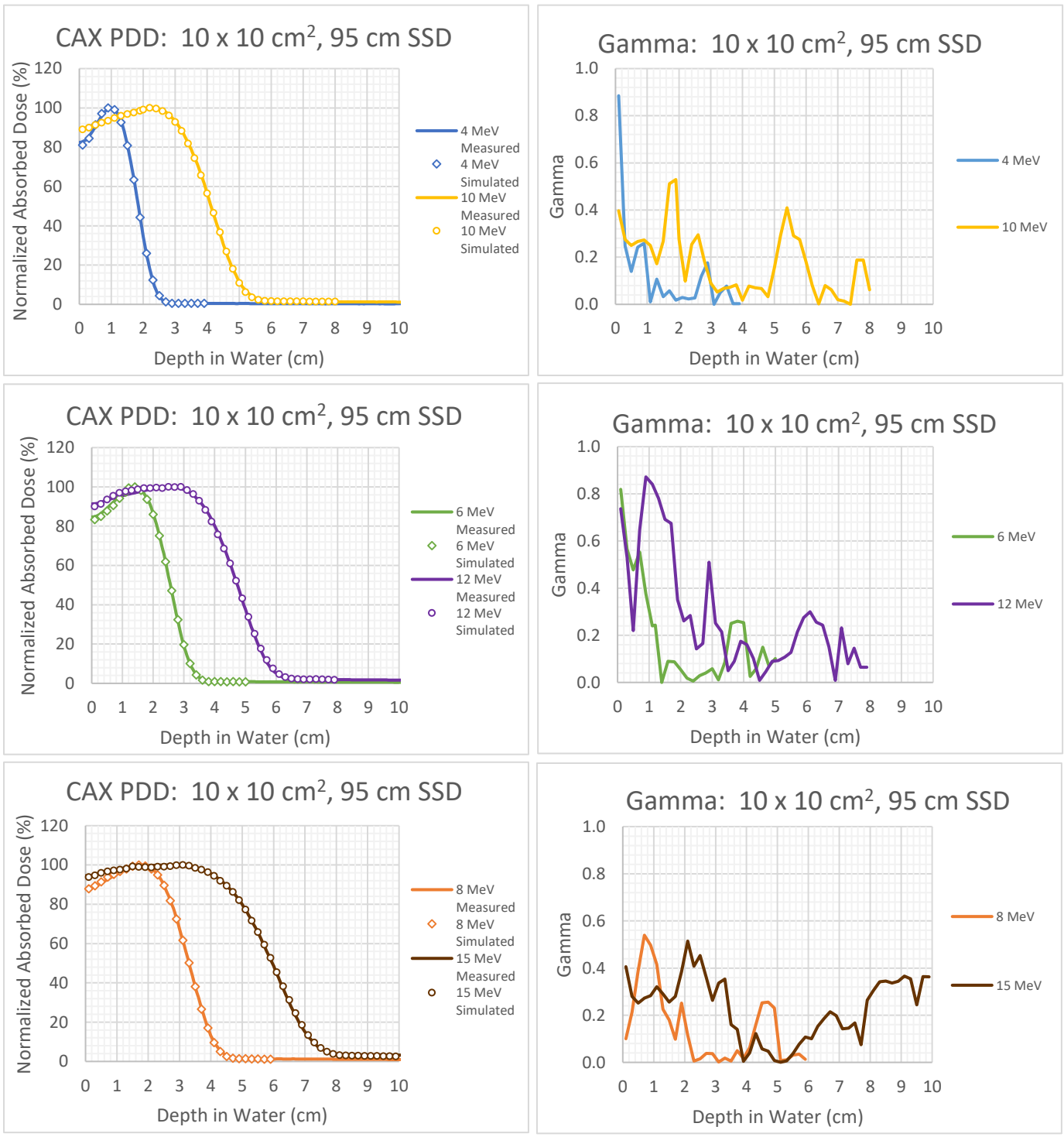

Figure 4-20: CAX PDDs (left sides) at 95 cm SSD for a 10 x 10 cm² field size and for electron nominal energies of 4-15 MeV. The associated Gamma analysis for each measured-simulated curve is indicated on the right side with a criterion of 2%/2mm.

4.5.1.8 10 x 20 cm²

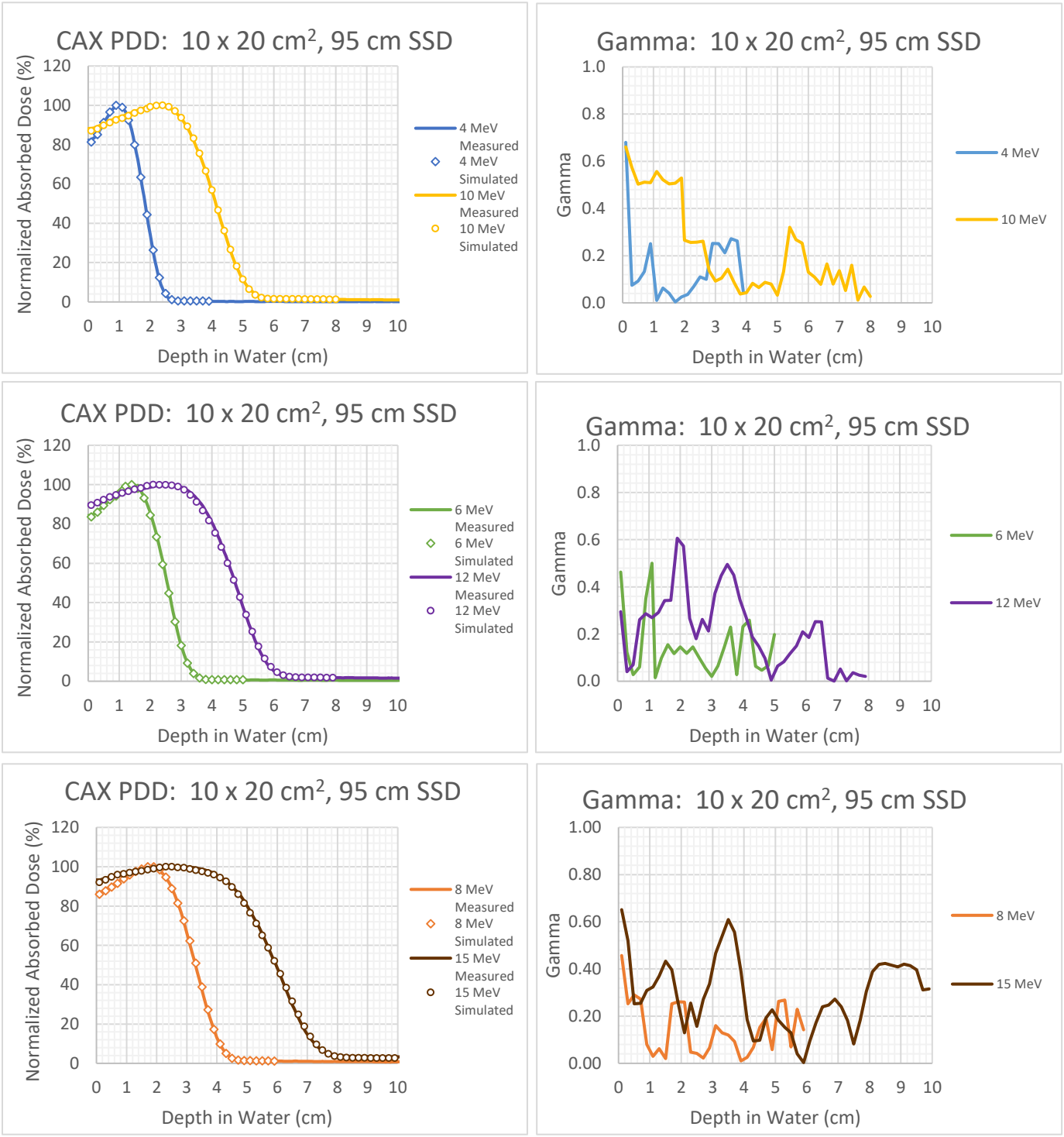

Figure 4-21: CAX PDDs (left sides) at 95 cm SSD for a 10 x 20 cm² field size and for electron nominal energies of 4-15 MeV. The associated Gamma analysis for each measured-simulated curve is indicated on the right side with a criterion of 2%/2mm.

4.5.1.9 14 x 14 cm²

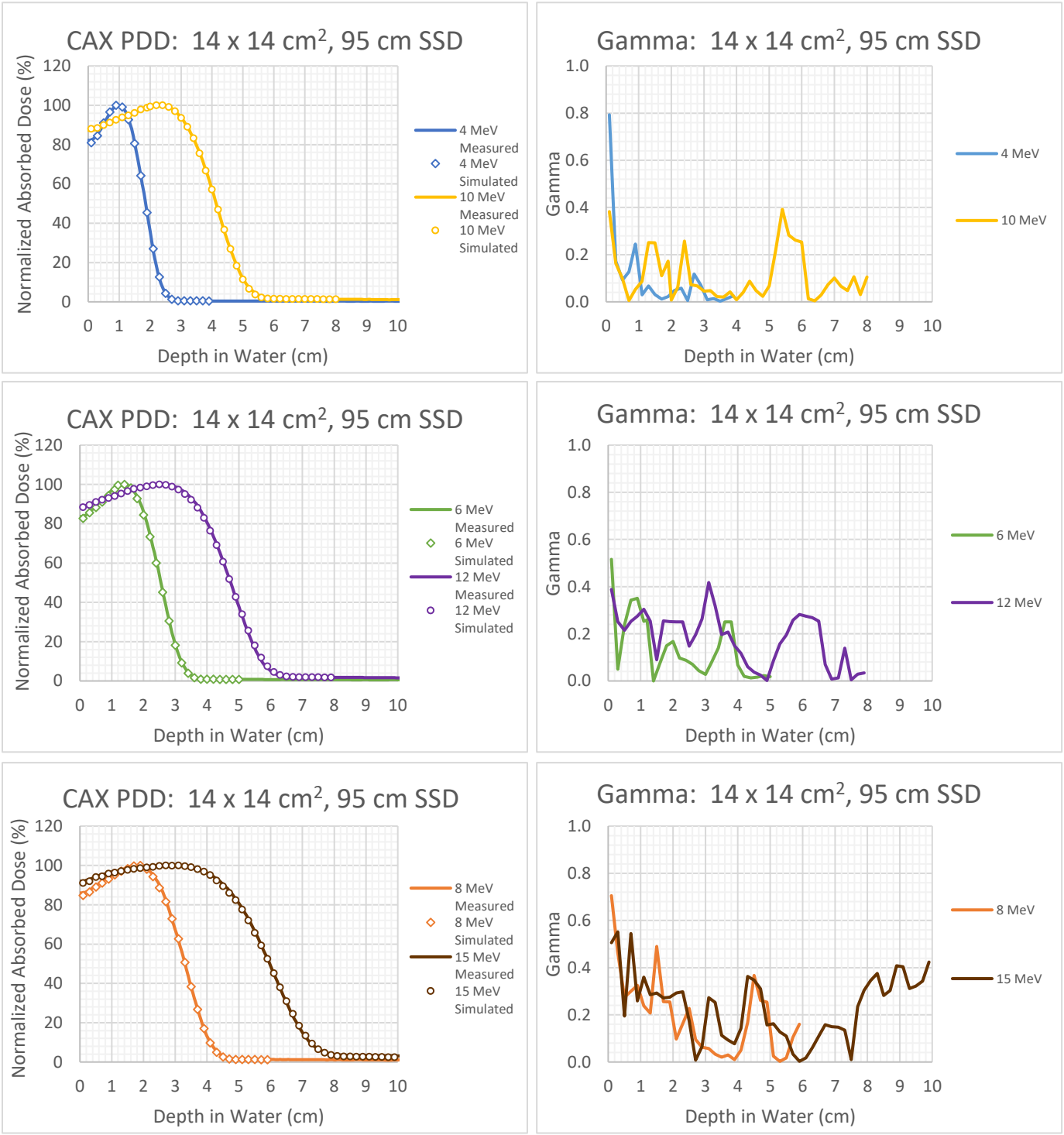

Figure 4-22: CAX PDDs (left sides) at 95 cm SSD for a 14 x 14 cm² field size and for electron nominal energies of 4-15 MeV. The associated Gamma analysis for each measured-simulated curve is indicated on the right side with a criterion of 2%/2mm.

4.5.1.10 20 x 20 cm²

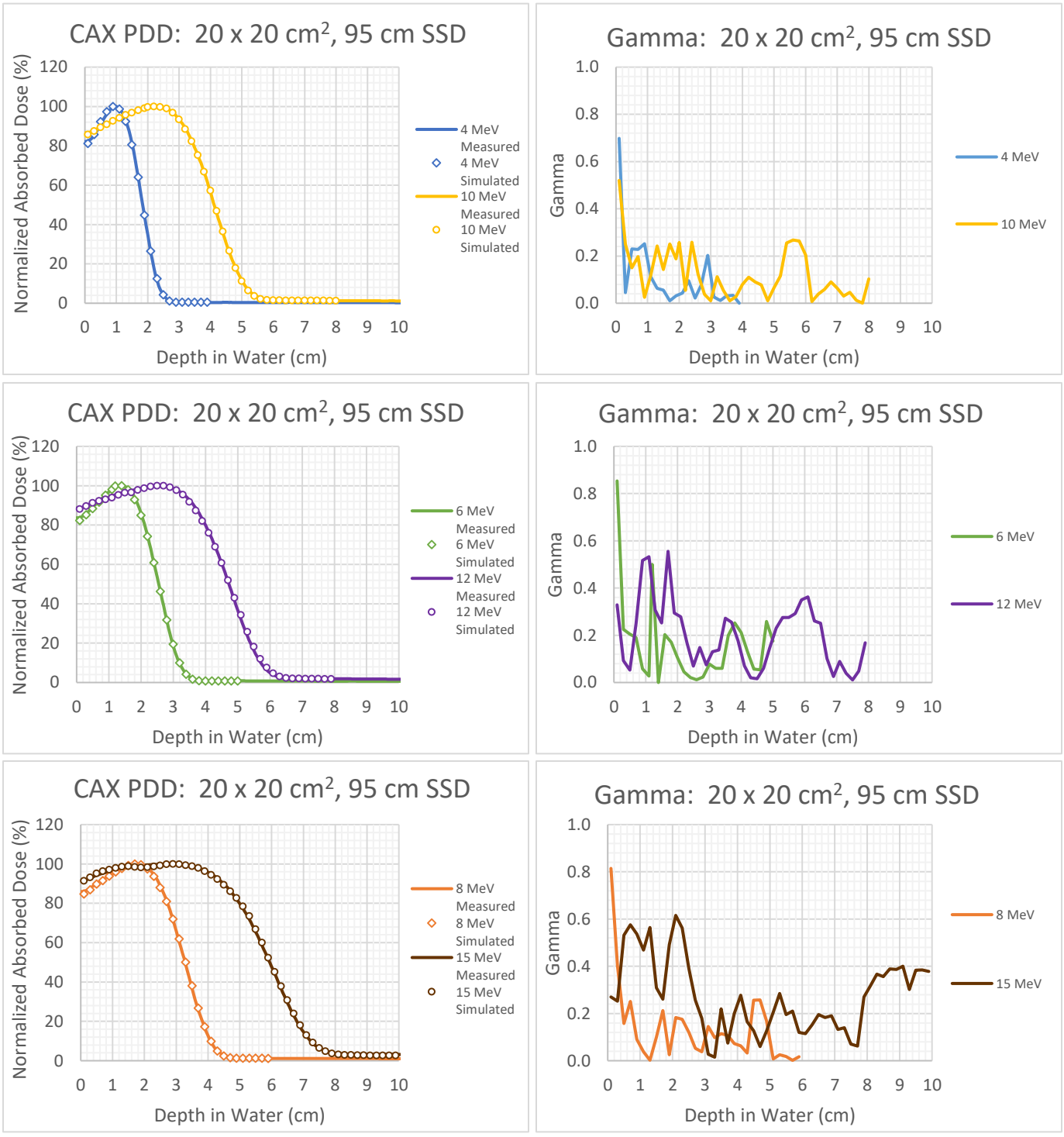

Figure 4-23: CAX PDDs (left sides) at 95 cm SSD for a 20 x 20 cm² field size and for electron nominal energies of 4-15 MeV. The associated Gamma analysis for each measured-simulated curve is indicated on the right side with a criterion of 2%/2mm.

4.5.1.11 4 cm Ø (3.54 x 3.54 cm²)

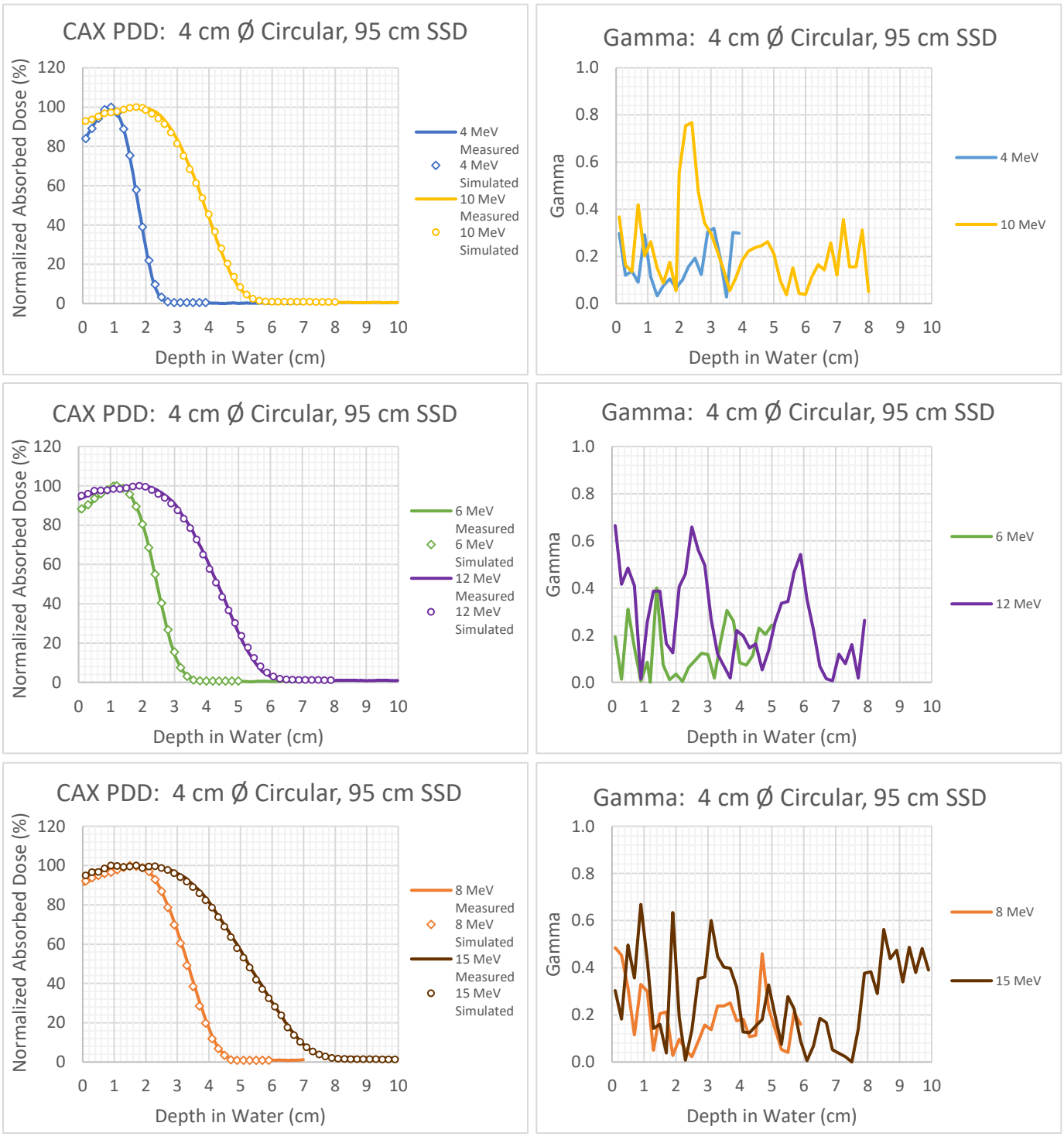

Figure 4-24: CAX PDDs (left sides) at 95 cm SSD for a 4 cm diameter field size and for electron nominal energies of 4-15 MeV. The associated Gamma analysis for each measured-simulated curve is indicated on the right side with a criterion of 2%/2mm.

4.5.2 100cm SSD

4.5.2.1 2 x 2 cm²

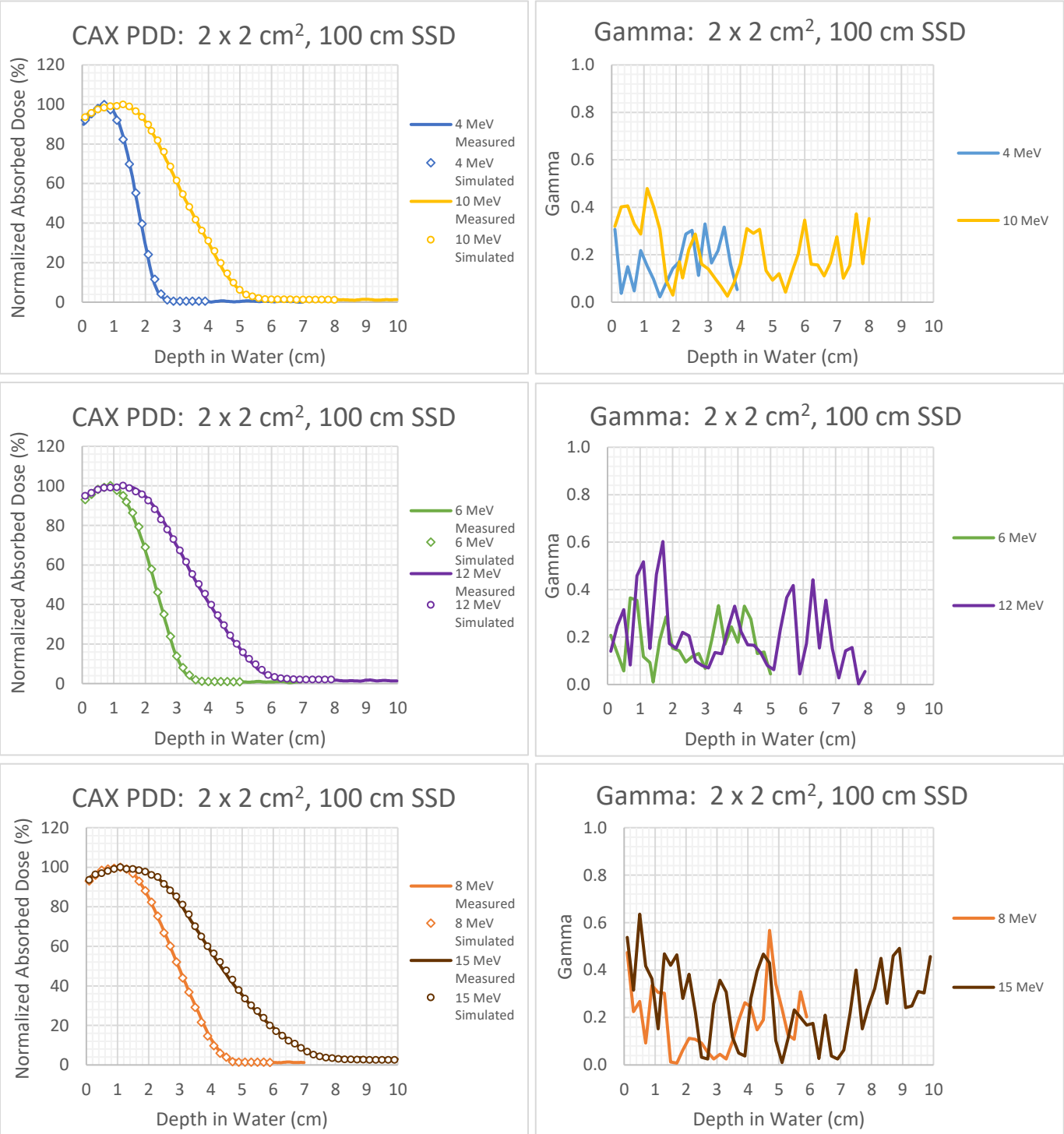

Figure 4-25: CAX PDDs (left sides) at 100 cm SSD for a 2 x 2 cm² field size and for electron nominal energies of 4-15 MeV. The associated Gamma analysis for each measured-simulated curve is indicated on the right side with a criterion of 2%/2mm.

4.5.2.2 3 x 3 cm²

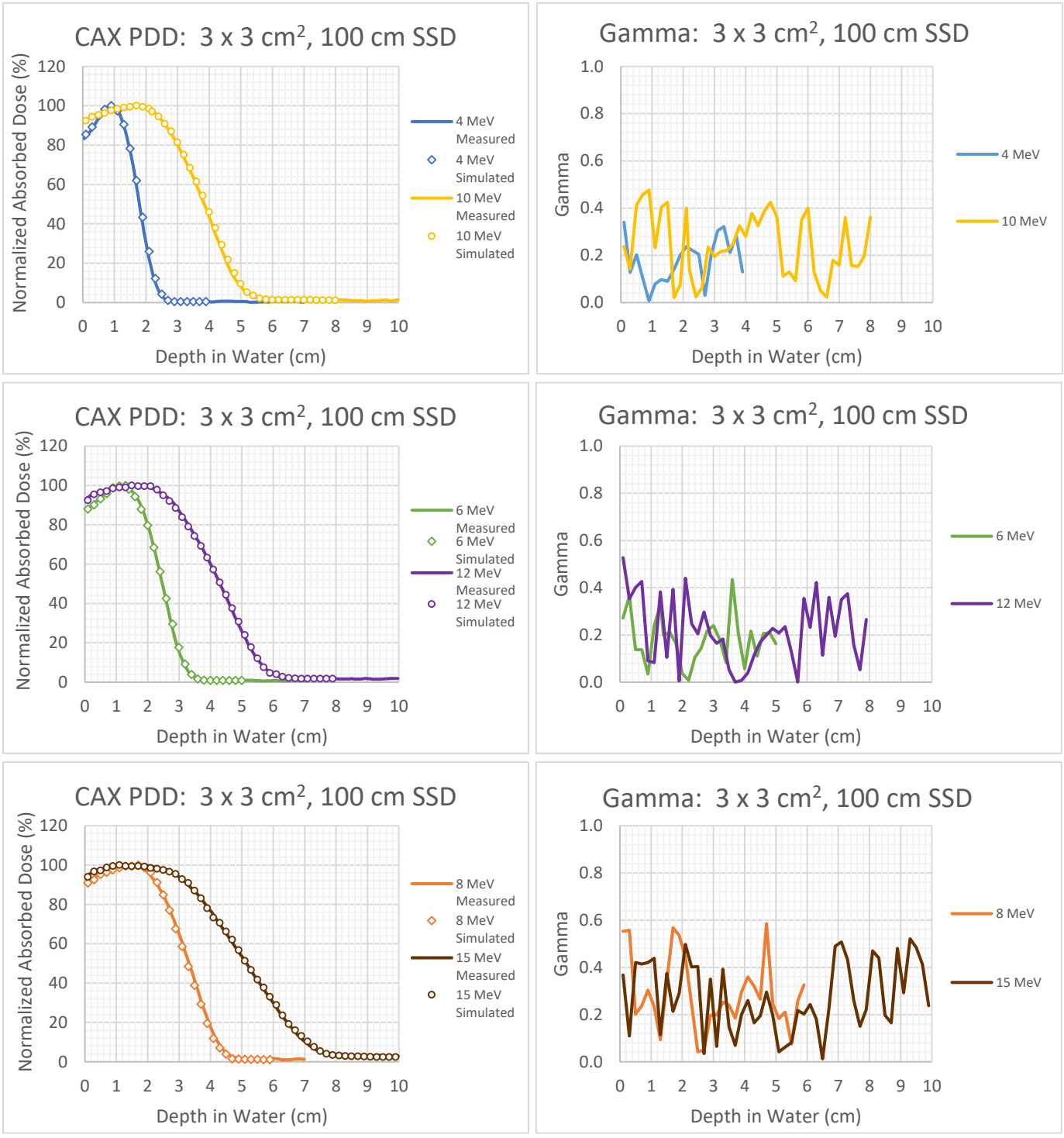

Figure 4-26: CAX PDDs (left sides) at 100 cm SSD for a 3 x 3 cm² field size and for electron nominal energies of 4-15 MeV. The associated Gamma analysis for each measured-simulated curve is indicated on the right side with a criterion of 2%/2mm.

4.5.2.3 6 x 6 cm²

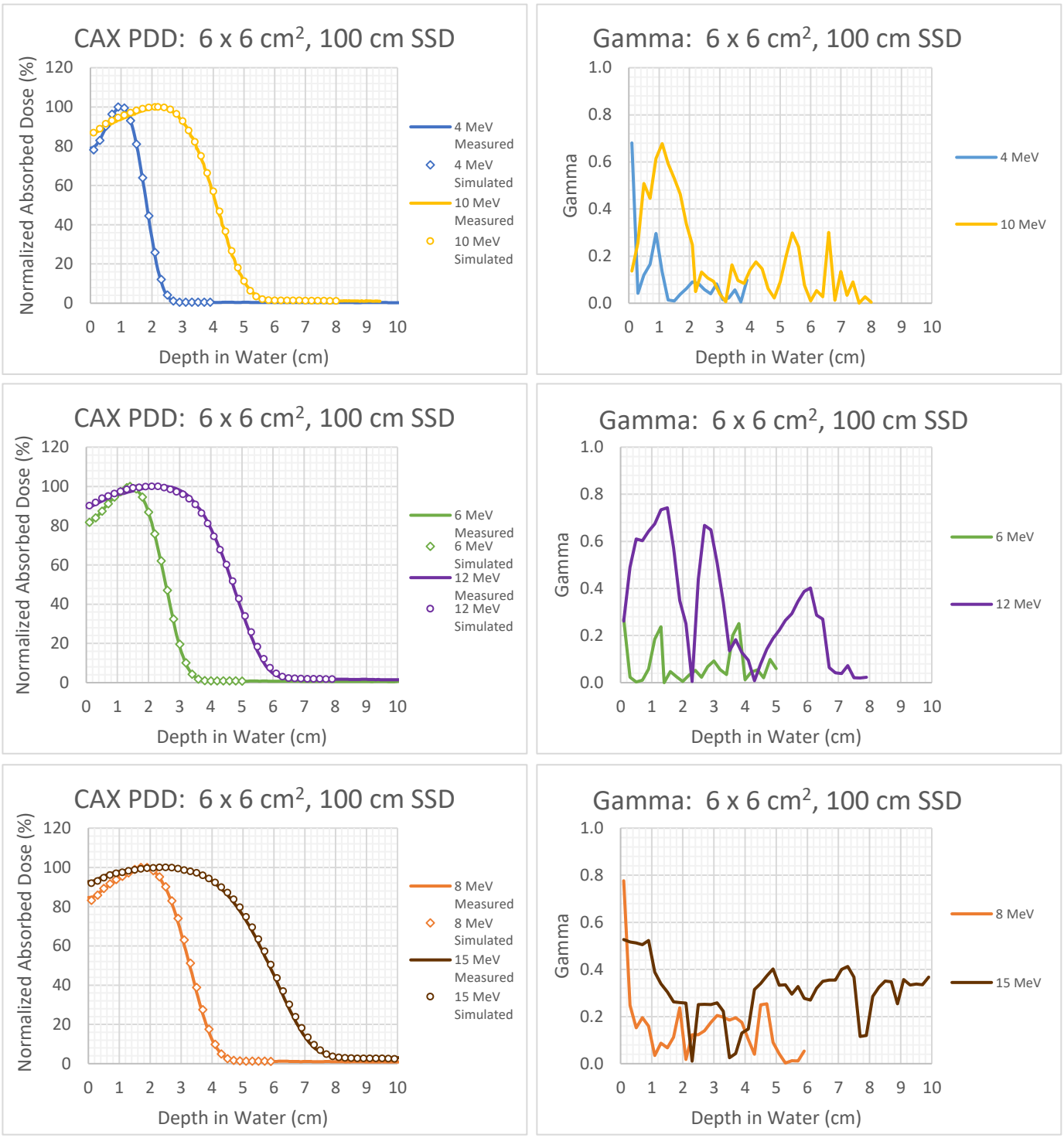

Figure 4-27: CAX PDDs (left sides) at 100 cm SSD for a 6 x 6 cm² field size and for electron nominal energies of 4-15 MeV. The associated Gamma analysis for each measured-simulated curve is indicated on the right side with a criterion of 2%/2mm.

4.5.2.4 6 x 10 cm^2

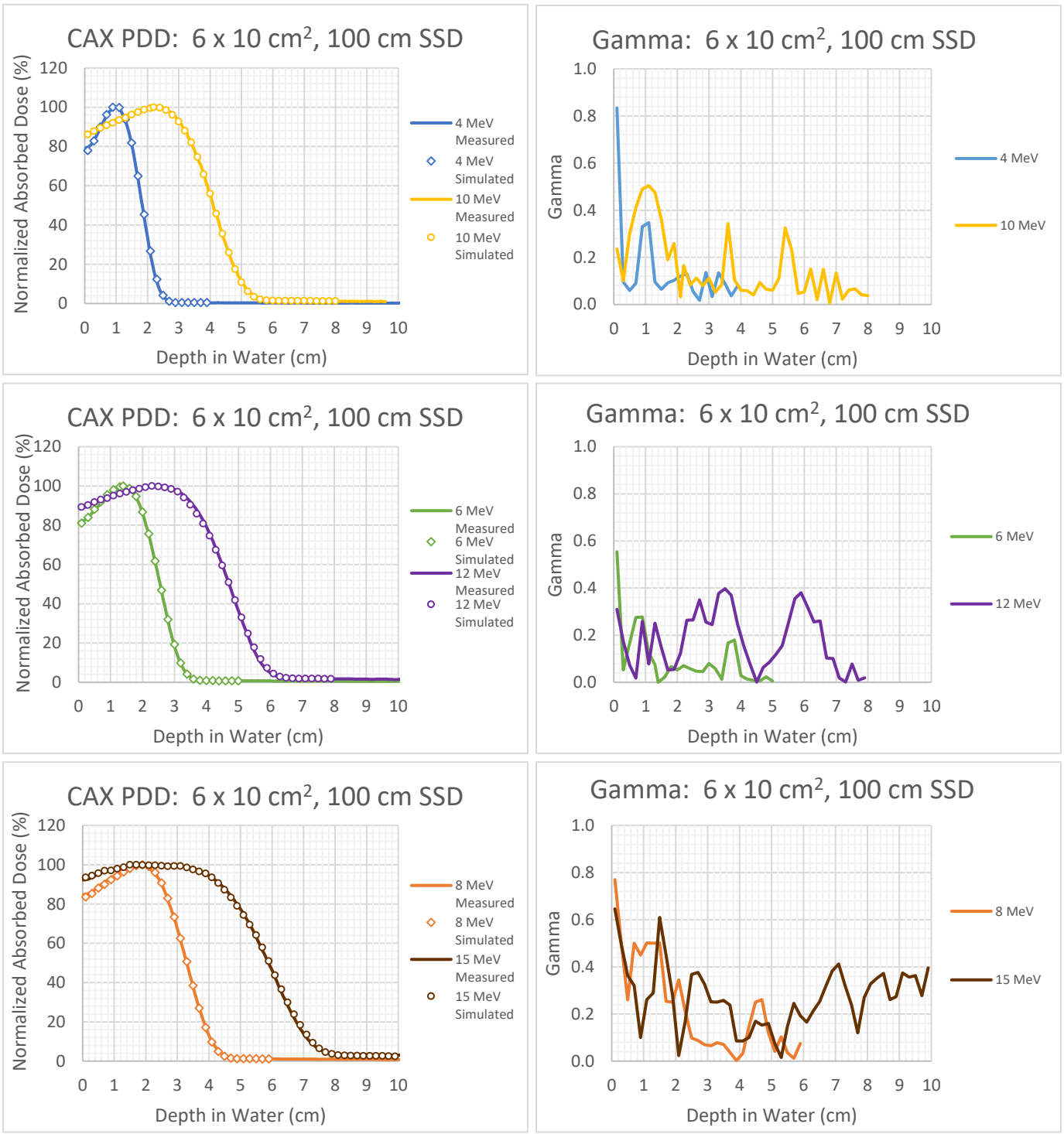

Figure 4-28: CAX PDDs (left sides) at 100 cm SSD for a 6 x 10 cm^2 field size and for electron nominal energies of 4-15 MeV. The associated Gamma analysis for each measured-simulated curve is indicated on the right side with a criterion of 2%/2mm.

4.5.2.5 6 x 14 cm²

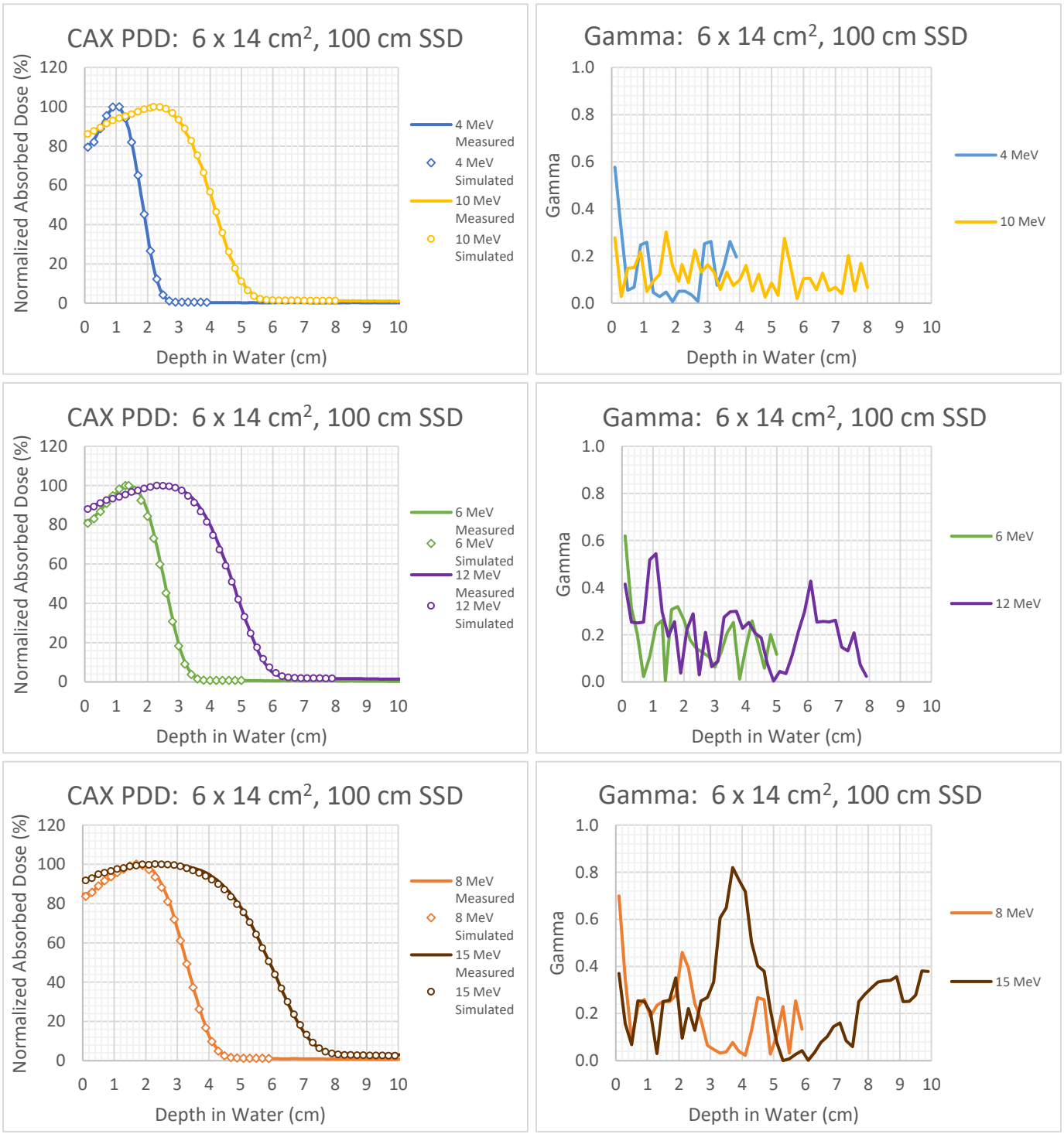

Figure 4-29: CAX PDDs (left sides) at 100 cm SSD for a 6 x 14 cm² field size and for electron nominal energies of 4-15 MeV. The associated Gamma analysis for each measured-simulated curve is indicated on the right side with a criterion of 2%/2mm.

4.5.2.6 8 x 16 cm²

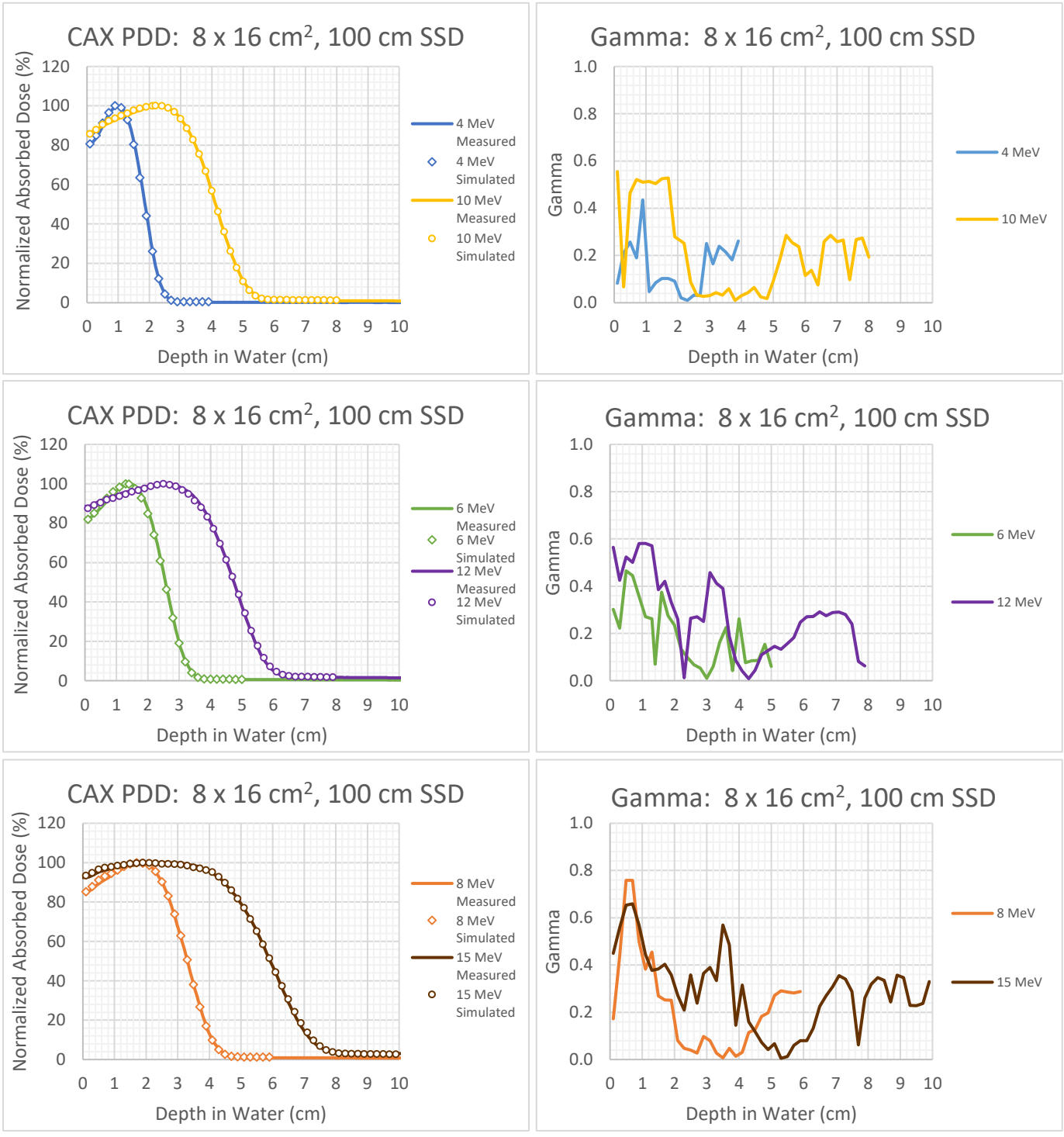

Figure 4-30: CAX PDDs (left sides) at 100 cm SSD for a 8 x 16 cm² field size and for electron nominal energies of 4-15 MeV. The associated Gamma analysis for each measured-simulated curve is indicated on the right side with a criterion of 2%/2mm.

4.5.2.7 10 x 10 cm²

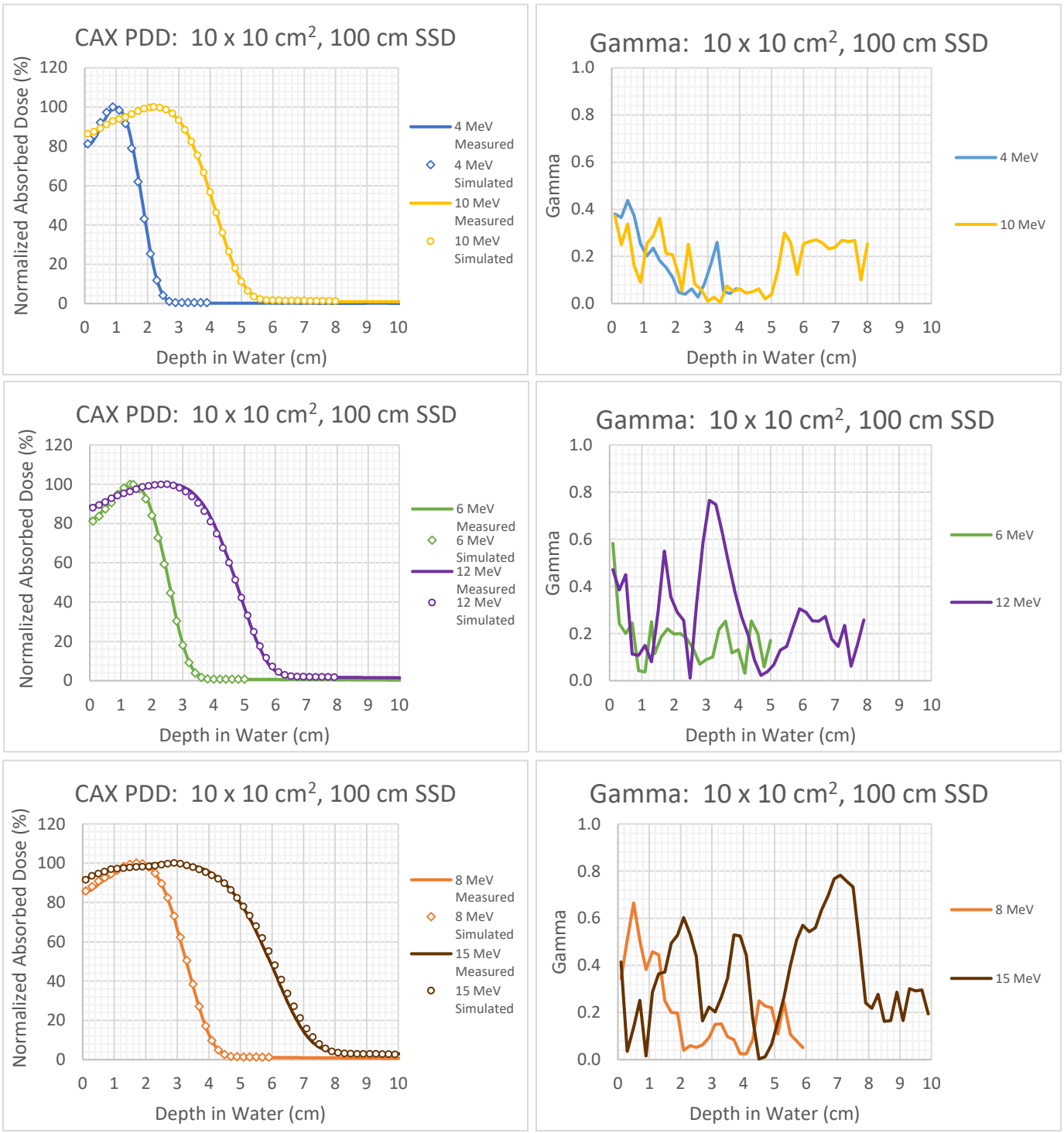

Figure 4-31: CAX PDDs (left sides) at 100 cm SSD for a 10 x 10 cm² field size and for electron nominal energies of 4-15 MeV. The associated Gamma analysis for each measured-simulated curve is indicated on the right side with a criterion of 2%/2mm.

4.5.2.8 10 x 20 cm²

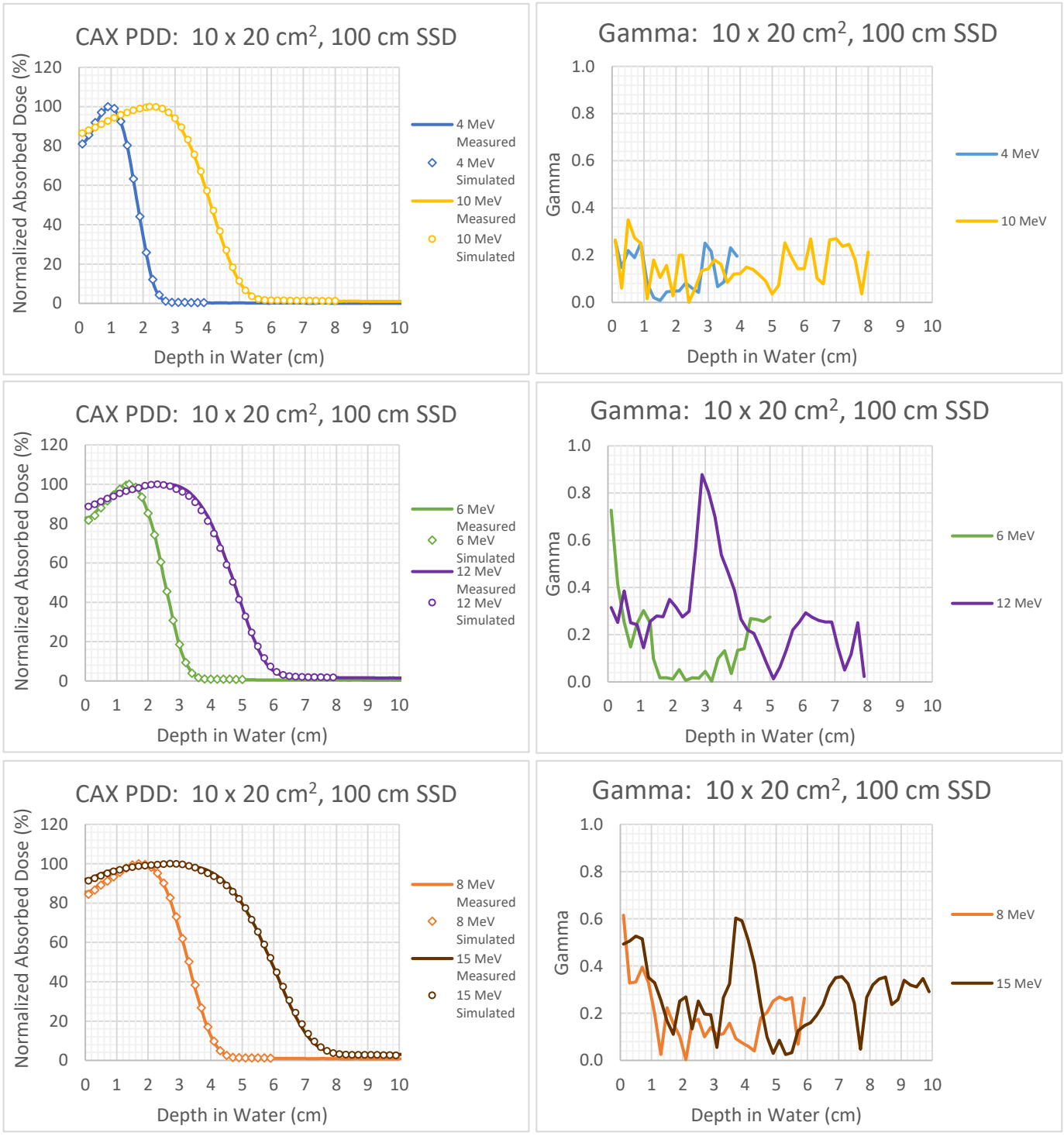

Figure 4-32: CAX PDDs (left sides) at 100 cm SSD for a 10 x 20 cm² field size and for electron nominal energies of 4-15 MeV. The associated Gamma analysis for each measured-simulated curve is indicated on the right side with a criterion of 2%/2mm.

4.5.2.9 14 x 14 cm²

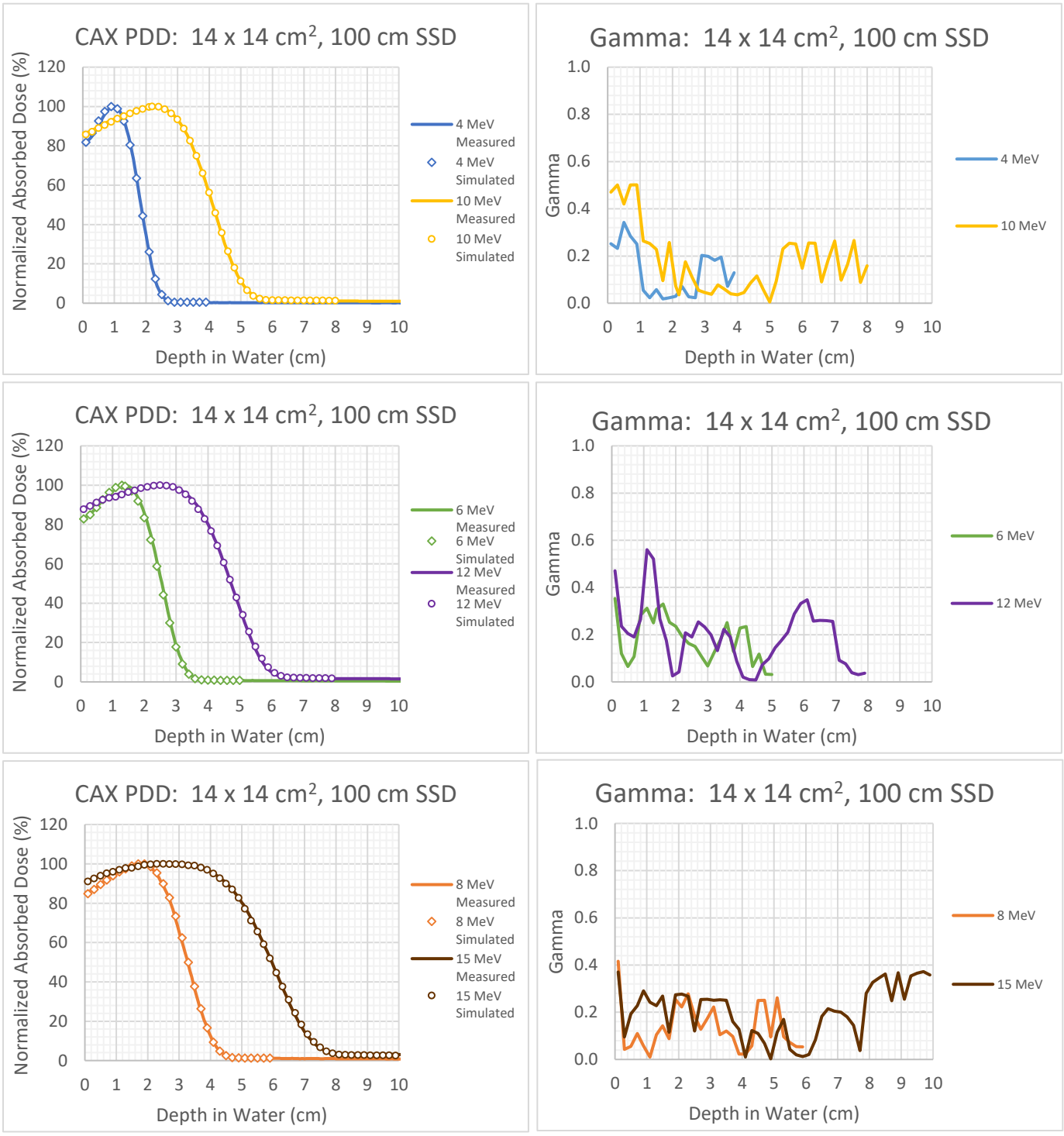

Figure 4-33: CAX PDDs (left sides) at 100 cm SSD for a 14 x 14 cm² field size and for electron nominal energies of 4-15 MeV. The associated Gamma analysis for each measured-simulated curve is indicated on the right side with a criterion of 2%/2mm.

4.5.2.10 20 x 20 cm²

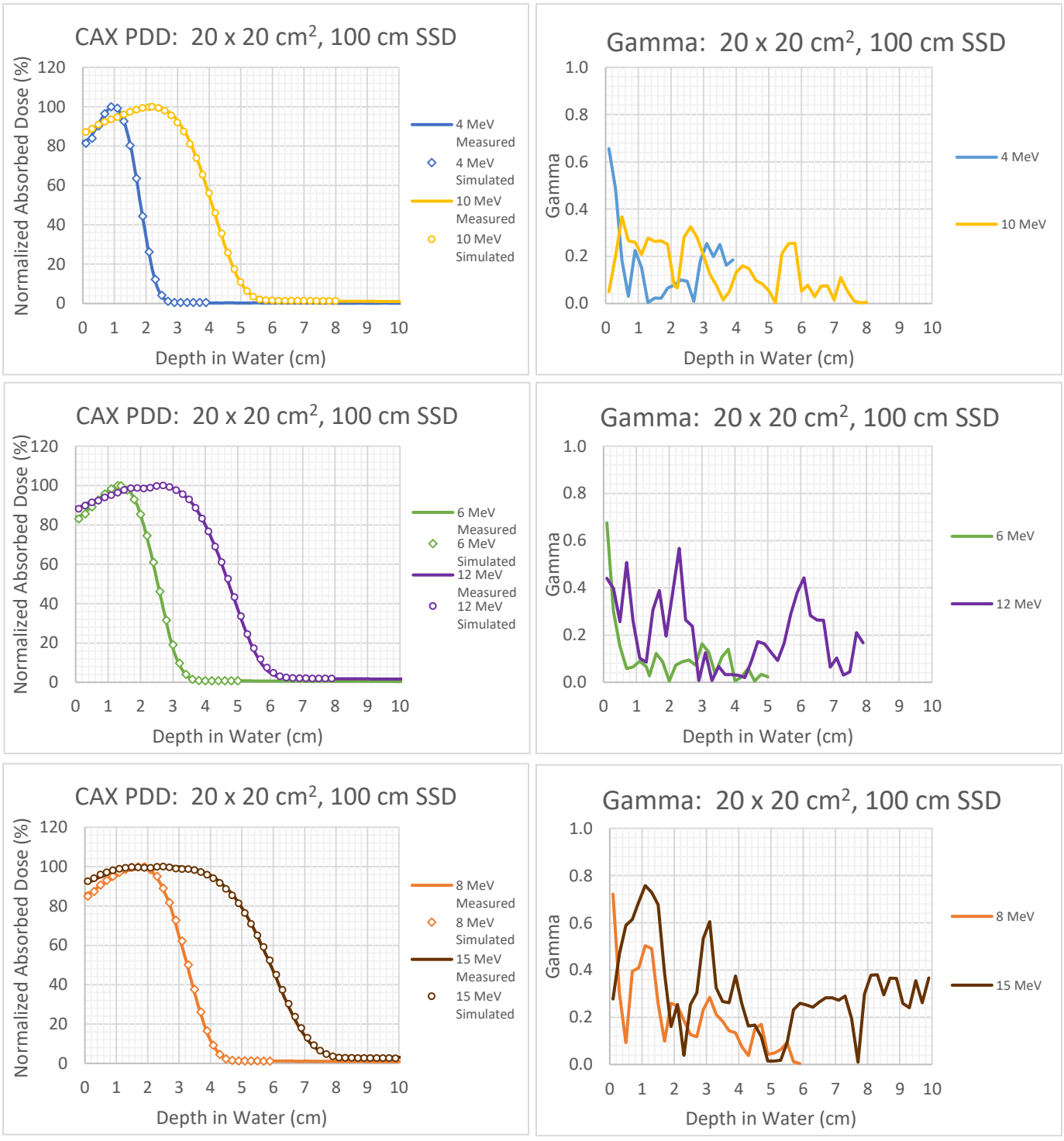

Figure 4-34: CAX PDDs (left sides) at 100 cm SSD for a 20 x 20 cm² field size and for electron nominal energies of 4-15 MeV. The associated Gamma analysis for each measured-simulated curve is indicated on the right side with a criterion of 2%/2mm.

4.5.2.11 4 cm Ø (3.54 x 3.54 cm²)

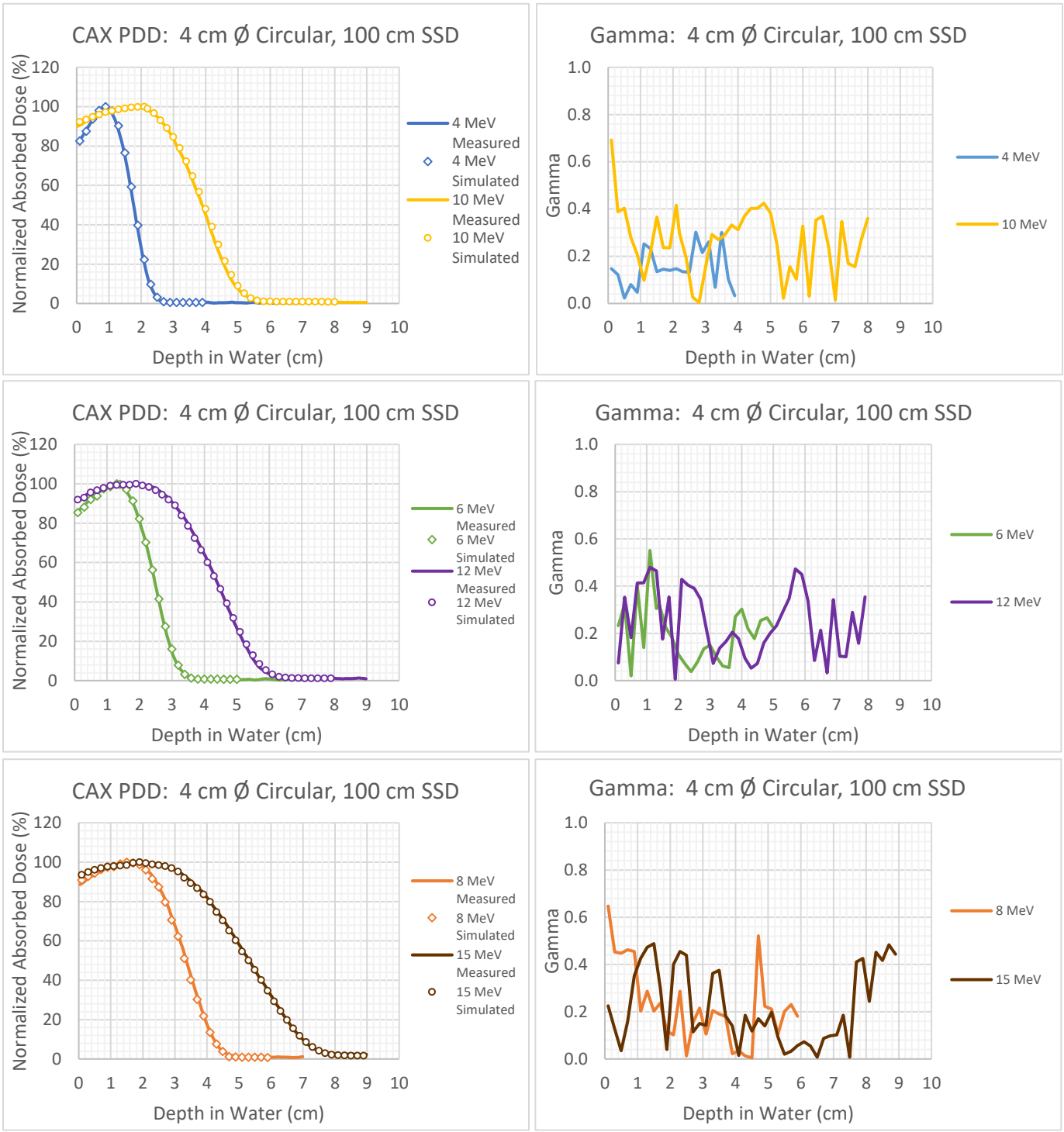

Figure 4-35: CAX PDDs (left sides) at 100 cm SSD for a 4 cm diameter circular field and for electron nominal energies of 4-15 MeV. The associated Gamma analysis for each measured-simulated curve is indicated on the right side with a criterion of 2%/2mm.

4.5.3 1%/1mm Gamma Criterion

Since the developed model produced PDDs with a 100 % pass rate using a 2%/2mm Gamma criterion, the 10 MeV electron beam was retested applying a more stringent 1%/1mm criterion for all fields and SSDs. Under this criterion, the BU region showed an increased sensitivity while the rest of the PDD remained relatively insensitive. The 2%/2mm pass rates dropped from 100% for both the 95cm and 100 cm SSDs to a minimum 1%/1mm pass rate of 75.61 % and 82.93 %, respectively, including the BU region. Most of the failed points occurred within the BU region (depth < 2.2 cm). The combined pass rate for the 1%/1mm criterion for all fields was 90.91 % for 95 cm SSD and 96.23 % for 100 cm SSD, hence the model was able to produce more accurate results at 100 cm SSD, except for the 8 x 16 cm^2 and 14 x 14 cm^2 fields.

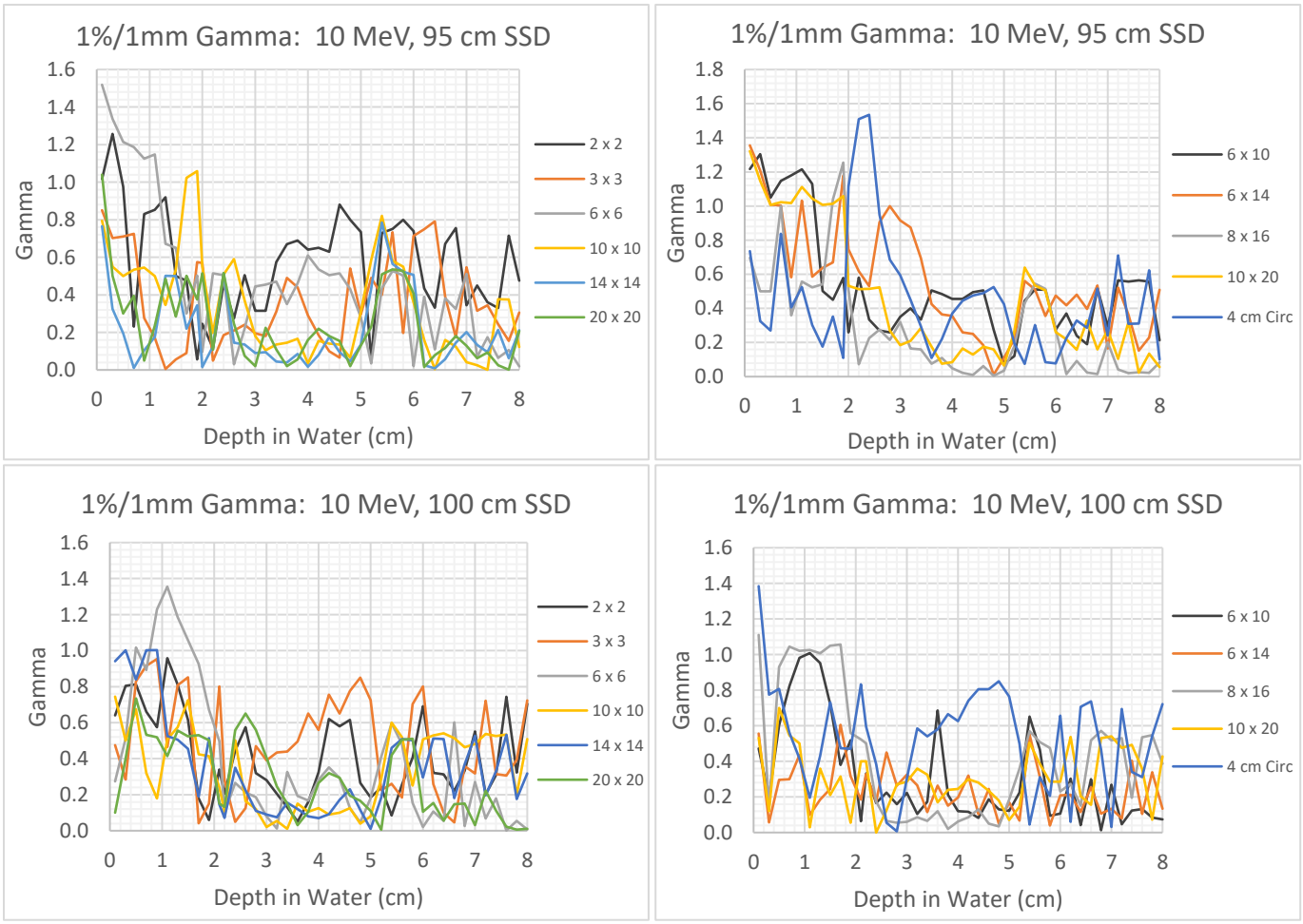

Figure 4-36: Gamma analysis results applying a 1%/1mm criterion to the 10 MeV electron beam for all field sizes at 95 cm (top graphs) and 100 cm (bottom curves) SSD.

4.6 Profiles

Crossline and inline off-axis profiles at 95 cm SSD are shown in Figure 4-37 - Figure 4-54. Profiles at this SSD were simulated with a pass rate of nearly 100 % using a 2%/2mm criterion, where failed points were attributed to simulation noise in regions of low dose gradients. Crossline and inline profiles at 100 cm SSD are shown in Figure 4-55 - Figure 4-72, where these profiles were also simulated with a pass rate of nearly 100 % using a 2%/2mm criterion. Noticeable from both the results at 95 cm SSD and 100 cm SSD is the overall improved fit of smaller fields. For these fields, the skindepth_for_BCA parameter was increased from the default value of 3 to 50 mean free paths in both `BEAMnrc` and `DOSXYZnrc` simulations, which effectively forces single scattering mode to occur further away from boundaries.[12] Though this increases simulation time in `BEAMnrc` and `DOSXYZnrc`, the number of voxels used for smaller fields are less than for larger fields, which means that a lower number of histories were required for a 1% statistical uncertainty. Another observation was the influence of beveled open field inserts. Initially open field inserts were not modelled with a bevel which produced simulated profiles with a dose overestimation in the shoulder regions. This was quickly rectified by modelling each insert with a bevel, which effectively narrows the top of the open field insert by 3 mm.

All profiles were measured and simulated at the depth of maximum dose, which was 0.9 cm, 1.4 cm, 1.7 cm, 2.2 cm, 2.4 cm and 2.9 cm for electron nominal energies of 4-, 6-, 8-, 10-, 12- and 15 MeV. Though the depth of maximum dose changes for small fields (see Figure 4-14, Figure 4-15, Figure 4-24, Figure 4-25, Figure 4-26 and Figure 4-35), especially for higher electron energies, both simulated and measured small field profiles were performed at the same depth of maximum dose as for the larger fields.

4.6.1 95 cm SSD

4.6.1.1 4 MeV

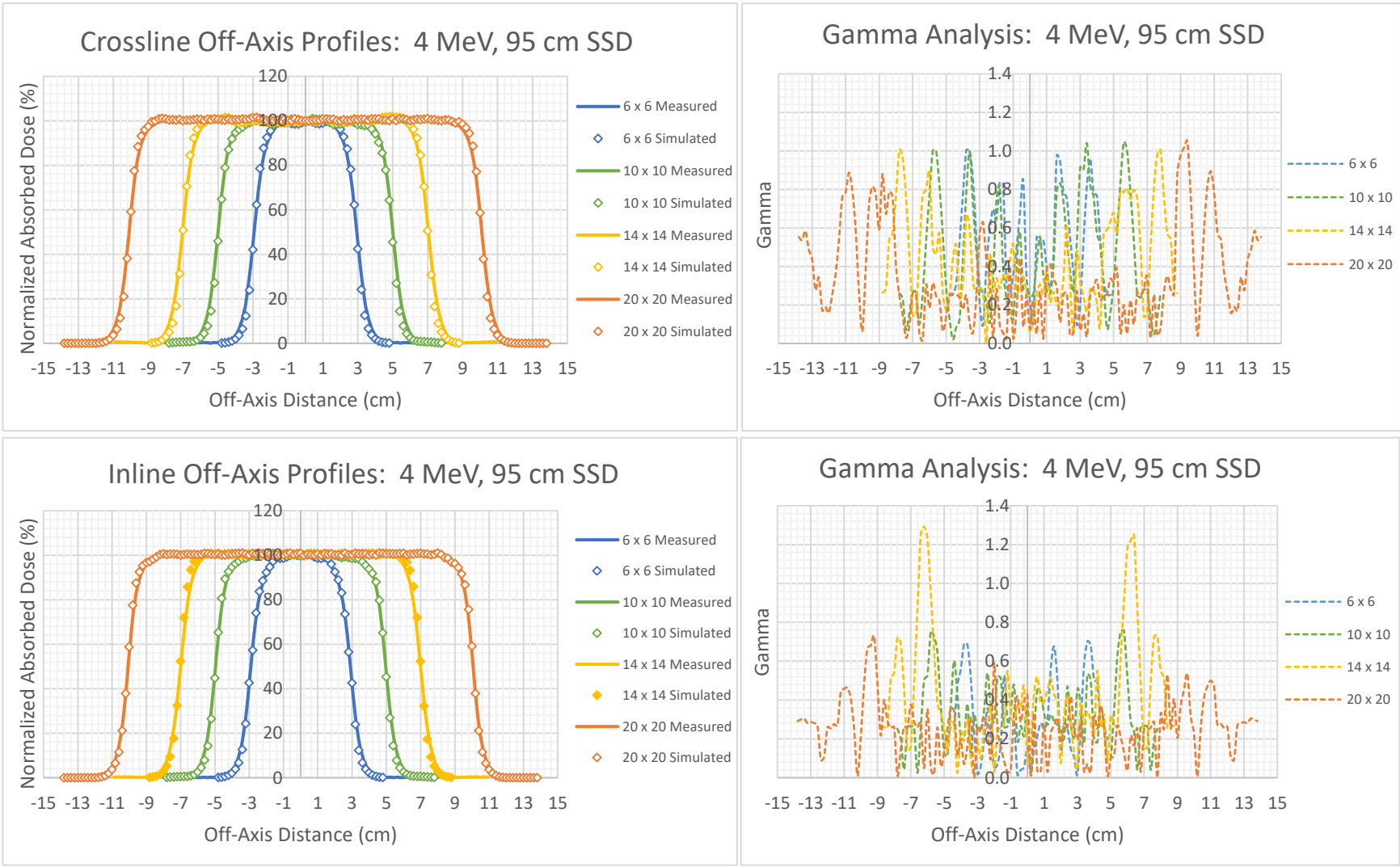

Figure 4-37: 4 MeV Crossline (top left) and Inline (bottom left) off-axis profiles for square field sizes measured and simulated at 95 cm SSD. The respective Gamma analysis for each curve is indicated on the right side with a tolerance criterion of 2%/2mm.

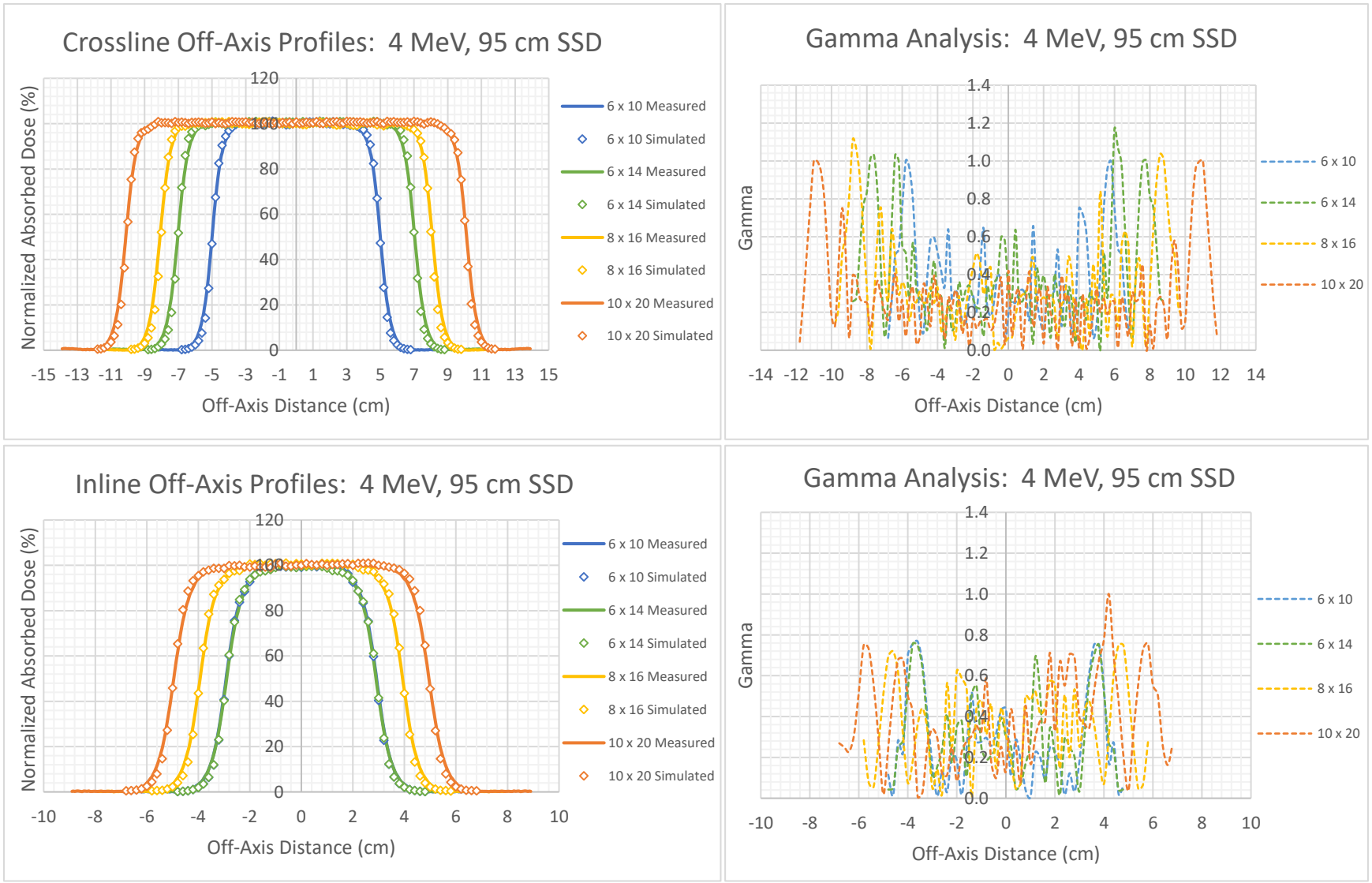

Figure 4-38: 4 MeV Crossline (top left) and Inline (bottom left) off-axis profiles for rectangular field sizes measured and simulated at 95 cm SSD. The respective Gamma analysis for each curve is indicated on the right side with a tolerance criterion of 2%/2mm.

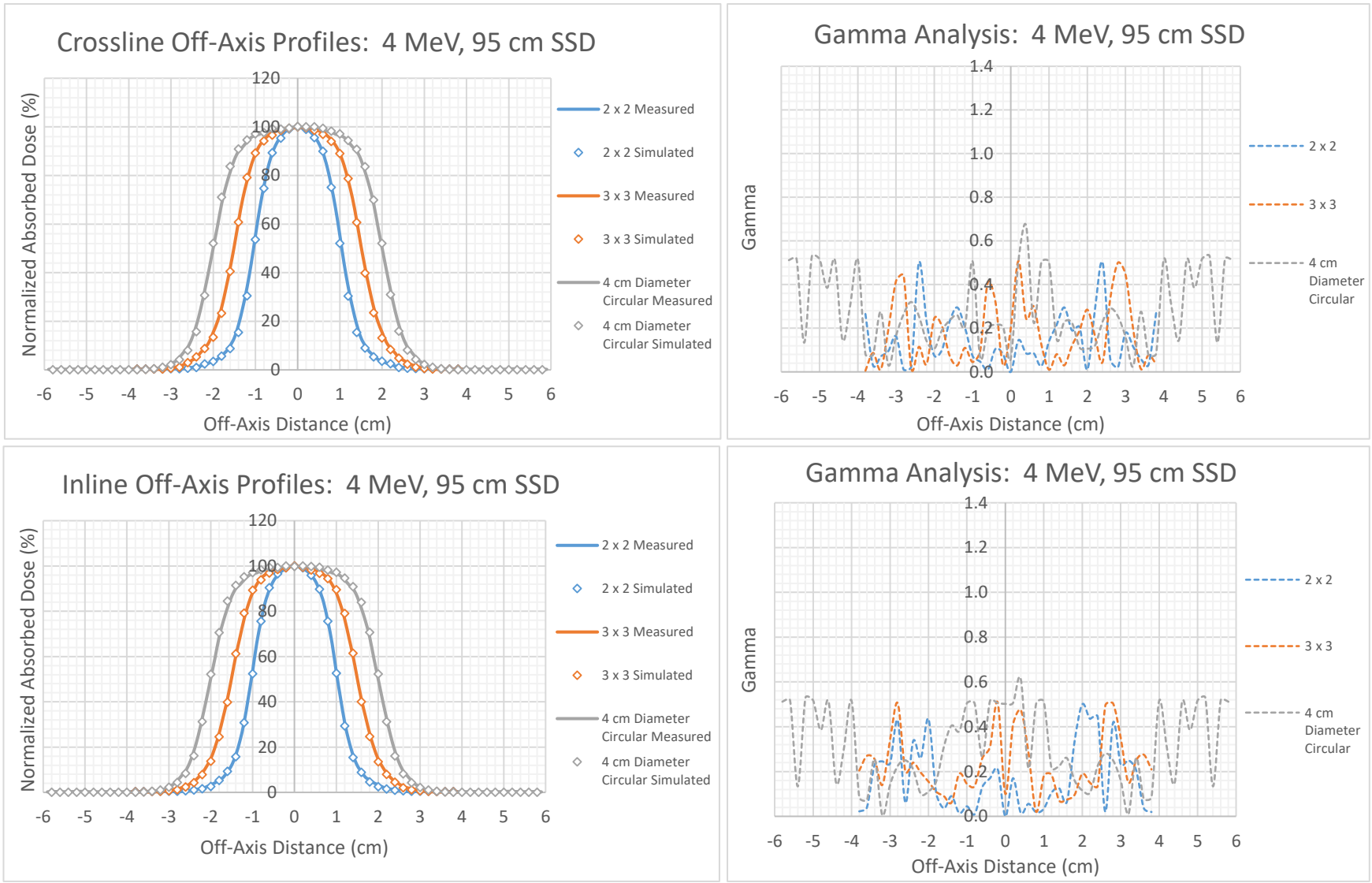

Figure 4-39: 4 MeV Crossline (top left) and Inline (bottom left) off-axis profiles for small field sizes measured and simulated at 95 cm SSD. The respective Gamma analysis for each curve is indicated on the right side with a tolerance criterion of 2%/2mm.

4.6.1.2 6 MeV

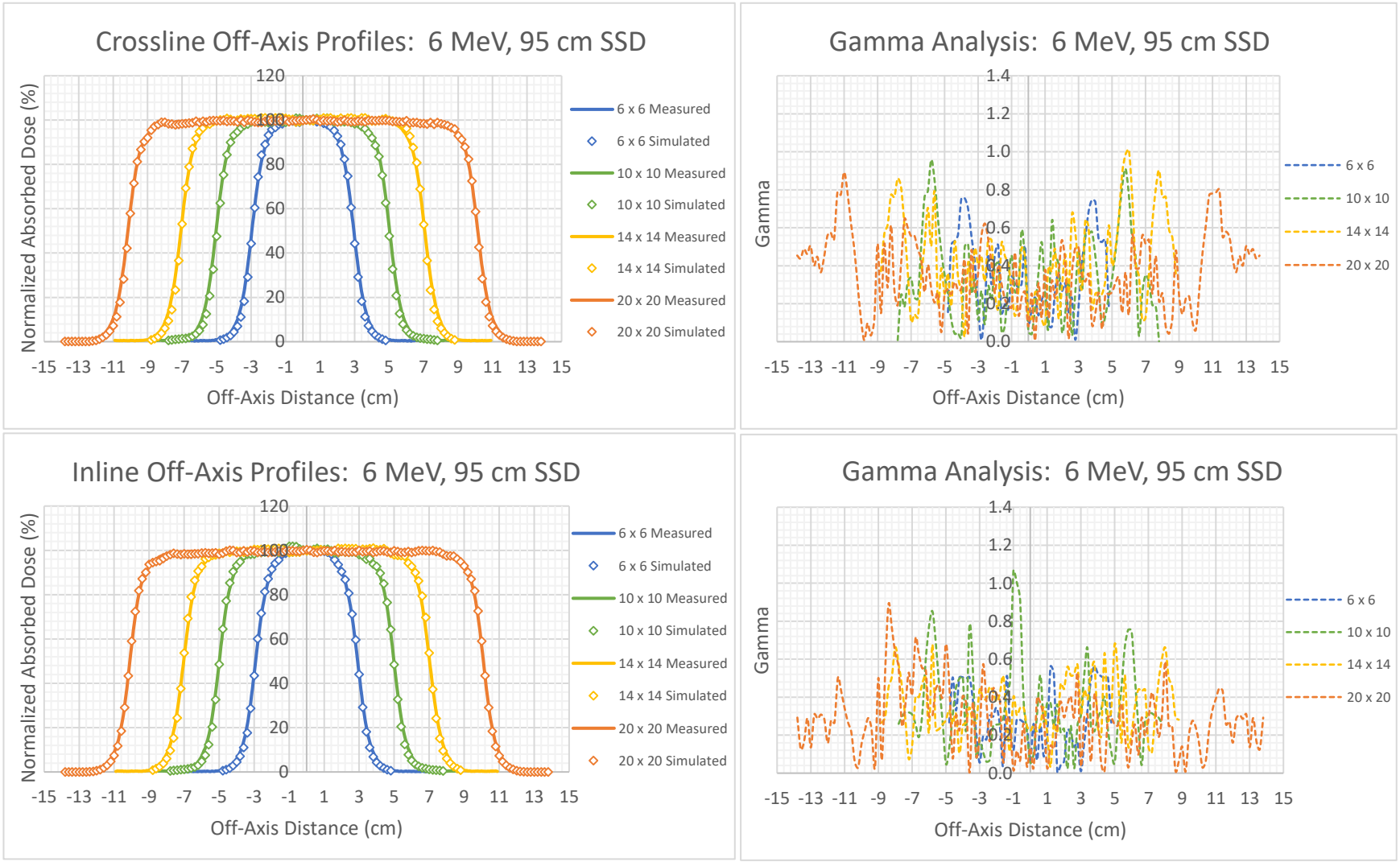

Figure 4-40: 6 MeV Crossline (top left) and Inline (bottom left) off-axis profiles for square field sizes measured and simulated at 95 cm SSD. The respective Gamma analysis for each curve is indicated on the right side with a tolerance criterion of 2%/2mm.

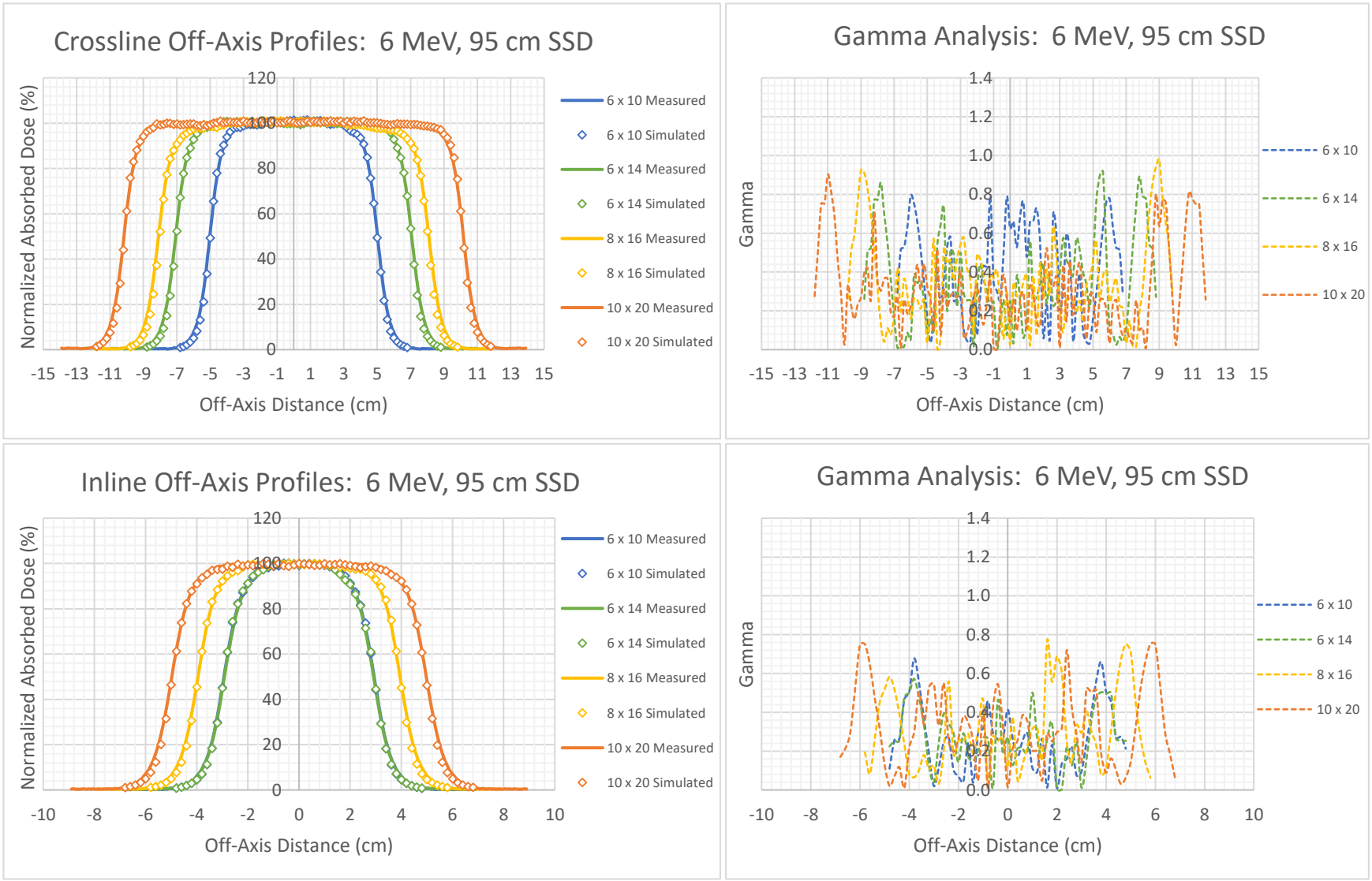

Figure 4-41: 6 MeV Crossline (top left) and Inline (bottom left) off-axis profiles for rectangular field sizes measured and simulated at 95 cm SSD. The respective Gamma analysis for each curve is indicated on the right side with a tolerance criterion of 2%/2mm.

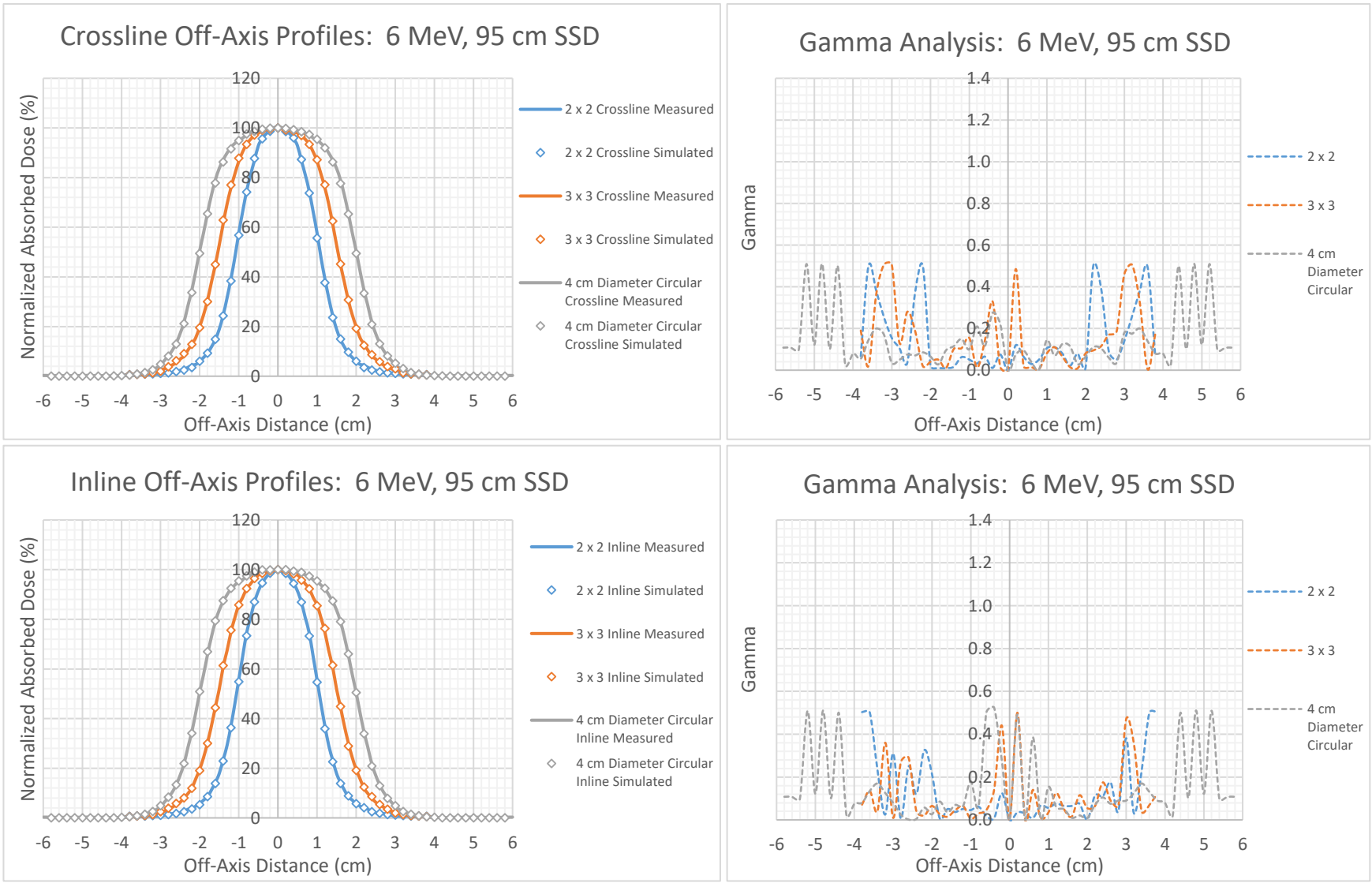

Figure 4-42: 6 MeV Crossline (top left) and Inline (bottom left) off-axis profiles for small field sizes measured and simulated at 95 cm SSD. The respective Gamma analysis for each curve is indicated on the right side with a tolerance criterion of 2%/2mm.

4.6.1.3 8 MeV

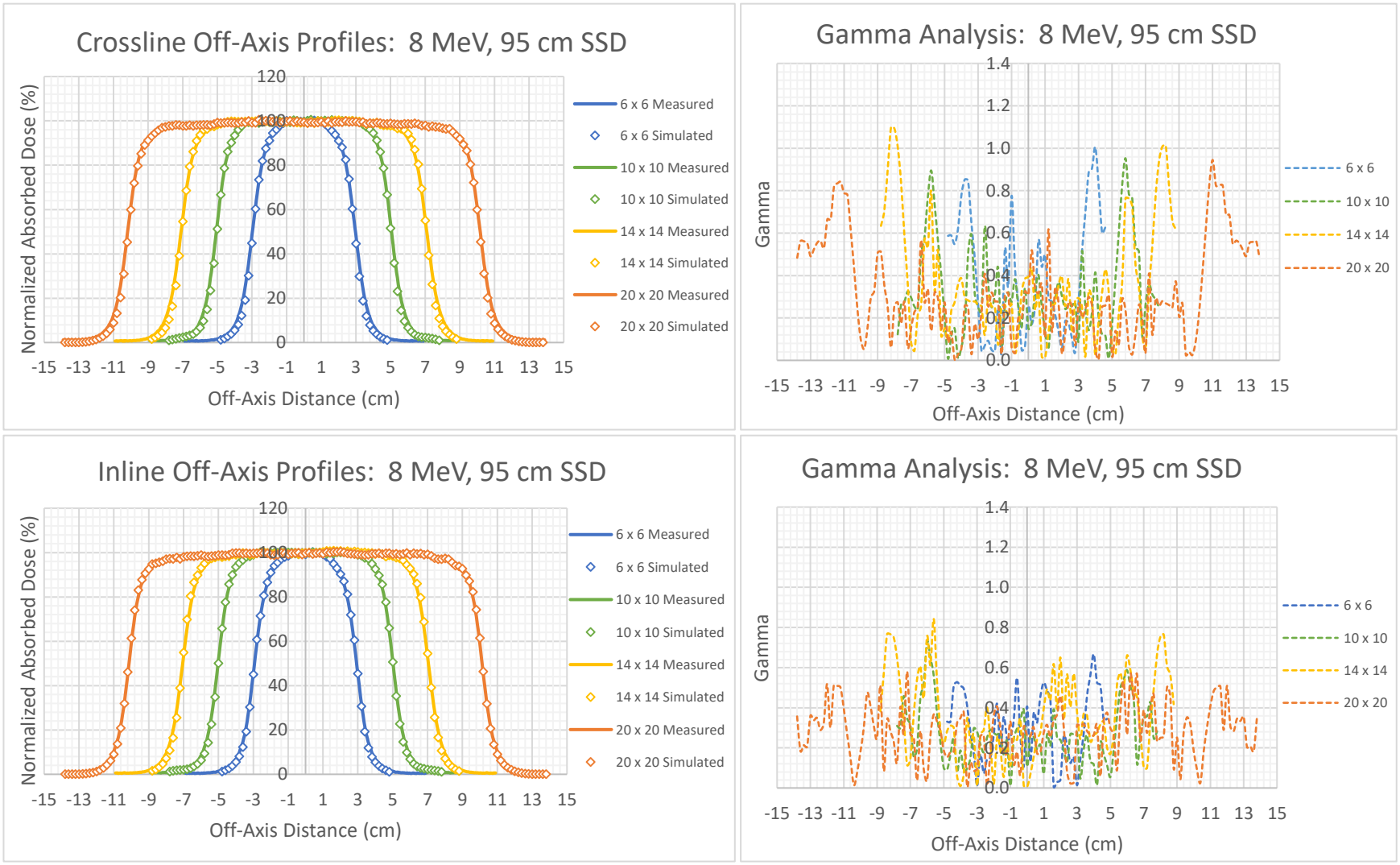

Figure 4-43: 8 MeV Crossline (top left) and Inline (bottom left) off-axis profiles for square field sizes measured and simulated at 95 cm SSD. The respective Gamma analysis for each curve is indicated on the right side with a tolerance criterion of 2%/2mm.

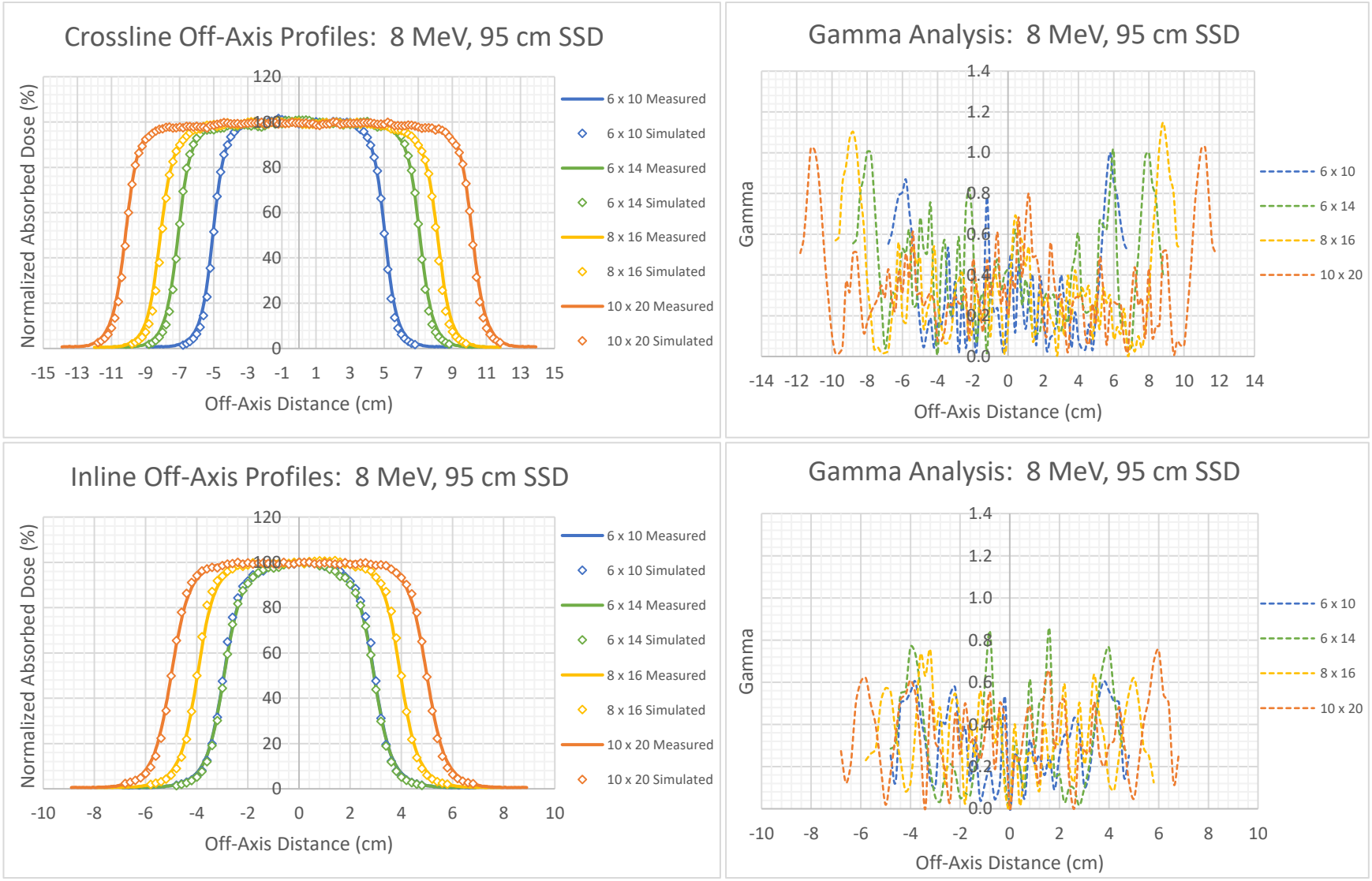

Figure 4-44: 8 MeV Crossline (top left) and Inline (bottom left) off-axis profiles for rectangular field sizes measured and simulated at 95 cm SSD. The respective Gamma analysis for each curve is indicated on the right side with a tolerance criterion of 2%/2mm.

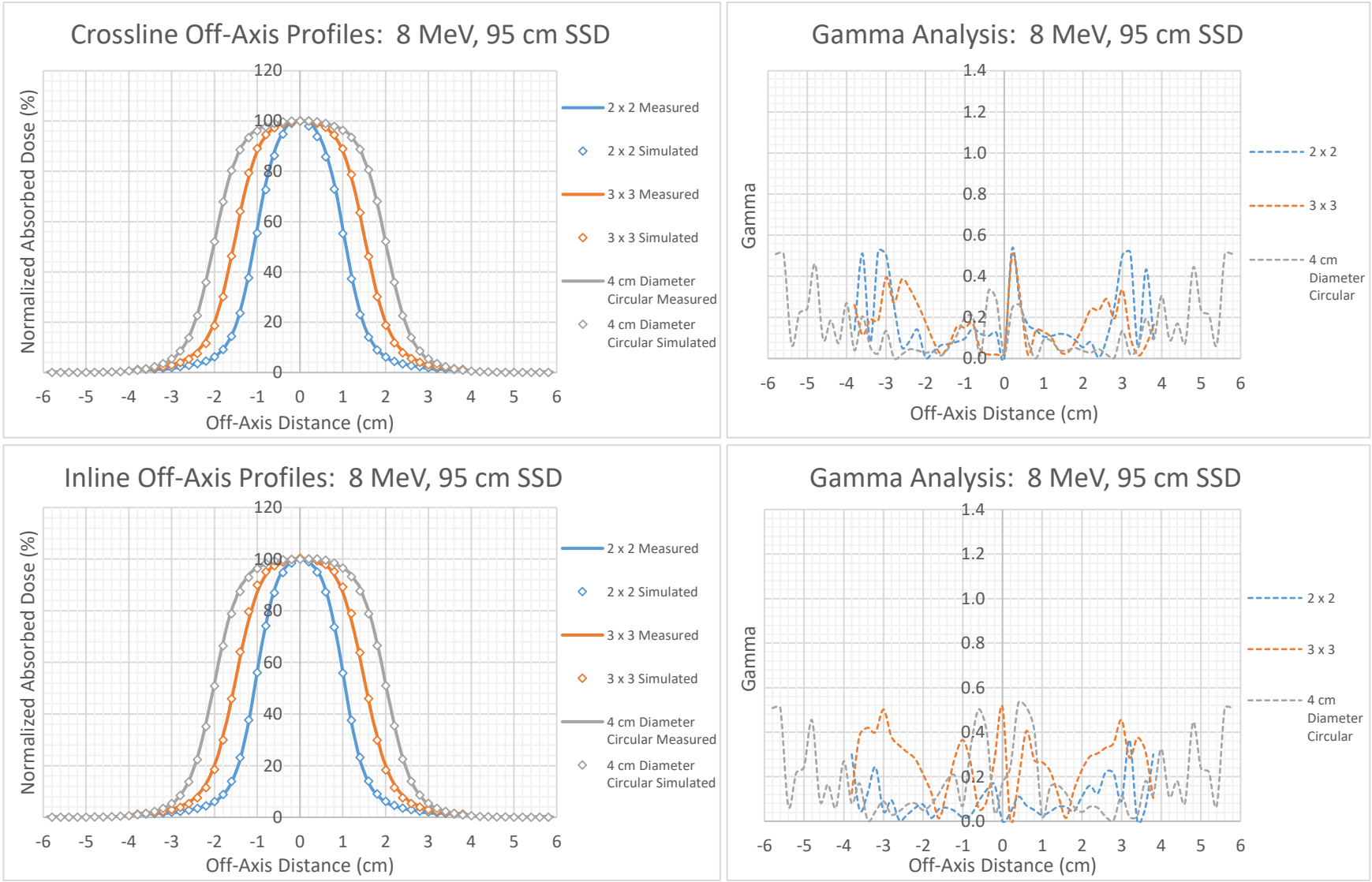

Figure 4-45: 8 MeV Crossline (top left) and Inline (bottom left) off-axis profiles for small field sizes measured and simulated at 95 cm SSD. The respective Gamma analysis for each curve is indicated on the right side with a tolerance criterion of 2%/2mm.

4.6.1.4 10 MeV

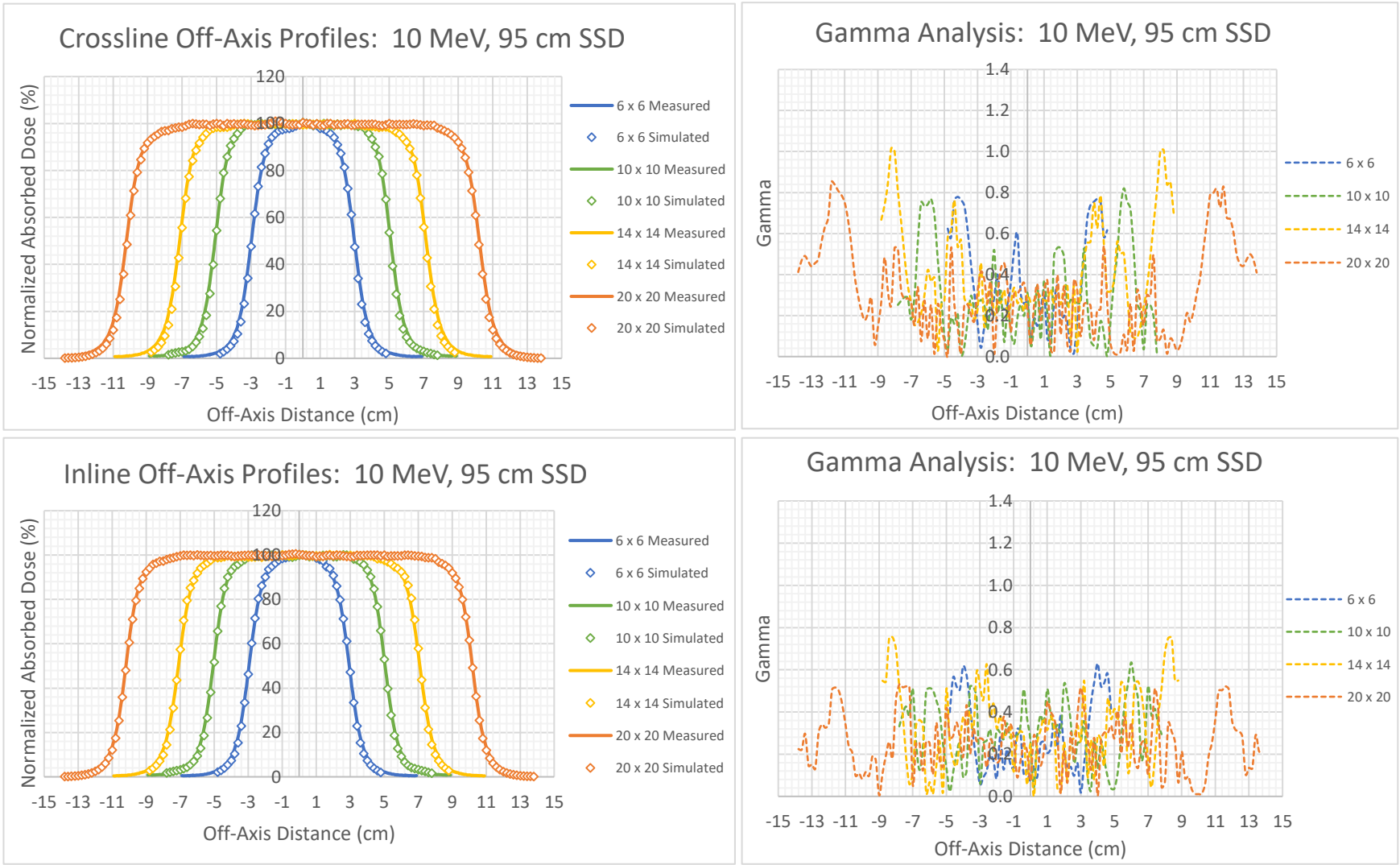

Figure 4-46: 10 MeV Crossline (top left) and Inline (bottom left) off-axis profiles for square field sizes measured and simulated at 95 cm SSD. The respective Gamma analysis for each curve is indicated on the right side with a tolerance criterion of 2%/2mm.

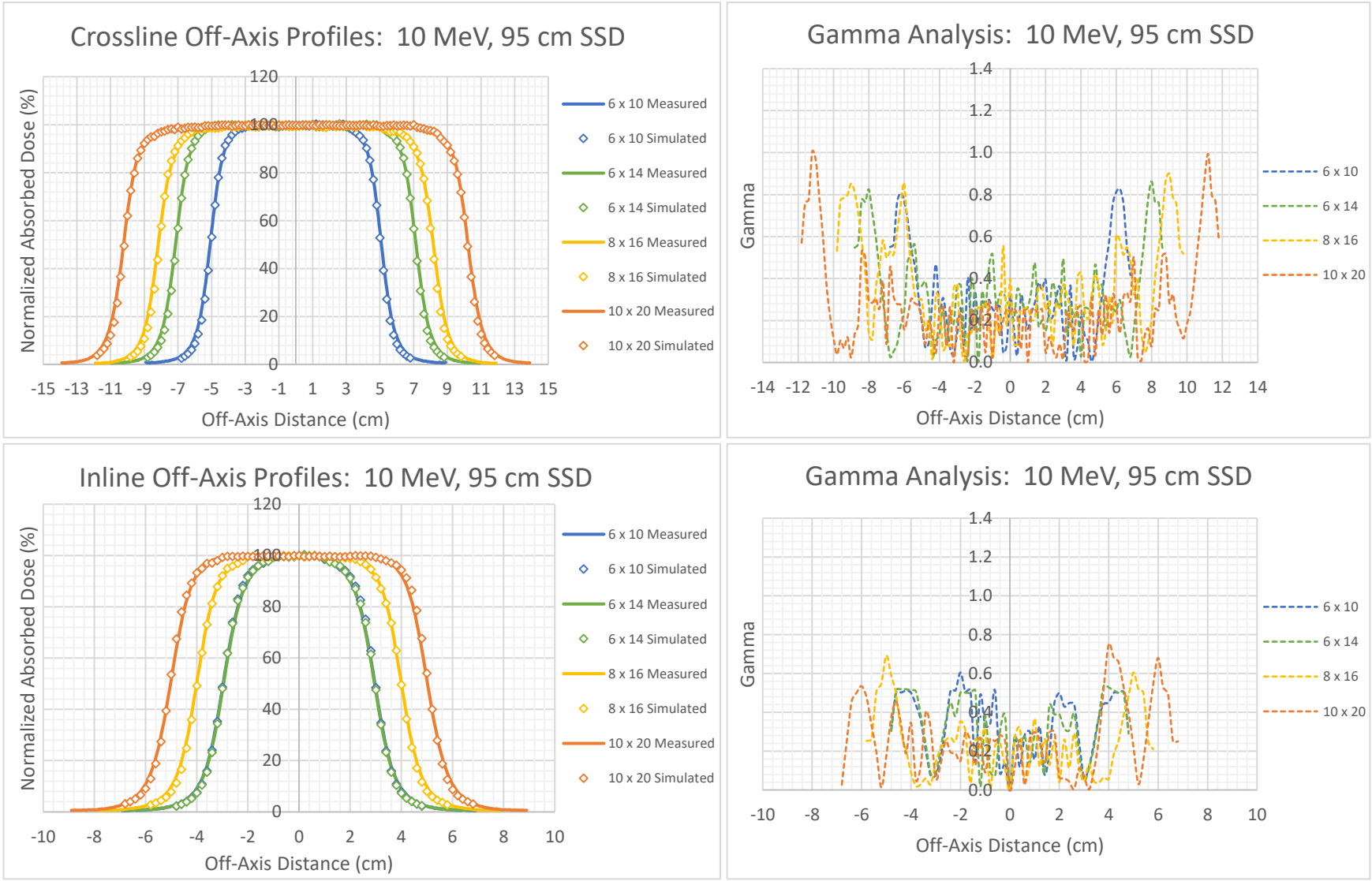

Figure 4-47: 10 MeV Crossline (top left) and Inline (bottom left) off-axis profiles for rectangular field sizes measured and simulated at 95 cm SSD. The respective Gamma analysis for each curve is indicated on the right side with a tolerance criterion of 2%/2mm.

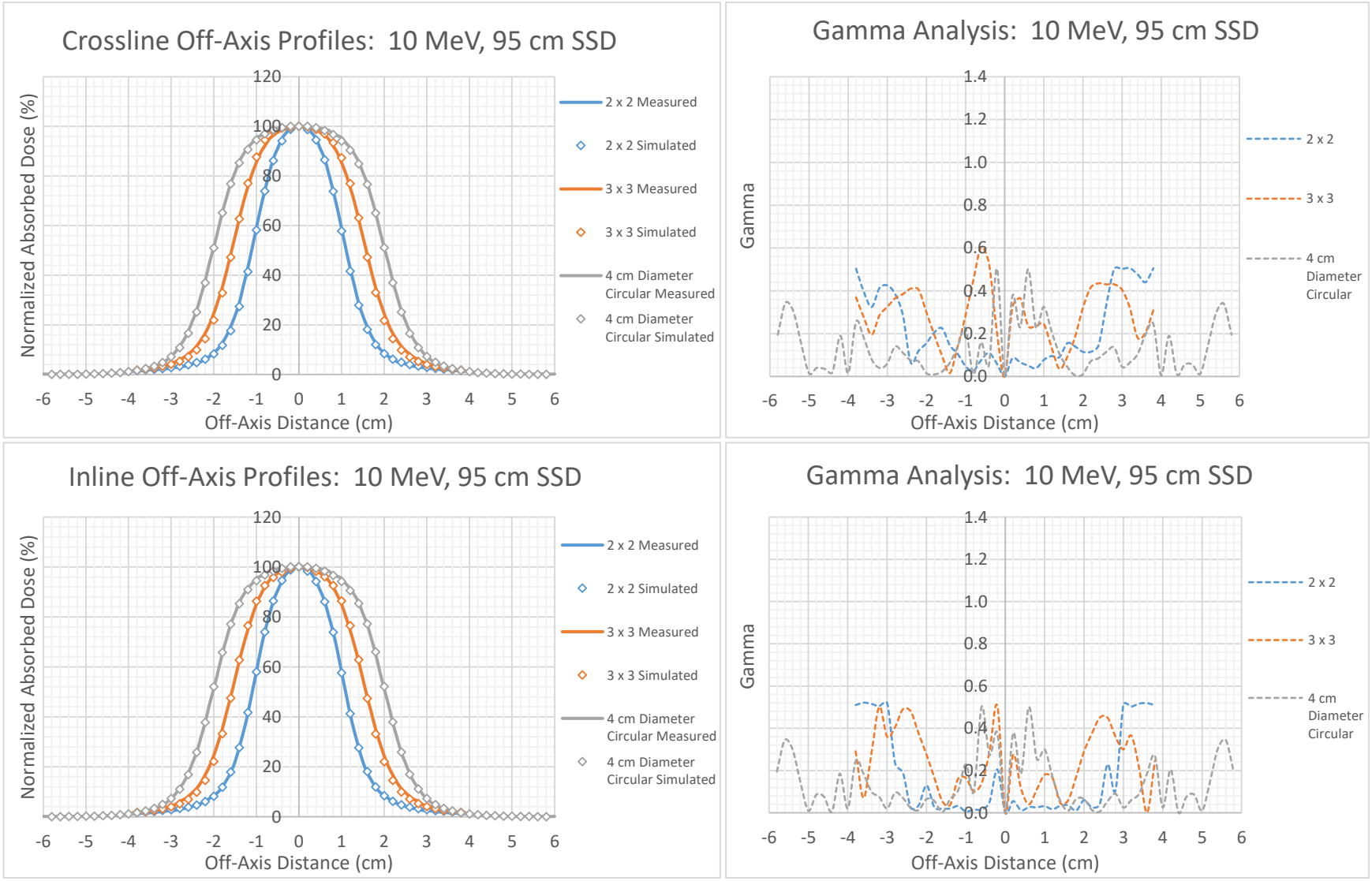

Figure 4-48: 10 MeV Crossline (top left) and Inline (bottom left) off-axis profiles for small field sizes measured and simulated at 95 cm SSD. The respective Gamma analysis for each curve is indicated on the right side with a tolerance criterion of 2%/2mm.

4.6.1.5 12 MeV

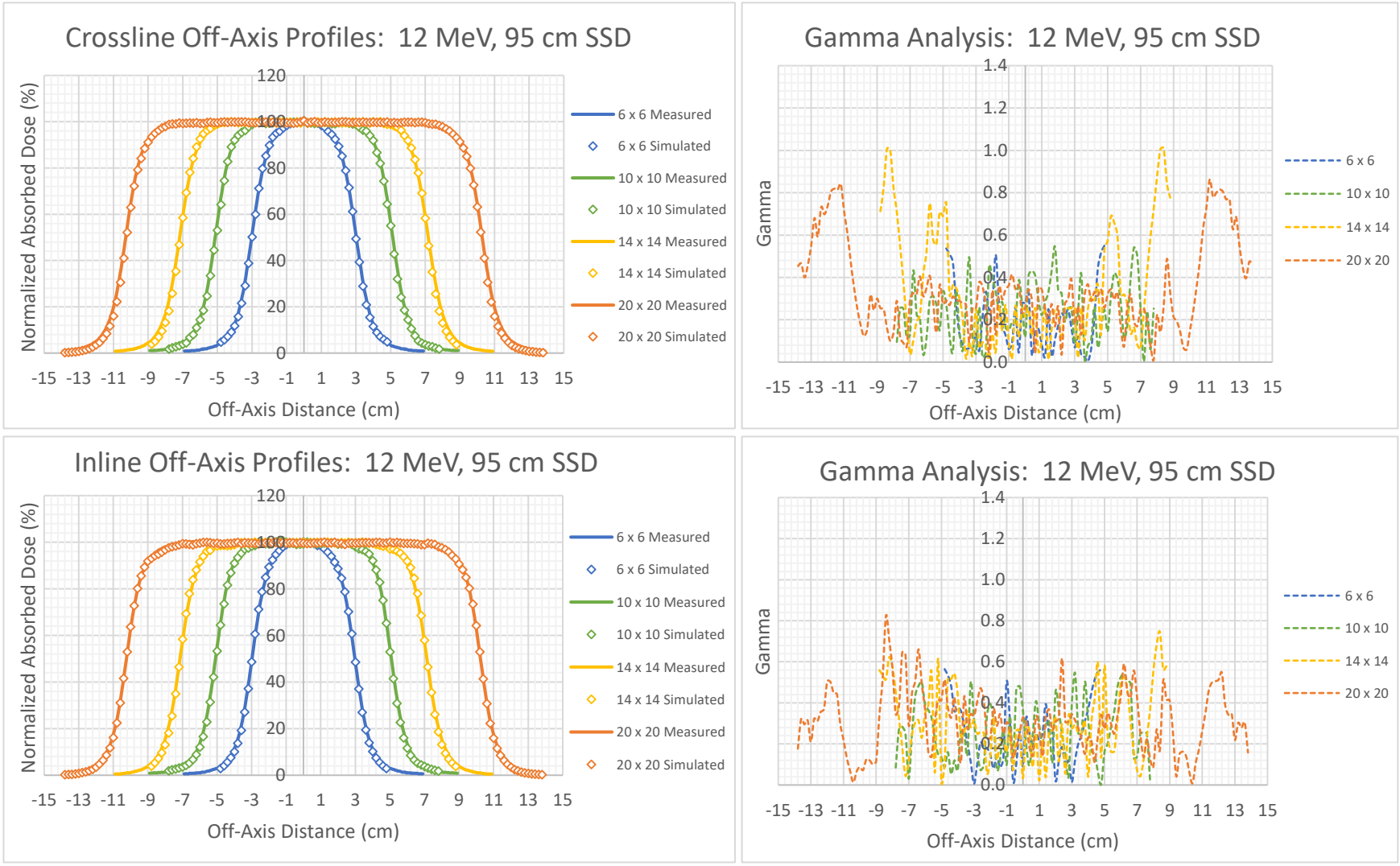

Figure 4-49: 12 MeV Crossline (top left) and Inline (bottom left) off-axis profiles for square field sizes measured and simulated at 95 cm SSD. The respective Gamma analysis for each curve is indicated on the right side with a tolerance criterion of 2%/2mm.

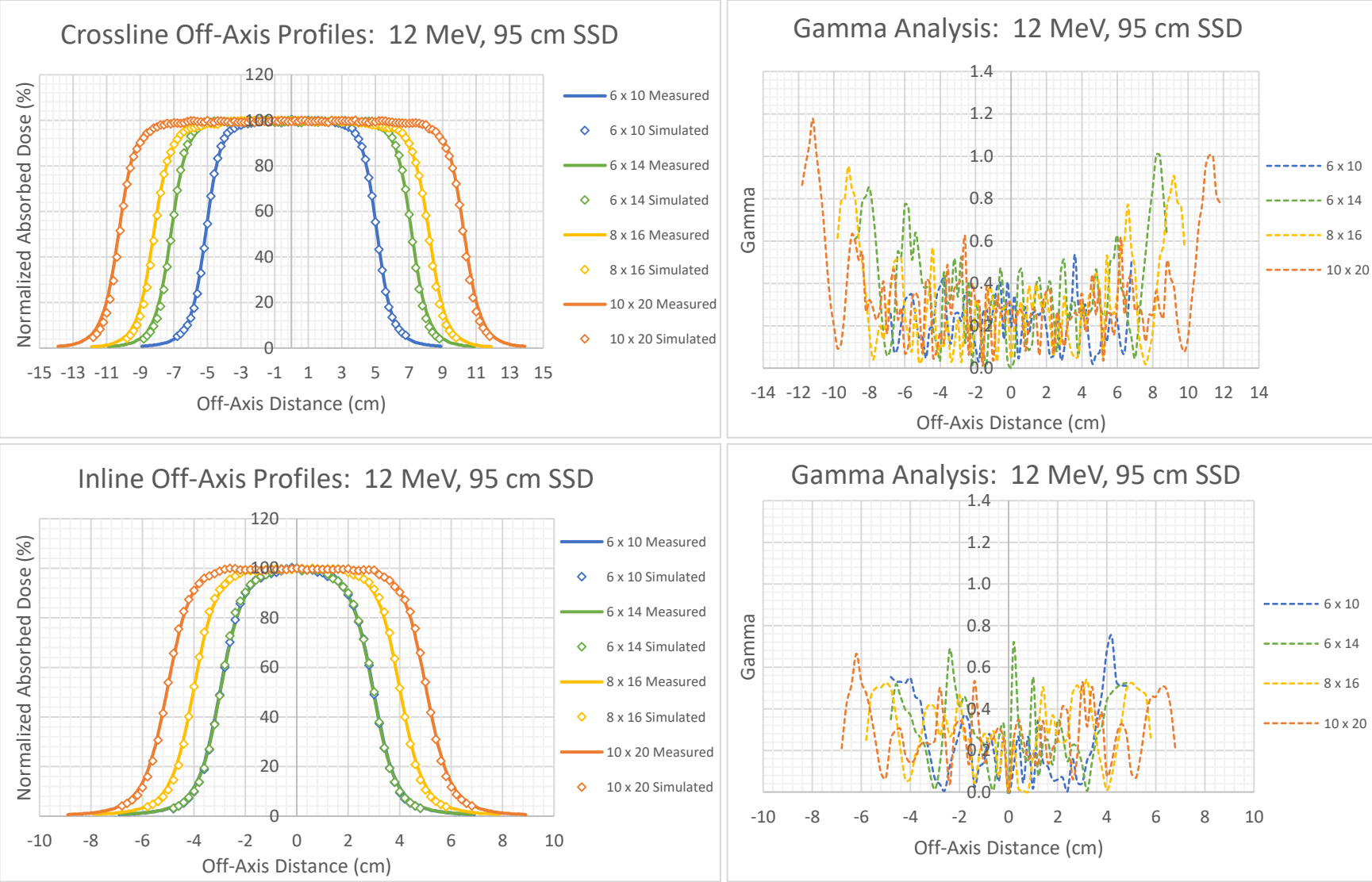

Figure 4-50: 12 MeV Crossline (top left) and Inline (bottom left) off-axis profiles for rectangular field sizes measured and simulated at 95 cm SSD. The respective Gamma analysis for each curve is indicated on the right side with a tolerance criterion of 2%/2mm.

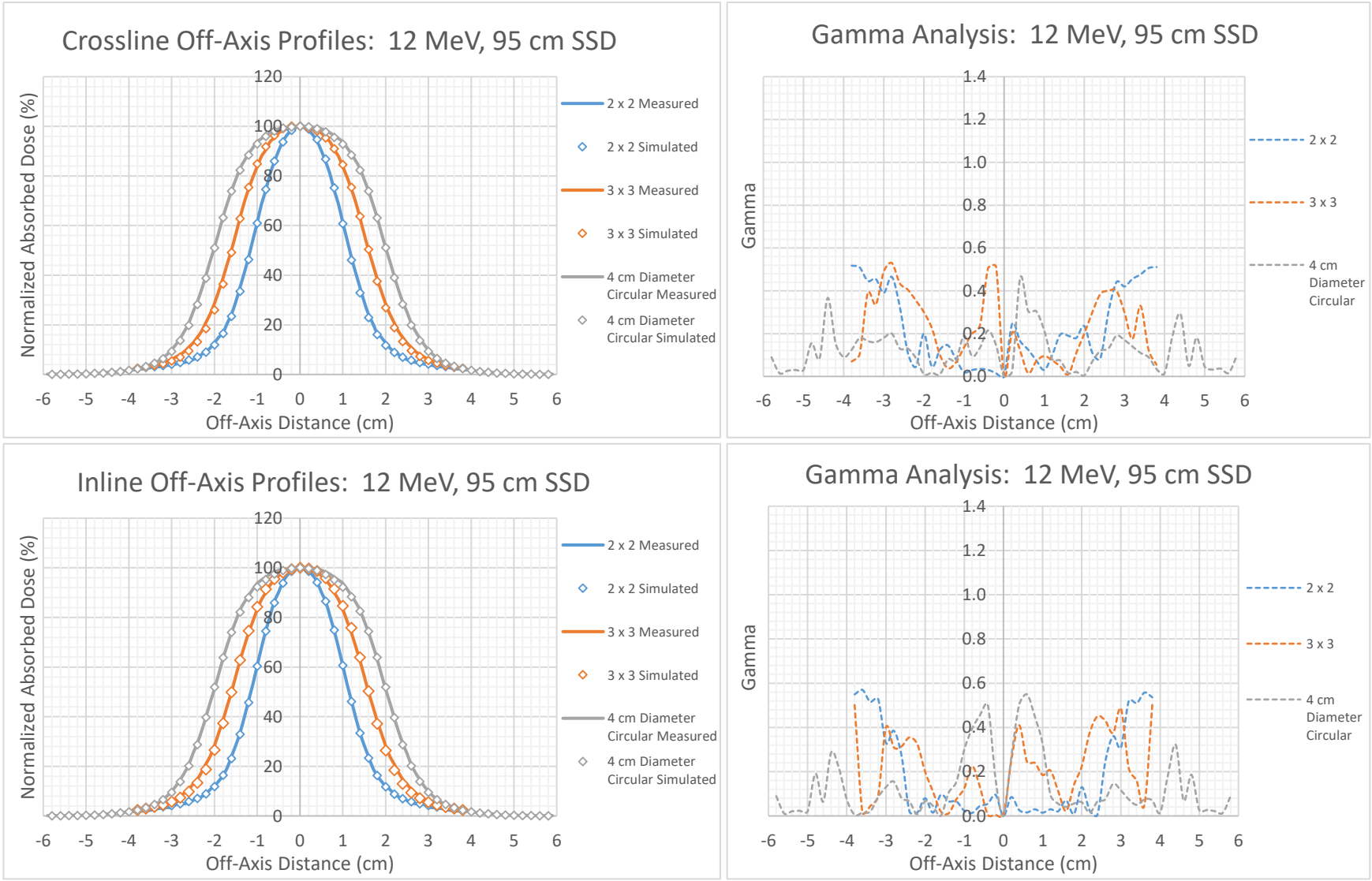

Figure 4-51: 12 MeV Crossline (top left) and Inline (bottom left) off-axis profiles for small field sizes measured and simulated at 95 cm SSD. The respective Gamma analysis for each curve is indicated on the right side with a tolerance criterion of 2%/2mm.

4.6.1.6 15 MeV

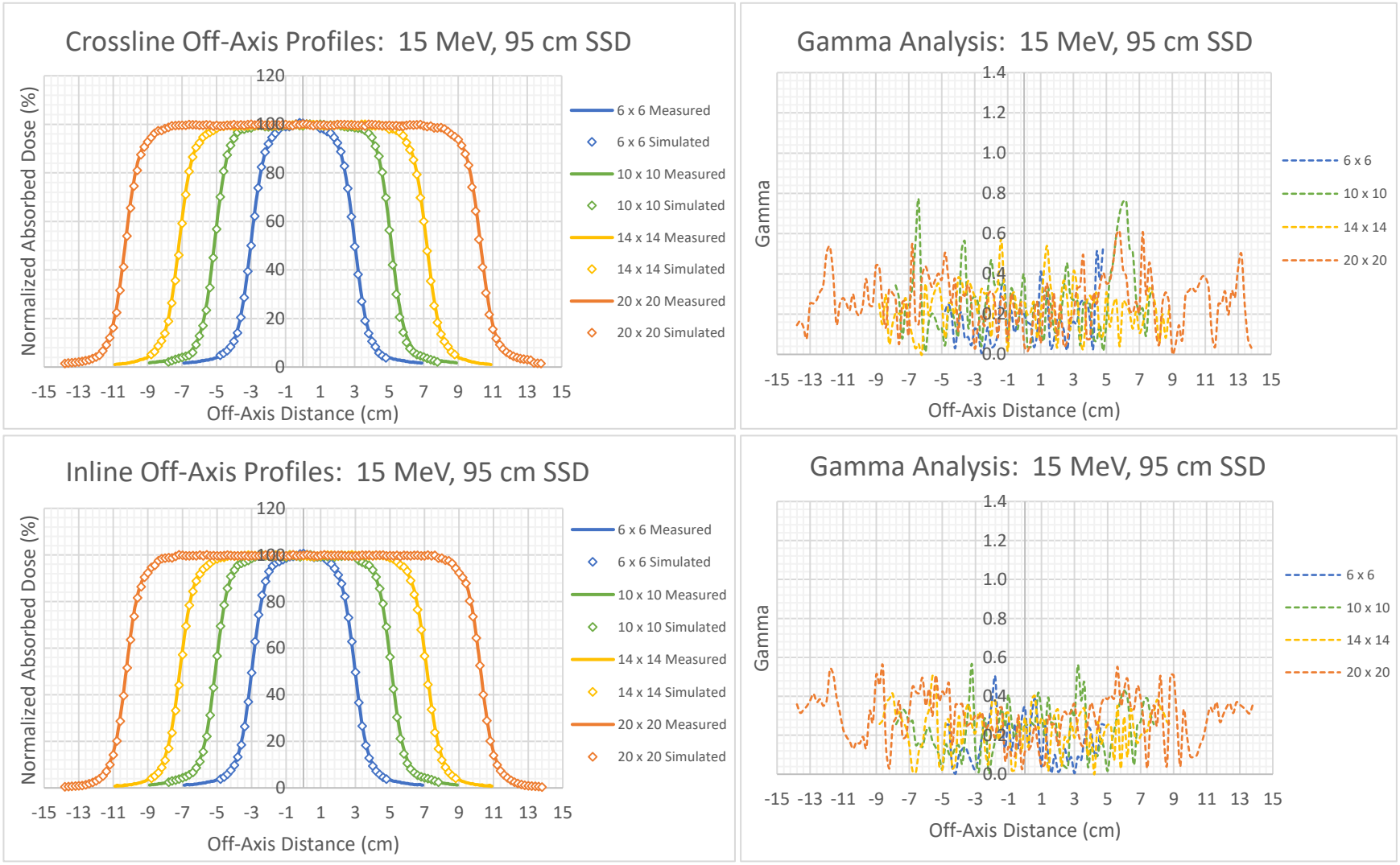

Figure 4-52: 15 MeV Crossline (top left) and Inline (bottom left) off-axis profiles for square field sizes measured and simulated at 95 cm SSD. The respective Gamma analysis for each curve is indicated on the right side with a tolerance criterion of 2%/2mm.

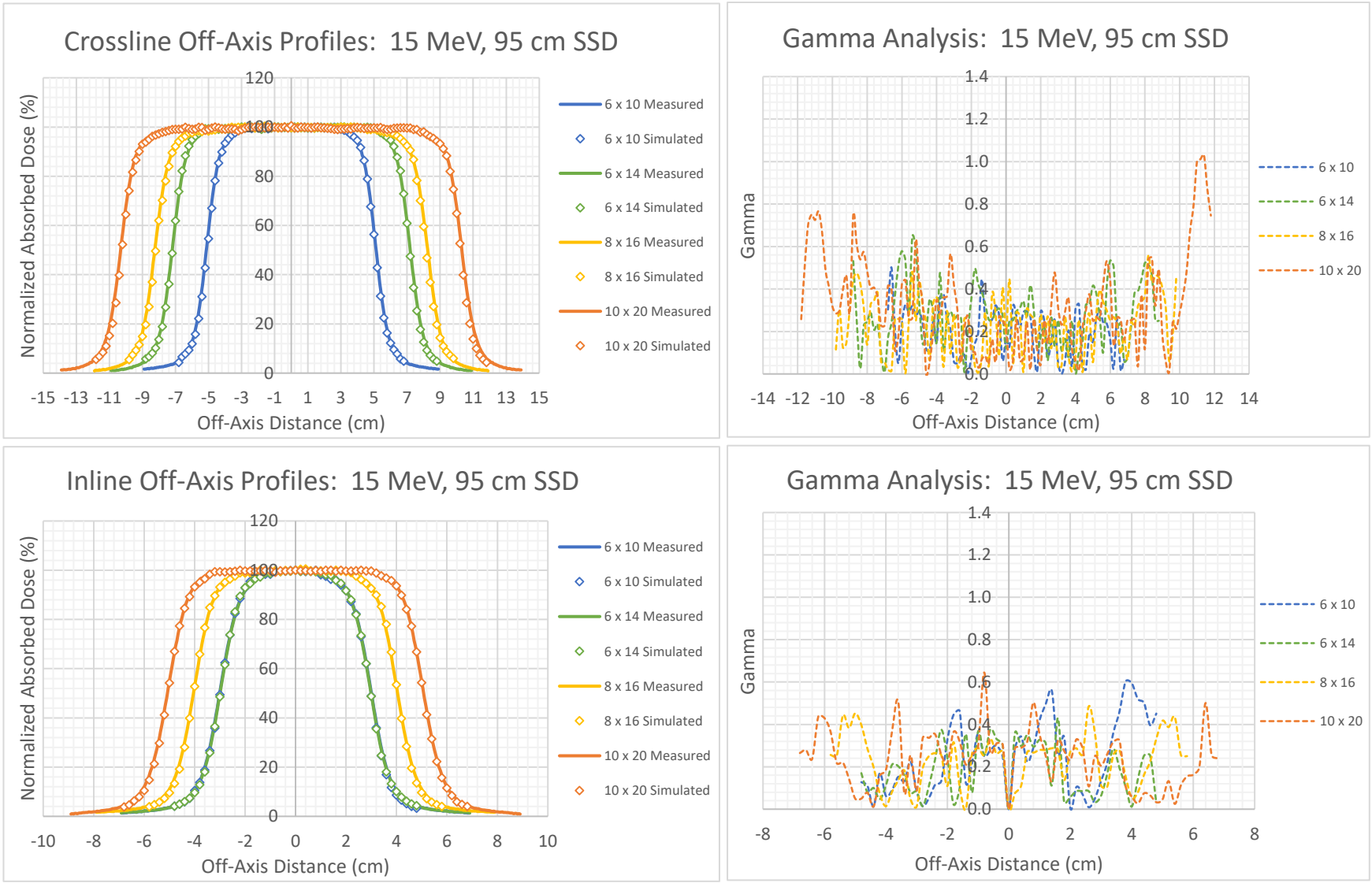

Figure 4-53: 15 MeV Crossline (top left) and Inline (bottom left) off-axis profiles for rectangular field sizes measured and simulated at 95 cm SSD. The respective Gamma analysis for each curve is indicated on the right side with a tolerance criterion of 2%/2mm.

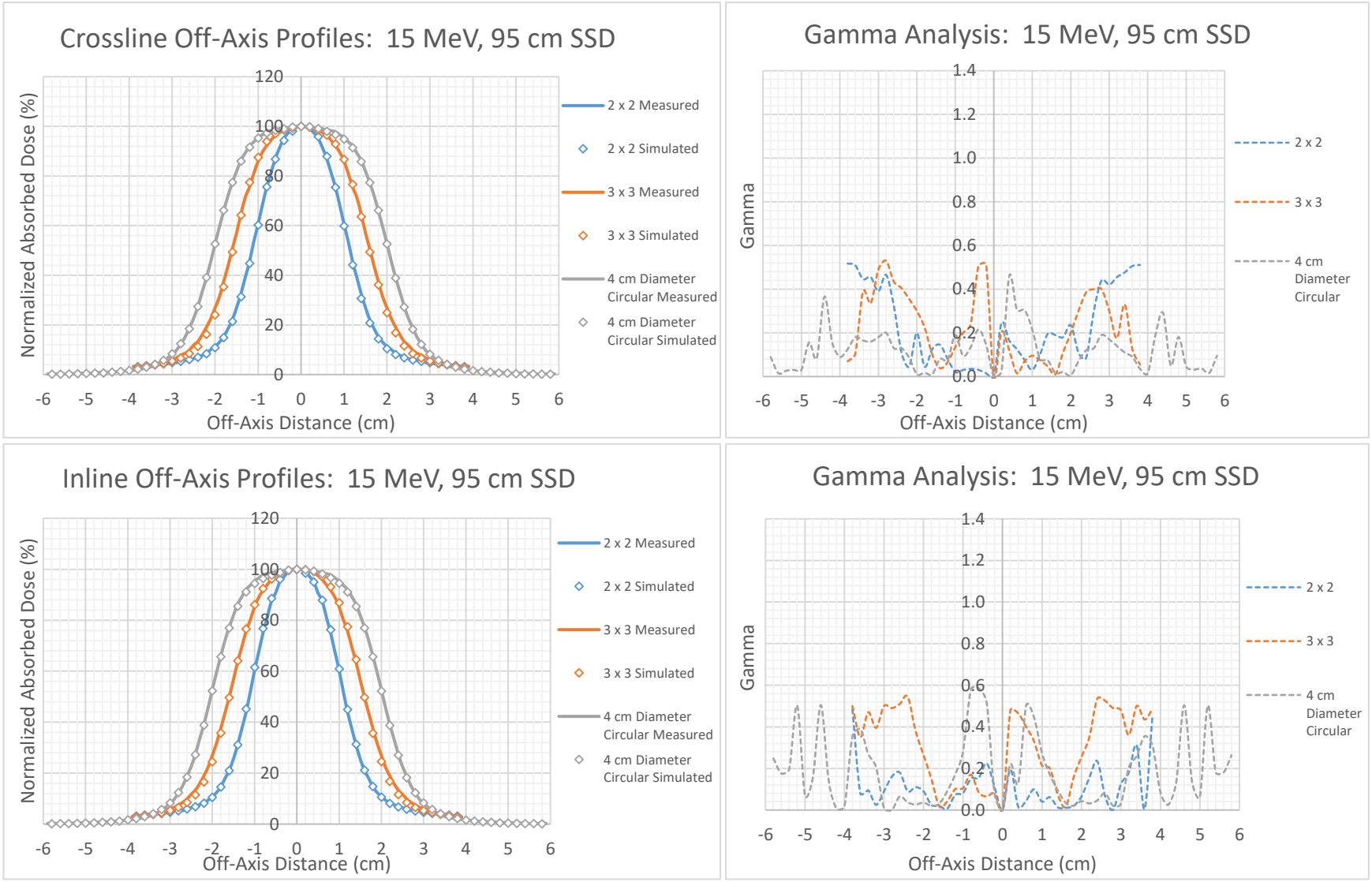

Figure 4-54: 15 MeV Crossline (top left) and Inline (bottom left) off-axis profiles for small field sizes measured and simulated at 95 cm SSD. The respective Gamma analysis for each curve is indicated on the right side with a tolerance criterion of 2%/2mm.

4.6.2 100 cm SSD

4.6.2.1 4 MeV

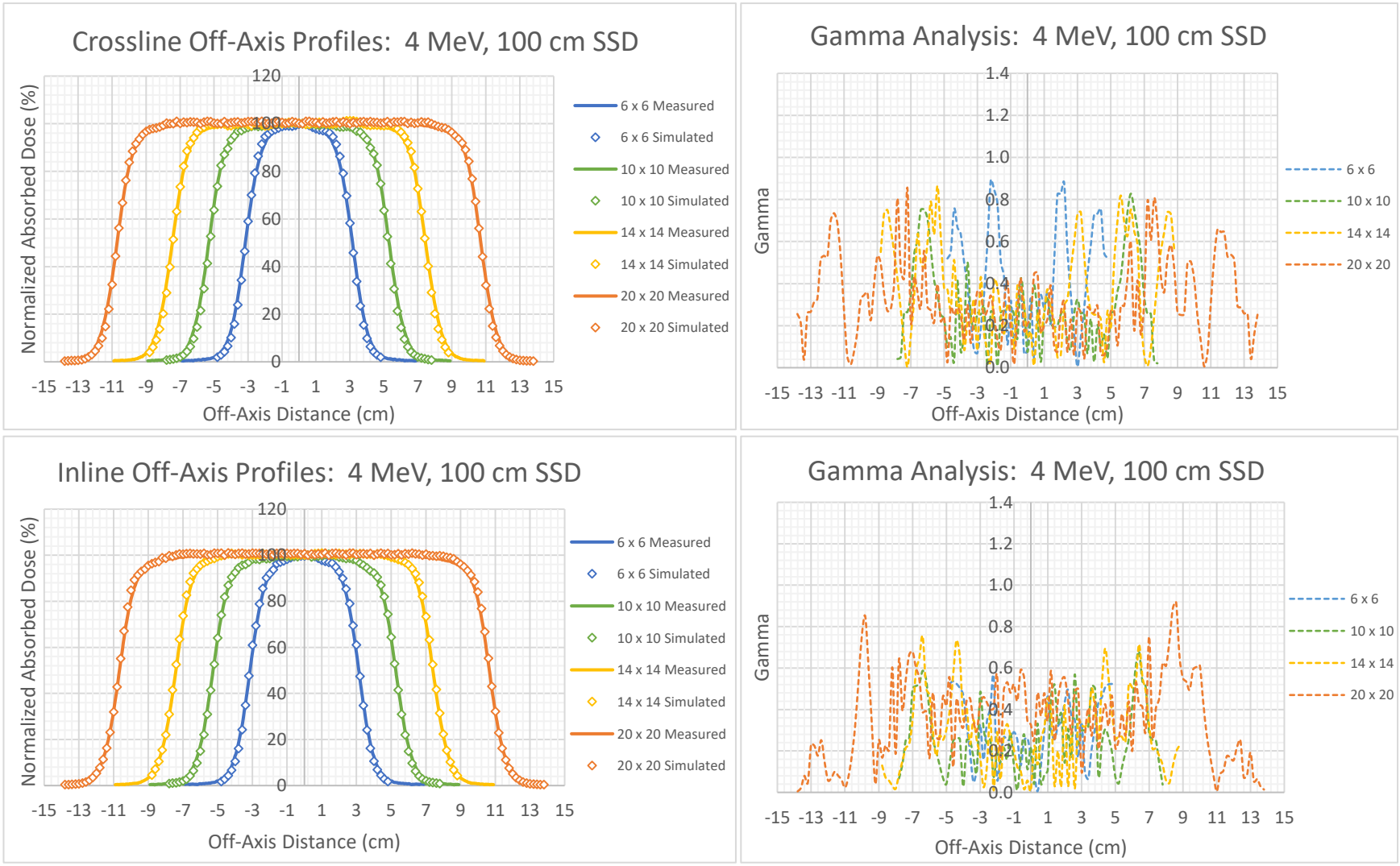

Figure 4-55: 4 MeV Crossline (top left) and Inline (bottom left) off-axis profiles for square field sizes measured and simulated at 100 cm SSD. The respective Gamma analysis for each curve is indicated on the right side with a tolerance criterion of 2%/2mm.

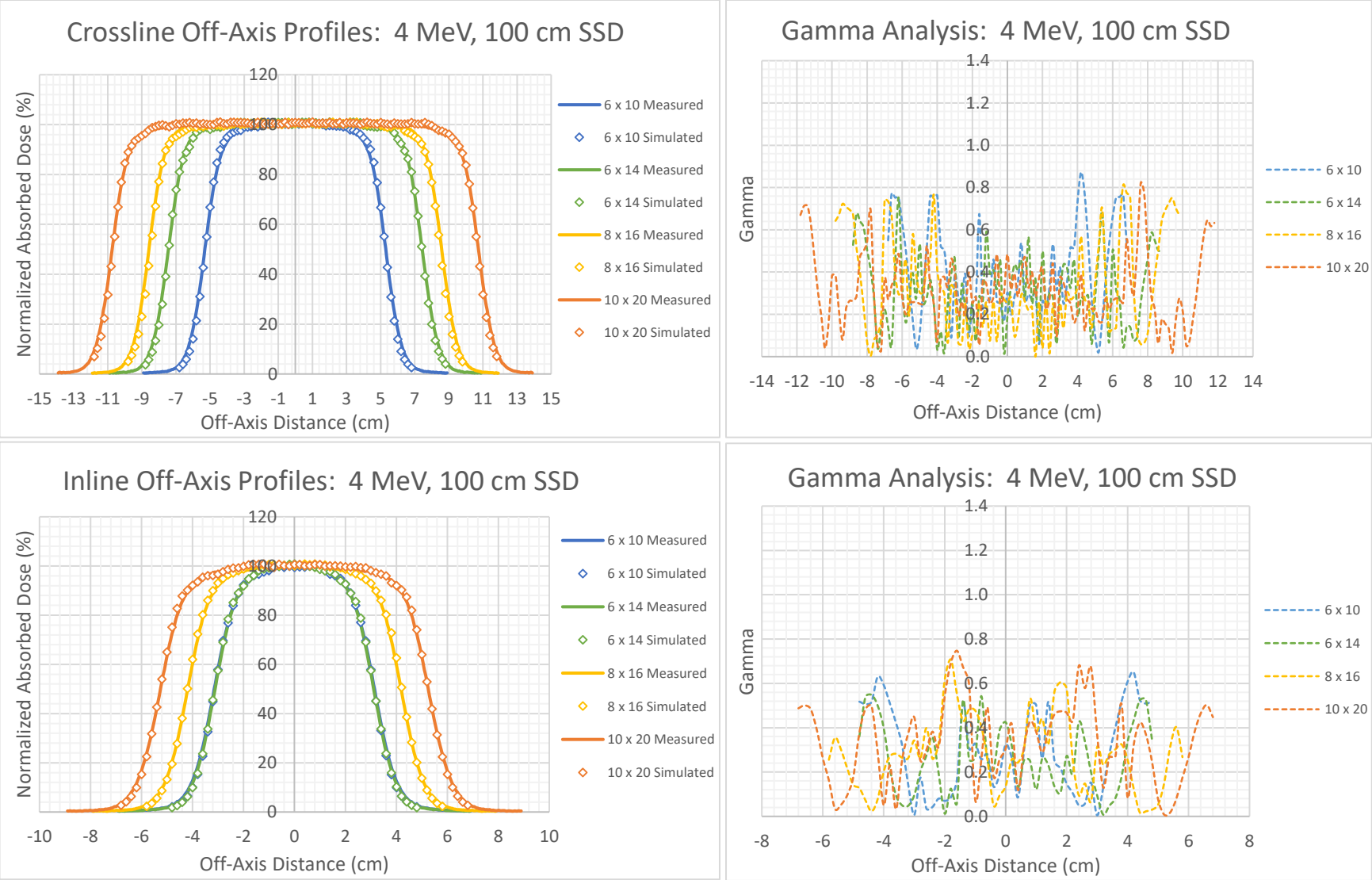

Figure 4-56: 4 MeV Crossline (top left) and Inline (bottom left) off-axis profiles for rectangular field sizes measured and simulated at 100 cm SSD. The respective Gamma analysis for each curve is indicated on the right side with a tolerance criterion of 2%/2mm.

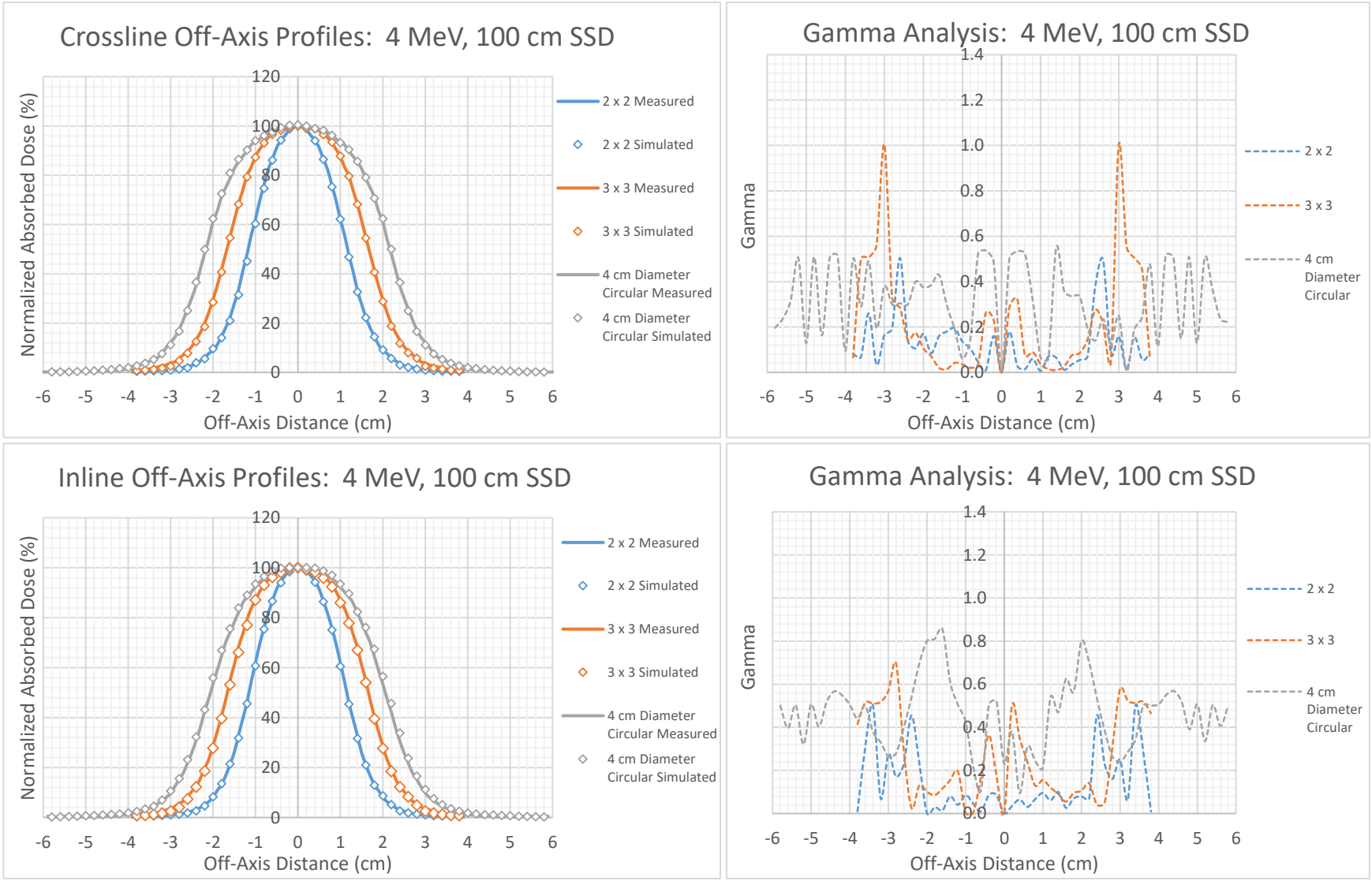

Figure 4-57: 4 MeV Crossline (top left) and Inline (bottom left) off-axis profiles for small field sizes measured and simulated at 100 cm SSD. The respective Gamma analysis for each curve is indicated on the right side with a tolerance criterion of 2%/2mm.

4.6.2.2 6 MeV

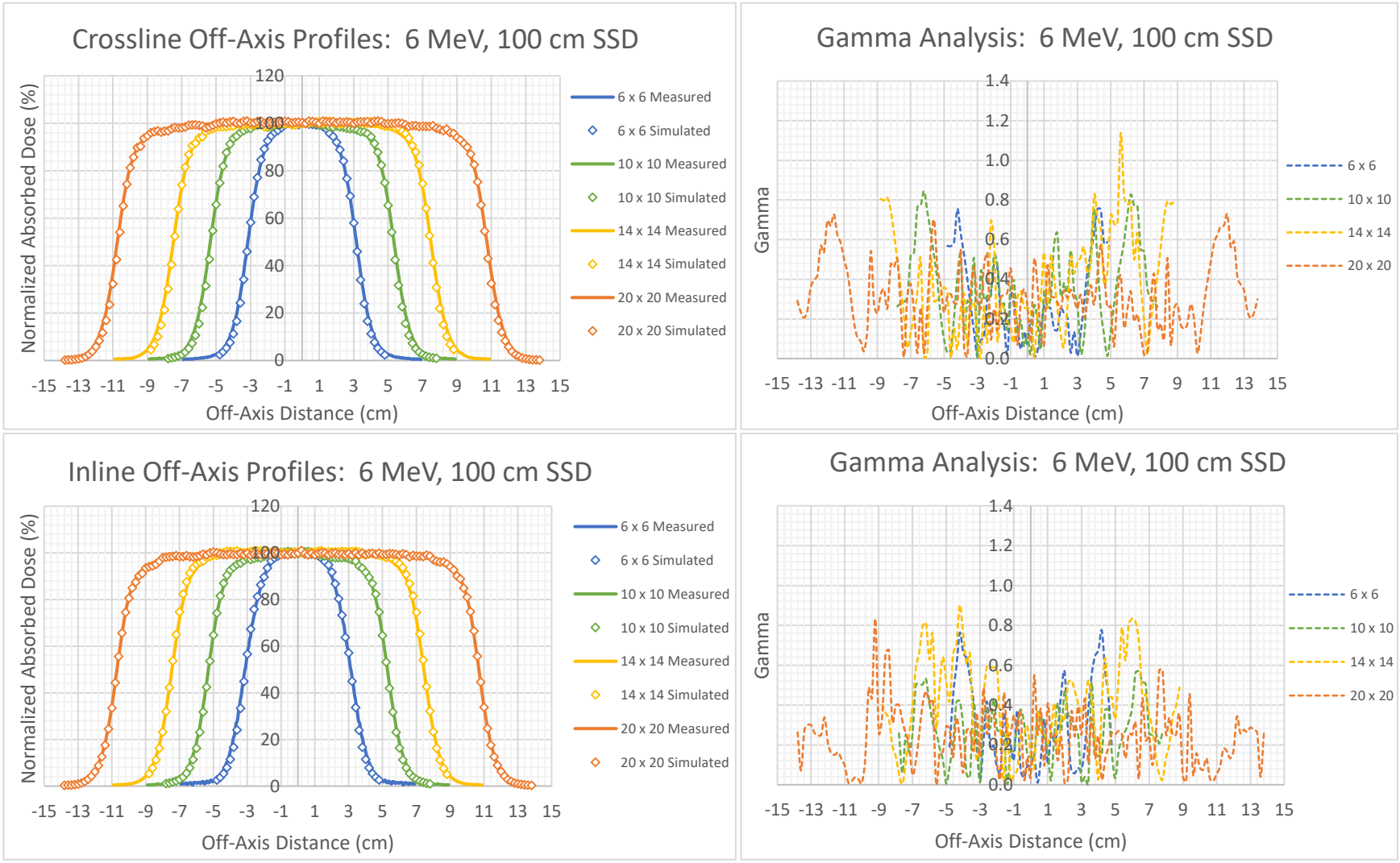

Figure 4-58: 6 MeV Crossline (top left) and Inline (bottom left) off-axis profiles for square field sizes measured and simulated at 100 cm SSD. The respective Gamma analysis for each curve is indicated on the right side with a tolerance criterion of 2%/2mm.

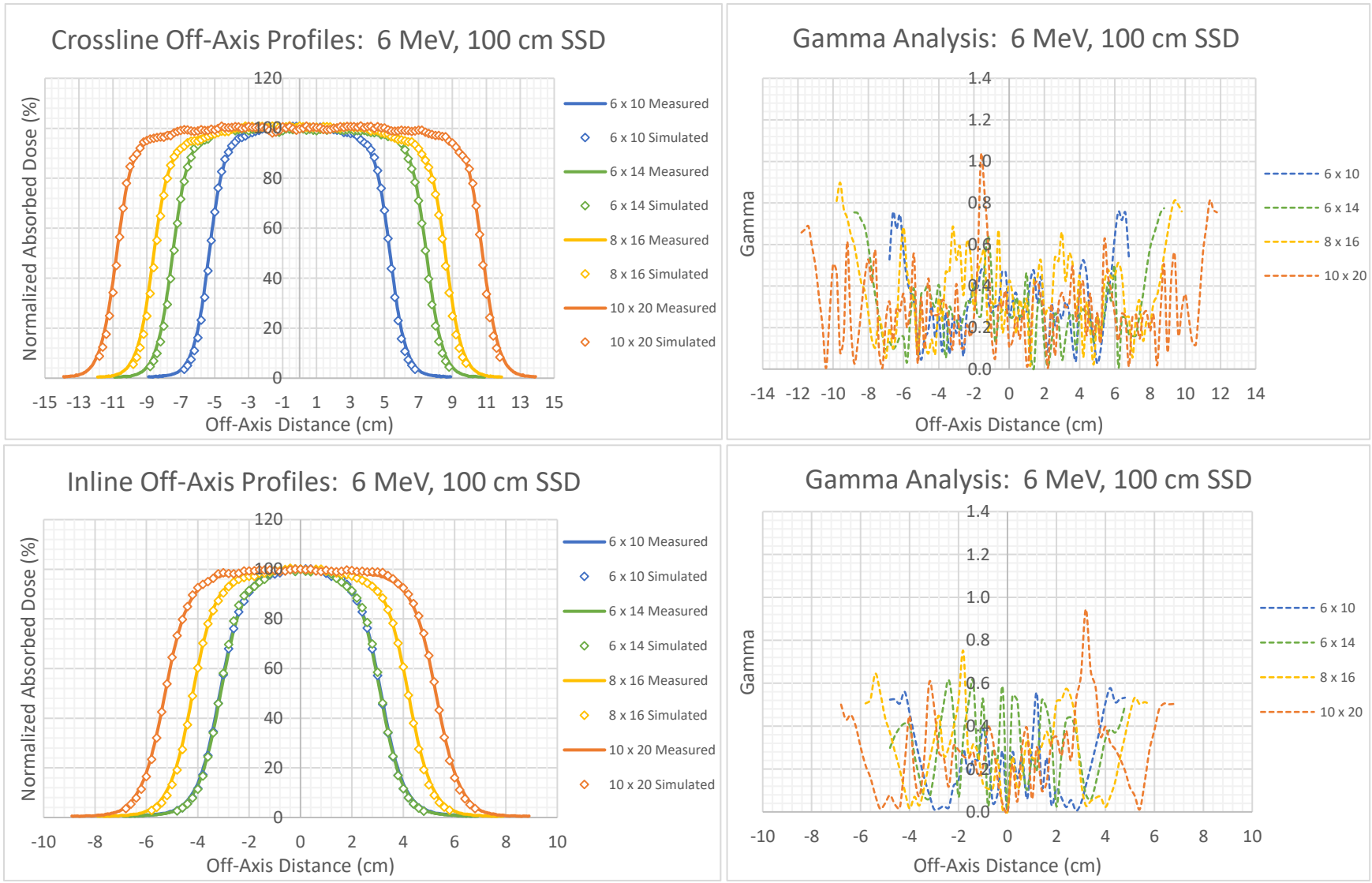

Figure 4-59: 6 MeV Crossline (top left) and Inline (bottom left) off-axis profiles for rectangular field sizes measured and simulated at 100 cm SSD. The respective Gamma analysis for each curve is indicated on the right side with a tolerance criterion of 2%/2mm.

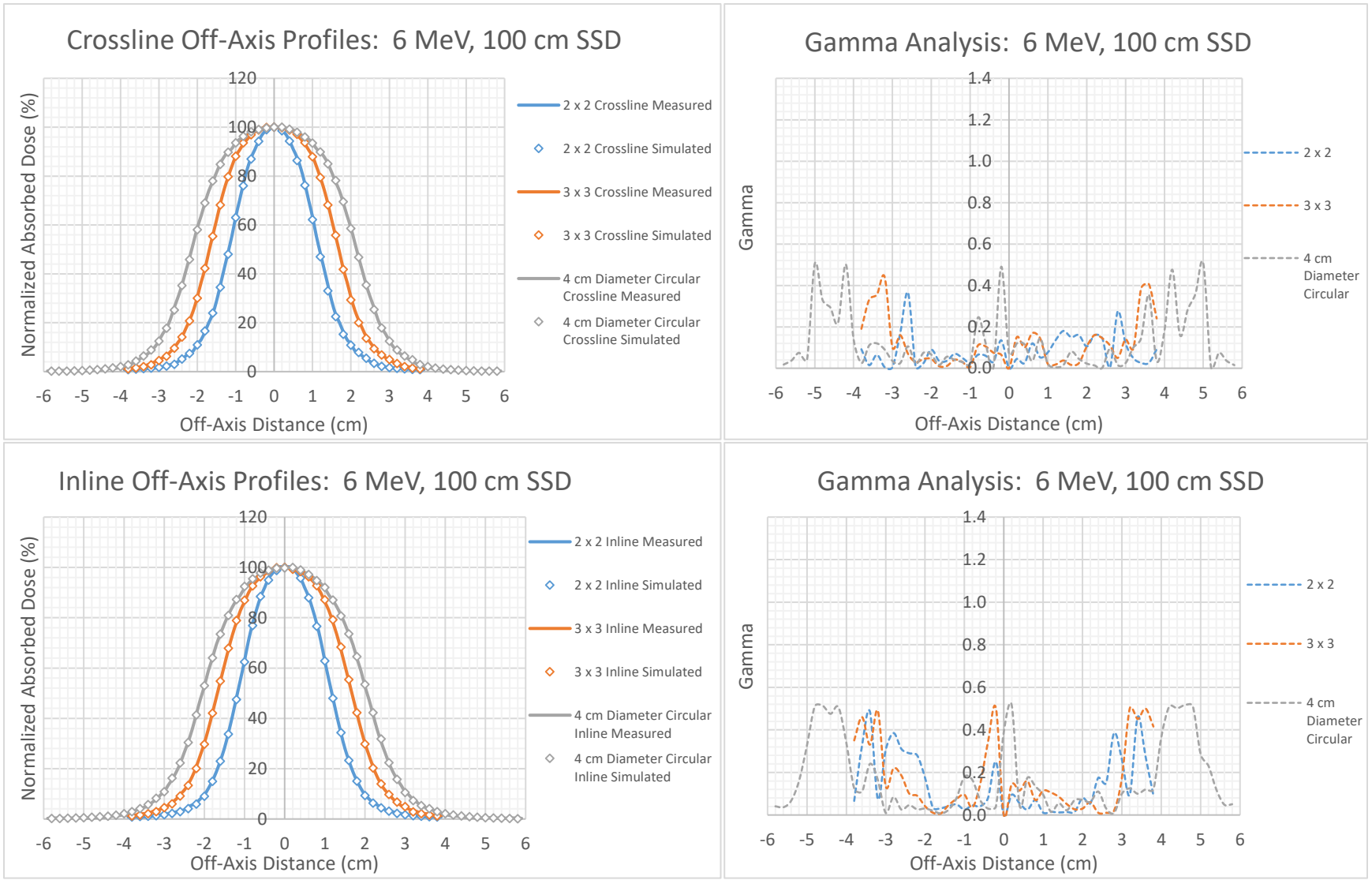

Figure 4-60: 6 MeV Crossline (top left) and Inline (bottom left) off-axis profiles for small field sizes measured and simulated at 100 cm SSD. The respective Gamma analysis for each curve is indicated on the right side with a tolerance criterion of 2%/2mm.

4.6.2.3 8 MeV

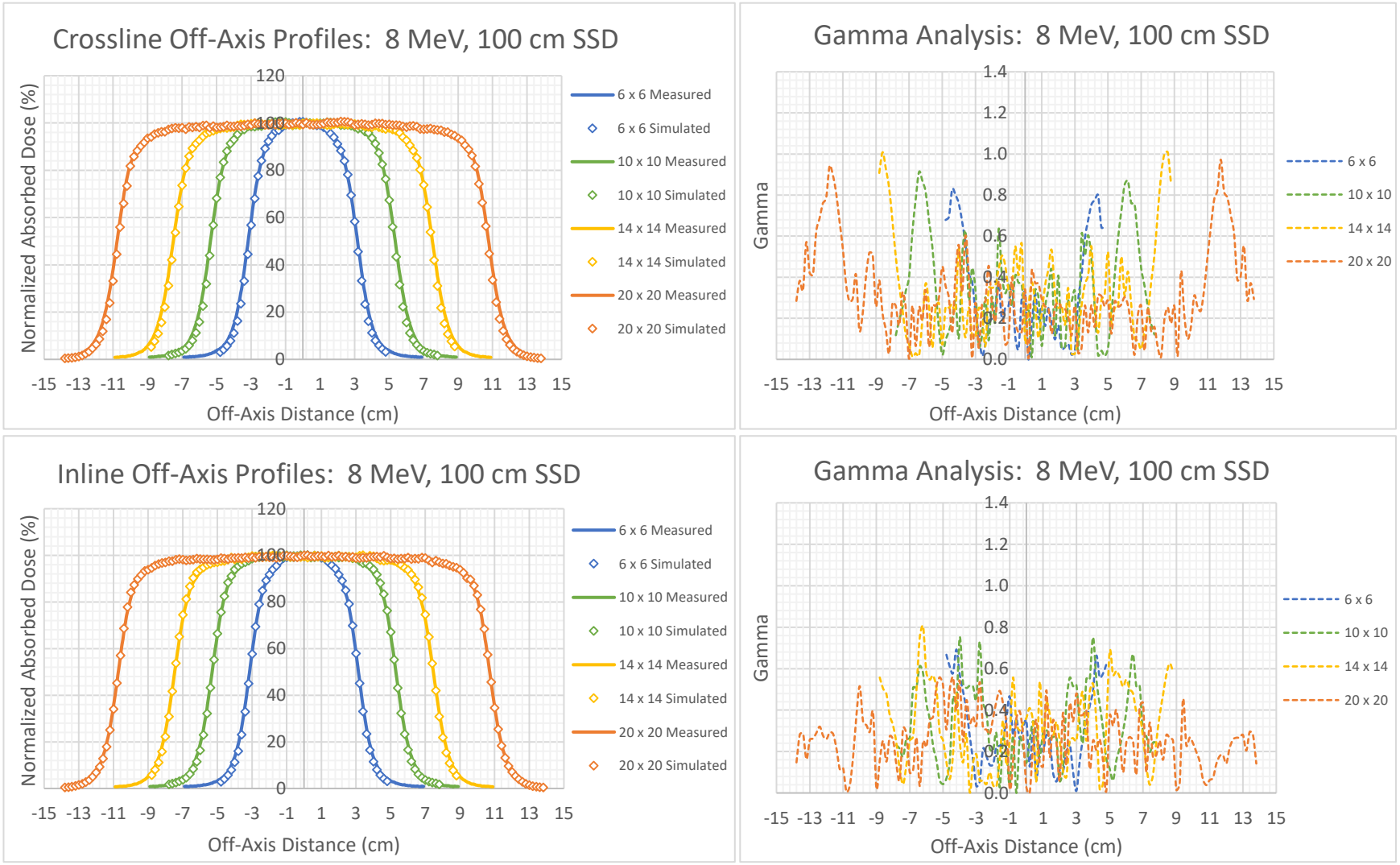

Figure 4-61: 8 MeV Crossline (top left) and Inline (bottom left) off-axis profiles for square field sizes measured and simulated at 100 cm SSD. The respective Gamma analysis for each curve is indicated on the right side with a tolerance criterion of 2%/2mm.

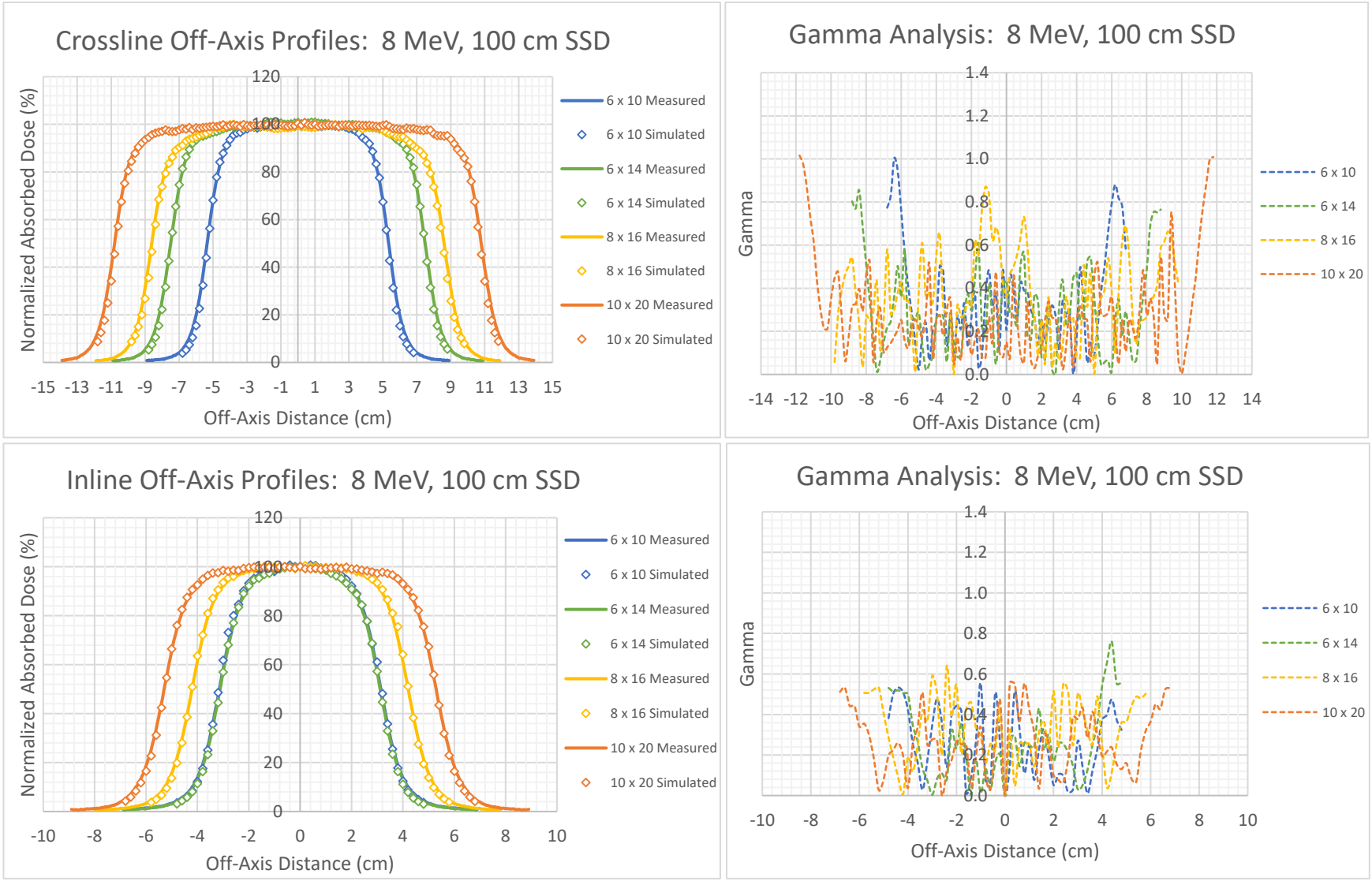

Figure 4-62: 8 MeV Crossline (top left) and Inline (bottom left) off-axis profiles for rectangular field sizes measured and simulated at 100 cm SSD. The respective Gamma analysis for each curve is indicated on the right side with a tolerance criterion of 2%/2mm.

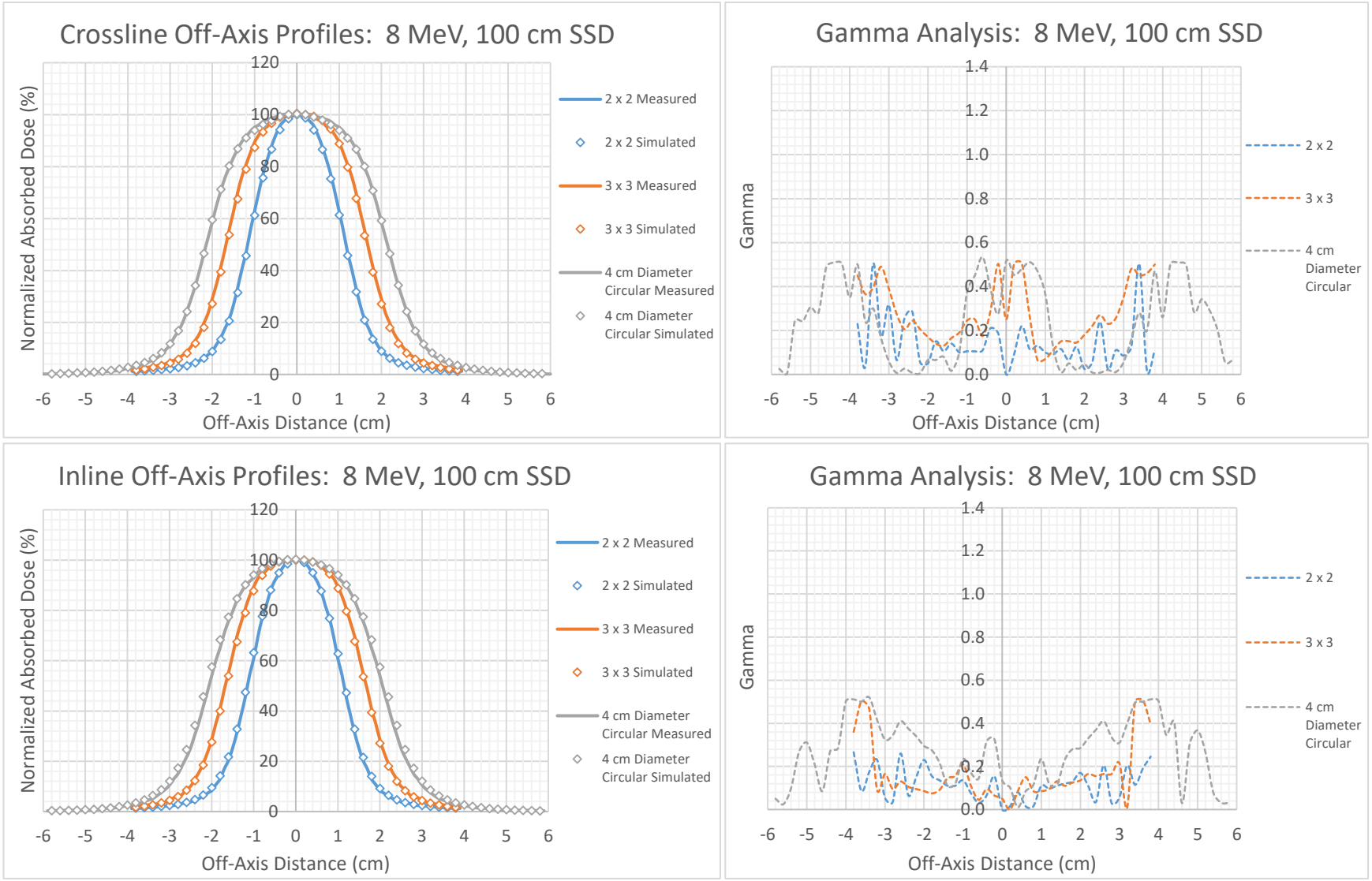

Figure 4-63: 8 MeV Crossline (top left) and Inline (bottom left) off-axis profiles for small field sizes measured and simulated at 100 cm SSD. The respective Gamma analysis for each curve is indicated on the right side with a tolerance criterion of 2%/2mm.

4.6.2.4 10 MeV

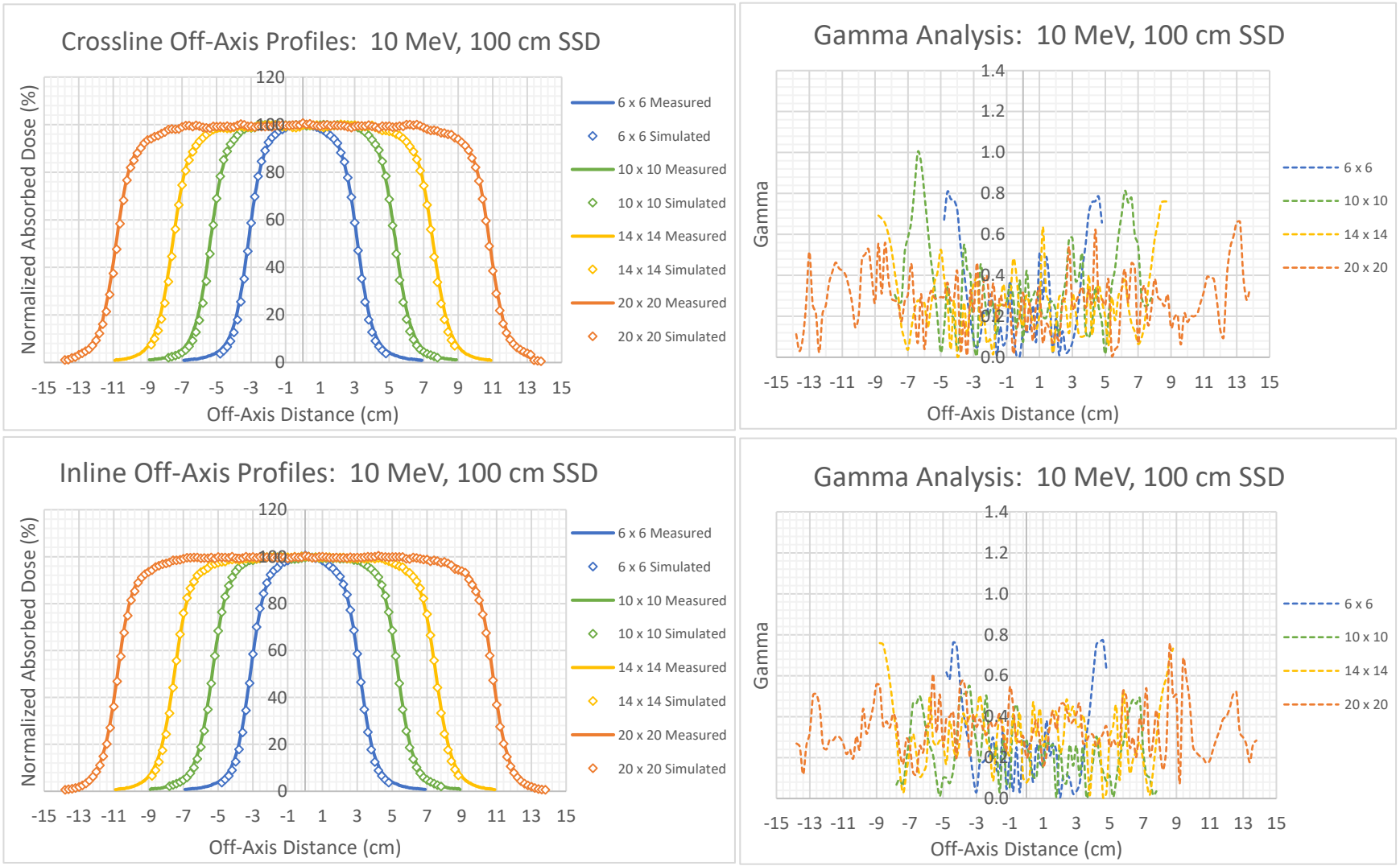

Figure 4-64: 10 MeV Crossline (top left) and Inline (bottom left) off-axis profiles for square field sizes measured and simulated at 100 cm SSD. The respective Gamma analysis for each curve is indicated on the right side with a tolerance criterion of 2%/2mm.

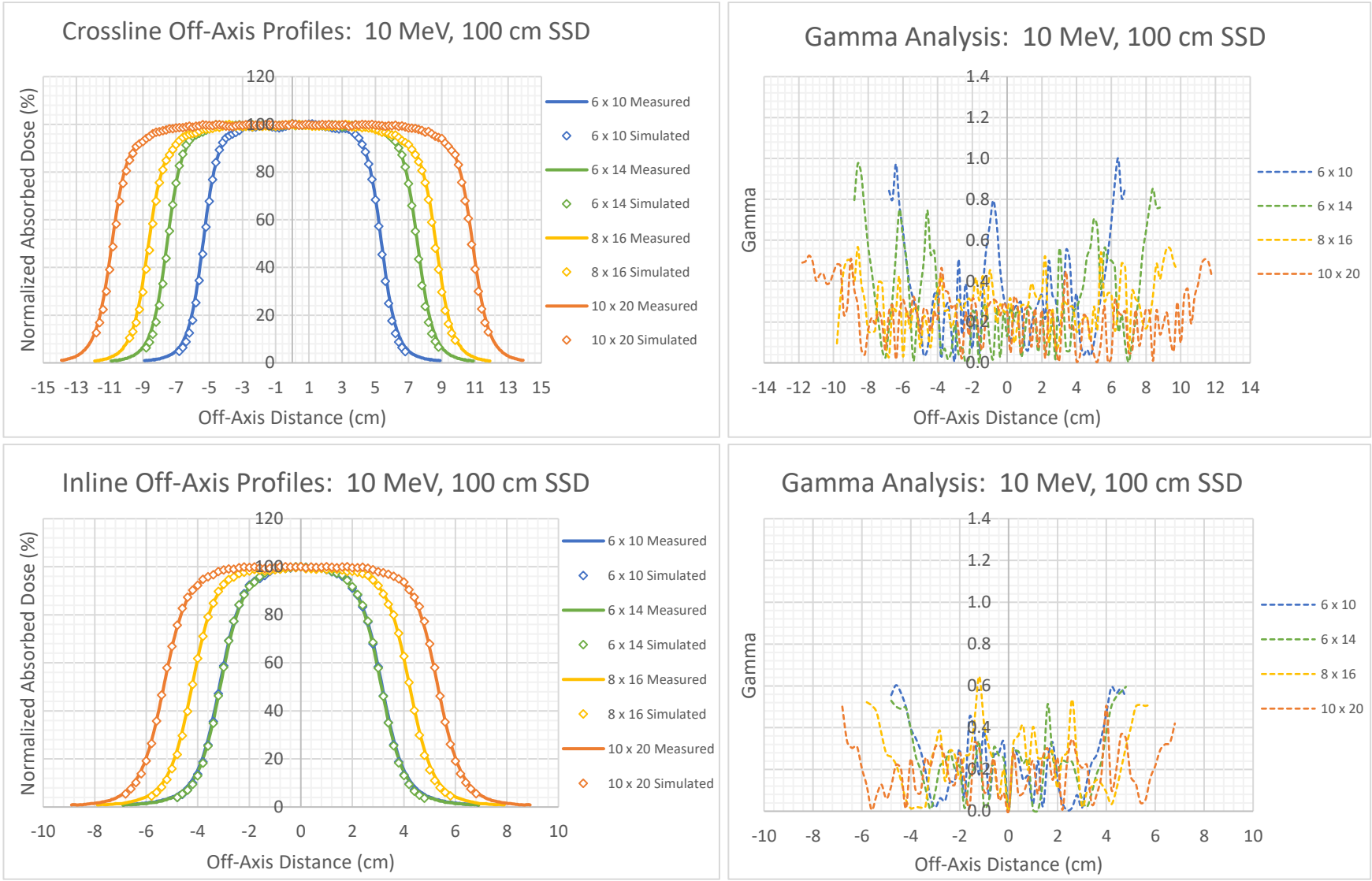

Figure 4-65: 10 MeV Crossline (top left) and Inline (bottom left) off-axis profiles for rectangular field sizes measured and simulated at 100 cm SSD. The respective Gamma analysis for each curve is indicated on the right side with a tolerance criterion of 2%/2mm.

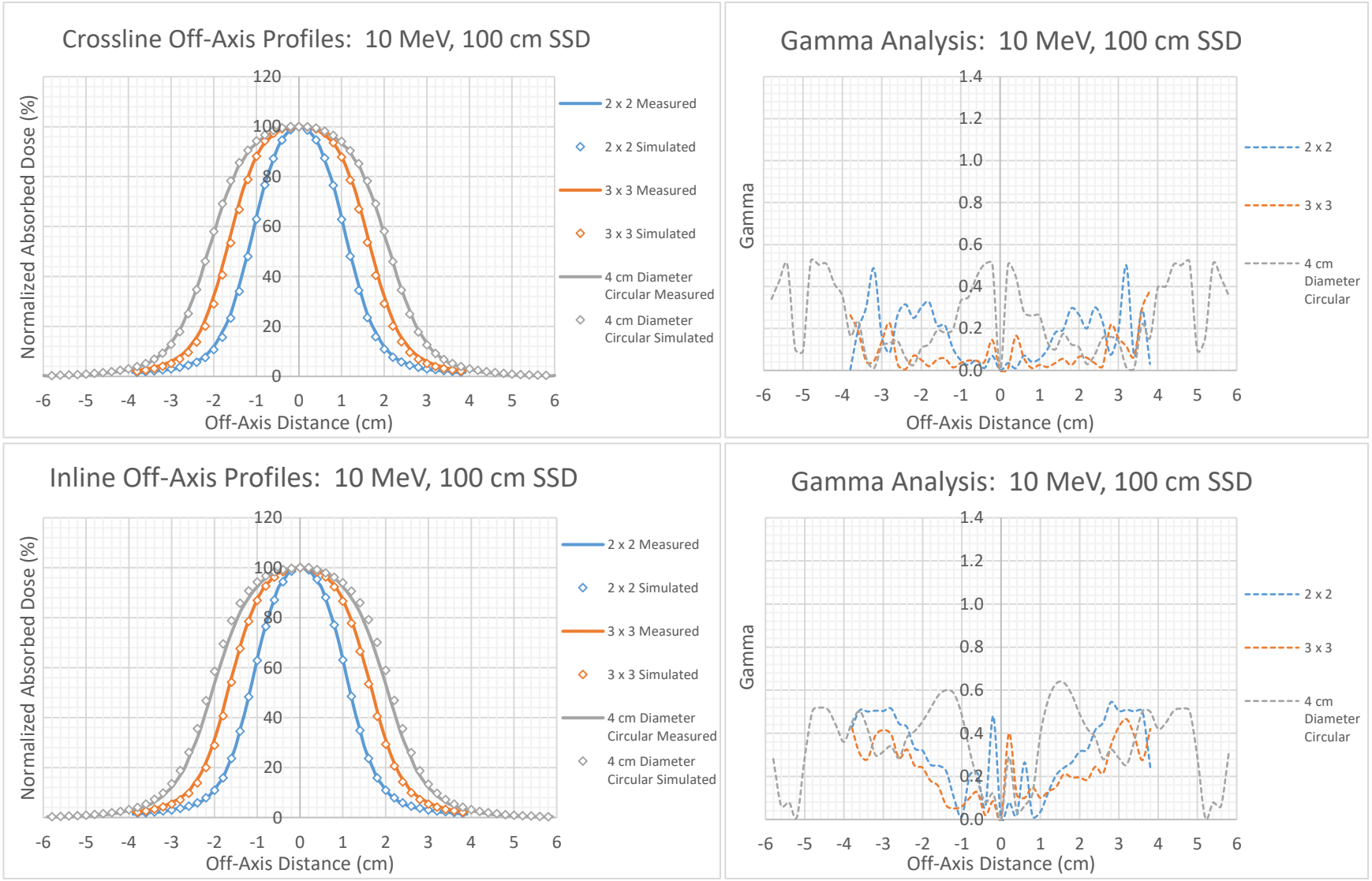

Figure 4-66: 10 MeV Crossline (top left) and Inline (bottom left) off-axis profiles for small field sizes measured and simulated at 100 cm SSD. The respective Gamma analysis for each curve is indicated on the right side with a tolerance criterion of 2%/2mm.

4.6.2.5 12 MeV

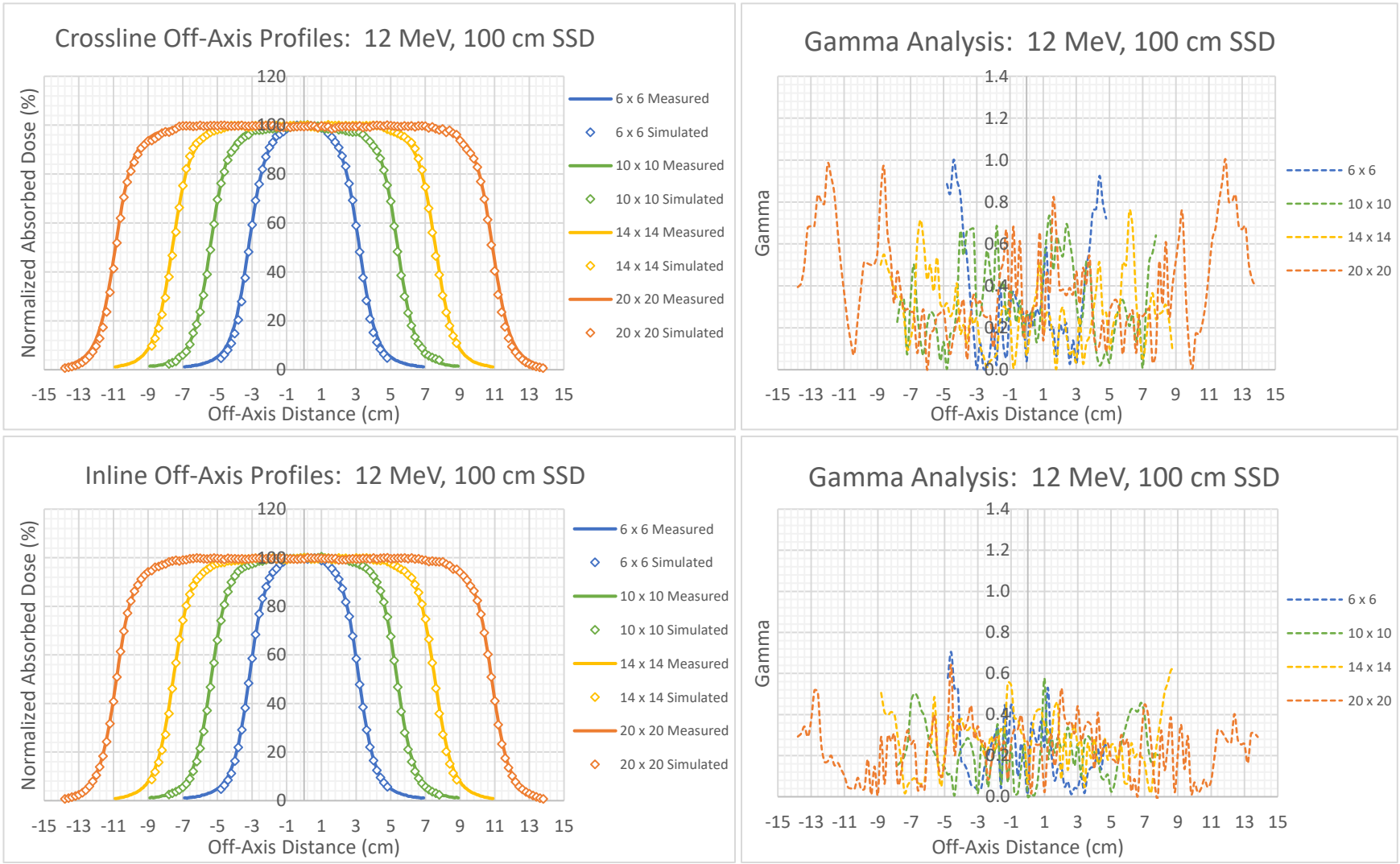

Figure 4-67: 12 MeV Crossline (top left) and Inline (bottom left) off-axis profiles for square field sizes measured and simulated at 100 cm SSD. The respective Gamma analysis for each curve is indicated on the right side with a tolerance criterion of 2%/2mm.

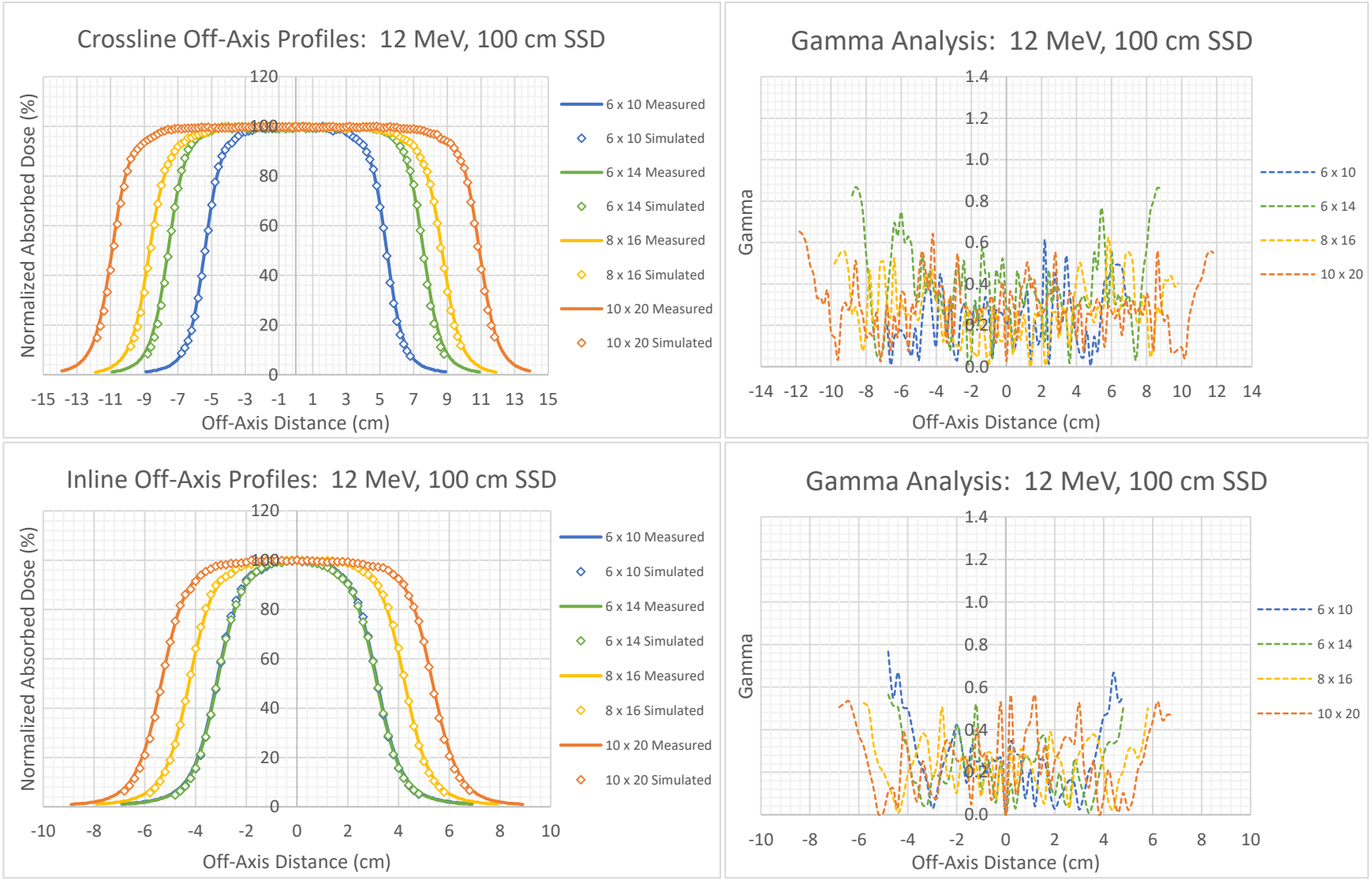

Figure 4-68: 12 MeV Crossline (top left) and Inline (bottom left) off-axis profiles for rectangular field sizes measured and simulated at 100 cm SSD. The respective Gamma analysis for each curve is indicated on the right side with a tolerance criterion of 2%/2mm.

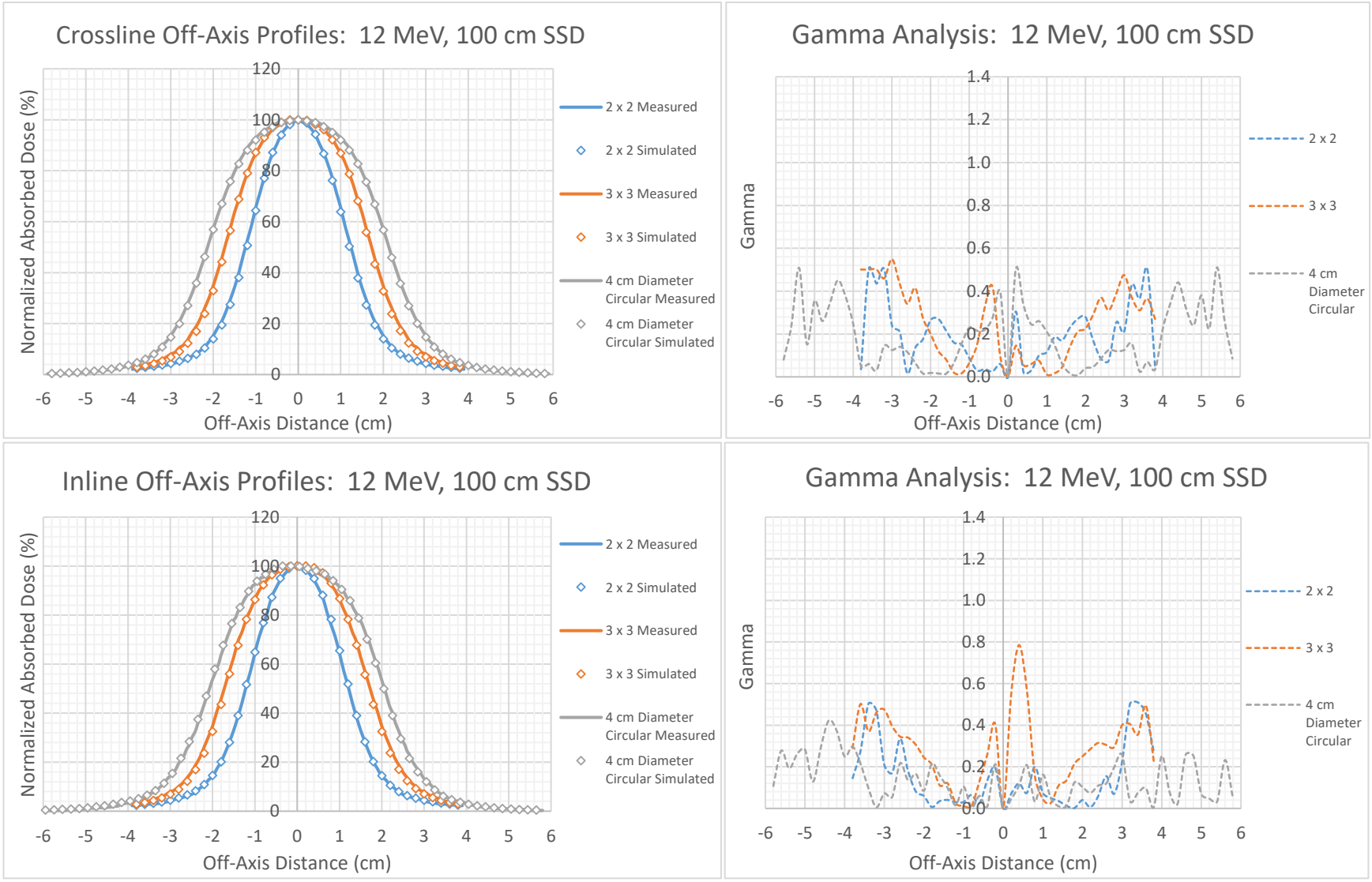

Figure 4-69: 12 MeV Crossline (top left) and Inline (bottom left) off-axis profiles for small field sizes measured and simulated at 100 cm SSD. The respective Gamma analysis for each curve is indicated on the right side with a tolerance criterion of 2%/2mm.

4.6.2.6 15 MeV

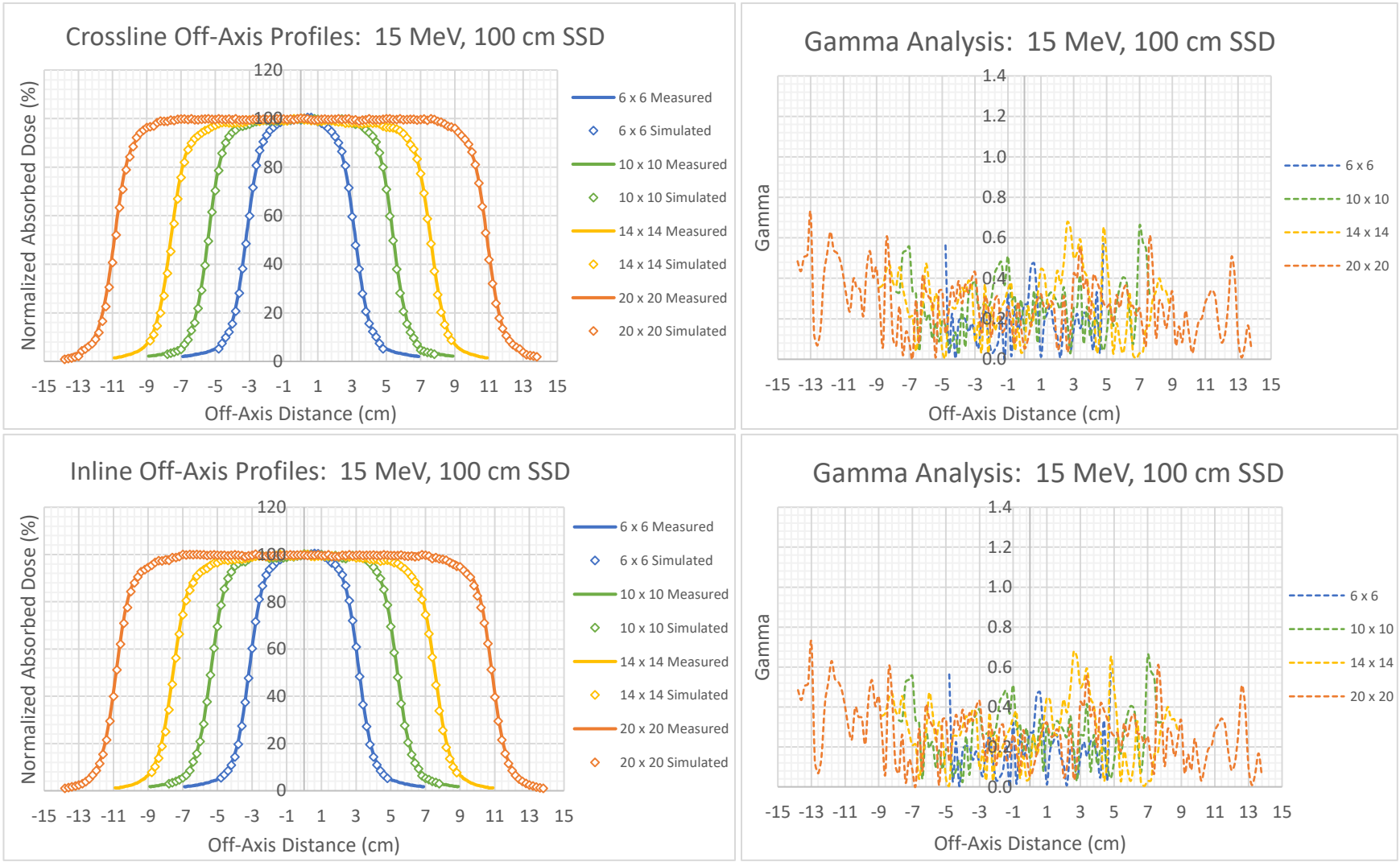

Figure 4-70: 15 MeV Crossline (top left) and Inline (bottom left) off-axis profiles for square field sizes measured and simulated at 100 cm SSD. The respective Gamma analysis for each curve is indicated on the right side with a tolerance criterion of 2%/2mm.

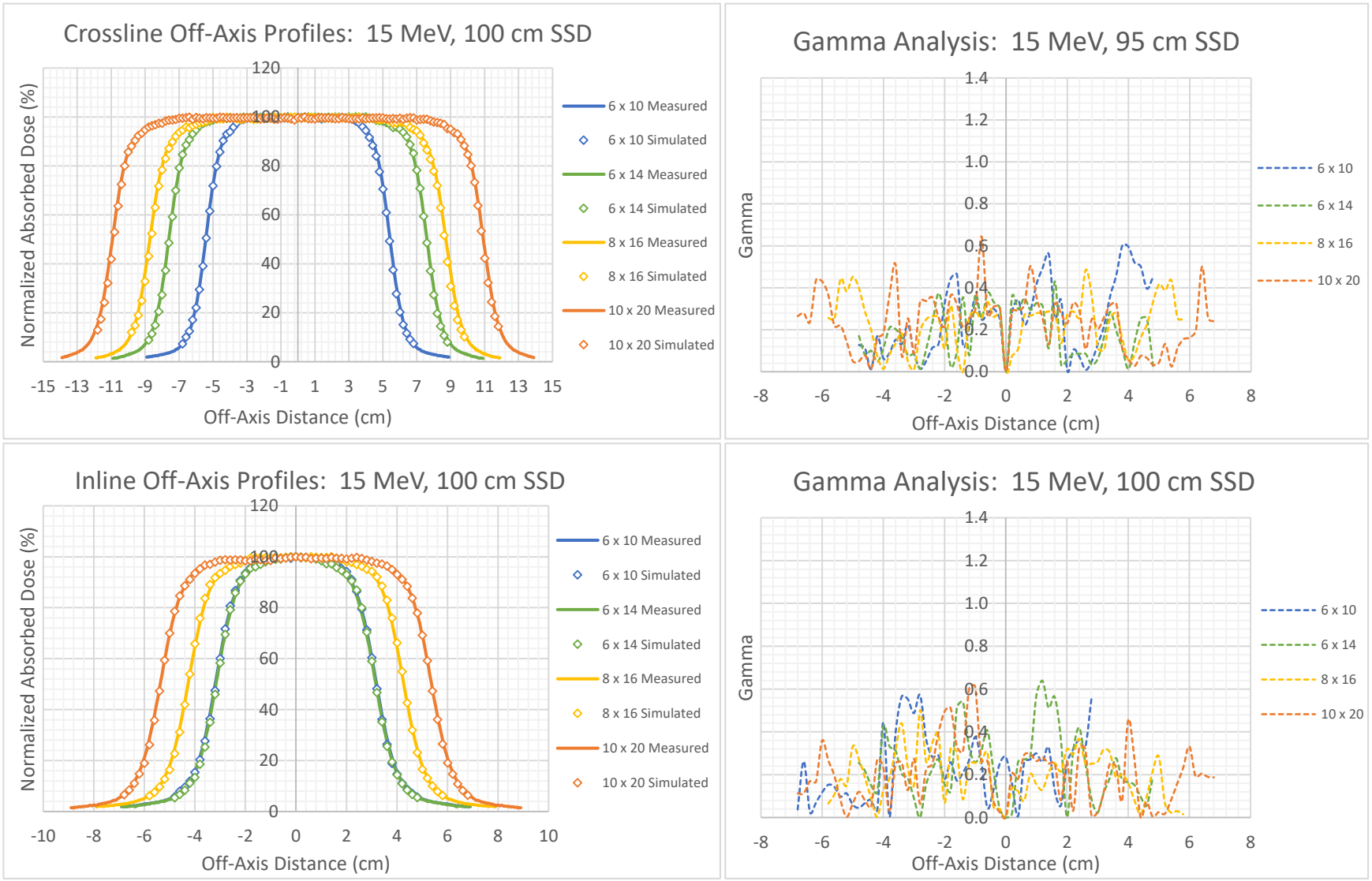

Figure 4-71: 15 MeV Crossline (top left) and Inline (bottom left) off-axis profiles for rectangular field sizes measured and simulated at 100 cm SSD. The respective Gamma analysis for each curve is indicated on the right side with a tolerance criterion of 2%/2mm.

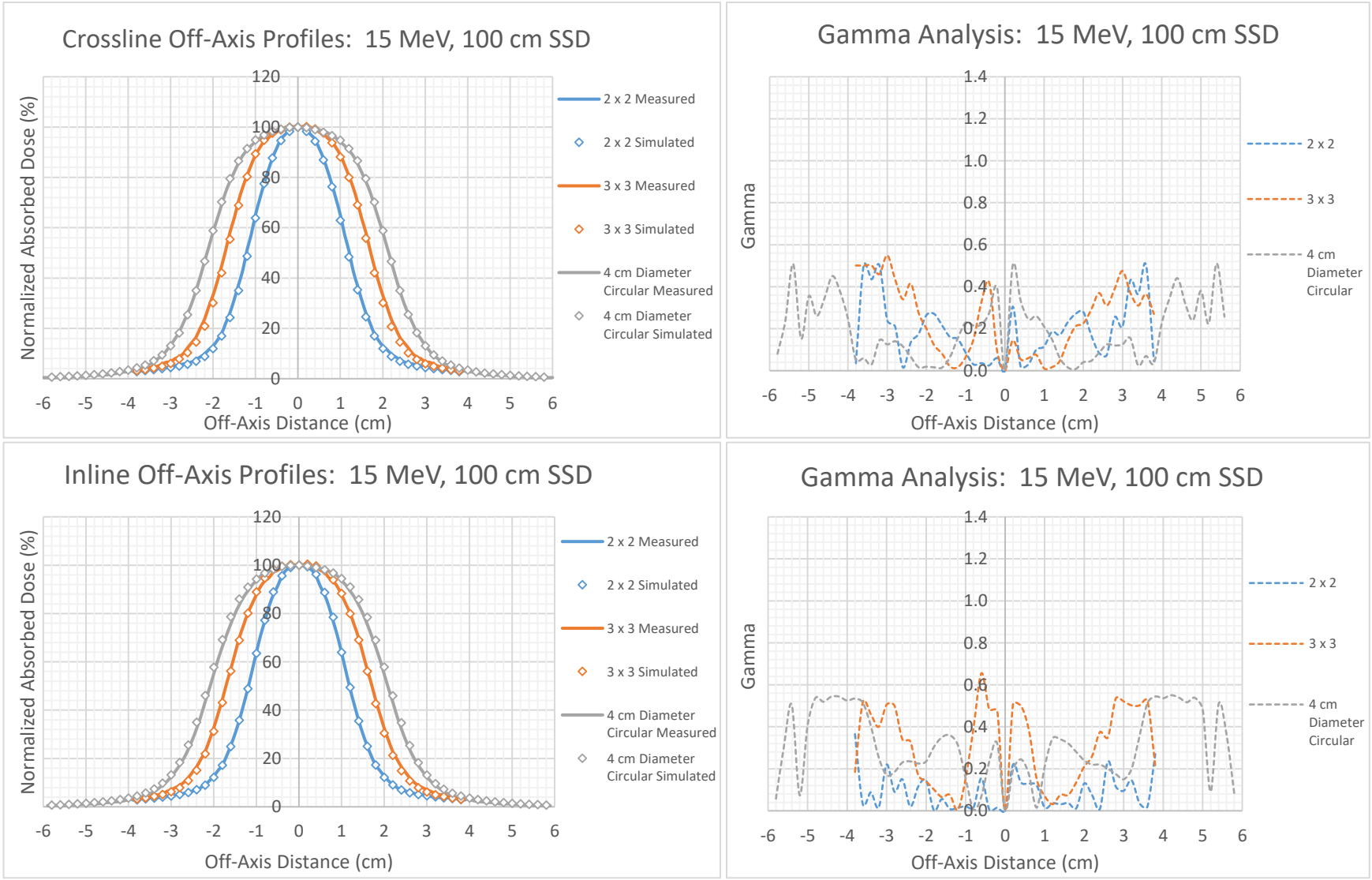

Figure 4-72: 15 MeV Crossline (top left) and Inline (bottom left) off-axis profiles for small field sizes measured and simulated at 100 cm SSD. The respective Gamma analysis for each curve is indicated on the right side with a tolerance criterion of 2%/2mm.

4.6.3 1%/1mm Criterion

As mentioned in section 4.5.3, the 10 MeV electron beam was retested under a 1%/1mm Gamma criterion. For off-axis profiles, the 100% pass rate associated with the 2%/2m criterion dropped to a combined pass rate of 82.33 % and 85.913 % for 95 cm and 100 cm SSD, respectively, as shown in Figure 4-73. The model therefore produced improved results for all fields at an extended SSD of 100 cm, except for the 4 cm Circular field. Failed data points mainly occurred within the umbra regions, which indicates that the model underestimates the Bremsstrahlung dose in these regions by 1-2 %.

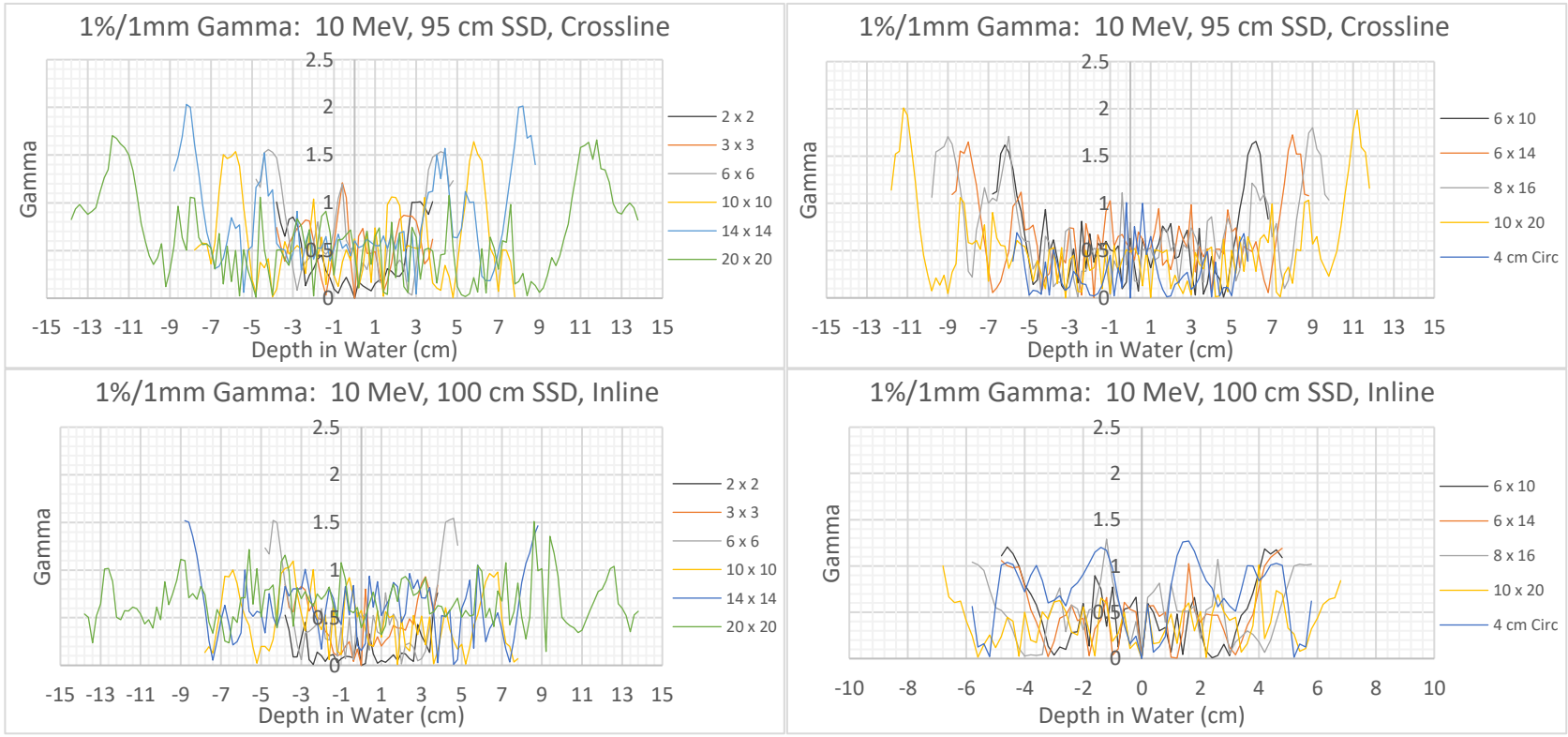

Figure 4-73: Gamma analysis results applying a 1%/1mm criterion to the 10 MeV electron beam for all field sizes at 95 cm (crossline, top graphs) and 100 cm (inline, bottom curves) SSD.

4.7 Relative Output Factors

ROFs were measured and simulated at the depth of maximum dose at both 95 cm and 100 cm SSD. Fields longer than and including 6 x 6 cm^2 were measured using a compact ionization chamber (CC13) in water. Furthermore, each applicator size was fitted with the corresponding open field insert size (for example, a 10 x 10 cm^2 applicator was fitted with a 10 x 10 cm^2 open field insert, etc.) and therefore the measured and simulated ROFs shown in Table 4-5 and Table 4-6 are cone factors. The circular applicator (with the 4 cm diameter insert) is included in the group, though it was measured differently. The circular field, 2 x 2 cm^2 and 3 x 3 cm^2 field was measured using a pinpoint ionization chamber (CC01) using Daisy chaining to relate the values to the 10 x 10 cm^2 field measured with a Farmer chamber in Perspex. The 2 x 2 cm^2 and 3 x 3 cm^2 output factors, or cutout factors (fitted to the 6 x 6 cm^2 applicator), are shown in Table 4-7 and Table 4-8 along with the 6 x 6 cm^2 insert, as obtained at an SSD of 95 cm and 100 cm, respectively. Cone factors are also illustrated graphically in Figure 4-74 (a-d) whereas cutout factors are shown in Figure 4-75(a-b). Simulations were performed as to use the same amount of histories for each field size, taking into consideration a 1 % statistical uncertainty.

The absolute difference between measured and simulated cone factors was on average 1.468 % (0.9 % standard deviation) with a maximum difference of 2.858 % at an SSD of 95 cm, whereas the average absolute difference at 100 cm SSD was 1.296 % (0.827 % standard deviation) with a maximum difference of 2.764 %. Cutout factors were simulated within an average absolute difference of 1.420 % (0.707 % standard deviation) of measured factors with a maximum difference of 2.560 % at an SSD of 95 cm, whereas at 100 cm SSD the average absolute difference was 1.685 % (0.503 % standard deviation) with a maximum difference of 2.736 %.

Refer to Figure 4-74. The output of the 4 MeV electron beam decreases exponentially with a decrease in the field size (the equivalent square field was calculated for rectangular and circular fields). However, this decrease in output becomes less significant with an increase in electron energy up to about 10 MeV, where beyond this energy there seems to be no real trend with the output with an increase or decrease in cone size. However, the output of the circular cone increases drastically with an increase in electron energy, where the output from 8 MeV and beyond produced an output above that for the 10 x 10 cm^2 cone. Cutout factors showed different behavior at 95 cm and 100 cm SSDs, where the output of the 3 x 3 cm^2 insert produced a lower output than the 3 x 3 cm^2 insert at 100 cm

SSD for all electron energies. However, at 95 cm SSD the output of the 3 x 3 cm^2 was observed to be lower than the 2 x 2 cm^2 insert for 4 MeV and 15 MeV.

Though the general trend for ROF is to decrease with a decrease in field size below 10 x 10 cm^2 across all electron energies, the observed change in the ROF for smaller field sizes for higher electron energies seemed to differ from the general trend. An argument can be made that the uncertainty in the ROF measurements is > 1 % and that some of the electron models need more fine tweaking. However, the trends for ROFs may be strongly dependent on the design of the linac head as well as the electron applicators, and therefore this aspect of the study might need some additional verification.

Table 4-5: Measured (light blue) and simulated (light green) cone factors for electron nominal energies of 4-15 MeV at 95 cm SSD. All cone factors were extracted at the respective depth of maximum dose and calculated relative to the output of the 10 x 10 cm^2 electron applicator. The percentage difference for each energy-applicator combination is indicated in orange.

		4 MeV			6 MeV			8 MeV		
Applicator (cm^2)	**Open Field Insert (cm^2)**	**M**	**S**	**Diff (%)**	**M**	**S**	**Diff (%)**	**M**	**S**	**Diff (%)**
Circular	4 cm Ø	0.578	0.597	1.862	0.905	0.906	0.172	1.079	1.096	1.681
6 x 6	6 x 6	0.752	0.778	2.560	0.932	0.910	2.223	0.961	0.942	1.890
6 x 10	6 x 10	0.898	0.895	0.366	0.962	0.953	0.878	0.979	0.959	1.980
6 x 14	6 x 14	0.910	0.933	2.292	0.967	0.959	0.803	0.971	0.994	2.273
8 x 16	8 x 16	0.980	1.006	2.579	0.987	0.998	1.055	0.986	0.985	0.133
10 x 10	10 x 10	1.000	1.000	0	1.000	1.000	0	1.000	1.000	0
10 x 20	10 x 20	1.008	1.026	1.846	1.006	0.980	2.611	0.995	1.022	2.633
20 x 20	20 x 20	1.029	1.058	2.858	1.016	1.031	1.452	0.991	1.012	2.127
		10 MeV			**12 MeV**			**15 MeV**		
Applicator (cm^2)	**Open Field Insert (cm^2)**	**M**	**S**	**Diff (%)**	**M**	**S**	**Diff (%)**	**M**	**S**	**Diff (%)**
Circular	4 cm Ø	1.159	1.131	2.783	1.266	1.250	1.650	1.127	1.148	2.120
6 x 6	6 x 6	0.978	0.981	0.282	0.986	0.991	0.507	1.001	1.021	2.002
6 x 10	6 x 10	0.985	0.984	0.072	0.993	1.010	1.683	1.003	1.025	2.216
6 x 14	6 x 14	0.973	0.993	1.998	0.984	0.993	0.907	0.989	1.014	2.544
8 x 16	8 x 16	0.984	1.005	2.096	0.999	1.016	1.639	1.004	1.022	1.790
10 x 10	10 x 10	1.000	1.000	0	1.000	1.000	0	1.000	1.000	0
10 x 20	10 x 20	0.986	1.006	2.028	0.994	1.012	1.824	0.990	1.009	1.868
20 x 20	20 x 20	0.973	0.997	2.467	0.983	0.986	0.302	0.972	0.993	2.109

Table 4-6: Measured (light blue) and simulated (light green) cone factors for electron nominal energies of 4-15 MeV at 100 cm SSD. All cone factors were extracted at the respective depth of maximum dose and calculated relative to the output of the 10 x 10 cm² electron applicator. The percentage difference for each energy-applicator combination is indicated in orange.

		4 MeV			6 MeV			8 MeV		
Applicator (cm²)	**Open Field Insert (cm²)**	**M**	**S**	**Diff (%)**	**M**	**S**	**Diff (%)**	**M**	**S**	**Diff (%)**
Circular	4 cm Ø	0.578	0.601	2.262	0.815	0.819	0.410	1.145	1.156	1.111
6 x 6	6 x 6	0.769	0.755	1.432	0.889	0.905	1.600	0.917	0.936	1.899
6 x 10	6 x 10	0.868	0.848	1.994	0.936	0.928	0.792	0.952	0.964	1.178
6 x 14	6 x 14	0.887	0.881	0.639	0.948	0.955	0.779	0.954	0.971	1.752
8 x 16	8 x 16	0.975	0.977	0.205	0.982	0.998	1.566	0.979	1.000	2.113
10 x 10	10 x 10	1.000	1.000	0	1.000	1.000	0	1.000	1.000	0
10 x 20	10 x 20	1.013	1.041	2.764	1.009	1.021	1.186	0.998	1.024	2.525
20 x 20	20 x 20	1.046	1.033	1.343	1.024	1.020	0.332	0.996	1.010	1.364
		10 MeV			**12 MeV**			**15 MeV**		
Applicator (cm²)	**Open Field Insert (cm²)**	**M**	**S**	**Diff (%)**	**M**	**S**	**Diff (%)**	**M**	**S**	**Diff (%)**
Circular	4 cm Ø	1.091	1.100	0.861	1.169	1.146	2.329	1.230	1.238	0.764
6 x 6	6 x 6	0.938	0.960	2.195	0.959	0.962	0.372	0.970	0.959	1.132
6 x 10	6 x 10	0.966	0.984	1.836	0.977	0.990	1.310	0.985	0.983	0.268
6 x 14	6 x 14	0.961	0.983	2.181	0.979	0.992	1.357	0.982	0.984	0.197
8 x 16	8 x 16	0.978	1.005	2.668	0.995	0.997	0.208	1.000	0.982	1.806
10 x 10	10 x 10	1.000	1.000	0	1.000	1.000	0	1.000	1.000	0
10 x 20	10 x 20	0.988	1.010	2.218	0.997	1.015	1.799	0.994	0.977	1.691
20 x 20	20 x 20	0.980	1.004	2.420	0.991	0.980	1.122	0.982	0.968	1.386

Table 4-7: Measured (light blue) and simulated (light green) cutout factors for the 6 x 6 cm² electron applicator and for nominal energies of 4-15 MeV at 95 cm SSD. All cutout factors were extracted at the respective depth of maximum dose and calculated relative to the output of the 10 x 10 cm² electron applicator. The percentage difference for each energy-applicator combination is indicated in orange.

		4 MeV			6 MeV			8 MeV		
Applicator (cm²)	**Open Field Insert (cm²)**	**M**	**S**	**Diff (%)**	**M**	**S**	**Diff (%)**	**M**	**S**	**Diff (%)**
6 x 6	2 x 2	0.730	0.745	1.484	0.760	0.742	1.826	0.878	0.877	0.097
	3 x 3	0.632	0.638	0.629	0.882	0.869	1.252	0.922	0.909	1.294
	6 x 6	0.752	0.778	2.560	0.932	0.910	2.223	0.961	0.942	1.890
10 x 10	10 x 10	1.000	1.000	0	1.000	1.000	0	1.000	1.000	0
		10 MeV			**12 MeV**			**15 MeV**		
Applicator (cm²)	**Open Field Insert (cm²)**	**M**	**S**	**Diff (%)**	**M**	**S**	**Diff (%)**	**M**	**S**	**Diff (%)**
6 x 6	2 x 2	0.945	0.960	1.503	0.950	0.956	0.527	0.916	0.934	1.825
	3 x 3	1.010	0.994	1.635	1.056	1.038	1.837	0.842	0.864	2.184
	6 x 6	0.978	0.981	0.282	0.986	0.991	0.507	1.001	1.021	2.002
10 x 10	10 x 10	1.000	1.000	0	1.000	1.000	0	1.000	1.000	0

Table 4-8: Measured (light blue) and simulated (light green) cutout factors for the 6 x 6 cm² electron applicator and for nominal energies of 4-15 MeV at 100 cm SSD. All cutout factors were extracted at the respective depth of maximum dose and calculated relative to the output of the 10 x 10 cm² electron applicator. The percentage difference for each energy-applicator combination is indicated in orange.

		4 MeV			6 MeV			8 MeV		
Applicator (cm²)	**Open Field Insert (cm²)**	**M**	**S**	**Diff (%)**	**M**	**S**	**Diff (%)**	**M**	**S**	**Diff (%)**
6 x 6	2 x 2	0.730	0.709	2.108	0.835	0.816	1.917	0.990	0.976	1.400
	3 x 3	0.632	0.649	1.729	0.742	0.753	1.108	0.931	0.904	2.736
	6 x 6	0.769	0.755	1.432	0.889	0.905	1.600	0.917	0.936	1.899
10 x 10	10 x 10	1.000	1.000	0	1.000	1.000	0	1.000	1.000	0
		10 MeV			**12 MeV**			**15 MeV**		
Applicator (cm²)	**Open Field Insert (cm²)**	**M**	**S**	**Diff (%)**	**M**	**S**	**Diff (%)**	**M**	**S**	**Diff (%)**
6 x 6	2 x 2	0.877	0.857	1.974	0.912	0.895	1.658	0.923	0.907	1.577
	3 x 3	0.834	0.856	2.187	0.873	0.891	1.788	0.897	0.882	1.514
	6 x 6	0.938	0.960	2.195	0.959	0.962	0.372	0.970	0.959	1.132
10 x 10	10 x 10	1.000	1.000	0	1.000	1.000	0	1.000	1.000	0

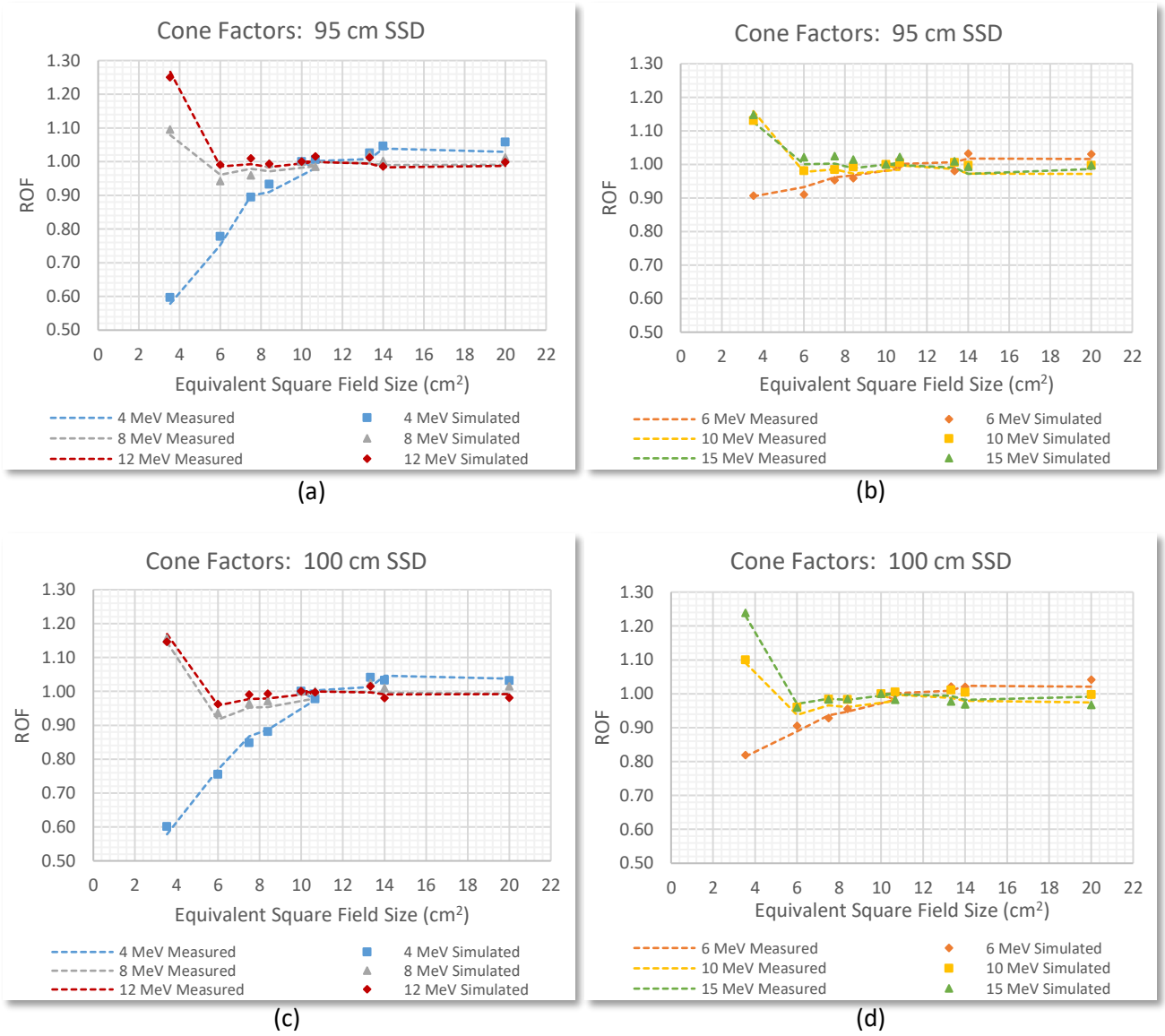

Figure 4-74: Plots of cone factors versus the equivalent square field size for electron energies of 4-15 MeV for an SSD of a-b) 95 cm and c-d) 100 cm. These plots correspond to values given in Table 4-5 and Table 4-6.

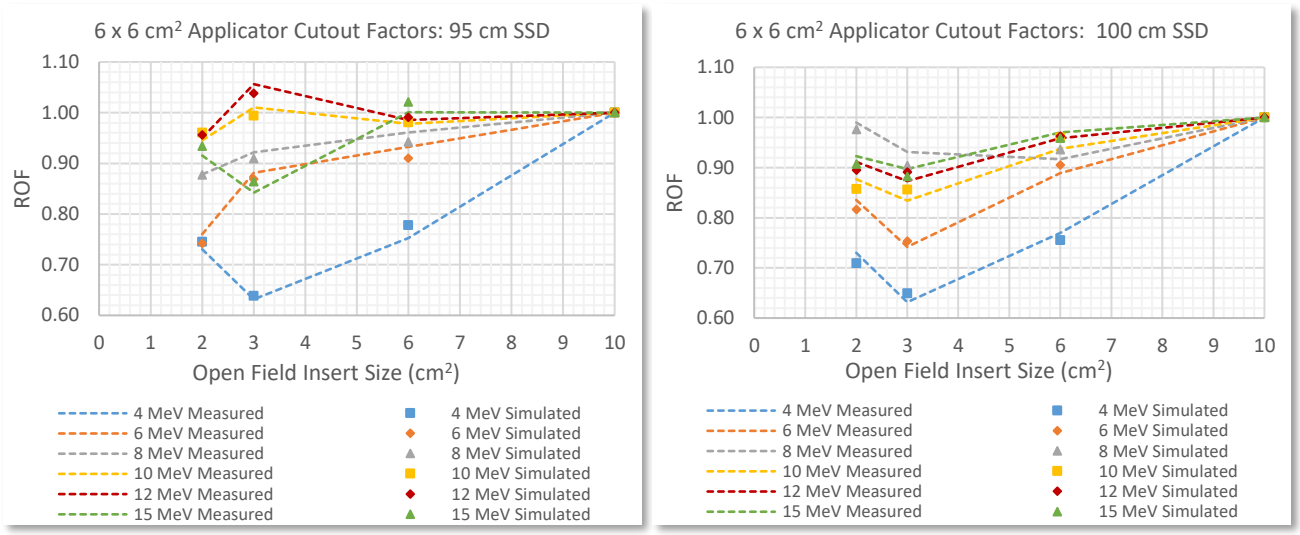

Figure 4-75: Plots of cutout factors for the 6 x 6 cm² electron applicator versus the open field insert size for electron energies of 4-15 MeV for an SSD of a) 95 cm and b) 100 cm. The output factor for the 10 x 10 cm² is shown for sake of reference. These plots correspond to values given in Table 4-7 and Table 4-8.

Chapter 5: Conclusion

5.1 Summary of Results

The aim for this study was to develop and validate an electron Monte Carlo model for an Elekta Synergy® Agility™ linear accelerator. The developed model was validated against measurements for 6 clinical electron nominal energies (4-, 6-, 8-, 10-, 12- and 15 MeV), 11 field sizes (including 9 different electron applicators) and two SSDs (95 cm and 100 cm) using a Gamma criterion of 2%/2mm on CAX PDDs and off-axis profiles. The observations from `BEAMnrc` and `DOSXYZnrc` simulations included the following:

1. The focal spot shape was determined to be circular in intensity distribution for all electron energies using measured inline and crossline off-axis profiles, as well as the shape of the secondary scattering foils as a guideline. The FWHM of the intensity distribution was obtained iteratively from simulations where a value of 1.5 mm was chosen since it produced the best match with measured CAX PDD and off-axis profile data. A change in the FWHM size influenced only the dose in the BU region of PDDs with little to no effect on the dose beyond the depth of maximum dose. This is reflected in the changes observed in the lower energy tails of energy spectra. The flatness of off-axis profiles varied between dose under- and over-estimation in the shoulder regions, whereas penumbra widths varied by 1 mm. Solving the focal spot shape and size by means of simulations eliminates the difficulties posed with the physical measurement of the focal spot.
2. The choice of the initial energy spectrum and its associated parameters mainly influences the match with measured CAX PDDs and off-axis profiles. Monoenergetic- and Gaussian energy spectra sufficed to produce a fit within 2%/2mm beyond the depth of maximum dose, however these spectra did not provide free parameters to alter in order to improve the match in the BU region without altering the dose beyond the depth of maximum dose. The Lévy energy spectrum solved this problem by improving the match in the BU region with the fine adjustment of the scaling parameter.

3. Adjusting the primary scattering foil thickness within the supplied tolerance values produces a small effect on CAX PDD dose and range parameters as well as on profile flatness and penumbra width. Therefore, a value can be chosen arbitrarily within this tolerance range and the energy spectra can be adjusted accordingly to produce a match with measured data.
4. Using a finely tuned Lévy energy spectrum for each nominal electron energy, CAX PDDs were produced with a 100 % pass rate for all fields and at both SSDs using the set 2%/2mm. Minimizing this criterion to 1%/1mm, the combined pass rates for the 10 MeV electron beam dropped to 90.91 % and 96.23 % for SSDs of 95 cm and 100 cm, respectively, where most of the failed points occurred in the BU region.
5. Off-axis profiles were simulated with an overall pass rate of nearly 100 % at both 95 cm and 100 cm SSD, where the failed points mainly occurred in regions of low dose gradients. Simulated small fields showed an improved match with measured data over larger fields, which is attributed to the increase of the skindepth_for_BCA parameter from 3 to 50 mean free paths in both `BEAMnrc` and `DOSXYZnrc` simulations. Using a 1%/1mm criterion, the combined pass rates at 95 cm and 100 SSD for the 10 MeV electron beam were 82.33 % and 85.91 %, respectively, with most failed points occurring in the umbra regions.
6. The developed model was able to simulate cone and cutout factors at 95 cm and 100 cm SSD with an average difference to measured factors of less than 2 %.
7. Overall, `BEAMnrc` could successfully be used to model the linac accurately and consequently `DOSXYZnrc` water simulations reflected a benchmarked model within 2%/2mm of measured data.

5.2 Future Work

Even though this study covered a lot of aspects involving beam modelling, some future work still lies ahead:

1. ***Quantification of energy spectra***. The energy spectra at $Z = 95$ cm can be quantified to relate changes in dose distributions (such as the changes in the BU region) to changes in spectra. This can then be used to determine a precise quantified method to determine the initial energy spectra as defined at $Z = 0$ cm, which then eliminates the current *trial-and-error* method. The quantification can be difficult and might need the input from a mathematical statistician.

2. ***Improving the match in umbra regions.*** The dose in the umbra regions of profiles (due to Bremsstrahlung) was underestimated by the model and can be improved by adjusting thicknesses of applicator scrapers. Though the dose/DTA discrepancies in the umbra regions were less than 2%/2mm, the match with measured data can be improved.
3. ***Verification of measured and simulated ROFs.*** Since the general trend for a decrease in ROF with a decrease in field size below 10 x 10 cm^2 was not observed for all electron energies, this may suggest that the model need some additional tweaking and that the measured ROFs must be verified.
4. ***Application of the developed benchmarked model.*** The model developed within this study is already used within a PhD study at the Medical Physics Department at the University of the Free State. The model was adapted in such a manner that electrons are only collimated by the MLC and the Jaws (basically only the electron applicator was removed from the model). Data are simulated and measured at shorter SSDs (typically 60-70 cm) than the nominal electron SSD for regular and irregular fields, as well as some patient plans. This aims to work towards the general objective to perform MERT at UAH.

REFERENCES

1. Mayles, P., Nahum, A. & Rosenwald, J. C. *Handbook of Radiotherapy Physics: Theory and Practice*. (Taylor & Francis, First Edition, 2008). doi:10.1118/1.2969650
2. Podgorsak, E. B. *Radiation Physics for Medical Physicists*. (Springer, Second Edition, 2010). doi:10.1007/978-1-4614-2146-7{_}2
3. Khan, F. M., Gibbons, J. P. & Sperduto, P. W. *Khan's Treatment Planning in Radiation Oncology*. (Wolters Kluwer, Fourth Edition, 2016).
4. Podgorsak, E. B. *Radiation Oncology Physics: A Handbook for Teachers and Students*. *International Atomic Energy Agency* (IAEA, 2005). doi:10.1038/sj.bjc.6604224
5. Khan, F. M. *et al.* Clinical electron-beam dosimetry: Report of AAPM Radiation Therapy Committee Task Group No. 25. *Med. Phys.* **18,** 73–109 (1991).
6. Karzmark, C. J., Nunan, C. S. & Tanabe, E. *Medical Electron Accelerators*. (McGraw-Hill, Incorporated, Health Professions Division, 1993).
7. Mihailidis, D. Therapeutic Electron Beams: Clinical Dosimetry and AAPM TG-70.
8. Piotrowski, T., Milecki, P., Skórska, M. & Fundowicz, D. Total skin electron irradiation techniques: A review. *Postep. Dermatologii i Alergol.* **30,** 50–55 (2013).
9. Papaconstadopoulos, P. & Seuntjens, J. A fast and accurate source model for energy and intensity modulated electron beams. in *Fifty-Eighth Annual Meeting of the Canadian Organization of Medical Physicists and the Canadian College of Physicists in Medicine* 4619–4647 (2012).
10. Papaconstadopoulos, P. & Seuntjens, J. A source model for modulated electron radiation therapy using dynamic jaw movements. *Med. Phys.* **40,** 1–12 (2013).
11. Grevillot, L., Bertrand, D., Dessy, F., Freud, N. & Sarrut, D. Monte Carlo based treatment planning for modulated electron beam radiation therapy. *Phys. Med. Biol.* **46,** 2177–2199 (2001).
12. Mihaljevic, J., Soukup, M., Dohm, O. & Alber, M. Monte Carlo simulation of small electron fields collimated by the integrated photon MLC. *Phys. Med. Biol.* **56,** 829–843 (2011).
13. Surucu, M., Klein, E. E., Mamalui-Hunter, M., Mansur, D. B. & Low, D. a. Planning tools for modulated electron radiotherapy. *Med. Phys.* **37,** 2215–2224 (2010).
14. Connell, T. *et al.* Delivery validation of an automated modulated electron radiotherapy plan. *Med. Phys.* **41,** 061715-1-061715-13 (2014).
15. Al-Yahya, K., Verhaegen, F. & Seuntjens, J. Design and dosimetry of a few leaf electron

collimator for energy modulated electron therapy. *Med. Phys.* **34,** 4782–4791 (2007).

16. Alexander, A., Soisson, E., Renaud, M. A. & Seuntjens, J. Direct aperture optimization for FLEC-based MERT and its application in mixed beam radiotherapy. *Med. Phys.* **39,** 4820–4831 (2012).
17. Chatelain, C. *et al.* Dosimetric properties of an amorphous silicon EPID for verification of modulated electron radiotherapy. *Med. Phys.* **40,** 1–15 (2013).
18. Henzen, D. *et al.* Forward treatment planning for modulated electron radiotherapy (MERT) employing Monte Carlo methods. *Med. Phys.* **41,** 1–11 (2014).
19. Alexander, A. & Seuntjens, J. Inverse treatment planning for modulated electrons and mixed photon and electron radiotherapy. in *Fifty-Eighth Annual Meeting of the Canadian Organization of Medical Physicists and the Canadian College of Physicists in Medicine* 4619–4647 (2012).
20. Martin, J. M. *et al.* Modulated Electron Radiation Therapy (MERT) for the Treatment of Large Scalp Lesions: A Dosimetric Feasibility Study. *Int. J. Radiat. Oncol.* **90,** S192 (2014).
21. Henzen, D. *et al.* Monte Carlo based beam model using a photon MLC for modulated electron radiotherapy. *Med. Phys.* **41,** 1–11 (2014).
22. Papanikolaou, N. *et al. AAPM report 85:Tissue Inhomogeneity Corrections for Megavoltage Photon Beams. Report of the AAPM radiation therapy committee task group 65. Medical Physics* (2004).
23. Eyges, L. Multiple Scattering with Energy Loss. *Phys. Rev.* **74,** 1534 (1948).
24. Molière, V. Theorie der Streuung schneller geladener Teilchen I. *Z. Naturforschg* **21,** 133–145 (1947).
25. Molière, V. Theorie der Streuung schneller geladener Teilchen II. *Z. Naturforschg* **34,** (1948).
26. Goudsmit, S. & Saunderson, J. Multiple Scattering of Electrons. *Phys. Rev.* **57,** 24 (1940).
27. Goudsmit, S. & Saunderson, J. Multiple Scattering of Electrons II. *Phys. Rev.* **58,** 36 (1940).
28. Rogers, D. & Bielajew, A. Monte Carlo Techniques of Electron and Photon Transport for Radiation Dosimetry. in *The Dosimetry of Ionizing Radiation* (eds. Kase, K., Bjarngard, B. & Attix, F.) (Academic Press, 1990).
29. ICRU. Radiation Dosimetry: Electron Beams with Energies Between 1 and 50 MeV. *Report 35* 1–168 (1984). doi:10.1118/1.595780
30. Rustgi, S. N. & Rodgers, J. E. Analysis of the bremsstrahlung component in 6-18 MeV electron beams. *Med. Phys.* **14,** 884–888 (1987).

31. Sorcini, B. B., Hyödynmaa, S. & Brahme, A. The role of phantom and treatment head generated bremsstrahlung in high-energy electron beam dosimetry. *Phys. Med. Biol.* **41,** 2657–2677 (1996).
32. Doppke, K. P. *et al. CLINICAL ELECTRON-BEAM DOSIMETRY*.
33. Nath, R. *et al. AAPM code of practice for radiotherapy accelerators: Report of AAPM Radiation Therapy Task Group No. 45*. *Medical Physics* **21,** (1994).
34. Chetty, I. J. *et al.* Report of the AAPM Task Group No. 105: Issues associated with clinical implementation of Monte Carlo-based photon and electron external beam treatment planning. *Med. Phys.* **34,** 4818–4853 (2007).
35. Andreo, P. Broad Beam Approaches to Dose Computation and their Limitations. in *The Computation of Dose Distributions in Electron Beam Radiotherapy* (ed. Nahum, A. E.) 128 (Sweden: Miniab/gotab, 1985).
36. Brahme, A. Brief review of current algorithms for electron beam dose planning. in *The Computation of Dose Distributions in Electron Beam Radiotherapy* (ed. Nahum, A. E.) 271 (Sweden: Miniab/gotab, 1985).
37. Huizenga, H. & den Hoed, D. Electron beam dose calculation algorithms review. in (1990). doi:10.13140/2.1.1064.2248
38. Sternick, E. Algorithms for computerized treatment planning. in *Practical Aspects of Electron Beam Treatment Planning Symposium* 52–69 (1977).
39. Möller, T. R. *et al.* ICRU Report 42: Use of Computers in External Beam Radiotherapy Procedures with High-Energy Photons and Electrons. *J. Int. Comm. Radiat. Units Meas.* **os22,** 65–67 (1987).
40. Laughlin, J. S. *et al.* Some Physical Aspects of Electron Beam Therapy. *Radiology* **60,** 165–185 (1953).
41. Laughlin, J. S. High Energy Electron Treatment Planning for Inhomogeneities. *Br. J. Radiol.* **38,** 143–147 (1965).
42. Bagne, F. Electron beam treatment-planning system. *Med. Phys.* **3,** 31–38 (1976).
43. Shabason, L. & Hendee, W. An analytic expression for central axis electron depth dose distributions. *Int. J. Radiat. Oncol. Biol. Phys.* **5,** 263 (1979).
44. Fehrentz, D., Kimmig, B. & Kepper, E. No Title. (1977).
45. Jette, D., Lanzl, L. H., Rozenfeld, M. & Pagnamenta, A. Analytic representation of electron central-axis depth dose data. *Med. Phys.* **8,** 877–881 (1981).

46. Holt, J. *et al.* Practical Aspects of Electron Beam Treatment Planning. *Med. Phys. Monogr.* **2,** 52 (1978).
47. Dahler, A., Baker, A. S. & Laughlin, J. S. COMPREHENSIVE ELECTRON-BEAM TREATMENT PLANNING. *Ann. N. Y. Acad. Sci.* **161,** 198–213 (1969).
48. Boone, M., Jardine, J., Wright, A. & Tapley, N. High-Energy Electron Dose Perturbations in Regions of Tissue Heterogeneity. *Radiology* **88,** 1136–1145 (1967).
49. Almond, P., Wright, A. & Boone, M. High-Energy Electron Dose Perturbations in Regions of Tissue Heterogeneity. *Radiology* **88,** 1146–1153 (1967).
50. Boone, M., Almond, P. & Wright, A. No Title. *Ann. N. Y. Acad. Sci.* **161,** 214 (1969).
51. Hogstrom, K. R., Mills, M. D. & Almond, P. R. Electron beam dose calculations. *Phys. Med. Biol.* **26,** 445–59 (1981).
52. Hogstrom, K. R. & Almond, P. Comparison of Experimental and Calculated Dose Distributions. Electron Beam Dose Planning at the M.D. Anderson Hospital. *Acta Radiol. Suppl.* **364,** 89–99 (1983).
53. Hogstrom, K. R. *et al.* Dosimetric evaluation of a pencil-beam algorithm for electrons employing a two-dimensional heterogeneity correction. *Int. J. Radiat. Oncol. Biol. Phys.* **10,** 561–569 (1984).
54. Brahme, A., Lax, I. & Andreo, P. Electron beam dose planning using discrete gaussian beams: Mathematical background. *Acta Oncol.* **20,** 147–158 (1981).
55. Lax, I. & Brahme, A. Electron beam dose planning using gaussian beams: Energy and spatial scaling with inhomogeneities. *Acta Oncol. (Madr).* **24,** 75–85 (1985).
56. Ade, N. & du Plessis, F. C. P. Measurement of the influence of titanium hip prosthesis on therapeutic electron beam dose distributions in a novel pelvic phantom. *Phys. Medica* **42,** 99–107 (2017).
57. Jabbari, N., Barati, A. H. & Rahmatnezhad, L. Multiple-source models for electron beams of a medical linear accelerator using BEAMDP computer code. *Reports Pract. Oncol. Radiother.* **17,** 211–219 (2012).
58. K G Hogstrom, J A Antolak, R J Kudchadker, C Ma, D. D. L. Modulated Electron Therapy. in *Modulated Electron Therapy* 749–782 (2003).
59. Mohammed, M., El Bardouni, T., Boukhal, H., Azahra, M. & Chakir, E. Implementation of the EGSnrc / BEAMnrc Monte Carlo code - Application to medical accelerator SATURNE43. *Int. J. Innov. Appl. Stud.* **6,** 635–641 (2014).

60. Ma, C. M., Faddegon, B. A., Rogers, D. W. O. & Mackie, T. R. Accurate characterization of Monte Carlo calculated electron beams for radiotherapy. *Med. Phys.* **24,** 401 (1997).
61. Spezi, E. & Lewis, G. An overview of Monte Carlo treatment planning for radiotherapy. *Radiat. Prot. Dosimetry* 1–7 (2008). doi:10.1093/rpd/ncn277
62. Zoubair, M. *et al.* Application of variance reduction techniques in Monte Carlo simulation of clinical electron linear accelerator. *Nucl. Inst. Methods Phys. Res. A* **661,** 93–97 (2012).
63. Rogers, D. W. O. BEAMnrc: a code to simulate radiotherapy external beam sources. 1–31 (2007).
64. Ojala, J., Hyödynmaa, S. & Pitkänen, M. BEAMnrc Monte Carlo modelling of linear accelerator using parallel computing grid - validation of a common, fixed geometry model for photon and electron beams. in *Proceedings of the XVIth ICCR* (2010).
65. Jiang, S. B., Kapur, A. & Ma, C. Electron beam modeling and commissioning for Monte Carlo treatment planning. *Med. Phys.* **27,** 180–191 (2000).
66. Ali, O. a., Willemse, C. a., Shaw, W., O'Reilly, F. H. J. & du Plessis, F. C. P. Monte Carlo electron source model validation for an Elekta Precise linac. *Med. Phys.* **38,** 2366 (2011).
67. Jabbari, N. & Hashemi-Malayeri, B. Monte Carlo modeling of electron beams from a Neptun 10PC medical linear accelerator. *Nukleonika* **54,** 233–238 (2009).
68. Bielajew, A. F., Hirayama, H., Nelson, W. R. & Rogers, D. W. O. *History , overview and recent improvements of EGS4 National Laboratory for High Energy Physics*. (1994).
69. I Kawrakow, E Mainegra-Hing, DWO Rogers, F Tessier, B. W. *The EGSnrc Code System : Monte Carlo Simulation of Electron and Photon Transport*. (2011).
70. Reynaert, N., Schaart, D. & Van Der Marck, S. Monte Carlo treatment planning for photon and electron beams. *Radiat. Phys. …* (2007).
71. James, F. RANLUX : A Fortran implementation of the high-quality pseudorandom number generator of Lüscher. *Comput. Phys. Commun.* **79,** 111–114 (1994).
72. Lüscher, M. A portable high-quality random number generator for lattice field theory simulations. *Comput. Phys. Commun. Phys. Commun.* **79,** 100–110 (1994).
73. Dabrowska-Boruch, A., Gancarczyk, G. & Wiatr, K. IMPLEMENTATION OF A RANLUX BASED PSEUDO-RANDOM NUMBER GENERATOR IN FPGA USING VHDL AND IMPULSE C Agnieszka Da ˛ browska-Boruch , Grzegorz Gancarczyk Kazimierz Wiatr. *Comput. Informatics* **32,** 1272–1292 (2013).
74. Rogers, D. W. O., Walters, B. & Kawrakow, I. *BEAMnrc Users Manual*. *NRCC Report PIRS-*

0509(A)revL **509,** (2011).

75. Shaw, W. & Du Plessis, F. Evaluation of a Commercial Radiation Oncology Treatment Planning System Against Monte Carlo Simulated Dose Distributions. (University of the Free State, 2007).
76. Hirayama, H., Namito, Y., Bielajew, A., Wilderman, S. J. & Nelson, W. R. Pegs User Manual. *SLAC 265 Appendix 3* 1–38 (2005). Available at: http://rcwww.kek.jp/research/egs/epub/manuals/append3.html.
77. Berger, M. Monte Carlo caluclation of the penetration and diffusion of fast charged particles. *Methods Comput. Phys.* **1,** 135–215 (1963).
78. Bielajew, A. & Rogers, D. PRESTA: The Parameter Reduced Electron-Step Transport Algorithm for electron Monte Carlotransport. *Nucl. Instruments Methods Phys. Res. B* **18,** 165–181 (1987).
79. Lockwood, G., Ruggles, L., MIller, G. & Halbleib, J. *Calorimetric measurement of electron energy deposition in extended media - Theory versus measurement, Sandia report SAND79-0414*. (1980).
80. Bethe, H. Molière's Theory of Multiple Scattering. *Phys. Rev.* **89,** (1953).
81. Sheikh-Bagheri, D., Kawrakow, I., Walters, B. & Rogers, D. W. O. Monte Carlo Simulations: Efficiency Improvement Techniques and Statistical Considerations. *Integr. New Technol. into Clin. Monte Carlo Image-Guided Radiat. Ther.* 71–91 (2006).
82. Metcalfe, P., Kron, T. & Hoban, P. *The Physics of Radiotherapy X-Rays and Electrons*. (Medical Physics Publishing Corporation, 2007).
83. Walters, B., Kawrakow, I. & Rogers, D. W. O. *DOSXYZnrc Users Manual*. *NRCC Report PIRS-0794revB* (2011). doi:10.1118/1.4773883
84. Rogers, D. W. O., Kawrakow, I., Seuntjens, J. P., Walters, B. R. B. & Mainegra-Hing, E. *NRC user codes for EGSnrc*. *NRCC Report PIRS-702 (RevC)* **702,** (2016).
85. Rogers, D. W. O. Fifty years of Monte Carlo simulations for medical physics. *Phys. Med. Biol.* **51,** R287–R301 (2006).
86. Faddegon, B. A. *et al.* Accuracy of EGSnrc, Geant4 and PENELOPE Monte Carlo systems for simulation of electron scatter in external beam radiotherapy. *Phys. Med. Biol.* **54,** 6151–6163 (2009).
87. Chetty, I. J. *et al.* Report of the AAPM Task Group No. 105: Issues associated with clinical implementation of Monte Carlo-based photon and electron external beam treatment

planning. *Med. Phys.* **34,** 4818–4853 (2007).

88. Hogstrom, K. R. & Almond, P. R. Review of electron beam therapy physics. *Phys. Med. Biol.* **51,** 455–489 (2006).
89. Fippel, M. & Fippel, M. Fast Monte Carlo dose calculation for photon beams based on the VMC electron algorithm. *Med. Phys.* **26,** 1466–1475 (1999).
90. Smit, J. J. L. Development and validation of an X-ray model for an Elekta Precise multileaf collimator to be used in Monte Carlo dose calculations. (University of the Free State, 2015).
91. Fix, M. *et al.* A multiple source model for 6 MV photon beam dose calculations using Monte Carlo. *Phys. Med. Biol.* **46,** 1407–1427 (2001).
92. Sego, Z. Multiple-source models for the beams from an Elekta SL25 clinical accelerator. (Department of Physics,Carleton University, 2006). doi:10.22215/etd/2006-07736
93. Chaves, A., Lopes, M. & Alves, C. Basic dosimetry of radiosurgery narrow beams using Monte Carlo simulations: a detailed study of depth of maximum dose. *Med. Phys.* **30,** 2904–2911 (2003).
94. Low, D. A. Gamma Dose Distribution Evaluation Tool. *J. Phys. Conf. Ser.* **250,** 1–11 (2010).
95. Björk, P., Knöös, T. & Nilsson, P. Influence of initial electron beam parameters on Monte Carlo calculated absorbed dose distributions …. *Phys. Med. Biol.* **47,** 4019–4041 (2002).
96. Huang, V. W., Seuntjens, J., Devic, S. & Verhaegen, F. Experimental determination of electron source parameters for accurate Monte Carlo calculation of large field electron therapy. *Phys Med Biol* **50,** 779–786 (2005).
97. Wang, L. L. W. & Leszczynski, K. Estimation of the focal spot size and shape for a medical linear accelerator by Monte Carlo simulation. *Med. Phys.* **34,** 485–488 (2007).
98. Rodrigues, A., Sawkey, D., Yin, F. & Wu, Q. A Monte Carlo simulation framework for electron beam dose calculations using Varian phase space files for TrueBeam Linacs. *Med. Phys.* **42,** 2389–2403 (2015).
99. Schreiber, E. C. & Faddegon, B. A. Sensitivity of large-field electron beams to variations in a Monte Carlo accelerator model. *Physics in Medicine and Biology* **50,** 769–778 (2005).
100. Kim, S. Characteristics of elliptical sources in BEAMnrc Monte Carlo system: Implementation and application. *Med. Phys.* **36,** 1046–1052 (2009).
101. Jabbari, K., Anvar, H. S., Tavakoli, M. B. & Amouheidari, A. Monte Carlo Simulation of Siemens ONCOR Linear Accelerator with BEAMnrc and DOSXYZnrc Code. *J. Med. Signals Sens.* **3,** 172–179 (2013).

102. Chibani, O., Moftah, B. & Ma, C. On Monte Carlo Modeling of Megavoltage Photon Beams: A Revisited Study on Beam Parameters Sensitivity. *Med. Phys.* **38,** 188–201 (2010).
103. Udale, M. A Monte Carlo investigation of surface doses for broad electron beams. *Phys. Med. Biol.* **33,** 939–954 (1988).
104. Akino, Y., Zhu, T. C. & Das, I. J. Parameterization of electron beam output factor. *Phys. Medica* **31,** 420–424 (2015).
105. Deng, J., Jiang, S. B., Pawlicki, T., Li, J. & Ma, C.-M. Derivation of electron and photon energy spectra from electron beam central axis depth dose curves. *Phys. Med. Biol.* **46,** 1429–1449 (2001).
106. Maskani, R., Tahmasebibirgani, M., Hoseini-Ghahfarokhi, M. & Fatahiasl, J. Determination of Initial Beam Parameters of Varian 2100 CD Linac for Various Therapeutic Electrons Using PRIMO. *Asian Pacific J. Cancer Prev.* **16,** 7795–7801 (2015).
107. Oprea, M., Constantin, C., Mihailescu, D. & Borcia, C. A Monte Carlo Investigation of the Influence of Initial Electron Beam CHaracteristics on the Absorbed DOse Distributions Obtained With a 9 MeV IORT Accelerator. *UPB Sci. Bull. Ser. A* **74,** (2012).
108. Rogers, D. W. O. *et al.* BEAM: a Monte Carlo code to simulate radiotherapy treatment units. *Med. Phys.* **22,** 503–524 (1995).
109. Fix, M. K. *et al.* Generalized eMC implementation for Monte Carlo dose calculation of electron beams from different machine types. *Phys. Med. Biol.* **58,** 2841–2859 (2013).
110. Campos, L. T., Braz, D., Antonio, L. & Rosa, R. Monte Carlo Simulations of Regular Fields for Electron Beams from a Medical Accelerator using EGSnrc. in *International Nuclear Atlantic Conference* (2009).
111. Landau, L. On the energy loss of fast particles by ionization. *J. Phys.* **8,** 201–205 (1944).
112. Nolan, J. P. Maximum Likelihood Estimation and Diagnostics for Stable Distributions. in *Lévy Processes: Theory and Applications* (eds. Barndorff-Nielsen, O. E., Resnick, S. I. & Mikosch, T.) 379–400 (Birkhäuser Boston, 2001). doi:10.1007/978-1-4612-0197-7_17
113. Ma, C. & Rogers, D. W. O. *BEAMDP Users Manual*. *NRCC Report PIRS-0509(C)revA* (2009).
114. Das, I. J. *et al.* Accelerator beam data commissioning equipment and procedures: Report of the TG-106 of the Therapy Physics Committee of the AAPM. *Med. Phys.* **35,** 4186–4215 (2008).
115. International Specialty Products. Gafchromic XR-Series. 8 (2010). Available at: http://www.elimpex.com/new/products/radiation_therapy/Gafchromic/content/GAFCHRO

MIC XR Series.pdf.

116. Setilo, I. & Du Plessis, F. Dosimetric comparison between XR-RV3 and EBT2 radiochromic film in megavoltage photon beams. *Int. J. Radiat. Res.* **14,** 149–152 (2015).

SUMMARY

Though the use of clinical electron beams in Radiotherapy for the treatment of cancer has been overwhelmed by photon delivering techniques such as intensity modulated Radiotherapy (IMRT) and Volumetric Modulated Arc Therapy (VMAT) at the Universitas Annex Hospital (UAH) in Bloemfontein, South Africa, the interest within a particular research group at the Medical Physics Department of the University of the Free state has shifted towards the implementation of modulated electron Radiotherapy (MERT). This requires an accurate Monte Carlo based electron model of the involved linear accelerator (linac) which was not available at the current time and brought about the motivation for this project. That is, to develop and validate a Monte Carlo (MC) `EGSnrc` based electron model for an Elekta Synergy® 160-leaf Agility™ linac. The requirement for this model was that it should be able to produce dose distributions within 2%/2mm of measured linac distributions in water. Since the model would be MC based, it is expected that it will be able to produce dose distributions in the presence of heterogenous media with similar accuracy, though not verified within this study.

`EGSnrc`/`BEAMnrc` was used to model the components in the linac when in electron mode using the supplied component modules (CMs). This includes the electron window, primary scattering foil(s), primary collimator, secondary scattering foils, dual ionization chamber, light field mirror, multi-leaf collimator (MLC), Jaw, screen and electron applicator(s). Linac components were modelled using vendor supplied information under a non-disclosure agreement with Elekta. MLC and Jaw positions for each electron energy-applicator combination were obtained by recording log files, which supplied the relative positions at isocentre. Initial electron beam properties including the focal spot shape and size and energy spectrum were not specified by the vendor and therefore required additional investigation. The focal spot shape was determined from measured inline and crossline off-axis profiles (OAPs). The focal spot was furthermore assumed to be represented by a Gaussian intensity distribution with a full width at half maximum (FWHM) determined iteratively from simulations, where the FHWM producing the best match with measure OAPs was chosen. A monoenergetic and two polyenergetic (Gaussian and asymmetrical negative skew distribution) initial energy spectra were investigated to determine the spectrum that would produce the best fit with measured data. A unit-density 30 x 30 x 15 cm^3 phantom was constructed in `EGSnrc`/`DOSXYZnrc`, where the phase space files produced by `BEAMnrc` was used as source input to calculate the dose distributions in water with a maximum statistical uncertainty of 1 %. Six electron nominal energies (4, 6, 8, 10, 12 and 15

MeV), 11 field sizes (2 x 2 cm^2, 3 x 3 cm^2, 6 x 6 cm^2, 6 x 10 cm^2, 6 x 14 cm^2, 8 x 16 cm^2, 10 x 10 cm^2, 10 x 20 cm^2, 14 x 14 cm^2, 20 x 20 cm^2 and a 4 cm circular field) and two source-to-surface distances (SSDs) of 95 cm and 100 cm were evaluated using central axis (CAX) percentage depth dose (PDD) curves, OAPs and relative output factors (ROFs). The same electron beam setups were measured on the linac within a water tank using a cylindrical ionization chamber (CC13, IBA Dosimetry, Bartlett, TN) for broad field OAPs, a plane parallel chamber (Roos® Chamber Type 34001, PTW, Freiburg, Germany) for broad field CAX PDDs and ROFs, and a pinpoint chamber (CC01, IBA Dosimetry, Bartlett, TN) for small field OAPs, CAX PDDs and ROFs. MATLAB® was used to write scripts to process measured and simulated data, as well as to compare relevant dose data using a Gamma analysis with a dose/distance-to-agreement criteria of 2%/2mm.

The CMs `BEAMnrc` supplied in could successfully be used to accurately model each component within the linac. Since the design of secondary scattering foils exemplified radial symmetry and measured inline and crossline OAPs agreed within 0.4 % of each other (normalized to the dose on the central axis), the focal spot was assumed to be circular in shape. Furthermore, a focal spot FWHM (inline and crossline) of 1.50 mm was chosen for all electron nominal energies as deduced iteratively from simulations. Though the monoenergetic and Gaussian initial energy spectra could produce a CAX PDD within 2%/2mm beyond the depth of maximum dose, larger dose discrepancies in the build-up (BU) region was observed and could not be solved by adjusting parameters in these spectra. However, the experimental asymmetrical negative skew (Lévy) energy spectrum provided a valuable free parameter (scaling parameter) which, by fine adjustment, solved the dose discrepancies in the BU region without significantly altering the CAX PDD beyond the depth of maximum dose. The optimum scaling parameter for each nominal electron energy was obtained iteratively from simulations. In addition, the effect of a change in primary scattering foil thickness and optimal MLC/JAW positions on CAX PDD and OAPs were investigated. A 100 % Gamma pass rate was achieved for both CAX PDDs and OAPs for all electron nominal energies, fields and SSDs under a 2%/2m criterion. The 10 MeV model was also tested under a stringent criterion of 1%/1mm which produced a minimum pass rate of 90.91 % for CAX PDDs and 82.33 % for OAPs, where most of the failed points occurred in the BU and penumbra/umbra regions, respectively. ROFs were calculated with maximum difference of 2.858 %.

The `EGSnrc` code package could successfully be utilized to model Elekta's Synergy® linac according to vendor supplied schematics. The focal spot properties could be determined from measured OAPs

and iterative simulations, which circumvented the difficulty associated with the physical measurement of the focal spot. Furthermore, the Lévy energy spectrum provided an adjustable parameter which improved the match in the BU region of dose distributions. The developed electron model complied with measured PDDs and OAPs with a 100 % pass rate using a 2%/2mm criterion, and complied with measured ROFs within 3 %.

ACKNOWLEDGEMENTS

I thank my study leader, Dr Freek du Plessis, who granted me the opportunity to do my MMedSc and from whom I have learned a lot during the past two years. You have always believed in me and allowed me to perform my research within my own bounds, while guiding me throughout the whole process. Your contributions are of highest value to me.

A very special thanks to my senior and fellow intern Medical Physicists at the Universitas Annex Hospital: Lourens, Dr W Shaw, Dedri, Cobus, Louise and Natasha. Without your inputs this study most definitely would not have been possible. Dr Shaw for setting an outstanding example and for providing me the required additional guidance, Dedri for always believing in me and for the lovely conversations that we have had (in particular the 56th SAAPMB congress in Pretoria), Cobus for the kind support and for including me in your beer brewery process, Louise for helping me with water tank measurements, and Natasha for her continued believe in my capabilities (also, the abundance of Scarlet pub sessions that I had with Louise and Natasha…). Lourens, I am left without words to describe what you have meant to me during the past two years. You have shared your office with me without hesitation, and quickly we have grown a relationship beyond that of Medical Physics. We have shared a great deal of conversations about music and did a lot of "online music window shopping" during lunch (which was probably one of the highlights of the past two years). You have also introduced me to Star Wars and you taught me that making lame jokes is "cool". You shared many other things with me and provided the continued believe and guidance that I so desperately (probably unknowingly) needed…it has been an absolute privilege. I am extremely grateful to you. Thank you all.

Lastly, to my family (my Father, Mother, Brother, Grandmother and late Grandfathers); you are my motivation. Everything I do is made possible due to your contributions. The sacrifices we have made for each other over the past six years have been difficult, but it was worth it. Thank you for your support, guidance, love and believe. This is for you.

“This research project was funded by the South African Medical Research Council (MRC) with funds from National Treasury under its Economic Competitiveness and Support Package.”

“Research and any publication thereof is the result of funding provided by the Medical Research Council of South Africa in terms of the MRC’s Flagship Awards Project SAMRC-RFA-UFSP-01-2013/HARD.”

APPENDIXES

1. `BEAmnrc` *input file for the 12 MeV invariant model* (`.egsinp`)

```
12 MeV                                                          #!GUI1.0
AIR700ICRU
0, 0, 0, 0, 0, 2, 0,  IWATCH ETC.
10000000, 98, 71, 500, 1, 200, 2, 0,  NCASE ETC.
-1, 19, -0.15, 0, 0, 1, 0, -0.15, 0.0, 0.0,  IQIN, ISOURCE + OPTIONS
1, SPECTRUM
/home/beamnrc/egsnrc_mp/BEAM_Synergy_Electron_Upper/12MeV 0.05
12.985.spectrum
1
0, 0, 0.7, 0.01, 0, 0, ,  0 , ECUT,PCUT,IREJCT,ESAVE
0, 0, 0, 0, 0,  PHOTON FORCING
1, 6,  SCORING INPUT
0,0
0,  DOSE COMPONENTS
0.0, Z TO FRONT FACE
*********** start of CM CONESTAK with identifier e_window  ***********
2, RMAX
Electron Window
0, 1.9, ZMIN, RBN
3, NUMBER OF LAYERS
0.85, 0.5, 0.5,
0.0125, 0.6, 0.6,
0.1375, 0.6, 0.6,
0.7, 0.01, 0, 2, OUTER WALL
CU700ICRU
0.7, 0.01, 0, 23,
AIR700ICRU
0.7, 0.01, 0, 2,
CU700ICRU
0.7, 0.01, 0, 1,
NI700ICRU
0.7, 0.01, 0, 2,
CU700ICRU
0.7, 0.01, 0, 23,
AIR700ICRU
0.7, 0.01, 0, 2,
CU700ICRU
*********** start of CM CONESTAK with identifier primscat  ***********
2, RMAX
Primary Scattering Foil
1.2, 1.9, ZMIN, RBN
1, NUMBER OF LAYERS
0.0108, 0.7, 0.7,
0.7, 0.01, 0, 3, OUTER WALL
SSTEEL_8P03_700
0.7, 0.01, 0, 4,
TA700ICRU
0.7, 0.01, 0, 3,
SSTEEL_8P03_700
*********** start of CM CONESTAK with identifier primcol  ***********
```

```
7, RMAX
Primary Collimator
1.5, 0, ZMIN, RBN
1, NUMBER OF LAYERS
10.1, 0.3712, 2.8707,
0.7, 0.01, 0, 23,
AIR700ICRU
0.7, 0.01, 0, 5,
WNIFE700
*********** start of CM FLATFILT with identifier secscat  ***********
4, RMAX
Secondary Scattering Foils
13.7, ZMIN
6, NUMBER OF LAYERS
1, 2.1048, # CONES, ZTHICK OF LAYER 1
3.7,
3.7,
2, 0.001, # CONES, ZTHICK OF LAYER 2
0.05, 3.7,
0.05, 3.7,
2, 0.055, # CONES, ZTHICK OF LAYER 3
1.25, 3.7,
1.25, 3.7,
2, 0.04, # CONES, ZTHICK OF LAYER 4
2.25, 3.7,
2.25, 3.7,
1, 0.0075, # CONES, ZTHICK OF LAYER 5
3.7,
3.7,
2, 0.001, # CONES, ZTHICK OF LAYER 6
0.05, 3.7,
0.05, 3.7,
0.7, 0.01, 0, 23,
AIR700ICRU
0.7, 0.01, 0, 1,
AL700ICRU
0.7, 0.01, 0, 1,
AL700ICRU
0.7, 0.01, 0, 23,
AIR700ICRU
0.7, 0.01, 0, 1,
AL700ICRU
0.7, 0.01, 0, 1,
AL700ICRU
0.7, 0.01, 0, 23,
AIR700ICRU
0.7, 0.01, 0, 1,
AL700ICRU
0.7, 0.01, 0, 1,
AL700ICRU
0.7, 0.01, 0, 23,
AIR700ICRU
0.7, 0.01, 0, 1,
AL700ICRU
0.7, 0.01, 0, 1,
AL700ICRU
0.7, 0.01, 0, 23,
```

```
AL700ICRU
0.7, 0.01, 0, 1,
AL700ICRU
0.7, 0.01, 0, 1,
AIR700ICRU
0.7, 0.01, 0, 0,
AL700ICRU
********** start of CM CHAMBER with identifier ioncham  **********
10, RMAX
Ionisation Chamber
16.4, ZMIN
0, 14, 0, N_TOP, N_CHM, N_BOT
4.5, 5, 6, RADII FOR CENTRAL PART
0.16, 0, ZTHICK, FLAG FOR LAYER 1 IN CENTRAL PART
0.7, 0.01, 0, 23,
AIR700ICRU
0.0012, 0, ZTHICK, FLAG FOR LAYER 2 IN CENTRAL PART
0.7, 0.01, 0, 8,
MYLAR700ICRU
0.1, 0, ZTHICK, FLAG FOR LAYER 3 IN CENTRAL PART
0.7, 0.01, 0, 23,
AIR700ICRU
0.0012, 0, ZTHICK, FLAG FOR LAYER 4 IN CENTRAL PART
0.7, 0.01, 0, 8,
MYLAR700ICRU
0.16, 0, ZTHICK, FLAG FOR LAYER 5 IN CENTRAL PART
0.7, 0.01, 0, 23,
AIR700ICRU
0.0012, 0, ZTHICK, FLAG FOR LAYER 6 IN CENTRAL PART
0.7, 0.01, 0, 8,
MYLAR700ICRU
0.1, 0, ZTHICK, FLAG FOR LAYER 7 IN CENTRAL PART
0.7, 0.01, 0, 23,
AIR700ICRU
0.0012, 0, ZTHICK, FLAG FOR LAYER 8 IN CENTRAL PART
0.7, 0.01, 0, 8,
MYLAR700ICRU
0.16, 0, ZTHICK, FLAG FOR LAYER 9 IN CENTRAL PART
0.7, 0.01, 0, 23,
AIR700ICRU
0.0012, 0, ZTHICK, FLAG FOR LAYER 10 IN CENTRAL PART
0.7, 0.01, 0, 8,
MYLAR700ICRU
0.22, 0, ZTHICK, FLAG FOR LAYER 11 IN CENTRAL PART
0.7, 0.01, 0, 23,
AIR700ICRU
0.0012, 0, ZTHICK, FLAG FOR LAYER 12 IN CENTRAL PART
0.7, 0.01, 0, 8,
MYLAR700ICRU
0.16, 0, ZTHICK, FLAG FOR LAYER 13 IN CENTRAL PART
0.7, 0.01, 0, 23,
AIR700ICRU
0.16, 0, ZTHICK, FLAG FOR LAYER 14 IN CENTRAL PART
0.7, 0.01, 0, 23,
AIR700ICRU
0.7, 0.01, 0, 7,   chamber wall
ALUMINA700ICRU
```

```
0.7, 0.01, 0, 7,   gap
ALUMINA700ICRU
0.7, 0.01, 0, 7,   container
ALUMINA700ICRU
0, MRNGE
*********** start of CM MIRROR with identifier mirror  ***********
6, RMAX
Mirror
18.15, 8.7, ZMIN, ZTHICK
3.2744, -3.4146, XFMIN, XBMIN
2, # LAYERS
0.0012,  thickness of layer 1
0.006,  thickness of layer 2
0.7, 0.01, 0, 9,
MYLAR700ICRU
0.7, 0.01, 0, 9,
AL700ICRU
0.7, 0.01, 0, 23,
AIR700ICRU
0.7, 0.01, 0, 23,
AIR700ICRU
*********************end of all CMs*****************************
 ##########################
 :Start MC Transport Parameter:

 Global ECUT= 0.7
 Global PCUT= 0.01
 Global SMAX= 1e10
 ESTEPE= 0.25
 XIMAX= 0.5
 Boundary crossing algorithm= EXACT
 Skin depth for BCA= 3
 Electron-step algorithm= PRESTA-II
 Spin effects= On
 Brems angular sampling= KM
 Brems cross sections= BH
 Bound Compton scattering= Off
 Compton cross sections= default
 Pair angular sampling= Simple
 Pair cross sections= BH
 Photoelectron angular sampling= Off
 Rayleigh scattering= Off
 Atomic relaxations= On
 Electron impact ionization= Off
 Photon cross sections= si
 Photon cross-sections output= Off

 :Stop MC Transport Parameter:
 ##########################
```

2. BEAmnrc *input file for the 12 MeV 10 x 10 cm² variant model* (.egsinp)

```
12MeV_10x10                                                    #!GUI1.0
AIR700ICRU
0, 0, 0, 0, 0, 2, 0,  IWATCH ETC.
300000000, 65, 59, 500, 1, 200, 2, 0,  NCASE ETC.
9, 21, 1, 0, 0, 0, 0, 0, 0, 0,  IQIN, ISOURCE + OPTIONS
```

```
/home/beamnrc/egsnrc_mp/BEAM_Synergy_Electron_Upper/12MeV.egsphsp1
0, 0, 0.7, 0.01, 0, 0, ,  0 , ECUT,PCUT,IREJCT,ESAVE
0, 0, 0, 0, 0,  PHOTON FORCING
1, 6,  SCORING INPUT
0,0
0,  DOSE COMPONENTS
26.85, Z TO FRONT FACE
********** start of CM SLABS with identifier Airgap  **********
30, RMAX
Airgap
1, NSLABS
26.85, ZMIN
4.329, 0.7, 0.01, 0, 23, 0
AIR700ICRU
********** start of CM MLCQ with identifier Xmlc  **********
21.5, RMAX
x MLC 10x10 4MeV
1, IDMLFC
31.18, ZMIN
9, ZTHICK
80, 15.28, # LEAVES, TOTAL WIDTH
-100000, ZFOCUS(1)
17, 34.93, R0LEAF, Z0LEAF
-17.1222, 17.1222, 16
-21.1916, 21.1916, 48
-17.1222, 17.1222, 16
0.7, 0.01, 0, 23,
AIR700ICRU
0.7, 0.01, 0, 12,
WNIFE700
********** start of CM MLCQ with identifier Yjaw  **********
20, RMAX
y JAW 10x10 4MeV
0, IDMLFC
43.2, ZMIN
7.7, ZTHICK
2, 15.28, # LEAVES, TOTAL WIDTH
-1000000, ZFOCUS(1)
13.5, 46.7, R0LEAF, Z0LEAF
-18.73507, 18.73507, 2
0.7, 0.01, 0, 23,
AIR700ICRU
0.7, 0.01, 0, 13,
WNIFE700
********** start of CM CONESTAK with identifier Screen  **********
14, RMAX
Screen
52.91, 0, ZMIN, RBN
1, NUMBER OF LAYERS
0.0175, 14, 14,
0.7, 0.01, 0, 12,
MYLAR700ICRU
0.7, 0.01, 0, 23,
AIR700ICRU
********** start of CM APPLICAT with identifier Applic  **********
18.25, RMAX
10 x 10 Applicator
```

```
94, ZBACK
6, 0, #SCRAPERS, SQUARE
54.22, 0.6, 7.1, 11.15, 0, 14
72.02, 0.6, 6.5, 5.4, 0, 14
72.63, 0.6, 6.5, 5.4, 0, 15
84.93, 0.6, 5.55, 4.7, 0, 15
85.54, 0.6, 5.55, 4.7, 0, 14
93.34, 0.6, 5.05, 2.25, 0, 14
0.7, 0.01, 0, 23,
AL700ICRU
AL700ICRU
PB700ICRU
PB700ICRU
AL700ICRU
AL700ICRU
********** start of CM PYRAMIDS with identifier Insert  **********
7.5, RMAX
10x10 Open Field Insert
1, 0, #LAYERS, AIR OUTSIDE
94.01, 95, 4.85, 5, -4.85, -5, 4.85, 5, -4.85, -5, 6.5, 6.5,
0.7, 0.01, 0, 23,  ECUT ETC. FOR AIR
0.7, 0.01, 0, 15,
PB700ICRU
**********end of all CMs**********
 ##########
 :Start MC Transport Parameter:

 Global ECUT= 0.7
 Global PCUT= 0.01
 Global SMAX= 1e10
 ESTEPE= 0.25
 XIMAX= 0.5
 Boundary crossing algorithm= EXACT
 Skin depth for BCA= 3
 Electron-step algorithm= PRESTA-II
 Spin effects= On
 Brems angular sampling= KM
 Brems cross sections= BH
 Bound Compton scattering= Off
 Compton cross sections= default
 Pair angular sampling= Simple
 Pair cross sections= BH
 Photoelectron angular sampling= Off
 Rayleigh scattering= Off
 Atomic relaxations= On
 Electron impact ionization= Off
 Photon cross sections= PEGS4
 Photon cross-sections output= Off

 :Stop MC Transport Parameter:
 ##########
```

3. *Phase Space Analysis*

Variant Model:

Energy (MeV)	*# Histories*	*Maximum Kinetic Energy (MeV)*	*Total Number of Particles*	*Total Number of Photons*
4	10000000	5.739	158004783	153913015
6	10000000	7.621	238812517	234397140
8	10000000	9.517	338223826	333287624
10	10000000	11.396	361078192	354253700
12	10000000	12.98	449795696	443110343
15	10000000	16.091	577995079	570828410

Invariant Model (10 x 10 cm² applicator):

Energy (MeV)	*# Histories*	*Total Number of Particles*	*Total Number of Photons*
4	18986768	44162413	43844016
6	12562156	52416995	52162022
8	8869866	65431048	65195768
10	8308449	101906958	101556238
12	6669695	98661785	98385971
15	5143927	125889288	125617360

4. *6 MeV initial energy spectrum file* (`.spectrum`)

```
6MeV Levy Scaled 0.07 Ep 7.605
199,0.01,1
0.215,0.0027
0.365,0.0028
0.515,0.0029
0.665,0.003
0.815,0.0031
0.965,0.0032
1.115,0.0033
1.265,0.0034
1.415,0.0035
1.565,0.0036
1.715,0.0038
1.865,0.0039
```

```
2.015,0.0041
2.165,0.0042
2.315,0.0044
2.465,0.0046
2.615,0.0048
2.765,0.005
2.915,0.0053
3.065,0.0055
3.215,0.0058
3.365,0.0061
3.515,0.0064
3.665,0.0068
3.815,0.0072
3.965,0.0076
4.115,0.0081
4.265,0.0087
4.415,0.0093
4.565,0.0099
4.715,0.0107
4.865,0.0115
5.015,0.0125
5.165,0.0136
5.315,0.015
5.465,0.0165
5.615,0.0183
5.765,0.0204
5.915,0.023
6.065,0.0263
6.075,0.0265
6.085,0.0268
6.095,0.027
6.105,0.0273
6.115,0.0275
6.125,0.0278
6.135,0.028
6.145,0.0283
6.155,0.0286
6.165,0.0289
6.175,0.0291
6.185,0.0294
6.195,0.0297
6.205,0.03
6.215,0.0303
6.225,0.0306
6.235,0.0309
6.245,0.0313
6.255,0.0316
6.265,0.0319
6.275,0.0322
6.285,0.0326
6.295,0.0329
6.305,0.0333
6.315,0.0336
6.325,0.034
6.335,0.0344
6.345,0.0347
6.355,0.0351
```

```
6.365,0.0355
6.375,0.0359
6.385,0.0363
6.395,0.0367
6.405,0.0372
6.415,0.0376
6.425,0.038
6.435,0.0385
6.445,0.0389
6.455,0.0394
6.465,0.0399
6.475,0.0404
6.485,0.0409
6.495,0.0414
6.505,0.0419
6.515,0.0424
6.525,0.0429
6.535,0.0435
6.545,0.0441
6.555,0.0446
6.565,0.0452
6.575,0.0458
6.585,0.0464
6.595,0.0471
6.605,0.0477
6.615,0.0483
6.625,0.049
6.635,0.0497
6.645,0.0504
6.655,0.0511
6.665,0.0519
6.675,0.0526
6.685,0.0534
6.695,0.0542
6.705,0.055
6.715,0.0558
6.725,0.0567
6.735,0.0575
6.745,0.0584
6.755,0.0593
6.765,0.0603
6.775,0.0613
6.785,0.0622
6.795,0.0633
6.805,0.0643
6.815,0.0654
6.825,0.0665
6.835,0.0676
6.845,0.0688
6.855,0.07
6.865,0.0713
6.875,0.0726
6.885,0.0739
6.895,0.0752
6.905,0.0766
6.915,0.0781
6.925,0.0796
```

```
6.935,0.0811
6.945,0.0827
6.955,0.0843
6.965,0.086
6.975,0.0878
6.985,0.0896
6.995,0.0915
7.005,0.0934
7.015,0.0954
7.025,0.0975
7.035,0.0997
7.045,0.1019
7.055,0.1043
7.065,0.1067
7.075,0.1092
7.085,0.1118
7.095,0.1146
7.105,0.1174
7.115,0.1203
7.125,0.1234
7.135,0.1266
7.145,0.13
7.155,0.1335
7.165,0.1371
7.175,0.141
7.185,0.145
7.195,0.1492
7.205,0.1536
7.215,0.1582
7.225,0.1631
7.235,0.1682
7.245,0.1735
7.255,0.1792
7.265,0.1852
7.275,0.1915
7.285,0.1982
7.295,0.2053
7.305,0.2128
7.315,0.2208
7.325,0.2292
7.335,0.2382
7.345,0.2479
7.355,0.2581
7.365,0.2691
7.375,0.2809
7.385,0.2935
7.395,0.3071
7.405,0.3217
7.415,0.3375
7.425,0.3545
7.435,0.373
7.445,0.3931
7.455,0.415
7.465,0.4389
7.475,0.4649
7.485,0.4935
7.495,0.5248
```

```
7.505,0.5592
7.515,0.597
7.525,0.6385
7.535,0.684
7.545,0.7335
7.555,0.7868
7.565,0.8432
7.575,0.9003
7.585,0.9535
7.595,0.9932
7.605,1
7.615,0.9368
7.625,0.7405
7.635,0.3586
7.645,0.0186
7.655,0
```

5. `DOSXYZnrc` 4 MeV, 10 x 10 cm^2, 95 cm SSD *input file example* (.egsinp*)*

```
WP_95_10x10_4                                                          #!GUI1.0
2
H2O700ICRU
AIR700ICRU
0.7, 0.01, 0, 0, 0
-1, -1, -1, 1
-8.1
0.2, 81
-8.1
0.2, 81
-5
0.2, 20
1, 81, 1, 81, 1, 20, 1, 1.0
0, 0, 0, 0, 0, 0, 0, 0
0, 0, 0, 0, 0, 0, 0, 0
1, 81, 1, 81, 1, 20, 1, 0
0, 0, 0, 0, 0, 0, 0, 0
2, 2, 0, 0, 0, 180, 180, 5, 0, 0, 0, 0, 0, 0
2, 0, 2, 0, 0, 0, 0, 0
/home/beamnrc/egsnrc_mp/BEAM_Synergy_Electron_Lower/10x10_4MeV.egsphsp1
700000000, 0, 500, 75, 89, 20, 1, 0, 0, 0, , 0, 0, 0, 1, 0
 ##########################
 :Start MC Transport Parameter:

 Global ECUT= 0.7
 Global PCUT= 0.01
 Global SMAX= 1e10
 ESTEPE= 0.25
 XIMAX= 0.5
 Boundary crossing algorithm= EXACT
 Skin depth for BCA= 3
 Electron-step algorithm= PRESTA-II
 Spin effects= On
 Brems angular sampling= KM
 Brems cross sections= BH
 Bound Compton scattering= Off
```

```
Compton cross sections= default
Pair angular sampling= Simple
Pair cross sections= BH
Photoelectron angular sampling= Off
Rayleigh scattering= Off
Atomic relaxations= On
Electron impact ionization= Off
Photon cross sections= PEGS4
Photon cross-sections output= Off

:Stop MC Transport Parameter:
##########################
```

6. MATLAB® Scripts

The following scripts were written to process and analyze both measurements and simulations:

PROCESSING

MEASUREMENTS		SIMULATIONS	
CAX PDDs	OAPs	CAX PDDs	OAPs
Normalization	Centralization	Extraction of CAX PDD from .3ddose file	Extraction of OAP at the depth of maximum dose from .3ddose file
	Symmetrizing	9-box (3-D) Averaging	9-box (3-D) Averaging
	Normalization	Normalization	Centralization
			Symmetrizing
			Normalization

ANALYSIS: 1-D Gamma Analysis

7. ELEKTA Proprietary Agreement

Elekta

Dr F.C.P. du Plessis
Senior Manager: Medical Physics
Universitas Hospital
BLOEMFONTEIN
Free State Our Ref. E17
Date: 28 February 2017

ELEKTA Agreement For Using Proprietary Radiation Machine Information In Research

Dear Sir,

Permission is hereby given to use proprietary information on our radiation equipment for research purposes with the following conditions;

That the information may only be used for research purposes.
That no information should be made public that could disclose the materials and exact dimensions of all components used for research purposes.
This agreement holds only for the Medical Physics department at the University of the Free State.

Yours faithfully

Yunus Munga | Business Unit Manager - Africa
Elekta (Pty) Ltd

Elekta (Pty) Ltd
2000/018814/07

Telephone
+27 11 075 1900

www.elekta.com

Maxwell Office Park
First Floor Building 3
Magwa Crescent
Waterfall City
Midrand, Johannesburg, 2090
South Africa

PostNet Suite 72
Private Bag X81
Halfway House
1685

Directors
JE Leksell (Swedish)
FG Pointurier (French)

VAT Number
402 019 1930

VITA

Karl Nicholas Sachse was born in Despatch, Eastern Cape, South Africa in 1994. In January 2013 he moved 670 km away from home to the City of Roses, Bloemfontein, to pursue his career in Medical Physics. He obtained a BMedSc (Radiation Sciences) degree from the University of the Free state in 2015 with distinction. In the following year he obtained a BMedSc Hons (with specialization in Medical Physics) degree from the same university, with distinction. In 2017 he enrolled for a MMedSc (Medical Physics) degree in Radiotherapy, where his research was performed at the Universitas Annex Hospital in Bloemfontein. The future for Karl entails a completed Medical Physics intern program and a PhD, as well as owning a music studio to record music.